

INTEGRATING *IN-SILICO* MODELS WITH *IN-VITRO* DATA TO
GENERATE NOVEL INSIGHTS INTO BIOLOGICAL SYSTEMS

DARREN CONWAY

A thesis submitted in partial fulfilment of the requirements of
Liverpool John Moores University for the degree of Doctor of
Philosophy

This research programme was carried out in collaboration with
the University of Liverpool

JULY 2018

Acknowledgements

I would firstly like to thank Steve, Chris, Andrea and Graham for giving me the opportunity to undertake this PhD and the BBSRC and LJMU for funding this work. I would also like to thank Dr Dinesh Kumar (Green lab, UoL), Dr Mark Murphy (GERI, LJMU), Dr Jo Wardyn (UoL) and Dr Mark Pogson (LJMU) for their collaboration and expertise in the completion of work for my chapters. A special thanks to Dr Joe Leedale for his incredible Matlab expertise and extremely helpful writing tips. The quality of work in this thesis has been dramatically improved through your outstanding input. Finally, I would like to personally thank Dr Steve Webb for his invaluable contribution to every aspect of my academic and personal life. I am certain I would never have reached this point without your constant encouragement and reassurance.

For making every day in work enjoyable and providing some much needed comic relief I have to thank team Webb lab. It's amazing how much procrastination can take place when such great minds come together. Outside of work, I need to thank all those who helped make Liverpool one of my second homes. There are far too many to name but I'm sure you know who you are whether we met during the MRes, in the Sherrington building, through Crown Place or from playing in the hockey or rugby teams. Special thanks however, must go to Ross and Dan. The friendship we formed during those dark MRes days has been one of the biggest reasons I will never regret choosing Liverpool for my postgraduate study. To the Irvinestown men, you get no thanks as you have been a constant and unwanted distraction. Finally, I thank Caroline for your love and support, especially during the last few months.

A special thanks to my family, especially mum, for supporting me over the last year and making sure I was well looked after. Your unconditional love and support has been greatly appreciated.

Abstract

Models and computational predictions are useful in identifying certain key parameters that play a central role in defining the overall behavior of the system, and thus lead to new and more informative experiments. In this thesis, *in-silico* models are developed over a range of individual biological scales (macroscopic, mesoscopic and microscopic) for a range of cellular phenomena (cellular interactions, migration and signalling pathways) in order to highlight the importance of combined *in-vitro* – *in-silico* investigations. It is widely accepted that Systems Biology aims to provide a simpler and more abstract framework to explain complex biological phenomena. However, integration of these models with experimental data is often underutilised. Incorporation of experimentally derived data sets into the mathematical framework of *in-silico* modelling results in reliable, well parameterised systems capable of replicating dynamical properties of the biological systems. Work in this thesis includes the development of a continuous macroscopic *in-silico* model to identify the key mechanisms of interaction between cells present within the gastric tumour microenvironment. This model of discovery is used in a predictive capacity to accept or reject hypotheses. Next, the construction of a discrete cell based model of fibroblast migration is used to determine the degree of bias fibroblast cells experience when migrating over different surface topologies. The key results from this model show that particular surface topographies can have an effect on migratory cell behaviour. Then, the parameterisation of a differential equation model is used to quantify the key mechanisms of Nrf2 regulation in the cytoplasm and nucleus. Validation with experimentally derived datasets results in the quantification of rate ratios important to the dynamics of this signalling pathway. Finally, a stochastic Petri-net model capable of simulating the dynamical behaviour of functional cross-talk between the Nrf2 and NF- κ B pathways is developed. This approach allows for the evaluation of a wide array of network responses, without the need for computationally expensive parameterisation. Together, these models exhibit how integration of *in-silico* models with *in-vitro* datasets can be used to generate new knowledge, or testable hypotheses.

Table of Contents

Chapter 1: Introduction to Systems Biology and its Applications	1
1.1 Background.....	2
1.2 <i>In-silico</i> modelling motivation	5
1.3 Mathematical models.....	6
1.3.1 Continuous vs discrete modelling	7
1.4 Continuous modelling of multicellular interactions.....	10
1.4.1 Basic organisation of the gastrointestinal tract.....	11
1.4.2 Myofibroblasts	13
1.4.3 Basic description of cancer and the tumour microenvironment.....	16
1.4.4 Cancer-associated myofibroblasts	18
1.4.5 Mechanisms of intercellular signalling	19
1.4.6 Mathematical models of the gastrointestinal tract.....	22
1.5 Discrete modelling of single cell migration	25
1.5.1 Basic cell structure	25
1.5.2 Cytoskeleton	26
1.5.3 Role the cytoskeleton plays in cell migration	30
1.5.4 The role of mechanotransduction	34
1.5.5 Replication of Extracellular Matrix (ECM) features	35
1.5.6 Mathematical models of cellular movement.....	36
1.6 <i>In-silico</i> approaches to protein signalling networks.....	40
1.6.1 Structure and function of the Nrf2 protein	40
1.6.2 Structure and function of the NF- κ B protein.....	45
1.6.3 Molecular cross-talk between Nrf2 and NF- κ B response pathways....	49
1.6.4 Mathematical models of NF- κ B and Nrf2	50
1.7 Thesis outline.....	54
Chapter 2: Systems Biology of the Tumour Microenvironment.....	56
2.1 Introduction.....	57
2.1.1 Chapter aims	59
2.2 Experimental Methods	60
2.2.1 Tissue culture	60
2.2.2 Migration assay	62

2.3	Mathematical modelling	64
2.3.1	Increased cell migration in epithelial cancer cells (AGS)	65
2.3.2	AGS cell migration appears directed.....	66
2.3.3	Model I – Simple diffusion	68
2.3.4	Model II – Density-dependent diffusion	72
2.3.5	Model III – Addition of inhibitory chemical to proximal cell migration 73	
2.3.6	Model IV - Addition of the action of an inhibitory chemical to distal cells 78	
2.4	Chapter Discussion	83
Chapter 3: Discrete Cell Based Model in Fibroblast Cell Migration.....		87
3.1	Introduction.....	88
3.1.1	Mathematical modelling of cell migration.....	89
3.1.2	Chapter aims	92
3.2	Materials and Methods	93
3.2.1	Cell culture	93
3.2.2	Cell migration assay	93
3.2.3	Measurement of cell trajectories, mean squared displacement and tortuosity	94
3.2.4	Mathematical model.....	97
3.3	Results	102
3.3.1	Cell trajectories	102
3.3.2	Experimental metrics	102
3.3.3	Applicability of the model for migration on Flat surfaces	109
3.3.4	Determination of random motility parameters.....	113
3.3.5	Determination of haptotactic responsiveness.....	118
3.4	Chapter Discussion	129
Chapter 4: Mathematical modelling of Nrf2 dynamics		133
4.1	Introduction.....	134
4.1.1	Chapter aims	135
4.2	Methods	136
4.2.1	Summary of wet lab experiments.....	136
4.2.2	Mathematical Model.....	137
4.2.3	Parameterisation and Latin Hypercube sampling.....	140

4.2.4	Fitting algorithm.....	142
4.3	Results	144
4.3.1	Nrf2 expression in cells using pDendra2.....	144
4.3.2	Model optimisation through data fitting.....	151
4.3.3	Further parameterisation of the model.....	156
4.3.4	Fitting of the experimental data	161
4.4	Discussion	167
Chapter 5:	Understanding Nrf2 and NF-κB cross-talk using <i>in-silico</i> modelling	170
5.1	Introduction.....	171
5.1.1	Overview	171
5.1.2	Chapter aims	173
5.2	Material & Methods	174
5.2.1	Stochastic Petri Net model.....	175
5.3	Results	178
5.3.1	Validation of PN model against experimental results	180
5.3.2	Characterisation of the dynamics of the pathways	184
5.4	Discussion	194
Chapter 6:	Discussion	198
Chapter 7:	Appendix	209
7.1	Appendix A – Mark Murphy lab methods	210
7.1.1	Preparation of stainless steel moulds.....	210
7.1.2	Abrasive patterned surface development	210
7.1.3	Casting polymer substrates.....	211
7.1.4	White light interferometry for surface characterisation	212
7.2	Appendix B – Chris Sanderson lab methods.....	213
7.2.1	Live Cell Imaging.....	213
7.2.2	Lambda Scan	214
7.2.3	pDendra2 Imaging.....	215
7.2.4	Image Analysis.....	215
7.2.5	Fluorescence Cross Correlation Spectroscopy (FCCS)	216
Chapter 8:	Bibliography.....	217

List of abbreviations

Abbreviation	Definition
HGP	Human Genome Project
ECM	Extracellular matrix
ODEs	Ordinary differential equations
PDEs	Partial differential equations
CA	Cellular Automata
IBMs	Individual Cell-Based Models
GI	Gastrointestinal
308 cells	Barrett's adenocarcinoma cancer-derived myofibroblasts
AGS cells	Gastro adenocarcinoma cancer cells
ECL	Histamine-secreting enterochromaffin-like cells
CCK-2	Cholecystokinin-2
α -SMA	Alpha-smooth muscle actin
EMT	Epithelial Mesenchymal transition
MSCs	Bone-marrow-derived mesenchymal cells
TGF- β 3	Transforming growth factor-beta 3
CAMs	Cancer associated myofibroblasts
TLRs	Toll-like receptors
MHC	Major histocompatibility complex
MMPs	Matrix metalloproteinases
uPA	Urokinase-like plasminogen activator
tPA	Tissue-type plasminogen activator
PAI-1	Plasminogen activator inhibitor-1
ADAMs	A disintegrin and metalloproteinase
ADAMTs	ADAMs with thrombospondin
IGFBP3	Insulin-like growth factor binding protein-3
FGF	Fibroblast growth factor
IGF	Insulin-like growth factor
TGF- β	Transforming growth factor-beta
MMP7	Matrilysin
IGFBP-5	Insulin-like growth factor binding protein-5
NTMs	Normal tissue myofibroblasts
CCK	Cholecystokinin
SST	Somatostatin
ICC	Interstitial cells of Cajal
SMC	Smooth muscle cells
MRI	Magnetic resonance imaging
FE	Finite element
FD	Finite difference
VPH	Virtual Physiological Human
ER	Endoplasmic reticulum
G-actin	Actin monomer
F-actin	Actin filament
IFs	Intermediate filaments

GFAP	Glial fibrillary acid protein
MTOCs	Microtubule organising centres
FAK	Focal adhesion kinase
CRWs	Correlated random walks
ROS	Reactive oxygen species
Nrf2	Nuclear factor erythroid 2–related factor 2
AP-1	Activator protein-1
CNC	Cap'n'Collar family of proteins
bZIP	Basic leucine zipper proteins
sMAF	Small MAF proteins
ARE	Antioxidant response element
Keap1	Kelch-like ECH-associated protein
Rbx1	Ring box 1
Cys	Reactive cysteine residues
GSK-3	Glycogen synthase kinase 3
NF-κB	Nuclear factor-κB
DUB	Deubiquitinating enzyme
RIP	Receptor interacting protein
SFP	Sulforaphane
CDDO-Im	2-cyano-3,12 dioxooleana-1,9 dien-28-imidazolide
PN	Petri-net
DMEM	Dulbecco's modified Eagle's medium
PBS	Phosphate buffered saline
FBS	Foetal bovine serum
FM	Full medium

Chapter 1: Introduction to Systems Biology and its Applications

1.1 Background

In this thesis, systems biology is used to model and discover emergent properties over multiple individual scales in biological systems. This holistic approach provides a greater insight into the systems as a whole, while also allowing dynamic and quantitative conclusions to be drawn. One of the advantages of the work carried out in this thesis, upon which the novelty and importance is also highlighted, is that experimentally derived raw data is used as the basis for the creation of the mathematical models within. Utilising experimental data in this way allows for the depiction of more accurate and robust models. This distinction is important for drawing conclusions from the models, both qualitatively and quantitatively, and can provide the platform for the design of further experimentation for validation or in a predictive capacity.

Systems biology is the computational and mathematical modelling of complex biological systems [1]. It is an interdisciplinary field of study that focuses on complex interactions within biological systems, using an integrated approach to biological research. Systems biology can be seen as an umbrella term which encompasses a variety of peripherally overlapping concepts, such as: applied mathematics [2], computational biology [3], quantitative systems pharmacology [4], integrative biology [5], systems biomedicine [6] and synthetic biology [7]. Almost two decades ago, the term was launched into the mainstream in correlation with the completion of the Human Genome Project (HGP) [8]. However, the origins of systems biology can be traced back even further, to the middle of the 20th century. For example, in 1973 the theory of metabolic control was developed and as a result, metabolic flux was

recognised as a systemic property [9]. From the completion of the HGP, interest in systems biology has increased, as evidenced by the increasing number of papers published in the field each year (Figure 1-1). This emergence can be attributed to the development of new and increasingly powerful computational approaches. It is this improved computational power that drives the evolution of systems biology, as more complex and sophisticated systems are created. This development falls under Moore's law [10] which states that the overall processing power of computers will double every two years. To put this into context, the HGP took 13 years to complete whereas, in the last few years, a full human genome can be sequenced in less than 24 hours [11].

Biological systems consist of a large number of functionally diverse components, which can interact in highly specific and non-linear ways to produce phenomena such as cell migration, cell signalling and gene transcription. Typically, the models used in systems biology require iterative building and stepwise improvements based on comparison with experiments [1]. These models, once sufficiently refined, can then be used to predict the behaviour of the biological system under different perturbations that may be of interest or simply deemed unfeasible in an experimental setting. This is particularly beneficial when it comes to estimating rate constants on reactions that take place rapidly *in-vitro*. The various models used in systems biology can have significant differences depending on several factors, relating to the scope of the study, such as: the level of description in the model, limitations in the knowledge of the biological system or the ability to observe the phenomena of interest experimentally for validation. For example, this thesis focuses on the dynamic behaviours of cellular interactions at multiple individual biological

scales, i.e. the multicellular (tissue) level, cellular level and cell signalling networks at the subcellular (molecular) level. At each individual scale, different systems biology approaches are utilised in this thesis.

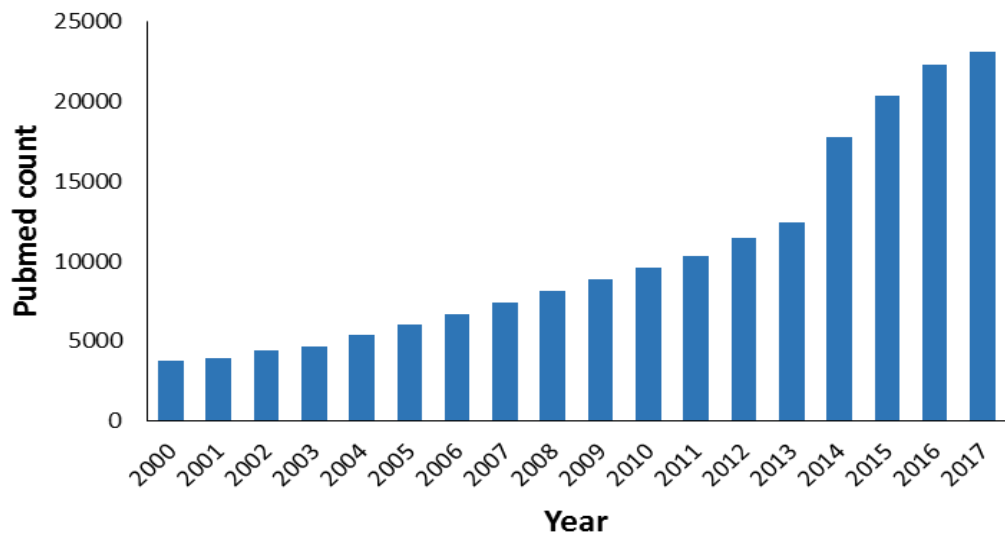


Figure 1-1. Search results for systems biology on Pubmed [12]. The number of papers referencing “systems biology” in the Pubmed database are organised by year of publication (2000-2017). In 2017, there were 23,070 results compared with 3,773 results in 2000.

1.2 *In-silico* modelling motivation

In the current age of technology, the high number and diversity of experimental data available has never been as easy to access [5]. The data available ranges from simple processes, such as enzymatic reactions, to the more complex, such as gene transcriptions in response to inflammatory stimuli of the cell. Regardless, representative models of these systems can be designed based on this empirical data. Thus, by combining raw experimental data with mathematical modelling, a more accurate model can be created, as it is designed with less theoretical assumptions and unknown parameter estimates. Another advantage when using an *in-silico* approach, rather than traditional biological techniques, is that the modelling algorithms can be reused many times and applied to differing biological systems. Not only does this provide a more cost-effective method, compared with organism-dependent experiments, but also allows for the replacement, reduction and refinement of animal-based experiments [13]. Systems biology is a powerful tool that can aid in the understanding of the dynamics of disease mechanisms, ranging from cancer [14] to degenerative disease [15], and can also be utilised in drug discovery [16]. These approaches have already provided a deeper understanding of diverse biochemical processes from individual metabolic pathways [17], signalling networks [18] and genome-scale metabolic pathways. Therefore, the continued development of *in-silico* models is an important endeavour to facilitate and enhance our understanding of key biological processes.

1.3 Mathematical models

All biological phenomena emerge from an intricate interconnection of multiple processes occurring at different levels of organisation. These levels include the tissue, cellular and molecular level which can be approximately connected to macroscopic (10^{-5} m), mesoscopic (10^{-6} m) and microscopic (10^{-7} m) scales, respectively [19,20]. The macroscopic scale typically corresponds to behaviours such as cell population dynamics and tissue mechanics. Adhesive interactions, between cells or between cells and the extracellular matrix (ECM), and mechanisms of cell motility are common phenomena observed at the mesoscopic scale. Finally, the microscopic scale refers to processes such as DNA signalling, activation of receptors and the transport of proteins (cell signalling networks) [21].

An exhaustive *in-silico* model would incorporate all these levels in a multiscale fashion. However, a valuable approach in systems biology is to build a model as simply as possible, focused on a single scale and based on a minimal set of assumptions that can be derived from experimental observations. This is the approach selected for the work incorporated within this thesis. Each model is contained within a singular scale, so as to capture the dynamics of the critical components examined. Gradually, it is then possible to add more components and complexity to the model, after refining and validating against experimental results. In turn, this allows for a concise description of the essential features of the system of interest, whilst also providing the possibility of identifying the most relevant mechanisms and parameters.

1.3.1 Continuous vs discrete modelling

There are many mathematical approaches to these problems which can broadly be defined into two main categories: continuous and discrete models. Additionally, there can be further classifications into deterministic or stochastic models, depending on whether they contain a degree of randomness. Continuous modelling can be described as the application of mathematics to continuous data, i.e., it generally doesn't require data, just the use of continuous variables [22]. This approach is characteristic of a macroscopic point of view, as these methods represent populations of biological identities, such as e.g., epithelial cells, as densities. This modelling strategy includes using systems of ordinary differential equations (ODEs) and partial differential equations (PDEs) to solve for transient or steady state solutions [22]. Traditionally, systems of ODEs have been used to represent chemical reactions, using the law of mass action kinetics [23,24]. This law is defined as the rate of a chemical reaction being directly proportional to the concentration of the reactants [25]. In most cases, ODEs contain one or more functions of an independent, continuous variable and the derivatives of the functions with respect to that variable. These equations can be used to model dynamics over time. Whereas, PDEs typically contain multivariable functions and can be used to determine multidimensional patterns in the data and model dynamics over several independent variables, e.g., spatial variables in addition to time [22]. Conversely, discrete models can be used to represent biological individuals (e.g. focusing on the cellular level), as a set of discrete units with rules describing the interactions and movements of individual cells. Examples of these models are Cellular Automata (CA)

[26,27] and Individual Cell-Based Models (IBMs), also known as Agent-Based Models (ABMs) [28].

Given the same parameters and initial conditions, deterministic models will produce the same result after each simulation, as there is no random element. While, stochastic models provide distributions of simulated outcomes as opposed to a single result [5]. Therefore, deterministic approaches are more suitable for modelling systems with large numbers of components, where the impact of small fluctuations is negligible. Stochastic approaches are more appropriate for modelling systems with a small number of components, where the impact of these small fluctuations is more relevant within the system. However, utilising both approaches is sometimes key for creating accurate models of large systems. One of the biggest challenges with these models is accurately obtaining parameter and rate constant values. These models form an iterative series of model building and simulation processes that are driven by hypotheses to understand how biological systems function as a network of biochemical reactions [29]. Linking models and data requires numerical values for all the mathematical parameters that describe the system of interest. A traditional approach to this challenge is to collect parameter values through a literature search. However, inferring the parameters from available experimental data would be a much more preferable method [30,31]. Optimisation-based approaches aim to reduce the discrepancy between the model predictions and experimental data by searching through parameter combinations [32]. Robustness and confidence in these optimised parameters presents a challenge also, as many parameter combinations could provide locally optimal fits [33]. Therefore, it is important to take measures to avoid over-fitting the data. Calibration with experimental data by fitting from initial

parameter estimates represents a routinely practiced method for obtaining these values. In general, *in-silico* model development can be broken down into the following initial steps [34]:

- 1) Make initial assumptions of what is influencing the observed experimental behaviour based upon the data.
- 2) Derive a system of differential equations (the model) to describe the dynamic events taking place.
- 3) Parameterise the model
- 4) Solve the model equations.
- 5) Verify the results by comparing the model simulations to the data using various statistical tests.
- 6) If the verification is unsuccessful, alter the model and repeat verification process.

1.4 Continuous modelling of multicellular interactions

In multicellular organisms, there are evolutionary advantages conferred by the differentiation of cells into different types with specialised functions. Coordinated cell-cell interactions become vital in maintaining the organisation and function of tissues containing multiple cell types, both in development and in tissue repair. In the gastrointestinal (GI) tract, for example, interactions between epithelial cells and stromal cells control cell proliferation, differentiation and apoptosis. These interactions are disrupted in a variety of diseases including inflammatory conditions and cancer. Since inflammation is recognised as a driver of cancer progression [35], there has been a growing appreciation of the role that cellular microenvironments play in carcinogenesis. Amongst the various cells contributing to the tumour niche, myofibroblasts have been highlighted by many studies [36-38]. These cells normally play an important role in the maintenance of tissue architecture and wound healing [39-42]. Myofibroblasts are a rich source of growth factors, cytokines, chemokines, extracellular matrix (ECM) proteins, proteases and their inhibitors [43]. However, the functional role of myofibroblasts in many cancers is not well understood. One of the aims in this thesis is to investigate the effect that Barrett's adenocarcinoma cancer-derived myofibroblasts (308 cells) have on gastro-adenocarcinoma cancer cells (AGS cells) and to develop a mechanistic model describing this interaction (Chapter 2). I begin by describing the environment that both these cell types reside within and how they behave *in-vivo*, i.e., their cellular phenotype and secretory profile.

1.4.1 Basic organisation of the gastrointestinal tract

The upper gastrointestinal tract, which consists of the salivary glands, oesophagus, stomach and the small intestine, functions to aid food digestion and nutrient absorption. The wall of the gastrointestinal tract is divided into layers: an outer muscle layer; a mucosal layer consisting of epithelial cells that continuously line the luminal surface; and a stromal layer, the lamina propria, consisting of blood vessels, ECM, lymphatics, inflammatory cells, immune cells, fibroblasts and myofibroblasts [44].

There are five main regions in the stomach: i) the cardia; ii) the fundus; iii) the corpus; iv) the pyloric antrum; and v) the pyloric sphincter [45]. The epithelium, within the stomach, is folded into gastric glands (Figure 1-2). The glands found in the fundus and corpus are populated by histamine-secreting enterochromaffin-like (ECL) cells, acid-secreting parietal cells and chief cells that release pepsinogen, whereas the glands found in the antrum are populated by gastrin-secreting G cells [46]. This antral hormone, gastrin, stimulates gastric acid secretion in parietal cells via the induction of histamine-secretion in ECL cells. Gastrin binds to cholecystokinin-2 (CCK-2) receptors expressed in ECL cells, inducing the synthesis and secretion of histamine. Then, histamine binds to its H₂-receptor on the surface of the parietal cells resulting in the secretion of gastric acid [47].

The maintenance of the gastrointestinal tract epithelium is achieved through the proliferation and differentiation of epithelium stem cells. The cells exhibit bidirectional movement towards the surface or base of the glands [48]. Cells moving up to the pit region from the isthmus differentiate into mucus-secreting cells,

whereas cells moving towards the gland base region differentiate into parietal and chief cells [49,50]. There is a tight network of myofibroblasts around the gastric glands that are thought to determine organisation and function of the epithelial cells.

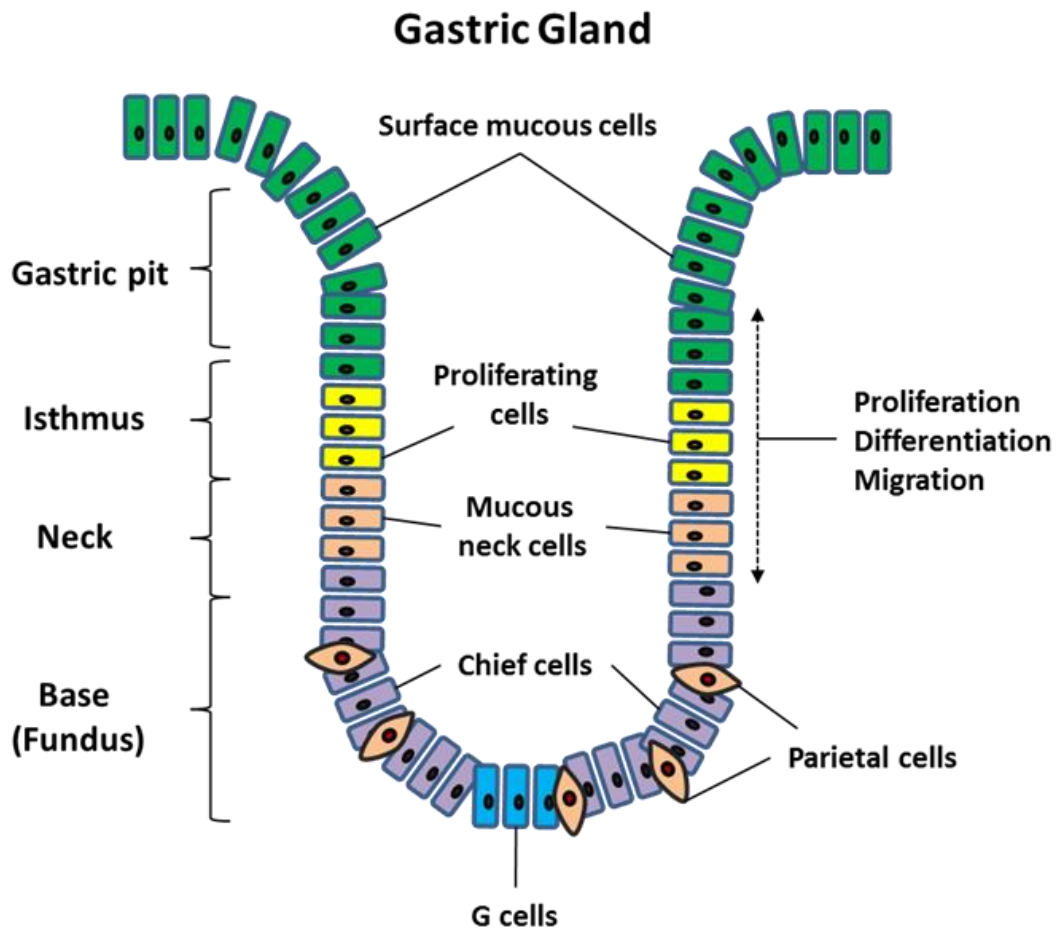


Figure 1-2. Schematic diagram of a gastric gland. Diagram showing the different cell types present in a gastric gland: surface mucous cells, proliferating cells, mucous neck cells, chief cells, G cells and parietal cells. The bi-directional migration of the cells occurs from the isthmus region to the gastric pit and the fundus region generating the differentiated cell types. Adapted from [45].

1.4.2 Myofibroblasts

Myofibroblasts are activated fibroblasts. They are dynamic, spindle-like cells sharing the functional characteristics of both fibrocytes and smooth muscle cells [51]. They are rarely found in most tissues, but in the gastrointestinal tract they are relatively abundant, where they are localized in a sub-epithelial compartment. Myofibroblasts express alpha-smooth muscle actin (α -SMA) and vimentin, which are specific histopathological markers of these cells. A variety of different origins of these cells have been discussed by a number of authors, including: (a) rapid stimulation of local fibroblasts to differentiate into myofibroblasts [52]; (b) epithelial cell transdifferentiation into myofibroblasts via epithelial mesenchymal transition (EMT) [37,53]; (c) local or bone-marrow-derived mesenchymal stem cells (MSCs) transformation into myofibroblasts [54].

Myofibroblasts are rarely found in healthy tissue. However, as described previously, they are abundant in the gastrointestinal tract and are also found to increase during wound healing within the tract. The key events that characterise GI tract wound healing include restitution after tissue damage, inflammation, re-epithelisation and tissue remodelling [55]. Restitution is defined as an epithelial migratory response to superficial damage in the gut by which a protective layer of epithelial cells is formed over the injured site [56]. In damaged tissue, fibrin forms a provisional ECM [57,58] that embeds platelets which are an early source of growth factors and chemokines, required to further drive coordinated wound healing [59,60]. Myofibroblasts regulate this migration and proliferation through the secretion of transforming growth factor-beta 3 (TGF- β 3), maintaining the integrity of the epithelium [61].

Myofibroblasts that reside in the cancer niche exhibit changes to their phenotype; they are designated “cancer associated myofibroblasts” (CAMs) (Section 1.4.4) [62].

There is also a role for myofibroblasts identified in mucosal immunology. Intestinal myofibroblasts have been associated with innate immune responses through regulation and expression of toll-like receptors (TLRs) [63]. When stimulated with bacterial lipopolysaccharide or lipoteichoic acid, the expression of TLR-2, TLR-3, TLR-4, TLR-6 and TLR-7 in intestinal myofibroblasts is increased, leading to the secretion of pro-inflammatory cytokines and chemotactic factors that recruit immune cells to sites of inflammation [63]. Furthermore, the expression of class II major histocompatibility complex (MHC) molecules in colonic myofibroblasts has been found, suggesting that these cells may function as antigen-presenting cells which activate CD4-positive T-cells during activation of adaptive immunity [64].

In addition, myofibroblasts have been shown to deposit ECM proteins (e.g. collagens, laminins and fibronectin) and secrete ECM-degrading proteases which regulate turnover of the ECM [65]. These proteases are classified into matrix metalloproteinases (MMPs); serine proteases, such as urokinase-like plasminogen activator (uPA) and tissue-type plasminogen activator (tPA); and cysteine proteases, such as collagen degrading cathepsins [66]. Fibrosis is the result of excessive deposition of ECM proteins, often with loss of some resident cell types, but increased numbers of myofibroblasts. Inefficient removal of scar matrix proteins leads to fibrosis [67]. Plasminogen activator inhibitor-1 (PAI-1) is an inhibitor of uPA and tPA. uPA regulates plasmin abundance, degradation of ECM proteins and also plays a role in activating MMPs [68]. The MMPs, which belong to a family of zinc-dependent

endopeptidases, are involved in physiological processes (e.g. embryonic development, wound healing) and cancer progression [69]. A total of 28 human MMPs has been identified, and they are classified into five main categories according to their substrate specificity, primary structures, and cellular localization, namely, the matrilysins (e.g. MMP7), collagenases (e.g. MMP1), stromelysins (e.g. MMP3), gelatinases (e.g. MMP2), and the membrane-type MMPs (e.g. MMP14) [70]. Other members of the metalloproteases include a disintegrin and metalloproteinases (ADAMs), which are transmembrane proteins, and ADAMs with thrombospondin motifs (ADAMTS), which are secreted and bound to ECM proteins [66].

The MMPs are synthesised as inactive zymogens (i.e. pro-MMPs) and mostly become activated after proteolytic cleavage within the extracellular environment [71]. The activity of MMPs is low in the normal state, and can be induced in response to external stimuli. For example, proinflammatory cytokines stimulate the secretion of MMP1, MMP2 and MMP3 in colonic myofibroblasts [72,73]. In intestinal and gastric myofibroblasts, the expression of MMP1, MMP2 and MMP3 has also been identified, suggesting the importance of these MMPs [74]. Substrates for MMP1, such as perlecan and insulin-like growth factor binding protein-3 (IGFBP3), have been shown to increase the bioavailability of fibroblast growth factor (FGF) and insulin-like growth factor (IGF), respectively [75]. Additionally, studies have shown the proteolytic activation of transforming growth factor-beta (TGF- β) by MMP2, and the cleavage of E-cadherin, an epithelial adhesion molecule, by MMP3 [71].

Matrilysin (i.e. MMP7), which is predominantly expressed in epithelium, is implicated in regulating myofibroblast function [74]. Gastro-epithelial cells secrete matrix metalloproteinase-7 which cleaves insulin-like growth factor binding protein-5

(IGFBP-5) secreted by myofibroblasts leading to release of IGF-II which stimulates both epithelial and myofibroblast proliferation [74].

The gastrointestinal tract is normally exposed to many different potentially damaging agents including acid, ingested toxins, resident and ingested microbiota. In the upper gastrointestinal tract, failure of the normal protective mechanisms is a feature of several common conditions including pathology associated with gastric infection with *Helicobacter-pylori*, and reflux of gastroduodenal contents into the oesophagus. In both cases chronic inflammation is associated with increased risk of cancer.

1.4.3 Basic description of cancer and the tumour microenvironment

Cancer can be described as a wound that fails to heal, indicating that there is a correlation between the mechanisms of wound healing and tumour cell response to inflammation [76]. Moreover, it is well established that abnormal secretion of growth factors and cytokines, dysregulation of signalling pathways, and genetic alterations all play a role in the promotion and progression of tumour growth. Famously, Hanahan & Weinberg [77] proposed the six hallmarks of cancer that dictate cancer growth and malignancy. These hallmarks are as follows: 1) self-sufficiency in growth signals, 2) insensitivity to anti-growth signals, 3) tissue invasion and metastasis, 4) limitless replicative potential, 5) sustained angiogenesis and 6) evading apoptosis. However, in addition to these hallmarks, it is stressed that there is also a key contribution of genetic and epigenetic alterations in cancer cells. Epithelial cells are characterised by having tight cell-cell adhesions, forming a continuous sheet that functions as a barrier. However, for tumour epithelial cells to become invasive, these tight adhesions must be shed in favour of loose cell-cell contacts, obtaining

mesenchymal properties. This process is known as EMT and is a key process in wound healing, fibrosis and metastasis of cancer [78]. Tumour stromal cells, such as cancer-associated myofibroblasts (CAMs), play a role in promoting tumour angiogenesis (formation of new blood vessels from previous vessels), cancer cell growth and invasion through ECM remodelling (Figure 1-3). These cells also activate cancer cell signalling pathways through the secretion of cytokines and growth factors [79].

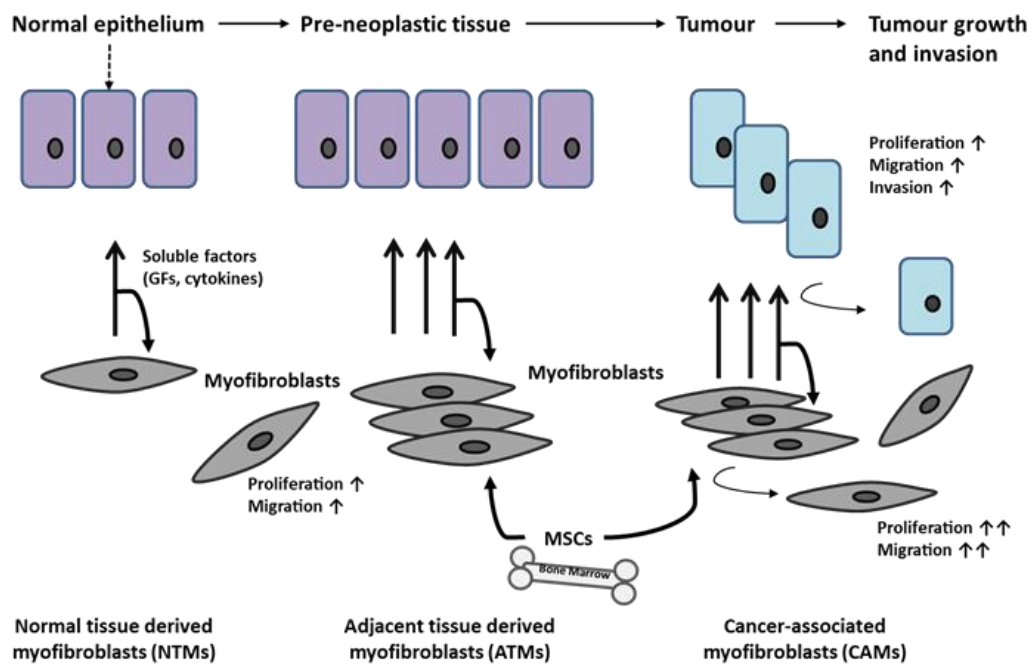


Figure 1-3. Epithelial-stromal interactions in tumour formation and progression. In normal mucosa, myofibroblasts (NTMs) are involved in regulating epithelial cell function. Chronic inflammation contributes to the formation of cancer through genetic and epigenetic changes of epithelial and myofibroblast cells in pre-neoplastic tissue. Paracrine signalling between cancer cells and CAMs result in cell growth and invasion. Myofibroblast populations are increased by bone marrow derived MSCs in cancerous tissue. This chemical environment supports EMT, metastasis and tumour growth. Adapted from [80].

The tumour microenvironment consists of ECM, blood vessels, soluble paracrine factors and non-malignant stromal cells, such as CAMs, endothelial cells and inflammatory cells [81]. Malignancy of the tumour and suppression of the anti-tumour immune response are products of the role these inflammatory cells have within the cancer niche [35]. Endothelial cells also contribute to this malignancy by maintaining normal physiology of the neoplastic blood vessels [82]. Non-malignant stromal cells, such as these, migrate into the tumour site from distant locations within the body. However, the cancer niche also depends on resident stromal cells from surrounding and neighbouring tissue, such as the myofibroblast. Stromal cells progressively increase in cancer either through inward migration, proliferation or transdifferentiation from other cell types [81]. In GI tumours, stromal cells constitute 60-90% of the mass of the tumour, with CAMs showed to play a crucial role in tumour progression [83].

1.4.4 Cancer-associated myofibroblasts

These cells undergo changes at the epigenetic level and a difference in gene expression [84] has been detected in CAMs from gastric cancer compared with “normal tissue myofibroblasts” (NTMs) [85]. This differential expression of genes relates to various cellular functions such as cancer cell proliferation, migration and invasion [79,86,87]. CAMs are phenotypically more migratory and proliferative compared to myofibroblasts from non-cancerous stroma [88,89]. The functional role of myofibroblasts in cancer cells is not well understood. However, they have been shown to influence proliferation and metastasis of cancer through disruption of autocrine and paracrine signalling pathways [43,90]. It has also been shown that cross-talk between CAMs and epithelial cancer cells, termed stromal-epithelial

interactions, promotes cancer cell growth and induces malignant transformation [79]. A decreased sensitivity to chemotherapy has also been demonstrated in CAMs, partly due to hypermethylation of CpG DNA and reduced expression of caspase and STAT-1 resulting in escape from apoptosis of cancer cells [91].

1.4.5 Mechanisms of intercellular signalling

Cell-cell signalling is mediated by various substances including hormones, growth factors, cytokines and chemokines [92,93]. In each case, a ligand activates receptors on target cells. Where ligands are released in close proximity to target cells the mechanisms are collectively known as paracrine signalling. Where they are carried in the blood stream to their targets the mechanisms are known as hormonal signalling [94]. In some cases, ligands may even act on their cell of origin, known as autocrine signalling [95]. Within a tissue, there are frequent interactions that are two-way. An example of this is epithelial-stromal cell interactions, where both cell types can be the source of signalling ligands and can respond to them by paracrine mechanisms (Figure 1-4).

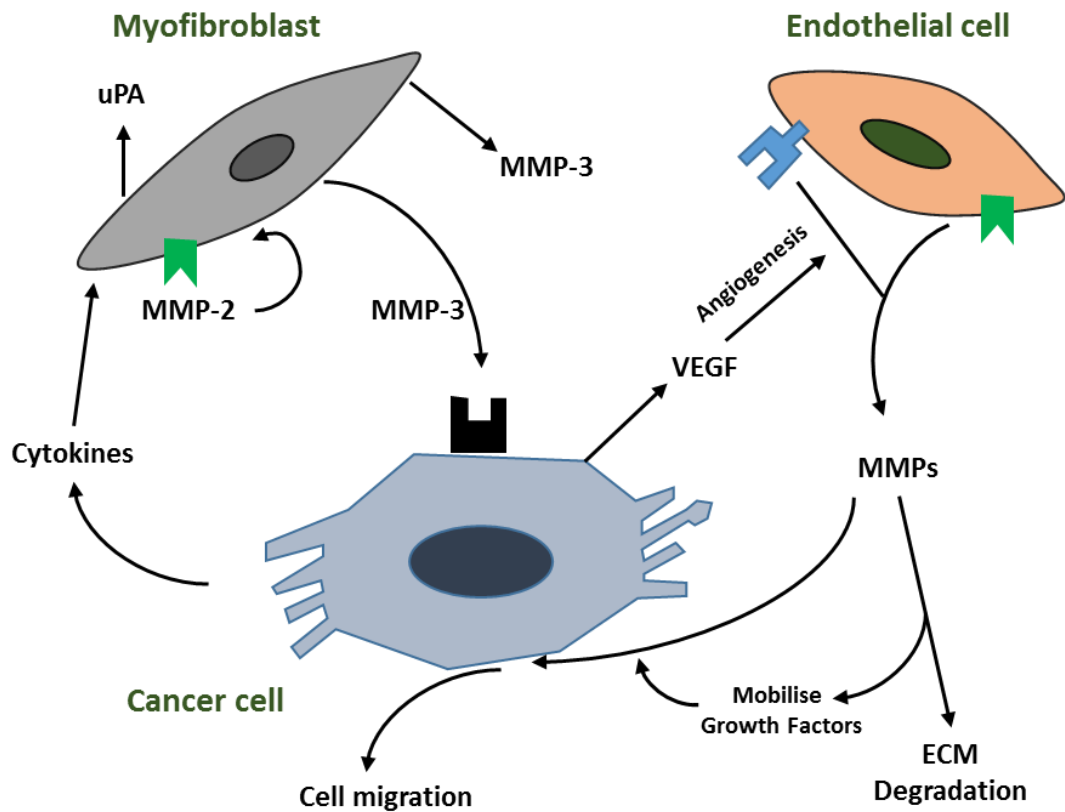


Figure 1-4. Schematic diagram highlighting paracrine and autocrine signalling within the tumour microenvironment. Cytokines released by the cancer cell stimulate the myfibroblast cell to release MMPs and uPA. VEGF is also released by the cancer cells and promotes angiogenesis. MMPs released by the myfibroblast activate receptors in the cancer cell as well as the myfibroblast's own receptors. The continued release of these compounds results in cell migration, ECM degradation and continued release of growth factors, cytokines and chemokines. Adapted from [96].

Gut hormones are shown to be involved in regulating gut secretion, motility and growth. The best characterised of these include gastrin, cholecystinin (CCK), secretin and somatostatin (SST) [97]. Cancer cells, stromal cells and epithelial cells are all potential sources of growth factors. There are multiple classes of growth factors including the families of EGF, IGF, VEGF, TGF- β , HGF, FGF, PDGF, Wnt, Hedgehog and Notch [98-102]. Most of these growth factor families play a role in GI mucosal regeneration [103]. Many cytokines, which are small cell signalling

molecules, are upregulated in cancer. They stimulate growth, differentiation and activation of immune cells [104]. Thus, they can either be classified as immunoregulatory or pro-inflammatory [104]. Chemokines are defined as chemotactic cytokines [105]. They are involved in metastasis and are vital for the infiltration of immune cells into the tumour site. Typically, the chemokines expressed in cancer belong to the inflammatory group and are induced by pro-inflammatory stimuli [105].

As previously described, in order for the cancer cells to invade normal tissue, they must undergo EMT. Therefore, loss of cell adhesions and removal from the primary site is necessary. A study has shown that E-cadherin was higher when cancer cells were co-cultured with fibroblasts as opposed to cancer cells that were cultured in isolation [106]. Contrastingly, when these cancer cells were co-cultured with CAMs, the expression of E-cadherin was downregulated, highlighting the possible role CAMs play in the EMT of epithelial cancer cells [106]. TGF- β is also a known inducer of EMT in epithelial cells and plays a crucial role in tumour progression by downregulating epithelial adhesion molecules [107]. TGF- β can be secreted by both cancer cells and CAMs within the primary tumour site. When secreted by cancer cells, TGF- β can also induce expression of MMP-9 in myofibroblasts. MMP-9, along with MMP-2, selectively degrades the components of the basement membrane, further contributing to the proliferation of the tumour [108]. Another well-known mechanism in cancer is that many neoplastic cells secrete VEGF, which plays a crucial role in angiogenesis, an essential mechanism for the development of tumour malignancy [109]. The role of CAMs in this process has not been clarified. However, many types of fibroblast have been shown to release VEGF in response to IL-6. It has

been demonstrated that myofibroblasts and CAMs secrete the same amounts of IL-6 when stimulated with TNF- α , an inflammatory factor [110]. Therefore, it can be hypothesised that some cytokine released from the cancer cells promotes transition of myofibroblasts to CAMs, resulting in the secretion of IL-6. Reports show that IL-6 plays an important role in cancer progression [108]. Finally, it is suggested that the CAMs use paracrine and autocrine signalling to increase the proliferation of cancer cells, as well as the continued activation of the CAMs themselves, through unregulated secretion of pro-inflammatory and pro-tumourigenic molecules.

1.4.6 Mathematical models of the gastrointestinal tract

Current mathematical models of the GI tract focus mainly on the electrical activity of the stomach wall, specifically, the electrical activity that organises motility of cells [111-114]. All these models incorporate a multiscale approach combining complex experimental findings with sophisticated systems biology techniques (i.e. such as biophysical models [115], channelopathy models [116,117], smooth muscle cell models [118] and gastric electrophysiology models [111]) to create a 'Virtual Stomach' [114]. The experiments focus on co-regulation of gastric waves from spontaneous depolarisations of interstitial cell of Cajal (ICC) membrane potentials and smooth muscle cells (SMC), ultimately generating GI motility [119]. Anatomically realistic models were generated using magnetic resonance images (MRI) and CT scans, creating over 60,000 data points [111]. Simulation of the electrical activity of the stomach was achieved by adapting an existing finite element (FE) derived finite difference (FD) continuum model used for solving cardiac activation problems [120]. This model has been shown to successfully replicate many of the electrical features of the stomach, by solving five ODEs, to include the coupling of ICC-ICCs, ICC-SMCs

and SMC-SMCs. These models are still in their infancy and further refinement and validation is needed for a wider application [111]. For a detailed review of these models and the Virtual Physiological Human (VPH) see [112] and [121]. Alternatively, there are also models of intestinal crypts [122,123], which are similar but not identical to gastric crypts. Meineke et al. [122] present a lattice-free model representing the spatial arrangement and migration of cells within the intestinal crypt based upon a scoring system. This model also include cell division, where daughter cells form at the bottom of the crypts and existing cells shift upwards. Similarly, the work of Van Leeuwen et al. [123] incorporates cell division and replacement of the cellular epithelium within the intestinal crypt structure. Furthermore, the model has been extended to multiple scales meaning that subcellular cell signalling events affect the mechanical cues of the cell migration.

It is evident from reviewing the literature that there are currently no computational approaches dedicated to the relationship between gastric cancer cells and CAMs. However, there are many models of cancer present in the literature, such as those models which describe stochastic and deterministic models of structured populations [124-127]. There are several themes present in these models that can be applied to the biological problem our current model is trying to answer. The first is to assume a constant population size in the cell mass [124]. At a macroscopic scale, the number of cancer cells in a given area may be approximated by a continuous density. This can be given by PDEs and any random spatial movements by the cells can be approximated as diffusion [125]. Not only can PDEs model the dynamics of tumour cell density, they can also model the tumour cells dependence on other diffusive factors, such as chemokines [126]. More sophisticated models exist where

the position, movement and state of each individual cell can be represented. This type of model is known as CA [127]. The dynamics of the cells in CA models are governed by a set of rules taking into account interactions with neighbouring cells and stimuli. The advantage of having each cell explicitly modelled is outweighed by the computational cost in this instance, as the aim is to develop a model that will highlight the dynamic behaviour between the cell populations of the gastric cancer cells and the CAMs.

1.5 Discrete modelling of single cell migration

1.5.1 Basic cell structure

The basic mammalian eukaryotic cell comprises of a variety of membrane-bound structures, a cytoplasm and a nucleus. Through the advancement of microscopy techniques, the basic structure and function of these fundamental units of life unfolded. Working inwards, the cell membrane is the outer boundary of the cell consisting of a bilayer of phospholipids [128]. The polarity of this double layer helps to facilitate the cell membranes role of regulating the exchange of substances between the external and internal cellular environments. The membrane surrounds the cytoplasm, which comprises cytosol (gel-like substance) and the organelles [129]. The major organelles suspended within the cytosol are the mitochondria, endoplasmic reticulum (ER) and the Golgi apparatus [130]. The mitochondria is the powerhouse of the cell and generates energy through a process called oxidative phosphorylation [131]. The ER is a transport network and one of its main functions is to transport newly synthesised proteins to the Golgi apparatus. The Golgi apparatus then completes the process of synthesising the proteins by packaging them in vesicles ready for exocytosis [130]. Finally, the nucleus is a membrane bound organelle responsible for controlling gene expression and replicating DNA during the cell cycle [132]. A cytoskeleton is also present in all mammalian cells. The cytoskeleton acts to maintain cell shape, anchor organelles in place and provide mechanical resistance to deformation [133].

1.5.2 Cytoskeleton

There are three cytoskeletal systems in mammalian cells: the actin cytoskeleton, the intermediate filament network and microtubules; all of which are involved in the regulation of cell motility. All three networks are interconnected and they are anchored at cell-ECM adhesions and at cell-cell junctions, providing the cell body with mechanical support [134]. The complexity of the cytoskeleton and its associated proteins have become clear through the advancement of molecular techniques. For example, it is widely understood that the cytoskeleton provides a structural framework for the cell, determining cell shape and cytoplasmic organisation, as well as being responsible for cell movements and internal transportation of organelles and other structures within the cytoplasm (Figure 1-5) [129]. In addition, disorganisation of the cytoskeleton has been associated with many pathological conditions, including cancer and cardiovascular diseases [135].

1.5.2.1 The actin cytoskeleton

The actin monomer (G-actin) is the basic building block of the actin filament (F-actin) [136]. Dimers and trimers are formed, through a process called nucleation, and rapid elongation of the filament commences. This elongation is a function of the available G-actin, the most abundant cytoskeleton protein in the mammalian cell [136]. Put more simply, each G-actin has binding sites that facilitate head-to-tail binding with two other G-actin monomers, resulting in polymerisation to form the F-actin filament. F-actin is a polar polymer with a right-handed helical twist [137]. The polarity stems from the identical orientation of G-actin and is important for further F-actin assembly (elongation) and for establishing a unique direction of myosin

movement, relative to actin. This polarity also results in F-actin having two distinguishable ends, called the plus (barbed) and minus (pointed) ends [137]. There is simultaneous assembly and disassembly of G-actin at the plus end and minus end respectively. This process is known as 'treadmilling' and is coupled with ATP hydrolysis [138].

F-actin plays an important role in epithelial cell cohesion, maintaining the integrity of cellular layers by a 'belt' of actin filaments, and in cell migration, as they are found in the plasma membrane protrusion where they form a 'mesh' [139]. F-actin can also promote edge retraction at the trailing edge of motile cells by converting energy, formed by ATP hydrolysis into tensile force. ATP hydrolysis is used by actin-associated myosin motor proteins to exert force against the stress fibres during muscle contraction [138]. Actin is essential for the survival of most eukaryotic cells as their filaments provide internal mechanical support, and force to drive cell movements as well as providing tracks for movement of intracellular materials.

1.5.2.2 The intermediate filament network

Intermediate filaments (IFs) are composed of one or more members of a large family of mainly cytoskeletal proteins. These can be classified into five major types. The first four types (I-IV) are cytoplasmic whereas type V IFs are located within the nucleus [140]. Type I and II are found in epithelial cells and are typically formed from acidic and neutral-basic keratins. Type III IFs are composed of homopolymers of vimentin, typically found in fibroblasts, as well as other cytoskeletal proteins such as desmin, peripheran and glial fibrillary acid protein (GFAP) [141]. Type IV and V IFs are expressed in the nervous system and are comprised of internexins and nuclear

laminins respectively [140]. Vimentin IFs preserve mechanical integrity of the cell by contributing to cytoplasmic stiffness and enhancing the elastic properties of the cell, suggesting that IF networks can adapt to mechanical changes in their environment [142].

1.5.2.3 The microtubules

The microtubule is a heterodimer of α - and β -tubulin dimers [143]. These tubulin dimers are assembled in a head-to-tail manner culminating in the formation of a protofilament. These protofilaments (typically 13) associate laterally and assemble into tubular microtubule structures [144]. As with the actin polymers, the microtubule is intrinsically polar, with a plus and minus end, due to the organisation of the tubulin dimers in the protofilament [145]. For both F-actin and the microtubule, the plus end grows more rapidly than the minus. The minus end of the microtubule is anchored close to the nucleus of the cell in structures called microtubule organising centres (MTOCs), this is known as a centrosome [143]. Microtubules are responsible for separating chromosomes and for the long-range transport of large particles. Each individual microtubule elongates and shrinks to fulfil a specific role (i.e. chromosome alignment). This phenomenon is termed “dynamic instability” [146].

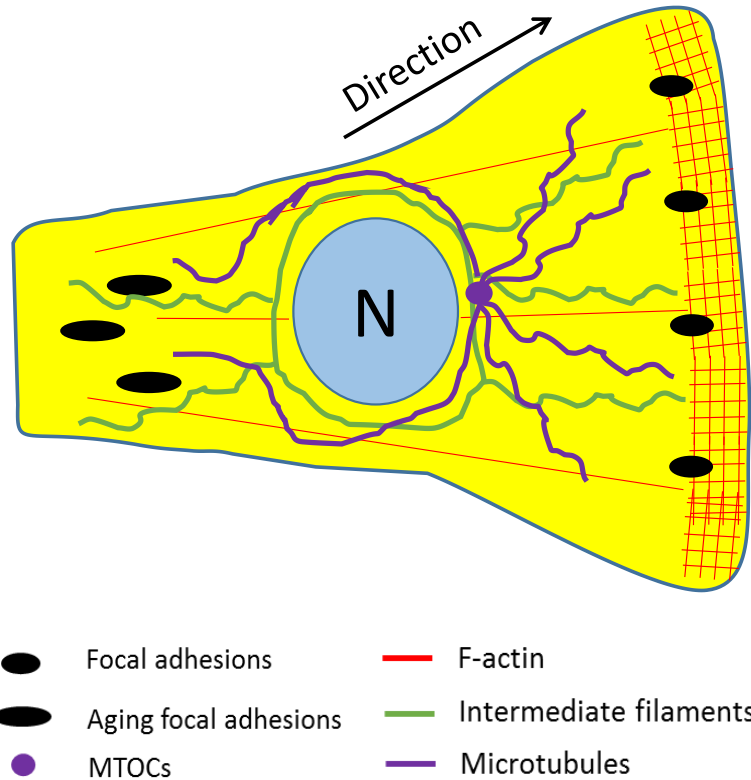


Figure 1-5. Schematic illustration of major cytoskeletal components in motile cells. The cross-hatched region represents the actin framework of the lamellipodia. F-actin is present throughout the cell. Aging focal adhesions in the rear are disassembled to allow retraction. Intermediate filaments surround the nucleus (N), some of which associate with focal adhesions in the lamellipodia. Microtubules are polarised along the direction of migration and accumulate toward the front of the cell. Adapted from [147].

1.5.3 Role the cytoskeleton plays in cell migration

The ability to migrate is one of the most remarkable properties of animal cells. To date the majority of the research carried out has been conducted on two-dimensional (2-D) surfaces, mainly for experimental convenience [148]. This research has been pivotal in our understanding of how cells migrate. A large percentage of cells migrate primarily within the ECM: during development, specialised cells manoeuvre within the embryo to reach their correct orientation, and in disease, cancer cells migrate from the primary tumour to metastasise secondary sites [149]. Fibroblasts often play a crucial role in the cell migration, for example in wound healing by migrating to the wound site and secreting extracellular matrix (ECM) proteins, such as collagen, glycosaminoglycans and glycoproteins, to maintain the structural integrity of the connective tissue [150].

It is generally understood that there are four steps involved in the cycle of cell migration (Figure 1-6) [147]. The first step is the formation of a protrusion, called the lamellipodia, at the front of the cell in response to biochemical and mechanical stimuli. Next, formation of new focal adhesions at the leading edge strengthen the cells attachment to the ECM. Third, increased activity of the actomyosin increases to reduce retraction of the rear. Finally, focal adhesions within the cell rear are disassembled to facilitate the forward movement of the whole cell body [138,151,152].

The dynamic formation of lamellipodia is regulated by local actin filament assembly and disassembly. During migration, these formations push the cell membrane forward to explore the surrounding environment. Depending on the suitability of the surrounding environment, the cell will either extend further forward or retract. There

are two patterns of actin assembly in lamellipodia, branching and elongation, which promote the formation of the actin mesh [153]. Focal adhesions, which are a type of adhesive contact between the cell and ECM, are actively assembled and disassembled in the front and tail of the cell, respectively. At the site of focal adhesion, the extracellular domains of transmembrane integrins connect to the ECM whilst their intracellular tails form attachments to linker proteins, such as vinculin and talin, which in turn bind to the actin cytoskeleton [147]. This chain of connections allow the cell to crawl along the ECM during migration. Subsequently, the triggering of this focal adhesion assembly results in the recruitment of structural proteins (α -actinin, talin, vinculin) and signalling proteins, including focal adhesion kinase (FAK) [154]. These structural proteins help to strengthen the attachment to the actin cytoskeleton and the signalling proteins promote further actin polymerisation and other pathways [155]. Further, after the connection between the ECM and actin cytoskeleton has been established, via focal adhesions, external signals induce stress fibre assembly. Stress fibres are contractile bundles containing both F-actin and myosin II filaments. The assembly of these stress fibres generates traction, via the activation of the actomyosin ATPase, propelling the cell forward [147,156].

IFs have been shown to physically interact with focal contacts in the lamellipodia, raising the possibility that they directly regulate focal adhesion dynamics, and thus cell migration. Cells which express high concentrations of vimentin have been shown to exhibit increased focal adhesion dynamics and destabilised desmosomes [157,158]. As IFs are widely distributed in the cytoplasm, they have also been shown to regulate cell contraction and nucleus rigidity. In most motile cells, microtubules do not enter the lamellipodia [159]. However, some pioneer cells can extend to the

protrusion sites. It is likely that microtubules promote the delivery of vesicles that are essential for cell protrusion [159]. They also promote the polarised delivery of integrins to the leading edge and facilitate the assembly and disassembly of mature focal adhesions within the cells rear, concluding that microtubules play a key role in cell protrusion and contraction [159].

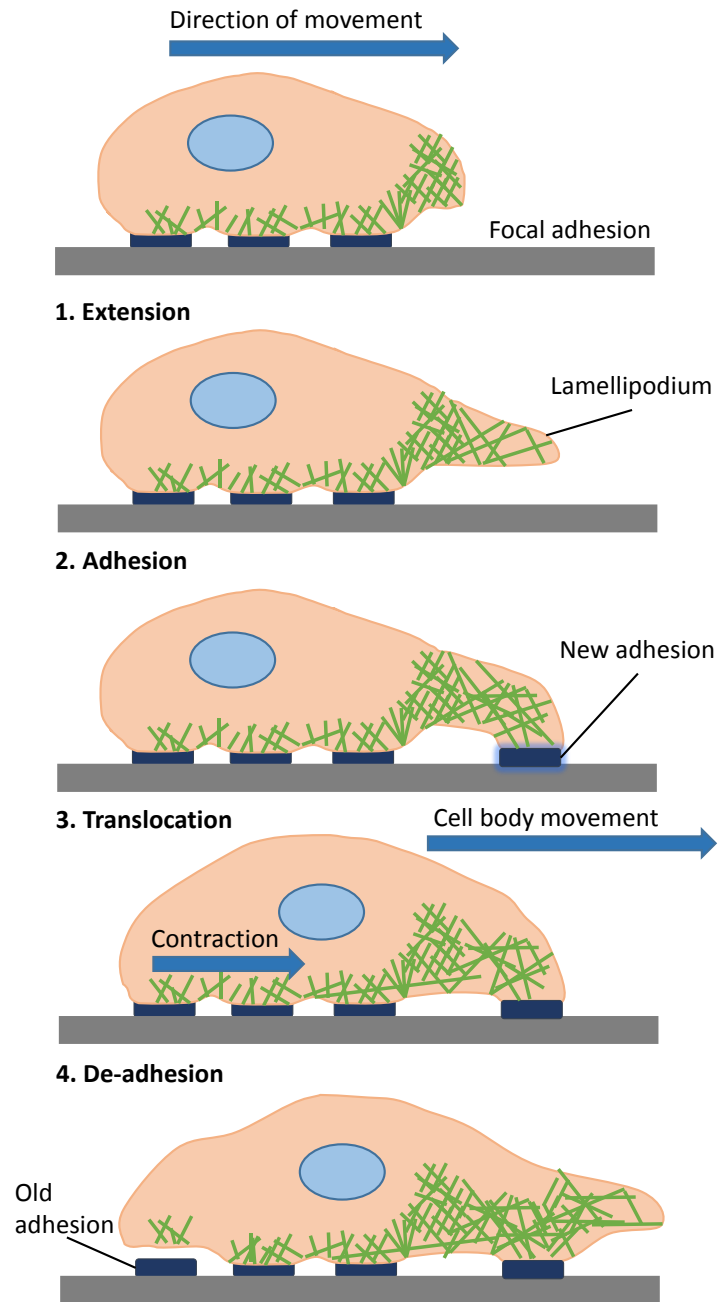


Figure 1-6 Schematic representation of the steps in 2D cell migration. 1. The extension of a lamellapodium. 2. The formation of a new adhesion. 3. The translocation of the cell body. 4. De-adhesion and retraction at the trailing edge. Adapted from [160].

1.5.4 The role of mechanotransduction

Mechanotransduction is a process whereby cells can sense their physical surroundings by converting mechanical stimuli into biochemical signals, via the activation of diverse intracellular signalling pathways [161]. This complex process is not yet fully understood. However, it is known that stretch-sensitive ion channels are key regulators of mechanotransduction [162]. The ECM of connective tissues bears a considerable physical load and provides protection to embedded cells from excessive mechanical forces [163]. Fibroblasts, which are abundant in connective tissues, firmly attach to the ECM, via focal adhesions. The link from ECM to the internal architecture of the cell, allows the propagation of mechanical forces in both directions. The opposing forces, felt internally and externally by the cell, cancel each other out in stationary cells [160]. However, an imbalance of force in either directions leads to cellular movement [164]. Due to these dynamic interactions, fibroblasts are able to use their adhesion contacts to sense the mechanical properties of the surrounding extracellular environment [165]. One of the ways in which fibroblasts gain information about the elasticity of the surrounding ECM is by pulling on an adhesion contact [160]. If there is resistance to the pulling of the fibroblast, this would indicate a stiff ECM and lead to the reinforcement of the focal adhesion site; conversely, any instability detected, via this mechanism, can result in the disassembly of focal adhesions and retraction of the cell [164,166]. Therefore, changes in a cells ability to respond to forces are associated with certain disease states, including; muscular dystrophies, cardiomyopathies, cancer progression and metastasis [161,167]. This process is the driver for the behaviour to be modelled in relation to fibroblasts reacting to their physical surroundings. By mimicking the ECM through patterned

surfaces, a model of the migrating cells can be built to predict how the fibroblast cells react to certain features.

1.5.5 Replication of Extracellular Matrix (ECM) features

The interaction between a cell and its environment is pivotal for many cellular behaviours such as migration, division, differentiation and proliferation. *In-vivo*, cells depend on an interaction with the ECM scaffold. In order to replicate this environment, significant research has focused on the development of cell substrates that mimic the features of the ECM [168-170]. This has largely been achieved by developing surfaces which have specifically designed features with defined geometries and sizes on a range of different materials. For example, surfaces patterned with micro- and nano-scale grooves [171], pillars [148] and pits [172] have been shown to influence cell adhesion [173] and migration [174] of a range of different cell types.

Although many methods are available for creating and modifying the topography of patterned surfaces, the most widely used technique involves placing a template mask over the surface that is due to be processed, thereby leaving a predetermined pattern. Such an approach can be seen in lithography-based approaches including; electron beam lithography [172,175,176], photolithography [171,177,178] and X-ray lithography [170,179]. The advantages to using these methods are evident in the wide range of well-defined geometries that can be produced on the substrates. However, the equipment they utilise is often expensive and time-consuming. A more effective method in the creation of micro-patterned surfaces is laser processing. Laser processing is a quicker, direct-write and flexible process [169]. It is also capable

of processing relatively large areas by a single exposure. Finally, abrasive polishing methods, which have so far been largely overlooked, can also develop textured surfaces comparable to those produced by lithography-based methods whilst also being cost-effective. It has been shown that abrasive polishing can produce patterned polyurethane surfaces having ordered, or random, nanoscale features that can affect cell adhesion and migration [180]. Note that because of this utility and cost effectiveness, an abrasive polishing method was chosen to create patterned surfaces for the migration experiments in this thesis.

Machine grinding was used for this purpose to generate the topographical patterns on the polyurethane surfaces. This method involves the micro-patterning of stainless steel, which can then be used to cast polymer substrates for observing the migration of fibroblasts [180]. An unprocessed plain polymer surface was used as a control and was labelled as 'Flat'. Next, a pattern of parallel lines was cast on the polymer surface and was labelled as 'Linear'. Finally, a pattern of random lines varying in direction was etched into the polymer surface and labelled appropriately as 'Random'. Subsequently, a previous study has shown that these machine ground surfaces promote adhesion and migration in fibroblast cells compared to unprocessed, flat surfaces [180].

1.5.6 Mathematical models of cellular movement

In-silico simulation aims to model cellular movement through the use of complex numerically implemented mathematical methods, with the goal of facilitating better understanding of the phenomena and its role in wound healing, tumour growth and tissue formation [181-186]. As previously described in section 1.3.1, these models

can be classified as continuous or discrete. As continuous models can be used to describe the average of cell populations with continuum variables, cell movement can be defined in terms of cell density and average velocities. This method has been utilised in the description of adhesion [187], wound healing [188-191] and angiogenesis models [192]. For example, continuum models of wound healing have been used qualitatively, in a predictive capacity, to aid the understanding of the complex underlying mechanisms involved in wound contraction. Murray et al. [190] use a base model, with three simplified assumptions, to describe the wound contraction mechanism of wound healing only. Qualitatively, there were problems when the model output was compared to contraction curves. However, extensions of this model, through functional changes of the cell function, allowed incorporation of alternative mechanisms of contraction resulting in several scenarios that can be considered for further novel *in-vitro* wound healing assays. Additionally, Arciero et al. [188] proposed a two-dimensional continuum model where cell migration occurs collectively in a sheet, based on mechanical principles governing its motion [193], such as those described in Figure 1-6. This model was able to capture known quantitative and qualitative features of a migrating cell layer, with calibration to data from scratch wound assays. Although these methods are advantageous in terms of requiring less computational power, they require more assumptions than discrete models, the individual cell movement cannot be tracked and dynamical individual cell behaviour cannot be predicted. However, if cells are interpreted as discrete elements, then each cell can be defined as an individual, whose properties can be modelled in relation to its position within a cell population [194], the local chemical and mechanical environment [195-198], or any other external stimuli that could

regulate cell behaviour. This distinction is important for the creation of the cell movement model (Chapter 3) proposed as it takes into account the mechanical environment that surrounds the individual cells.

It is clear that mathematical modelling of the movement of cells has great relevance in the field of biology. Again, there are many different forms of cell movement models. However, the most widely used are based on the extensions of simple random walk processes [199]. It is these models that I will base the model for Chapter 3 upon, as they incorporate random movement or Brownian motion into their assumptions. Brownian motion can be described as the random movement of particles due to their collisions with other atoms and molecules. This concept is named after Scottish botanist Robert Brown, who in 1827, observed pollen grains moving randomly in the water [200]. However, he was unable to explain the phenomena he had observed and it remained undescribed until 1905, when Albert Einstein published a paper explaining that the fast-moving water molecules in the liquid moved the pollen [201]. The Weiner process is often used to model Brownian motion in cell migration models. The Weiner process is defined as a continuous-time stochastic process and is named in honour of Norbert Weiner. Brownian motion is considered a Gaussian-Markov process, it has normally distributed random variables over a continuous time constant and is considered a memoryless process [199]. These walks are uncorrelated and unbiased. Correlated random walks (CRWs) involve correlation between successive step orientations, which is termed as 'persistence'. This creates a directional bias where the influence of the initial direction of motion gradually diminishes over time [202]. These types of models provide a lot of potential in terms of implementing a bias term and can apply to a lot of different situations.

For instance, a global directional bias can be introduced by making the likelihood of a cell migrating in a particular direction greater. This is most common in chemotaxis models where fixed external environmental factors are applied [203,204]. The goal is to utilise these models and modify the bias term so that it represents a mechanical gradient on the surface that the cells migrate upon.

1.6 *In-silico* approaches to protein signalling networks

1.6.1 Structure and function of the Nrf2 protein

The engulfment of aerobic mitochondria by our single cell ancestors, yielded higher energy through effective respiratory processes and facilitated the inception of more complex life forms. However, the cost of this 'upgrade' to the host cell was the requirement for an efficient detoxification system to deal with the constant production of reactive oxygen species (ROS), which are associated with normal mitochondrial activity [205]. More efficient respiration due to oxidative phosphorylation results in more ROS being produced. This symbiotic relationship significantly contributes to the process of aging and all age-related diseases. The aerobic cell defends itself by encoding sensor proteins that react to ROS by turning on a collection of cytoprotective antioxidant genes through transcription. The nuclear factor erythroid 2-related factor 2 (Nrf2) performs a central role in this process, regulating around 1% of human gene expression, many of which perform powerful protective functions [206]. Therefore, an increase in ROS leads to a higher production of Nrf2 and subsequently, an increase in the transcription of antioxidant genes.

The Nrf2 coding sequence was first characterised by Yuet Wai Kan [207], who revealed that Nrf2 was able to bind activator protein-1 (AP-1) and the NEF-E2 tandem repeat consensus DNA sequence. The Nrf2 protein belongs to the Cap'n'Collar family of proteins (CNC) and to the subfamily of basic leucine zipper (bZIP) proteins [208,209]. The transcriptional activity of the Nrf2 protein requires the formation of a heterodimer complex with another member of the bZIP subfamily, the small MAF

(sMaf) proteins [210]. This interaction facilitates binding to a *cis* regulatory DNA element called the Antioxidant Response Element (ARE), which is contained within the promoters of Nrf2 target genes [209,211]. The key characteristic of this transcription factor is its very low basal activity and its stringent regulation, as the half-life of Nrf2 protein has been estimated to last only 10-30 minutes [212]. The stability of Nrf2 dramatically increases as a result of diverse stimuli including plant-derived phytochemicals and intracellular and extracellular stress factors, such as ultraviolet (UV) and gamma (or ionising) radiation, electrophiles, pollution, inflammation and ROS [211,213]. Expression levels of the Nrf2 protein are primarily controlled at a post-transcriptional level, through an interaction with proteins that trigger proteasome mediated degradation [206,210].

The best understood negative regulator of Nrf2 is the Kelch-like ECH-associated protein (Keap1), which is an actin-bound zinc metalloprotein that acts as an E3-ligase, facilitating the attachment of ubiquitin chain to Nrf2 [214]. Keap1 binds as a dimer to the Neh2 domain within Nrf2 forming bonds with the high affinity ETGE and low affinity DLG amino acid sequences. This interaction brings the Nrf2 protein into proximity with Cullin3 and Ring Box 1 (Rbx1), which then catalyse the process of ubiquitin attachment (Figure 1-7) [215]. Keap1 is located mainly in the cytosol where it constantly sequesters Nrf2, thereby restricting basal Nrf2 activity to very low levels. An unusually high number of reactive cysteine (Cys) residues are encoded within Keap1 (27 Cys residues), which makes it an extremely sensitive sensor of oxidative stress, with C151, C257, C273, C288 and C297 being especially sensitive to oxidation [211,216]. The oxidation of thiols within Cys residues leads to the formation of disulphide bridges between cysteines, resulting in a conformational change in Keap1

protein structure, which in turn prevents the effective ubiquitination and degradation of Nrf2 [215,217].

Newly formed Nrf2 proteins will still bind to free Keap1 dimers. However, as Keap1 becomes saturated, free Nrf2 is then allowed to enter the nucleus, where it will subsequently heterodimerise with sMaf and bind to ARE containing promoter sequences (Figure 1-7) [215]. Therefore, antioxidant pathway activation will rely on Nrf2 protein synthesis to overcome the levels of Keap1, which are usually present in cells, at very low (near-saturated) levels [218]. The Keap1/Cull3/Rbx1 complex is extremely robust and efficient in restricting Nrf2 protein expression. However, several other negative regulators of Nrf2 protein expression have been described. Glycogen synthase kinase 3 (GSK-3) is a serine/threonine kinase and is encoded by two isoforms (GSK-3 α and GSK-3 β) [219]. GSK-3 is active basally and requires priming phosphorylation of its targets, which then prompts further attachment of a phosphate group onto a serine or threonine residue. In the presence of glucose, the insulin/Akt/PI3K pathway leads to GSK-3 phosphorylation at Ser9 (β isoform) and Ser21 (α isoform), which terminates its activity [219]. Nrf2 is also a target for GSK-3 phosphorylation, on the Neh6 domain, facilitating docking of the β -TrCP E3 ubiquitin ligase and formation of the β -TrCP/Skp1/Cull1/Rbx1 complex, which like Keap1/Cull3/Rbx1 catalyses the ubiquitination of Nrf2 and subsequent degradation [220,221]. While Keap1 is thought to dominate the control of cytoplasmic Nrf2 levels, the GSK-3/ β -TrCP axis is thought to be predominantly active in the nucleus, directing Nrf2 protein for nuclear proteasomal degradation [220]. Ultimately, Nrf2 controls the transcription of over 200 genes and depending on the tissue context, these genes have prominent roles in the maintenance of redox status and the generation of

reducing equivalents, protein folding and degradation, cell metabolism, calcium homeostasis and drug metabolism [222,223].

It is clear from the research described above that Nrf2 is a key transcriptional factor in the regulation of cellular response to oxidative stress. However, in most tissues, cells are not only exposed to frequent changes in levels of oxidative stress, but also inflammation [224]. The key transcriptional factor controlling cellular response to inflammation is nuclear factor- κ B (NF- κ B) and it has been shown, through pharmacological [225,226] and genetic [227,228] studies, that there exists a functional cross-talk between these two important regulators.

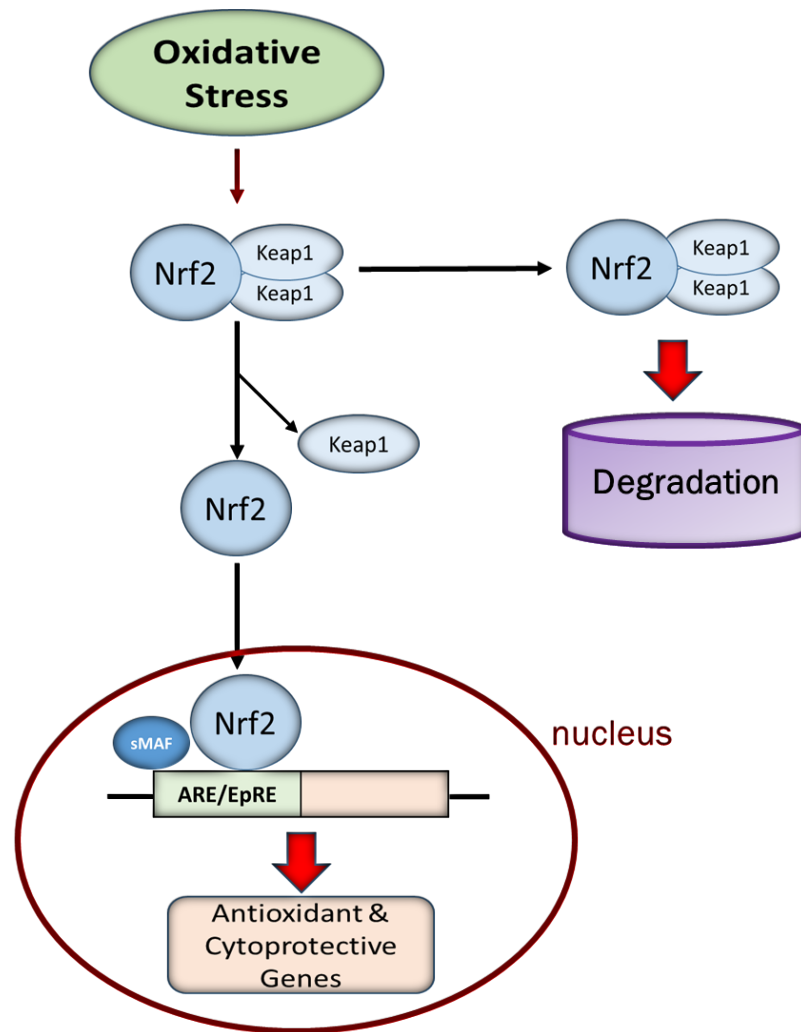


Figure 1-7. Keap1-dependent Nrf2 regulation. Schematic diagram of the Nrf2 pathway. Nrf2 is sequestered by Keap1 under normal conditions and the complex closes allowing attachment of the ubiquitin chain. Keap1 is then recycled and binds to another Nrf2 molecule. During oxidative stress, there is a modification of cysteine residues on Keap1 by oxidation or attachment of electrophilic compounds. Keap1 is unable to form the closed complex and therefore catalyse the ubiquitin attachment. The newly made Nrf2 is then accumulated in the nuclear space and leads to the transcription of ARE genes.

1.6.2 Structure and function of the NF- κ B protein

The NF- κ B transcription factor mediates immune responses to bacterial and viral infections, as well as initiating gene expression supporting inflammation, cell development, proliferation, anti-apoptotic pathways, oxidative metabolism and protection against UV radiation [229-231]. NF- κ B is actually a family of transcription factors including RelA (p65), RelB, c-rel, p50 and p52 subunits, which act as homo- or hetero-dimers [232]. Only the p65, RelB and c-rel contain the transactivation domain required to drive transcription [233]. The p50 and p52 subunits are detected basally in the nucleus of unstimulated cells and are thought to have an inhibitory effect on gene expression, exerted by blocking DNA sequence availability [232,233]. A complex network of protein interactions usually initiated by an extracellular stimulus (e.g. stress, cytokines, free radicals, bacterial and viral antigens) mediates NF- κ B signalling [234]. The NF- κ B subunits form homo- and hetero-dimers through their Rel homology domains (RHD), which are also necessary for their dimerization, DNA binding and association with the I κ B α inhibitor [232,234].

The p65/p50 (NF- κ B) heterodimer is sequestered in the cytoplasm by association with I κ B α , which obscures one out of two NLS and limits its nuclear entry [232,235,236]. Importantly, NF- κ B gene transcription is inducible by variety of stress stimuli and over 150 different factors have been identified as activators of NF- κ B mediated gene expression: *e.g.* LPS, exotoxin B, muramyl peptide, viruses *e.g.* Hepatitis B, Adenovirus, Herpex Simplex Virus-1, HIV, cytokines, but also physical stress, UV radiation, shear stress, ischemia oxidative stress and environmental hazards [237,238]. NF- κ B plays a central role in the maintenance of the immune responses by initiating the genetic program designed to modulate the local

environment and to attract the immune cells to the site of infection or injury. It was found to mediate the expression of approximately 300 genes, including numerous cytokines and their receptors, anti-apoptotic genes and adhesion molecules [238,239].

TNF α is one of the best-studied cytokines and is a potent activator of NF- κ B - mediated gene expression, playing an important role in systemic inflammation and the induction of fever [240,241]. It has pleiotropic effects as it can induce a range of cellular responses such as proliferation, chemotaxis, apoptosis and inflammation, as its downstream signalling can trigger several molecular cascades [242]. Pro-inflammatory cytokines such as TNF α and IL-1 β activate the canonical signalling cascade by engaging their extracellular receptors and initiating a relay of intracellular phosphorylation events, which co-ordinate signalling and conditional cell responses [243]. Activation of the TNFR1 receptor initiates the TRADD/RIP signalling cascade, which removes the phosphate group from the IKK kinases complex, comprised of the IKK α and IKK β catalytic subunits and IKK γ (NF- κ B essential modifier, NEMO) (Figure 1-8). IKK activation results in the phosphorylation of IKB α on Ser32 and Ser36 and parallel activation of several kinases, such as MAPK p38, JNK [232,234,242]. Phosphorylation primes IKB α for interaction with the β -TrCP/Skp1/Cullin1 complex, which drives IKB α ubiquitination and proteasomal degradation, finally releasing the NF- κ B subunits to the nucleus [244].

The entire signalling process from TNFR1 activation to κ B transcription is very rapid, taking place within minutes [234]. The activation of inflammatory gene transcription also initiates multiple negative feedback loops, which prevents the inflammatory signalling uncontrollably increasing. The IKB α protein is one of the earliest gene

targets of NF- κ B signalling, in response to the TNF α cytokine. Shortly following translation, I κ B α localises to the nucleus and removes p65 from the DNA, and sequesters it back into the cytoplasm [245]. In addition, NF- κ B also transcribes the deubiquitinating enzyme (DUB) A20, which terminates the signalling cascade upstream of the IKK complex by modification of the receptor interacting protein (RIP), which is essential for TNFRF1 receptor signalling (Figure 1-8). The A20 protein removes Lys-63 chains from the RIP protein leading to Lys-48 ubiquitination and targeting for proteasomal degradation, leading to inactivation of the downstream phosphor-relay signalling [246,247]. Therefore, both I κ B α and A20 create safety loops which can terminate the signalling from the inflammatory signalling.

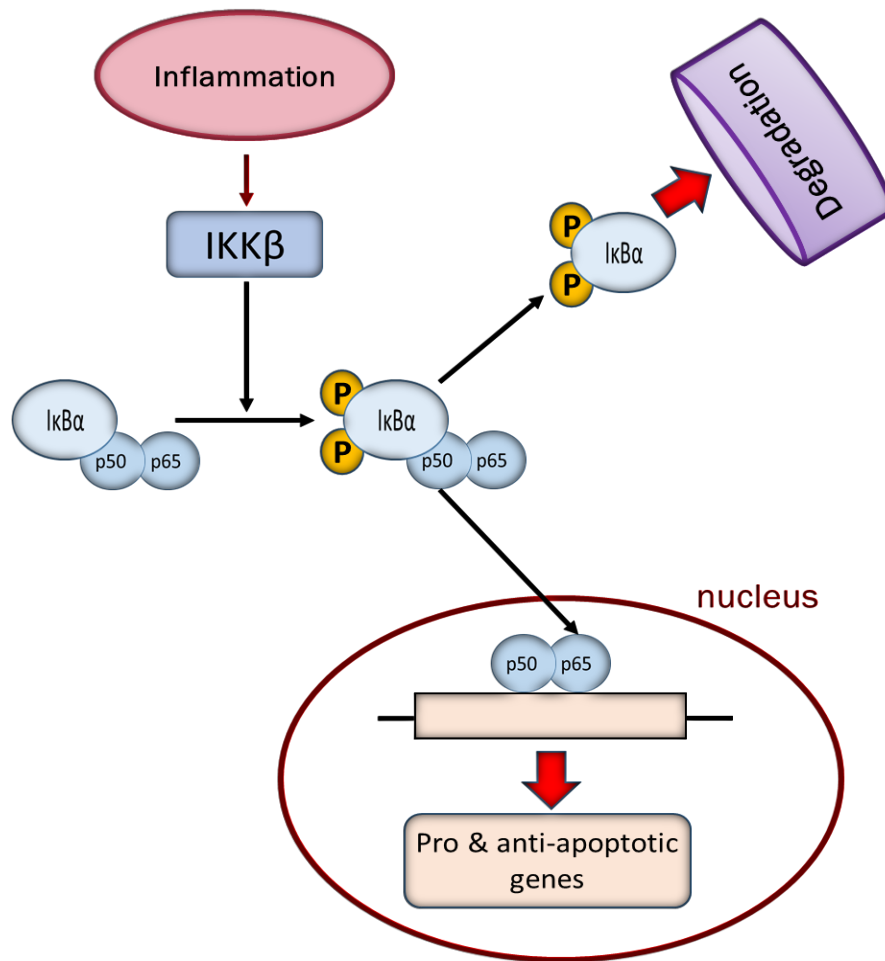


Figure 1-8. The Canonical NF-κB Pathway. Schematic diagram of the NF-κB pathway. The canonical/classical pathway of NF-κB activation involves inflammation that triggers a downstream cascade of ubiquitination and phosphorylation events leading to nuclear occupancy of p65/p50 heterodimers. The p65/p50 dimer then translocates to the nucleus and mediates transcription of κB driven genes.

1.6.3 Molecular cross-talk between Nrf2 and NF- κ B response pathways

The initial insights to an existing functional cross-talk between the Nrf2 and NF- κ B pathways came through the study of Nrf2 knockout (KO) mice, which exhibit a phenotype of neurodegeneration. This loss of Nrf2 results in enhanced NF- κ B dependent inflammation via the augmentation of cytokines [227]. Moreover, further studies have shown comparable results of amplified cytokine production in mouse models lacking Nrf2, resulting in pronounced levels of NF- κ B activity [228,248,249]. Additionally, pharmacological studies focusing on the application of Nrf2 activating phytochemicals, such as sulforaphane (SFP), or synthetic inducers of Nrf2, such as 2-cyano-3,12 dioxooleana-1,9 dien-28-imidazolide (CDDO-Im). The result of these studies concluded that pre-stimulation of Nrf2 caused a dampening of inflammatory cytokines and therefore a decrease in NF- κ B activity [225,250]. Furthermore, HO-1 is an Nrf2 target gene and is central to the Nrf2-mediated inhibition of the NF- κ B response pathway [251]. Finally, another link between these two pathways is the Keap1 protein [252]. Aside from its regulatory role in the Nrf2-ARE pathway, Keap1 has been found to inhibit the phosphorylation and degradation of IKK β . This ultimately leads to the stabilisation of IKK α and the negative regulation of NF- κ B [252]. Despite this evidence, many aspects of the cross-talk dynamics remain unknown. As such, many important features of co-regulation, feedback loops and competitive binding remain undefined. However, the importance of this cross-talk cannot be understated, as these pathways regulate the fine balance of cellular redox status and response to stress and inflammation. Deeper understanding of these cross-talk points can facilitate in the identification of therapeutic targets, as the anti-inflammatory potential of the Nrf2 protein can be utilised in the treatment of many

neurodegenerative diseases, such as amyotrophic lateral sclerosis (ALS), multiple sclerosis (MS) and Parkinson's disease (PD) [253-255].

1.6.4 Mathematical models of NF- κ B and Nrf2

In a recent review, Quanstrom et al [256] discussed the current state of computational modelling of the NF- κ B signalling pathway. There have been a number of computational models developed of the signalling pathway over the past two decades. It is increasingly appreciated that the robustness of various cellular processes (i.e. signalling pathways, regulatory mechanisms) is rooted in the dynamic interactions among the cell's many constituents, such as proteins, DNA, RNA and small molecules [256]. A significant body of knowledge has been generated through wet-lab experimentation since the discovery of NF- κ B in 1986. Recently, equation-based and agent-based models have been used within a predictive capacity to generate hypotheses for testing through this supportive wet-lab experimentation [257-259]. The first model of NF- κ B dynamics used mass action derived kinetics to focus on I κ B α association and dissociation rates, along with I κ B α and NF- κ B nuclear import and export rates [260]. Hoffmann et al [261], then developed an ordinary differential equation (ODE)-based model that incorporated the wider NF- κ B network, including the other I κ B isoforms. This model also focuses on reactions that affect I κ B dynamics, paying particular attention to the temporal control of NF- κ B activation through the coordinated synthesis and degradation of I κ B proteins. Other authors have since built on this deterministic ODE model by performing new wet-lab knockout experiments on I κ B isoforms [262] and recalibrating the model with outputs from single cell analysis rather than population-based wet-lab experiments [263]. This approach yielded the first working model to show NF- κ B oscillations at the

single cell level. In recent years, additional components of the pathway have been added by various authors, to include IKK, A20 and their subsequent feedback loops [264]. An alternative method is to model cells or molecules individually and assign probabilities to each possible interaction or state change through rule-based techniques. It may then be aggregated up to system-level dynamics, to be extrapolated in order to make predictions of the system-level behaviours in the real biology [265,266]. The first such agent-based model of NF- κ B used the concept of communicating X-machines, which is a formalised version of an ABM, to represent the individual agents and their associated interactions [267]. An important aspect of communicating X-machines is that each agent has memory, which in this instance, holds the current physical location and current state to further instil stochasticity into the model. Graphical visualisation of the resulting reactions then allows us to view the dynamics of the system over time. However, it has been argued by several groups that the complexity of such models makes them too computationally expensive to run and also requires complicated analytic tools to make inferences from the simulated results.

In contrast, computational models of the Nrf2 pathway are limited, with work mainly focusing on *in-vivo* and *in-vitro* models [268]. Khalil et al [269] developed a model describing the Nrf2-keap1-dependent mechanism of redox homeostasis regulation and Nrf2 signalling. This kinetic model of Nrf2 signalling comprises 16 ODEs with parameters that were chosen based on experimental data. The model they proposed captures the Keap1-dependent degradation of Nrf2, and gene regulation of the antioxidant system. This lack of published Nrf2 models is a consequence of the limited quantitative data available. Due to the lack of *in-silico* models available in the

literature, a minimalist approach was taken in the process of the model build i.e., only key components were included based on a review of the literature. Additionally, the parameter values from the Khalil et al. paper will be used as initial estimates for the parameter optimisation. In this thesis, a quantitative model of the Nrf2 pathway (Chapter 4) combining mathematical assumptions with raw experimental data is proposed. This data will be used to inform and validate the model in the hope of extracting vital information regarding the dynamical interactions of the individual pathway components. This illustrates the novelty of the work being carried out in this study. In addition, a further petri-net (PN) model is to be developed, incorporating both the Nrf2 and NF-kB response pathways (Chapter 5), and highlighting the areas of cross-talk in an effort to draw conclusions on the cyclic behaviour of their interactions, based upon feedback loops of activation and inhibition.

Although quantitative mathematical models are well established tools for modelling complex biological phenomena, they typically require an exhaustive set of kinetic parameters to be estimated for each reaction. This approach is manageable for smaller models that align to the dynamics of a few components. However, these models tend to suffer from limitations in accuracy as the scale and complexity of the model is increased to capture more realistic details at a system-level. As such, we utilise minimal modelling for the creation of the Nrf2 quantitative system, as they have been shown to replicate the majority of the phenomenological behaviours with the minimum number of equations possible [270-273]. An alternative approach is PNs. The classical PN is a directed bipartite graph [274]. The two types of nodes are called *places* and *transitions*. In a PN, places and transitions are connected via *arcs*. Places are graphically represented by circles, transitions by boxes or bars. Places can

store *tokens*, represented by black dots or numbers. A distribution of tokens on the places of a net is called a *marking*, and corresponds to the “state” of the PN [275]. A transition of a net is *enabled* at a marking if all its input places (the places from which some edge leads to it) contain at least one token. An enabled transition can fire: it removes one token from each of the input places, and adds one token to each of its output places. This is called the *firing rule*. This flow of tokens represents the dynamical behaviour of the model [276]. While such approaches somewhat relax the necessity for biologically exact kinetic parameters, current PN-based approaches still require the selection of weights and/or probability distributions for individual interactions in the model. As a result, selecting the values for PN parameters presents challenges similar to those encountered in ODE modelling. PNs have been extensively used for simulating the dynamics of signalling networks [277-280]. These PN models are constructed with the same framework as described above. Places represent the entities within the signalling pathway, such as proteins. Transitions represent processes such as enzymatic reactions and lead to new places which represent the outcome of the process i.e., binding of proteins. Token numbers are equivalent to the amount of protein present and can be weighted to specific reactions. For example, in the Nrf2 pathway two keap1 tokens would react with one token of Nrf2. In general, the following steps are followed in model design [279]:

1. Identification of the key events in the selected pathway
2. Identification of objects related to the key events that also need to be represented as places
3. Identification of the interactions between the objects, which are then represented by transitions

1.7 Thesis outline

In this thesis, there is a combination of experimental data with mathematical formulae to produce several *in-silico* models depicting cellular phenomena across a range of individual scales (macroscopic, mesoscopic and microscopic). The advantage and novelty to creating mathematical models in this way, results from the higher accuracy achieved through the utilisation of experimental data. Furthermore, the models proposed in this thesis, require less theoretical assumptions or estimation of parameters.

Chapter 2 describes a continuous macroscopic *in-silico* model of the tumour microenvironment of the gut. The model was reduced so that only the cancer and immune cells involved in the experiments are relevant in the model. This continuous model is used to determine the dynamic nature of the interactions between the cells and provide insight into the underlying mechanisms of cell-cell communication.

Moving down a scale, Chapter 3 describes a discrete model of individual fibroblast migration. This model incorporates cell migration mechanics with surface topography to assess the effect of differing topographical features on cell speed and direction. Microscopy image data was uploaded into the model the simulated migration paths were compared to the experimental observations to determine which, if any, of the surface features resulted in more directed cell migration of the fibroblast cell.

Continuing with the progression down biological scales, Chapter 4 describes a molecular quantitative model depicting the processes involved in the life cycle of the Nrf2 protein. These processes include the production, translocation, degradation and

decay of the protein. A minimal model was generated to describe these components based on ODEs. Parameterisation and fitting of the model resulted in quantitatively derived values for the kinetic rates in the equations. Subsequently, the model was able to provide kinetic rates describing the dynamics of the Nrf2 protein.

Finally, staying on the microscopic scale, Chapter 5 describes the interaction of the Nrf2 protein with the NF- κ B protein. The pathways of both these proteins are extensive with multiple cross-over points. Therefore, these pathways were reduced to their key functional components, through analysis of the relevant biological literature. As with Chapter 4, the model comprises the production, translocation, degradation and decay of the proteins. However, this model also includes activation and inhibition of the proteins as part of the mechanism of cross-talk between the pathways. This model was used to provide important insights into the dynamic properties of the cross-talk mechanisms that were not feasible through experimentation alone.

Chapter 2: Systems Biology of the Tumour Microenvironment

2.1 Introduction

In this chapter, a continuous macroscopic *in-silico* model of the tumour microenvironment of the gut is introduced. More specifically, a model that aims to investigate the underlying mechanisms involved in the interaction between epithelial cancer cells (AGS) and stromal myofibroblasts (308/1). As previously mentioned in Section 1.4, both of these cell types reside in the gastrointestinal tract. Due to the harsh nature of this environment, continued maintenance and regulation of the gastrointestinal tract epithelium is essential. When this epithelial layer becomes compromised, through inflammation and cancer, myofibroblasts form a key part of the immune response. They are involved in many vital processes of wound healing, such as tissue remodelling [46] and re-epithelialisation [47]. Myofibroblasts regulate these processes through secretion of cytokines and other factors, such as TGF- β [52]. Again, as highlighted previously cancer can be considered as a wound that does not heal [66]. The inflammatory response from the presence of these cancer cells promotes the recruitment of myofibroblasts to the cancer site, where they can undergo phenotypic changes and become designated as CAMs [74]. The functional role of these CAMs and the underlying mechanism of the cell-cell signalling between them and the cancer cells is not very well understood. However, as it is abundantly clear that myofibroblasts release a plethora of chemicals in response to stress (i.e. as a result of injury caused by inflammation and cancer), this will form the basis of the investigation into the mechanism at play between the cells. *In-silico* models allow us to study dynamics of biological cells which cannot be easily defined using experimental approaches. The strength of the modelling in this chapter is based upon

the experimental data that is used in its design. To my knowledge, there are no existing models in the literature based upon the interaction between these cell types. The experimental approach to the problem in this chapter involves carrying out cell migration assays on both cell types simultaneously. Ordinarily with these types of experiments, a scratch wound assay is performed on a monolayer of the first cell type in the presence of complemented media from the second cell type [281]. However, in the experiments described in this chapter, there is a monolayer of both cell types. These monolayers are separated by a uniform gap, created through the use of a gel-insert. This allows the interaction between the cells to be recorded via time-lapse microscopy, with the resulting data utilised to create and inform the model. The key hypothesis is to investigate whether a ‘chemical inhibitor’ produced by the myofibroblasts is the driver (i.e. main influencer) of the observed cell migrations.

In summation, this chapter describes the evolution of a continuous model from a simple diffusion based approach to a system that incorporates chemotaxis and density-based diffusion. By using computational approaches to reproduce properties that the biological system displays, a better understanding of how the mechanism of interaction between the myofibroblast cells and the cancer cells can be discovered [282]. It is important to stress that the models in this chapter are semi-quantitative. In other words, the research is primarily explorative and the models are being used to gain an understanding of the underlying interactions between the different cell types.

2.1.1 Chapter aims

1. To complete *in-vitro* experiments on AGS and 308/1 cells.
2. To use *in-vitro* results to develop an *in-silico* model that best describes the phenomena captured by the experimental data.
3. Compare simulated output to the experimental data to assess appropriateness of model design and refine if necessary.
4. Explore the underlying mechanism of interaction.

2.2 Experimental Methods

Cell culture materials, namely 0.25 % w/v trypsin-EDTA, Dulbecco's modified Eagle's medium (DMEM), L-glutamine, non-essential amino acids, antibiotic-antimycotic solution, penicillin-streptomycin solution and phosphate buffered saline (PBS) were obtained from Sigma (Dorset, UK); Recovery™ cell freezing medium came from Invitrogen (Paisley, UK). Foetal bovine serum (FBS) was purchased from Lonza. Ibidi cell culture inserts for migration assays was purchased from SLS (Nottingham, UK). The gastro adenocarcinoma cancer cell line (AGS) were derived from fragments of a tumour resected from a patient who had received no prior therapy. AGS was obtained from American type culture collection, ATCC, VA, US. Human primary myofibroblasts were obtained from resected oesophageal cancers and adjacent non-cancerous tissue during surgery for removal of tumours at First Department of Surgery, University of Szeged, Szeged, Hungary. Myofibroblasts were prepared in the Department of Medicine, University of Szeged, Hungary as described in [74] and transported to the University of Liverpool in liquid nitrogen and cryopreserved until use. Myofibroblasts were derived from three Barrett's adenocarcinoma, recovered from the oesophagus and oesophagus/cardiac junction. From each patient, CAMs and ATMs were cultured.

2.2.1 Tissue culture

2.2.1.1 Human myofibroblasts.

The myofibroblasts (referred to hereafter as "308/1" unless otherwise stated) were maintained in T-75 flasks in DMEM supplemented with 10% v/v FBS, 1% v/v penicillin-streptomycin, 2% v/v antibiotic-antimycotic and 1% v/v non-essential amino acids. This is referred to as "full medium" (FM) unless otherwise stated. Cells were grown at 37°C in a 5% v/v CO₂ atmosphere and the medium was changed every 48 h. For passaging, cells at 80% confluence or above were washed twice with PBS followed by

incubation for 5-8 min in 2 ml 0.25 % w/v trypsin-EDTA. Trypsinised single cell suspensions were then added to 8 ml of FM and cells were re-plated in T-75 flasks. Aliquots of 10 μ l of cell suspensions were used for cell counting using a haemocytometer.

2.2.1.2 Human gastro adenocarcinoma cancer cell line.

Gastro adenocarcinoma cancer cell lines (referred to hereafter as "AGS") were cultured in Ham's F-12 Nutrient mixture supplemented with 10% v/v FBS, 1% v/v penicillin-streptomycin, 2% v/v L-glutamine. Cells were maintained at 37°C in a 5 % v/v CO₂ atmosphere, and media was changed every 48-72 h. Confluent cells at 80% were washed twice with PBS, trypsinised using 0.25% w/v trypsin-EDTA and cells were added to 8 ml FM and re-plated in T-75 flasks.

2.2.1.3 Cryopreservation of cell lines.

Cells were trypsinised at 80% confluence, centrifuged at 800 x g for 7 min at 4°C and supernatants discarded. Pellets were resuspended in 1 ml recovery cell freezing medium and cell suspensions stored in 1.5 ml cryovials. These vials were placed in a plastic holder in a bath containing propane-1, 2,-diol and then transferred to a -80°C freezer overnight and then to liquid nitrogen for long-term storage.

2.2.1.4 Recovering frozen cell lines.

Cells were removed from liquid nitrogen, thawed by hand or in a water bath at 37°C and added to a T-75 culture flask with 19 ml FM and maintained 37°C in a 5 % v/v CO₂ atmosphere.

2.2.2 Migration assay

Cells were grown to confluence in six-well dishes. In co-culture experiments, 100,000 AGS and 50,000 308/1 cells were cultured in each well. The experiment was setup using an Ibidi chamber, which is a small gel insert containing two wells with the dimensions 7000 μm x 3250 μm . The two cell types were segregated into different parts of the well by applying them to either side of the Ibidi chamber. A monolayer of 100,000 AGS cells were added to the left well and a monolayer of 50,000 308/1 cells were added to the right layer. Before removing the Ibidi chamber, cells were kept in an incubator for 24 h (in FM). Ibidi chambers were then removed, leaving a uniform gap of 500 μm between the cell populations (Figure 2-1), and each well underwent a double PBS wash before 800 μl of 50/50 mixed DMEM and F12-Hams medium with 2% FCS was added to each well. The number of cells crossing a margin of 500 μm into an acellular area was recorded using time-lapse microscopy. Time-lapse image series were analysed using Scion Image software (Scion, Frederick, MD), which is based on the National Institutes of Health Image. Cell tracking and frame-by-frame recording of movements were used to calculate cell speed over 30-minute periods. Manual cell tracking was performed with Image J using the *Manual Tracking* plugin. Statistical analysis was performed in Microsoft Excel and MATLAB.

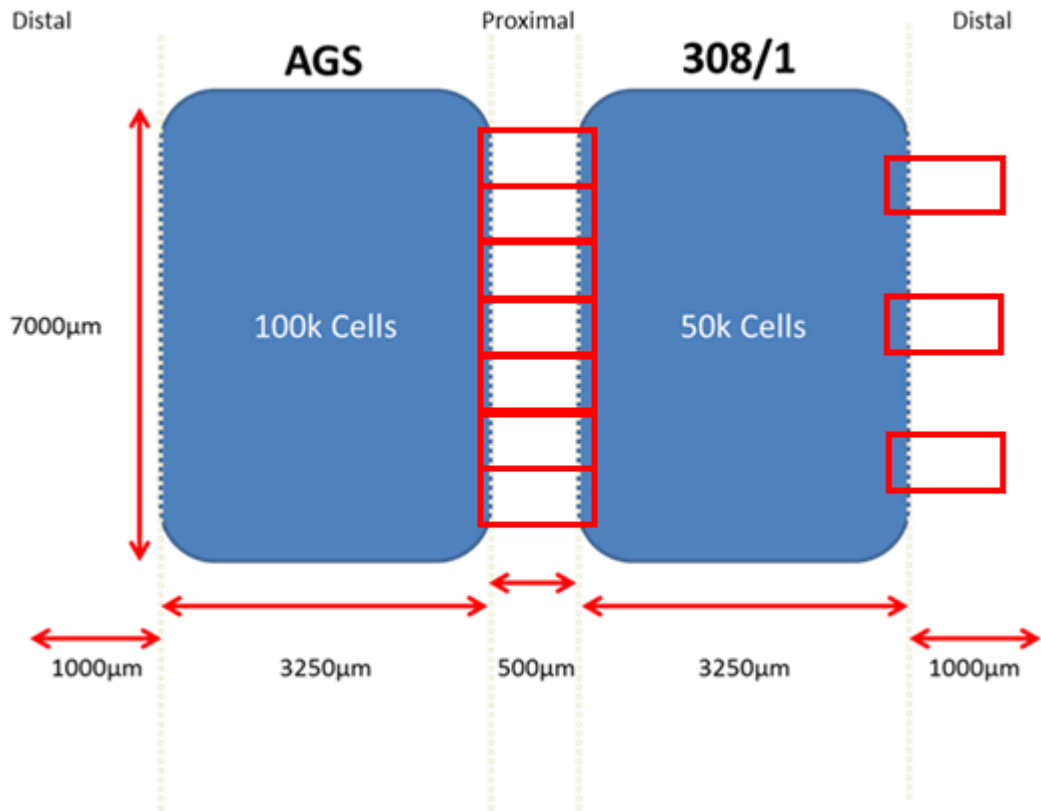


Figure 2-1. Diagram showing the dimensions of the cell populations in each well of the Ibidi chamber. Wells are 7000 µm x 3250 µm with a 500 µm gap. The left and right well contain a monolayer of approximately 100,000 AGS cells and 50,000 308/1 cells respectively. The inner cell boundaries either side of the gap are referred to as the 'proximal' side of the cells, while the opposite outer boundaries are referred to as the 'distal' side. Red squares indicate the area recorded by time-lapse microscope. The red squares for the distal side of the AGS cell population have been excluded for readability. However, it is identical to the red squares visible for the distal side of the 308/1 population.

2.3 Mathematical modelling

The cell migration assays were performed under a time-lapse microscope. Images of the assay were taken every 30 minutes over a period of 24 hours. Cell migration videos were manufactured by stitching these images together and later analysed using ImageJ software. In the first frame of the video ($t=0$), the area of the cell mass, visible in the frame, was measured for each cell type on both the proximal and distal side of the experiment. For each subsequent frame of the video, this initial cell area was subtracted from the new total area of the cells measured, to give the area of migration from the cell mass. Collectively, this data was used to produce a graph showing the average of the total cell migration of the two cell types over time (Figure 2-2). The cells located on the proximal sides were labelled as 'AGS proximal' and '308/1 proximal'. The cells located on the distal sides were used as a control and were labelled as 'AGS distal' and '308/1 distal'. To incorporate the total proximal edge of each cell population, 7 videos were recorded per experiment (Figure 2-1, red squares). Similarly, the distal edges had 3 videos recorded per experiment (Figure 2-1, red squares).

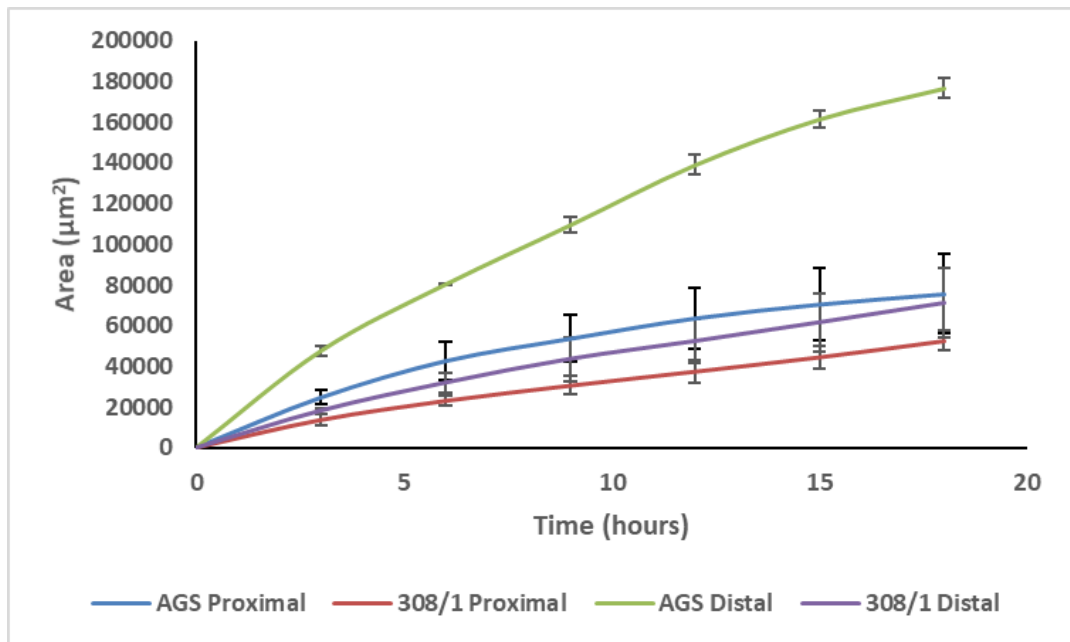


Figure 2-2: AGS cells exhibit increased migration. Graph showing migration of AGS and 308/1 cells over time. The AGS and 308/1 proximal cells are represented by the blue and red lines respectively. The AGS and 308/1 distal cells are represented by the green and purple lines respectively. Error bars are also included for each of the cells.

2.3.1 Increased cell migration in epithelial cancer cells (AGS)

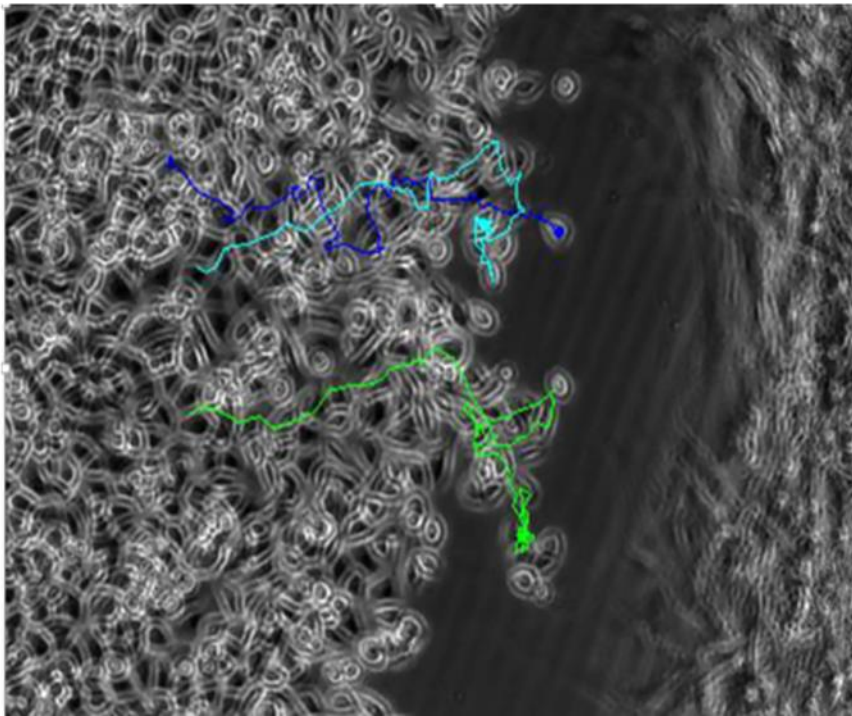
AGS cells exhibited loss of epithelial phenotype from $t=0$. That is, the cells underwent EMT and quickly began migration into the 500 micron space. The proximity of myofibroblasts had a pronounced effect on the speed of migration of the AGS proximal cells (Figure 2-2), as the divide between cell types narrows, the AGS cell progression on the proximal side decreases (approx. $t=4h$). Initially, the 308/1 proximal cells maintain cellular phenotype and exhibit low amounts of cell migration. In subsequent modelling of the proximal AGS cells, it is assumed that the 308/1 cell population is non-migratory for simplicity. This is reasonable given the much lower migratory potential of the 308/1 cells vs the AGS cells displayed in the experiments but is something that could potentially be explored in the future.

At the moment of initial contact between the cell types, there is a decrease in cell migration of AGS cells and inversely, an increase in the cell migration of the 308/1 proximal cells observed in the time-lapse videos. Significantly, an increase can be seen in cell migration between the proximal AGS cells and the distal AGS control cells. At t=18h, the AGS distal cells have migrated into an area 2.5 times larger than that of the AGS proximal cells. In contrast, there is also a larger increase in the area covered by the 308/1 distal cells than that of the 308/1 proximal cells, although on a much smaller scale. The AGS distal cells exhibit the biggest increase in cell migration.

2.3.2 AGS cell migration appears directed

Using manual tracking software on Image J, individual AGS cells were tracked from t=0 to t=18h, using images taken every 15 minutes from a time-lapse microscope (Figure 2-3). The data obtained from these tracks show a direct migration pattern away from the original colony of AGS cells. As shown in the migration assays, the AGS proximal cells migratory behaviour changes with increased proximity to the 308/1 proximal cells. For example, in Figure 2-3A, the direction of migration by the cell denoted with a green track appears to be directed towards the 308/1 proximal cells but then switches to apparent random behaviour as it approaches the 308/1 proximal cells. The cells appear to exhibit the characteristics of random motion once this degree of proximity to the 308/1 cells has been reached. The AGS distal cells exhibit a similar pattern of migration (Figure 2-3B).

A: AGS Proximal



B: AGS Distal

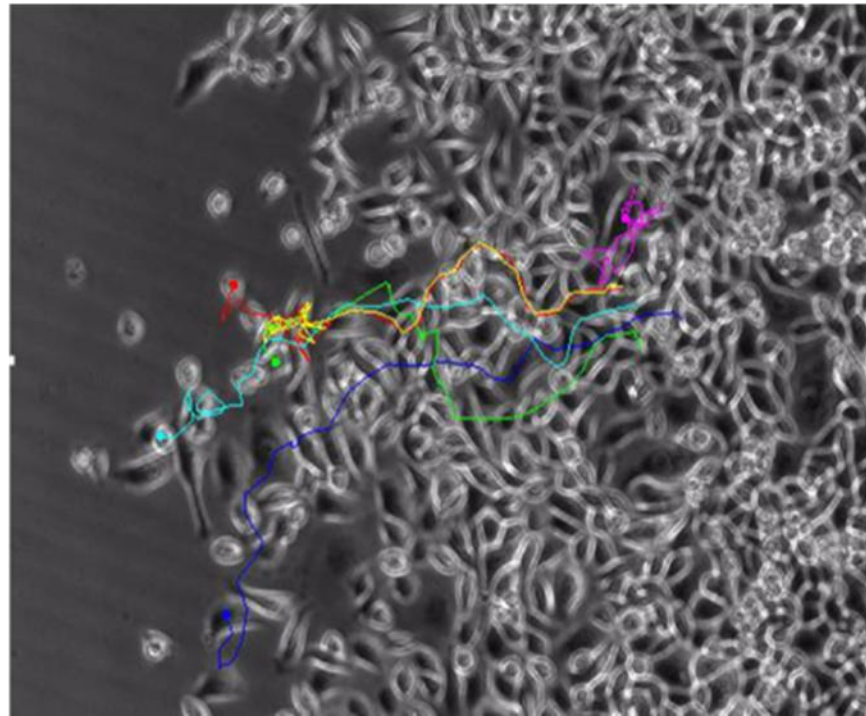


Figure 2-3. Cell migration tracking data. Image showing the migration track patterns of individual AGS cells on the proximal side (A) and distal side (B). Initial migration appears directed. However, the trajectory of the paths tend towards a more random pattern as the AGS proximal cells approach the 308/1 cell mass (A, right hand side). AGS distal cells exhibit similar features. The directed migration trajectory appears to last longer with cells at the distal side.

2.3.3 Model I – Simple diffusion

Subsequent cell migration simulations are used to inform and refine model equations and ultimately explore the underlying mechanisms of interaction present in the biological experiment. Diffusion occurs when particles spread. Fick's law describes diffusion as the net movement of cells from a region of high concentration to a region of low concentration [283]. In particular, the diffusive flux versus the concentration gradient of the variable under the assumption is given by:

$$J = -D \frac{\partial u}{\partial x}, \quad (2-1)$$

in which J ($\text{mol}/\mu\text{m}^2/\text{h}$) represents the particle flux and is proportional to the diffusion coefficient, D ($\mu\text{m}^2/\text{h}$), and negative gradient of the concentration $\frac{\partial u}{\partial x}$ ($\text{mol}/\mu\text{m}^4$). For the modelling, we assume that the 2D experiment can be sufficiently modelled in one dimension, i.e. it is assumed there is no significant variance in the y -direction and that the dominant migration direction is in the x -direction. This is informed by the experimental observations. For simplicity, it is also initially hypothesised that any cell movement from the distal side of the cell populations can be attributed to the effects of diffusion only, although we later readdress this assumption. Therefore, the preliminary model of distal cell movement can be represented using the following partial differential equation (PDE):

$$\frac{\partial u}{\partial t} = -\frac{\partial J}{\partial x} = D \frac{\partial^2 u}{\partial x^2}, \quad (2-2)$$

where cell density is represented by u ($\text{cells}/\mu\text{m}^2$), the location of the cell is represented by x (μm) and D ($\mu\text{m}^2/\text{h}$), is the diffusion coefficient. The diffusion coefficient can be derived from experimental data by taking the average cell

extension in the x-direction and substituting it into Einstein's formula for Brownian motion, which is defined as relating the diffusion coefficient to the mean squared displacement of a Brownian particle. It can be defined as follows:

$$\langle x^2 \rangle = 2Dt. \quad (2-3)$$

This expresses the mean squared displacement $\langle x^2 \rangle$ in terms of time-elapsd, t_i and the diffusion coefficient, D . Therefore, the diffusion coefficient is the result of $\frac{x^2}{2t}$. For example, at $t=18\text{h}$, the mean squared displacement of the AGS proximal cells is $41157 \mu\text{m}^2$, resulting in a diffusion coefficient of $1143.25 \mu\text{m}^2 \text{h}^{-1}$. A further assumption made within the model is that there is a fixed cell density at the source mass of cells ($x = 0$). This is based on the assumption that there is a large enough supply within the monolayer population to maintain this density at the distal and proximal regions. The cell density is rescaled so that $u \in [0,1]$ and u is equal to the maximum density ($u=1$) at the monolayer cell boundary. In relation to Figure 2-1, $x=0$ refers to the boundary of the cell monolayer (on either the distal or proximal sides, depending on the reference point-of-view for the chosen simulation). As time increases, the cells migrate outwards from the cell monolayer to a maximum value of L . Here, L represents either the gap (proximal side) or a sufficiently long, arbitrary distance away from the original cell population within the wells (distal side) in which the migration assay takes place, to give the following initial condition for the cells:

$$u(x, 0) = \begin{cases} 1, & x = 0 \\ 0, & \text{elsewhere} \end{cases} \quad (2-4)$$

with boundary conditions,

$$u(0, t) = 1, \quad \frac{\partial u(L, t)}{\partial x} = 0. \quad (2-5)$$

The boundary conditions state that at $x=0$ the density is fixed at the maximal level and if x equals the right-hand boundary, L , there is zero flux. As flux can be defined as the action of flowing or movement, zero flux is the result of the cell migration ending. As mentioned above, on the proximal side of the cell monolayer, L represents the location of the boundary of the other cell mass (308/1 proximal).

2.3.3.1 Analysis of the cell migration

Figure 2-4 shows model simulations based on the experimental data for the AGS distal and 308/1 distal cells previously plotted in Figure 2-2. The experimental ‘area’ values were converted to migration distances so that there would be consistent output from the experiments and simulations. The simulated migration distance, “Xmean”, was matched to the experiments for the AGS and 308/1 distal cells by using Equation 2-3 to simulate migration distances for different values of D . For example, the Xmean for the AGS distal cells (Figure 2-4A, subplot) and 308/1 distal cells (Figure 2-4B, subplot) is approximately 225 and 90 μm at $t=18\text{h}$, respectively. This approximately relates to the distance the simulated cell front has migrated, using $u = 0.5$ as a reference cell density. Comparatively, the AGS distal cells (Figure 2-4A) migrated into 2.5 times more space than the 308/1 distal cells (Figure 2-4B) over the same time period ($\sim 600 \mu\text{m}$ vs $\sim 225 \mu\text{m}$). Also, the AGS distal cells migrate into the space approximately seven times faster than the 308/1 distal cells when comparing the diffusion coefficients (1143.25 vs $174.79 \mu\text{m}^2 \text{h}^{-1}$).

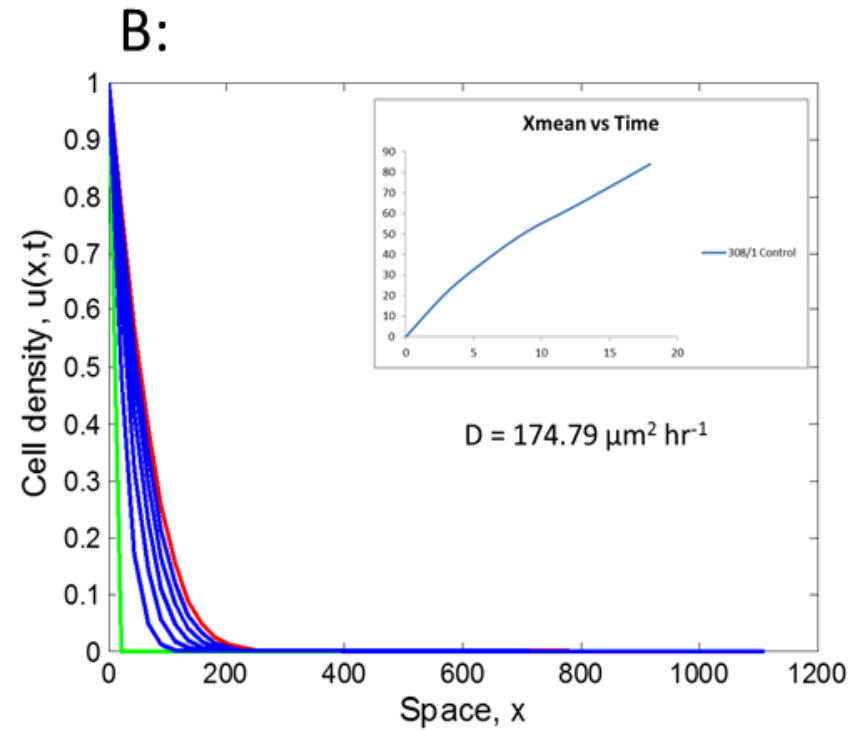
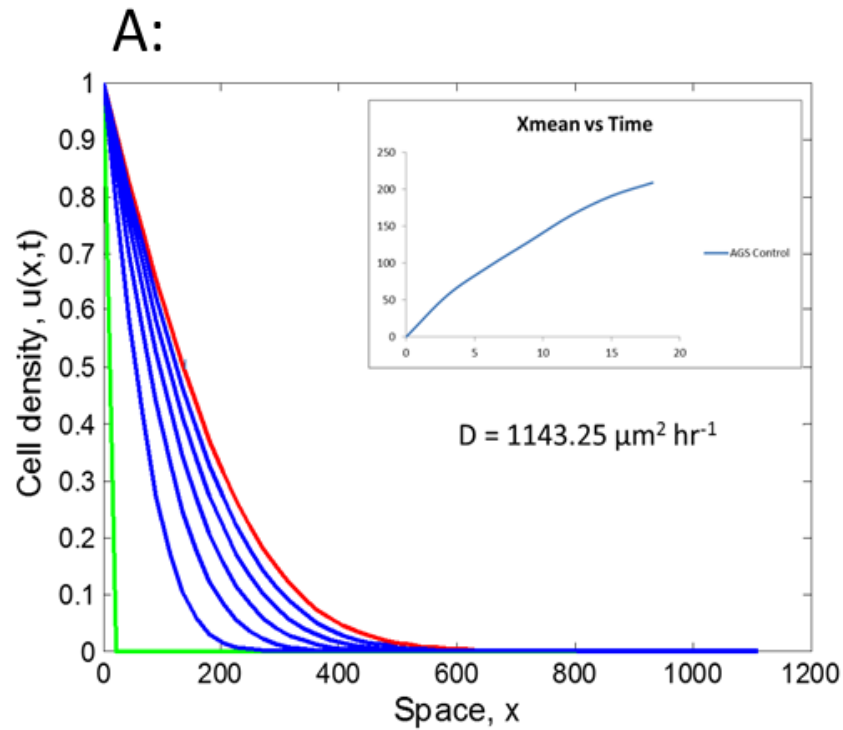


Figure 2-4. Distal cell population migration into space. Simulation of the distal side of the AGS cell population (A) and 308/1 cell population (B) into surrounding area, x . The green line represents the boundary of the cell at $t = 0$ where cell density is 1 (normalised scale). The five blue lines represent the distance travelled by the cells for each subsequent time-point. The red line represents the final time-point ($t = 18\text{h}$). Subplot graphs show experimental data highlighting the x -mean over time. X -mean is equivalent to the distance travelled by 50% of the cell populations i.e., $u = 0.5$. The diffusion coefficient for each cell population is indicated below these subplots.

2.3.4 Model II – Density-dependent diffusion

At $x=L=500\mu m$ on the proximal side, the migrating AGS cells meet the 308/1 cells which they are unable to pass through, resulting in zero flux. As Equation 2-2 results in solutions that are non-compactly supported i.e., $u \rightarrow 0$ as $x \rightarrow \infty$, this made it difficult to estimate the true migration front in the simulations. Consequently, comparison of the simulations to the experiments also proved difficult. Therefore, Equation 2-6 is preferred as it has a clearly defined migration front:

$$\frac{\partial u}{\partial t} = D \frac{\partial}{\partial x} \left(u^n \frac{\partial u}{\partial x} \right). \quad (2-6)$$

The effect of crowding due to the movement of cells based upon density is represented by n . This density-dependent diffusion model can be simulated by using Equation 2-6. The boundary conditions remain the same and the results from the simulation are plotted on Figure 2-5B.

2.3.5 Model III – Addition of inhibitory chemical to proximal cell migration

Due to the observable differences between the proximal and distal cell movement characteristics (Figure 2-2), the third model makes the assumption that the proximal side of the AGS population are affected by some inhibitory chemical, I , produced by the 308/1 cell population, namely,

$$\frac{\partial u}{\partial t} = \frac{\partial}{\partial x} \left(ku^n \frac{\partial u}{\partial x} + \alpha u \frac{\partial I}{\partial x} \right), \quad (2-7)$$

with inhibitor chemical dynamics, described by,

$$\frac{\partial I}{\partial t} = D_I \frac{\partial^2 I}{\partial x^2} - \sigma I, \quad (2-8)$$

and boundary conditions,

$$I(L) = 1, \quad \lim_{x \rightarrow -\infty} I = 0. \quad (2-9)$$

The additional flux term, $\alpha u \partial I / \partial x$ represents cells moving down a gradient of I at some rate, α . For simplicity, we assume that the concentration of inhibitor I equilibrates quickly as it is assumed to be a small rapidly diffusing chemical with dynamics that are much faster than that of the slowly moving cells. To solve for I , a steady state is assumed for Equation 2-8, to give:

$$\frac{d^2 I}{dx^2} - \frac{\sigma}{D_I} I = 0. \quad (2-10)$$

This is a second order homogeneous differential equation and so we assume a solution of exponential form, namely:

$$I = e^{mx} \Rightarrow I'' = m^2 e^{mx}, \quad (2-11)$$

where m is a constant, to be determined, and prime represents derivative with respect to x . Substituting this into Equation 2-10 gives:

$$I'' - \frac{\sigma}{D_I} I = e^{mx} \left(m^2 - \frac{\sigma}{D_I} \right) = 0 \Rightarrow m = \pm \sqrt{\frac{\sigma}{D_I}}. \quad (2-12)$$

This gives us a general solution for I as follows:

$$I = Ae^{\sqrt{\frac{\sigma}{D_I}}x} + Be^{-\sqrt{\frac{\sigma}{D_I}}x}, \quad (2-13)$$

where A and B are constants defined by the boundary conditions. By applying the boundary conditions from Equation 2-9 to this formula for I , the following is obtained:

$$\begin{aligned} I(L) &= Ae^{\sqrt{\frac{\sigma}{D_I}}L} + Be^{-\sqrt{\frac{\sigma}{D_I}}L} = 1, \\ \Rightarrow A &= e^{-\sqrt{\frac{\sigma}{D_I}}L} - Be^{-2\sqrt{\frac{\sigma}{D_I}}L}, \end{aligned} \quad (2-14)$$

and

$$\lim_{x \rightarrow -\infty} \left(Ae^{\sqrt{\frac{\sigma}{D_I}}x} + Be^{-\sqrt{\frac{\sigma}{D_I}}x} \right) = 0. \quad (2-15)$$

To satisfy the second boundary condition (Equation 2-15), it must have $B=0$.

Therefore, the solution for A and I is as follows:

$$A = e^{-\sqrt{\frac{\sigma}{D_I}}L}, \quad (2-16)$$

and therefore,

$$I = e^{\sqrt{\frac{\sigma}{D_I}}(x-L)}. \quad (2-17)$$

Equations 2-7 and 2-17 are used to represent density-dependent diffusion with an inhibitory chemical substance, I , for the proximal side of the cells.

2.3.5.1 Addition of chemotaxis to the model

The solution of this modified density-dependent diffusion model with inhibitory chemical is plotted in Figure 2-5C. Again, the model appears to give a good account of the qualitative dynamics observed *in-vitro*. However, comparison of the 3 model simulations to the experimental plots (Figure 2-6) suggests that the non-inhibition *in-silico* simulations do not appear to fit the data for the proximal side very well. In particular, this graph shows that the simple diffusion model (blue trace) appears unable to describe the proximal AGS cell data. The density-dependent model shows similar qualitative features and comparison to the data for the distal side as the diffusion data. But the best comparison to the data for the proximal side comes from the inhibitor density dependent model. These comparisons have been explored for a range of parameters producing the same key result i.e., proximal AGS cell migration is best described by a model with density dependence coupled with the effect of an inhibitory chemical.

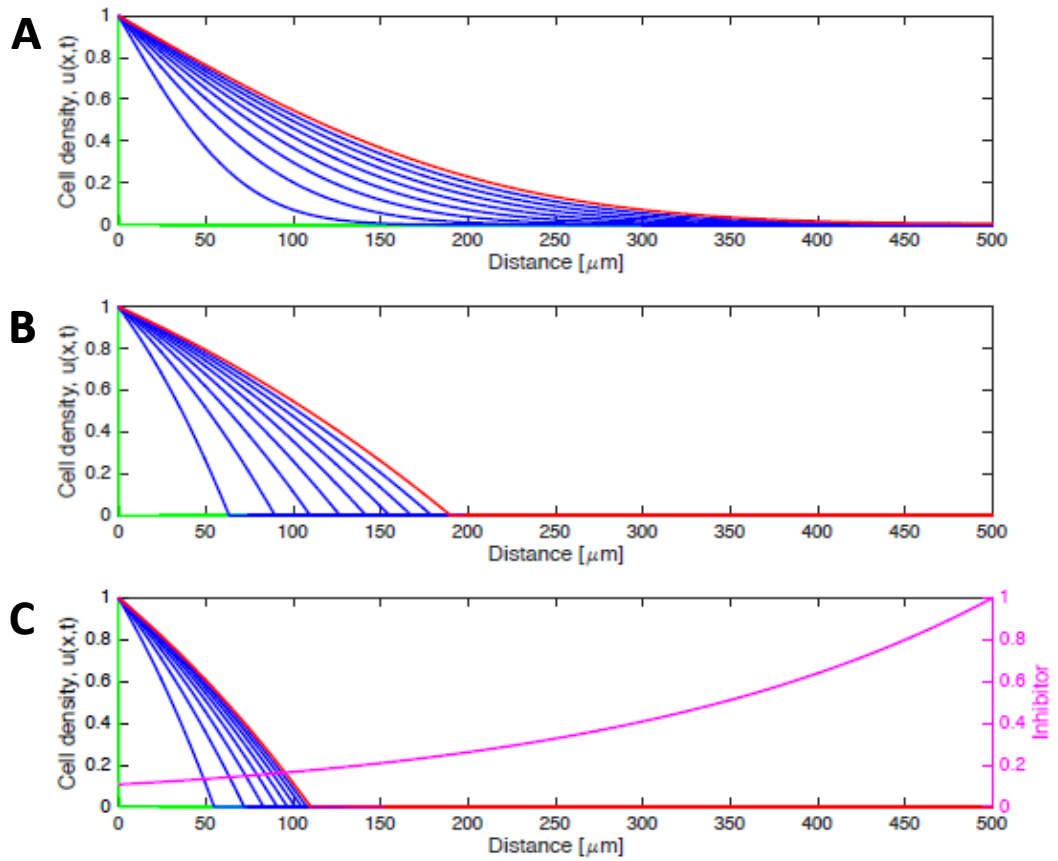


Figure 2-5. Model simulations of migrating AGS cells. All graphs show AGS cells spatially extending into open space over time. Each blue trace represents a time point of three hours. The green trace represents $t=0$ and the red trace represents $t=18$. (A) Simple diffusion simulation of AGS distal cells. (B) Density-dependent diffusion model of AGS distal cells. (C) Density-dependent diffusion model with chemotaxis of AGS proximal cells. The magenta trace represents the amount of inhibitory chemical, I .

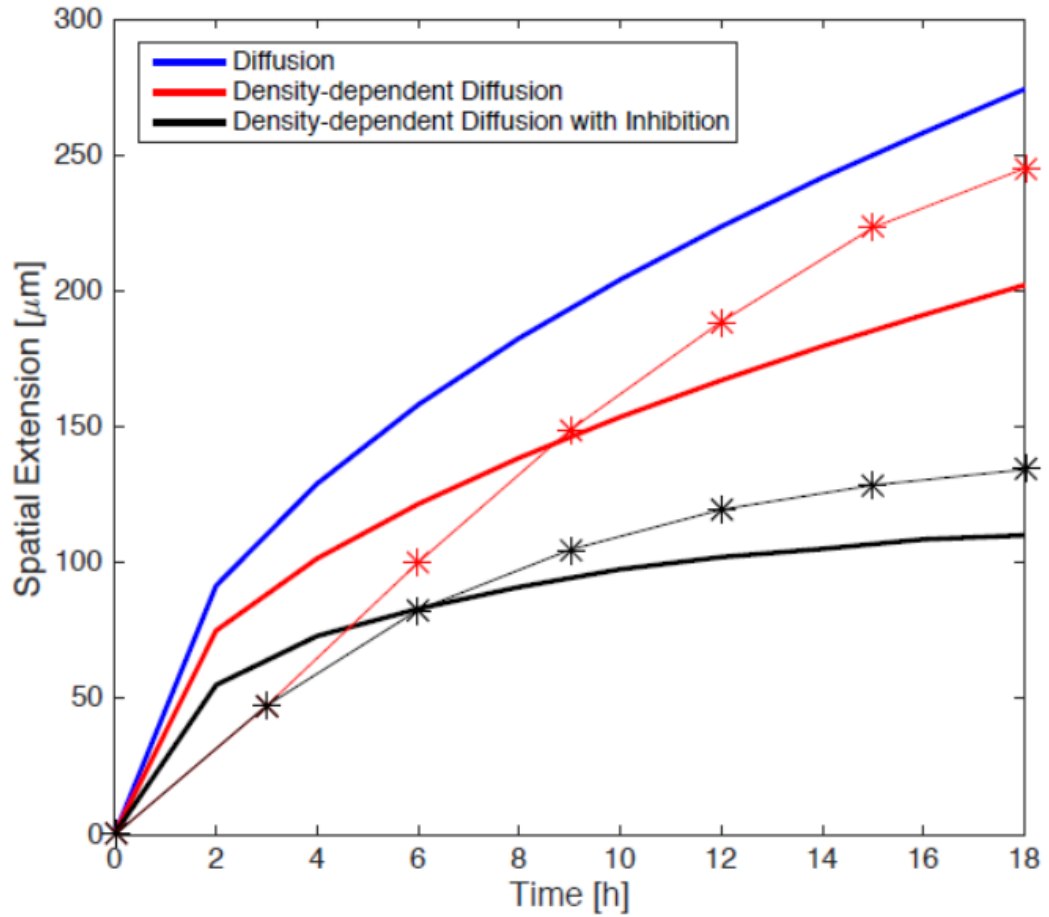


Figure 2-6. Comparison of the three simulated model results with the experimental data. AGS cell extension was plotted over time for the simple diffusion model (blue), density-dependent diffusion model (red) and the density-dependent diffusion model with chemotaxis (black). These were compared to the experimental results of the AGS distal cells (red asterisk) and AGS proximal cells (black asterisk).

2.3.6 Model IV - Addition of the action of an inhibitory chemical to distal cells

In order to model the effect of an inhibitor on the distal cells, the following equations are used,

$$\frac{\partial u}{\partial t} = \frac{\partial}{\partial x} \left(ku^n \frac{\partial u}{\partial x} + \alpha u \frac{\partial \hat{I}}{\partial x} \right) \quad (2-18)$$

with inhibitor chemical dynamics, described by,

$$\frac{\partial \hat{I}}{\partial t} = D_I \frac{\partial \hat{I}^2}{\partial x^2} - \sigma \hat{I}, \quad (2-19)$$

and boundary conditions,

$$\hat{I}(0) = e^{\sqrt{\frac{\sigma}{D_I}}(-3250-L)}, \quad \lim_{x \rightarrow \infty} \hat{I} = 0. \quad (2-20)$$

where 3250 represents the width in μm of the AGS cell mass (Figure 2-1). Different boundary conditions are needed for this model as the distal side of the AGS cell mass is further away from the source of the inhibitory chemical (308/1 cells). Again, we can solve for \hat{I} by assuming a steady state and applying the boundary conditions (Equation 2-20) to give:

$$\hat{I} = Ae^{\sqrt{\frac{\sigma}{D_I}}x} + Be^{-\sqrt{\frac{\sigma}{D_I}}x}, \quad (2-21)$$

where A and B are constants. Now, we apply the boundary conditions from Equation 2-20, namely:

$$\hat{I}(0) = A + B = e^{\sqrt{\frac{\sigma}{D_I}}(-3250-L)} \quad (2-22)$$

$$\Rightarrow A = e^{\sqrt{\frac{\sigma}{D_I}}(-3250-L)} - B \quad (2-23)$$

and

$$\lim_{x \rightarrow \infty} \left(A e^{\sqrt{\frac{\sigma}{D_I}} x} + B e^{-\sqrt{\frac{\sigma}{D_I}} x} \right) = 0. \quad (2-24)$$

In this instance, A=0 in order to satisfy the second boundary condition, resulting in the following solutions for B and \hat{I} :

$$B = e^{\sqrt{\frac{\sigma}{D_I}}(-3250-L)}, \quad (2-25)$$

$$\hat{I} = e^{\sqrt{\frac{\sigma}{D_I}}(-3250-L-x)}. \quad (2-26)$$

As with the proximal AGS cells model, it is assumed that the inhibiting chemical, \hat{I} , has an effect on the distal AGS cells, which reduces as the cells migrate away from the source. Secondly, the parameters are the same as they were for the proximal AGS cell model, but the spatial reference is different and thus the model simulation is achieved through calculating new inhibitory dynamics and boundary conditions, using Equations 2-18, 2-19 and 2-20. The results for the density-dependent diffusion models with added inhibitory chemical effect are plotted in Figure 2-7. The inhibitory chemical, \hat{I} , decreases exponentially with distance relative to the normalised maximum chemical concentration at the source ($u=1$). On the distal side of the AGS cells (Figure 2-7A), the amount of chemical acting on these cells is smaller (8 orders of magnitude lower) when compared to the concentration of inhibitor at the proximal side of the AGS cells. Comparison of these simulations to the AGS experimental data (Figure 2-8) suggest that the inclusion of this inhibitor chemical doesn't significantly alter the migration of the distal AGS cells. This is rather intuitive as the distal cells are a significant distance from the potential inhibitor source and so its effects would be relatively diminished.

In summary, there are four distinct models describing the *in-vitro* experiments. Model I attempts to describe the cell migration due to effects of simple diffusion only (Equation 2-2), whereas model II describes the experiment results as a density-dependent diffusion model (Equation 2-6). Motivated by the experimental data, model III incorporates a chemical gradient of substance, I , into the density-dependent diffusion model and is applied to the proximal side of the cell AGS cell mass only (Equation 2-7). Finally, model IV is adapted from model III and applied to the distal side of the cell mass (Equation 2-18). The key finding is that distal AGS cell movement appears to depend on the action of an inhibitor chemical produced by the 308 cells. These results are inconclusive regarding the migration of the proximal cells, which are equally modelled well with either simple diffusion or density/inhibitor effects.

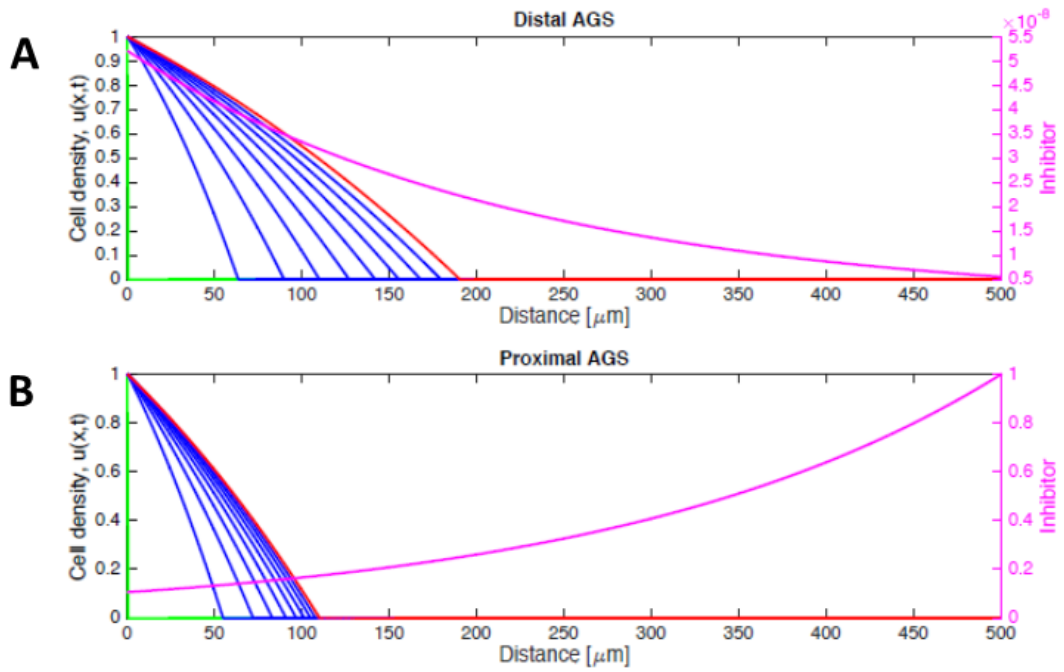


Figure 2-7. Effect of inhibition on dynamic profile of AGS cell migration. All graphs show AGS cells spatially extending into open space over time. Each blue trace represents a time point of three hours. The green trace represents $t=0$ and the red trace represents $t=18\text{h}$. Magenta traces represent amount of inhibitory chemical, I . (A) Density-dependent diffusion model with chemotaxis of AGS cells on the distal side. (B) Density-dependent diffusion model with chemotaxis of AGS cells on the proximal side.

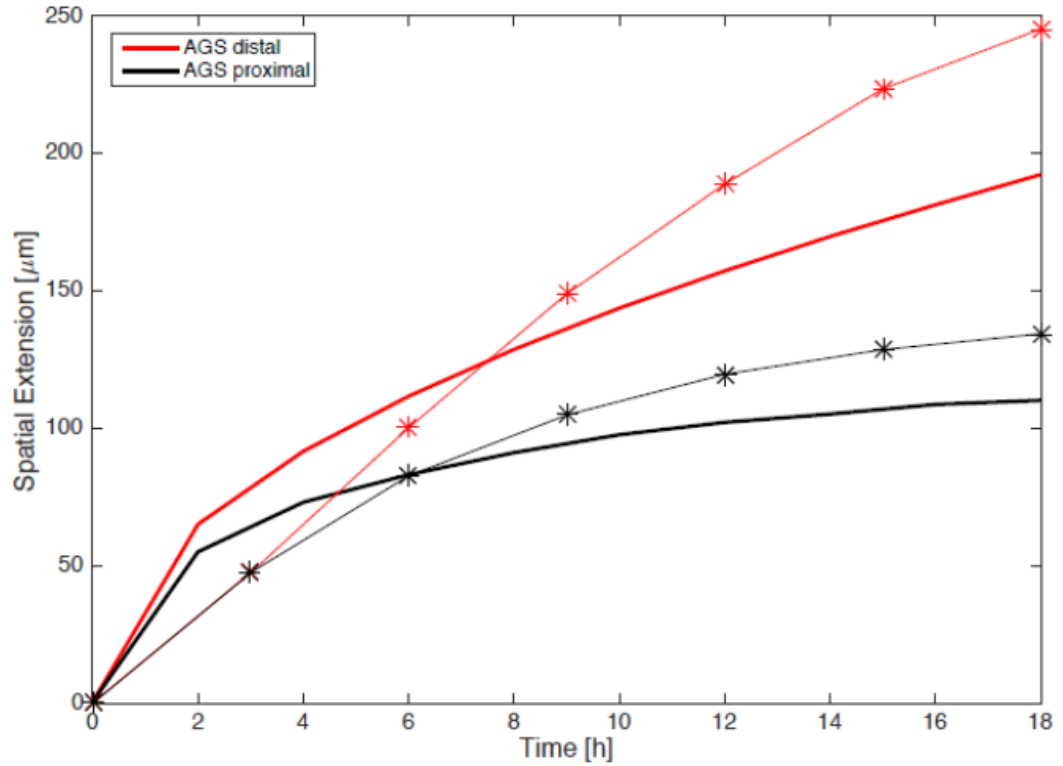


Figure 2-8. Comparison of the inhibition model simulations with the experimental data. Simulated AGS cell extension was plotted over time for the density-dependent diffusion model with added chemotaxis for the AGS distal cells (red) and the AGS proximal cells (black). These were compared to the experimental results for the AGS distal cells (red asterisk) and AGS proximal cells (black asterisk).

2.4 Chapter Discussion

This chapter describes the evolution of a number of *in-silico* models in an effort to describe the migratory cellular phenomena observed during *in-vitro* cell migration assays. Furthermore, this approach was extended to include interaction between the AGS proximal cells and 308/1 proximal cells, through the addition of an inhibitory chemical. Initially, the migration of the AGS cells are described by a simple diffusion model. Upon comparison with corresponding traces from the experimental data (Figure 2-6), this model was deemed insufficient, in terms of describing the dynamic movement exhibited by the AGS cells on the distal side. Therefore, the model required updating to replicate the observations from the *in-vitro* experiments. Before the cell migration assay began, the AGS cells, which are epithelial cancer cells, were cultured in a monolayer. This means they were exhibiting an epithelial phenotype, tight cell-cell adhesions, before undergoing EMT. This cell-cell adhesion provided motivation for a density-dependent dispersal form of diffusion. Therefore, we modified the model to account for density-dependent diffusion (Model II). Model II appeared to better describe the dynamic characteristics exhibited by the migratory AGS cells. However, the expansion of these cells into the acellular space appeared too rapid. This observation provided the motivation to add the inhibiting chemical, *I*. The manual tracking data also suggests an inhibition model would be appropriate, as it clearly shows the direct migration of the AGS cells followed by a delayed inhibition. In Figure 2-6A, the tracked cells migrated in a direct, unidirectional manner and as the acellular space between the AGS and 308/1 cells decreased, so too did the direct migration pattern of the tracked cells. In contrast, the cessation of direct migration

by the tracked cells in Figure 2-6B was less obvious as there was no decrease in acellular space.

Fick's first law describes that the flux due to diffusion is proportional to the concentration gradient [283]. Qualitatively and quantitatively, the time lapse microscopy data can be used to observe and predict the cellular migration patterns of the cell types. This is where *in-silico* modelling approaches prove useful. For example, the diffusion coefficient, D , was calculated from the input of cellular density, u , and extension of the cells into the space, x , using Equation 2-3. The diffusion coefficient represents the driving force which arises from the differential surface energies in the system, i.e. the difference in surface energy between homotypic cells, heterotypic cells and between the cells and the external environment. The AGS cells on the distal side have a diffusion coefficient of $1143.25 \mu\text{m}^2 \text{hr}^{-1}$ and the AGS cells on the proximal side have a diffusion coefficient of $174.79 \mu\text{m}^2 \text{hr}^{-1}$. This greatly reduced diffusion coefficient on the proximal side provides further support for the assumption that the 308/1 cells release an inhibitory chemical. Subsequently, to describe the proximal side of the AGS cell movement, further modification was again needed. As previously mentioned, 308/1 cells are CAMs and it has been shown that CAMs are involved in multiple cell signalling networks and express a range of growth factors, cytokines and chemokines. Therefore, their interaction with the AGS cells needs to be taken into account within the model, by incorporating an inhibitory chemical effect into model II. The simulations of model II and III were also plotted against the experimental traces in Figure 2-6. Model III showed a better fit to the AGS proximal data from the experiments (black traces), than model I and II (red traces). Next, the effect of the

chemical, I , on the distal side of the AGS cells was tested, but the effect was found to be minimal, which is intuitive given the distance of these cells from the inhibitor source. However, future work for this project can clarify these assumptions through the addition of controls to the study. For example, the next logical experiment to be performed would be a cell migration assay containing two independent cell monolayers of AGS cells. The data obtained from observing these cells migrate in the absence of the 308/1 cells could indicate exactly the type of effect the 308/1 cells had on the AGS population i.e., attraction, inhibition or a combination of the two. Unfortunately, due to technical difficulties with the equipment and a change in institution, this work was prematurely ended. Additionally, further control experiments with just the CAM cell monolayers present would help to focus the direction of subsequent model building.

The key result is that the inhibitor model appears to describe the dynamic profile exhibited in the *in-vitro* experiments better than the simple diffusion and density-dependent diffusion models. However, it is still insufficient to describe the system fully. There is increasing evidence that the presence of CAMs contribute to tumour growth [284]. The mechanisms of homing and migration remain incompletely understood. Previous studies have reported that CAMs evoke a more aggressive phenotype in cancer cells compared with myofibroblasts derived from normal tissue environments [96]. This was observed from the experimental data where, initially, the AGS proximal cells migrated directly towards the 308/1 cells. Nevertheless, inhibition was also present between the cell types, as the experiments displayed a decrease in migration as the AGS cells encroached upon 308/1 cell monolayer. Potential theories as to why this happened include: (a) contact inhibition from the

decrease in acellular space for the AGS cells to migrate into [285]; (b) the release of a compound from the CAMs that directly inhibits the migration of the AGS cells, or; (c) the AGS cells slow down due to the energy spend required to remodel the extracellular network that has been laid down by the myofibroblasts [80]. Recently, an integrated multi-omics study [286] revealed for the first time that myofibroblasts derived from the site of gastric adenocarcinomas (CAMS) are epigenetically reprogrammed through DNA methylation and enhance the proliferation and migration of cancer cells. Therefore, this study provides motivation for further model refinement to include mechanisms of attraction in an attempt to define the underlying mechanism of interaction between these key cell types.

Chapter 3: Discrete Cell Based Model in Fibroblast Cell Migration

3.1 Introduction

This chapter focuses on modelling cell movement at the mesoscopic scale. The internal architecture and mechanisms, described previously in section **Error! Reference source not found.**, involved in the migration of an individual cell are not considered explicitly in this model. However, the role they play in mechanotransduction and polarised cell movement are reflected implicitly. For example, the cell is considered to sense its external environment and extend through a leading edge, by forming adhesions and assembling cytoskeletal machinery. Thus, it can be assumed that the cell will migrate in the direction of the leading edge. In other words, it is assumed that the cell is unlikely to make sudden 180° turns in its migration pathway and is much more likely to make smaller, smoother gradual movements as it senses the surrounding environment. Cell migration assays conducted on polyurethane surfaces containing varying topographical features were used to inform and validate the mathematical model. Using this model in combination with the experimental data, key question of whether surface topology affects the migratory cell path of fibroblasts can be addressed. This work on mechanotransduction offers great potential into the possibility of controlling cell behaviour, using physical cues. Biofilm formation and the impact of implant integration are some of the key areas that may benefit from this control [287]. Biofilms are communities of adherent cells held together in a self-produced matrix of extracellular polymeric substances (EPS) [288]. The formation of biofilms during infection in wound sites and in inorganic materials such as catheters and stents can be detrimental as they exhibit increased protection from antibiotics [288,289].

Therefore, understanding how to control cellular behaviour in such a system by altering its physical environment could provide the platform for a major breakthrough into tackling this complex problem. Also, it has been shown that increasing the surface roughness on the implants also increases the adhesive properties for fibroblast cells and suggests that there could be an improvement in wound healing, limiting the risk of capsular contracture [290].

3.1.1 Mathematical modelling of cell migration

Multiple mathematical models exist to describe the process of cell migration, as previously described in section 1.5.6. However, random walk models were determined to be the most appropriate for modelling the experimental observations in this chapter. These random walk models are based primarily on Brownian motion [199]. Brownian motion can be described as the random movement of particles due to their collisions with other atoms and molecules. A theoretical process describing Brownian motion is called the Wiener process [199]. The Wiener process is defined as a continuous-time stochastic process and is named in honour of Norbert Wiener [199]. Brownian motion is considered a Gaussian-Markov process, in that it has normally distributed random variables over a continuous time constant and is considered a memoryless process [199].

In this chapter, a stochastic mathematical model is proposed for the random motility and mechanotransduction of single cells and evaluate the migration paths on patterned surfaces. In the model, cell velocity is described as a persistent random walk using the Ornstein-Uhlenbeck (O-U) process [291].

3.1.1.1 Ornstein-Uhlenbeck process

The advantage of using this model is that it allows the simulation of individual cell migration paths. The O-U process has previously been proposed to quantify individual cell random motility in a number of studies [291-294]. For example, by incorporating a discrete description of the O-U process, Dunn and Brown [295] were able to successfully demonstrate that the O-U process characterizes fibroblast random motility through use of the autocorrelation functions of cell displacements during discrete time intervals.

In general terms, using the O-U process, the velocity of a cell can be described in terms of two processes: i) stochastic fluctuations in velocity and ii) deterministic resistance to the current velocity. The stochastic term represents all of the probabilistic processes that might affect cell velocity (e.g. response mechanisms to gradient of the cell surface features, etc). The deterministic term affects the persistence of motion mimicking e.g. surface friction, viscosity, etc.

This approach was extended by Stokes et al. [291]: first by using a continuous version of the O-U process; and second, by adding a term to represent directional bias in response to the presence of a chemoattractant gradient. In the present work, the directional bias term is adapted to represent an environmental gradient (i.e. surface pattern) instead of a chemical gradient. This is applied to an extended model to analyse the experimental data of migrating lung fibroblast (LL24) cells on three different surface types with varying topological features (Flat, Linear and Random).

This chapter begins with a description of the continuous version of the O-U process with the adapted directional bias extension. The standard O-U process is characterised by two parameters. These parameters are α ($\mu\text{m}^2/\text{min}^4$) and β (1/min) and these represent magnitudes of random fluctuations in velocity and velocity decay, respectively. The model's applicability is validated for random fibroblast migration and provides relative estimates for α and β . Then, an additional parameter, κ ($\mu\text{m}/\text{min}^2$), is introduced to account for the directed motion of the fibroblast cell in response to the surface gradients. The κ -parameter could not be measured directly but it is shown how it can be estimated using model-generated cell paths.

3.1.2 Chapter aims

1. To create an extended continuous O-U model to accurately describe random motility and surface bias.
2. To use combined *in-silico* and *in-vitro* results to determine the mobility parameters α and β and the bias parameter κ .
3. To validate the *in-silico* output with the experimental data.
4. Use the *in-silico* model outputs to predict how different surfaces (Flat, Linear, Random) can affect cell motility.

3.2 Materials and Methods

The experiments performed in this chapter were completed in collaboration with Dr Mark Murphy's lab in the General Engineering Research Institute (GERI) at Liverpool John Moores University (LJMU). The generation of the patterned surfaces were conducted by this lab and a summary of these methods are contained in Appendix A (Section 7.1). All the other experiments including cell culture, migration assays and mathematical modelling were performed by myself and are detailed below.

3.2.1 Cell culture

The cells described in this work are human lung fibroblast cells (LL24) which have been purchased from the European Collection of Animal Cell Cultures (ECACC) UK. Fibroblast cells were chosen because there is extensive evidence showing that fibroblast cells respond to changes in surface topography both *in-vitro* and *in-vivo* [180]. The LL24 cell line was chosen as it is a well characterised, stable, normal human diploid cell line [180]. All cell culture work was carried out under aseptic conditions in a grade II laminar flow cabinet (EBSCO). Cells were maintained at 37 °C in a humidified 5% CO₂/95% air atmosphere in Dulbecco's Modified Eagles Medium (DMEM) (Sigma-Aldrich, D6429) supplemented with 10% foetal bovine serum (Sigma-Aldrich, 0804) and 1% penicillin-streptomycin. All experiments were carried out using cells at passage numbers 20–24.

3.2.2 Cell migration assay

To determine if the different surfaces affected cell migration, time-lapse imaging and subsequent cell tracking was performed over a four-hour period using a Zeiss LSM 510 confocal microscope. Briefly, the polymer surfaces were sterilised in 70%

ethanol, washed in PBS then placed into 35 mm cell culture dishes. Next 100,000 cell/cm² were seeded onto the polymer surfaces and the dish was placed into a microscope environmental chamber (S-2, PeCon GmbH, Germany). The chamber was maintained at 37°C, 5% CO₂ in a 60–70% humidified air atmosphere using a Temcontrol 37-2 and CTI-controller 3700 (PeCon GmbH, Germany). Images were taken every 10 min for 2.5 h using a 20× Plan-Apo/0.75 NA DIC objective lens, while scanning using a Helium- Neon (HeNe) laser at 543 nm. Images of the patterned surfaces without any seeded cells were also taken. This was done so that the specific features of each surface could be transferred to the *in-silico* model framework (Figure 3-2).

3.2.3 Measurement of cell trajectories, mean squared displacement and tortuosity

Cell movement tracks were analysed using ImageJ software (National Institute of Health, NIH) with a manual tracking plugin (Institute Curie, France) used to analyse the data produced from the time-lapse image series. The centroid of the cell area was used to represent the cell position. The time increment between image frames was ten minutes. This was long enough to discern cell movement without losing track of the cell's position. The result was a series of migration distances vs time for each individual cell. The net displacement was calculated by the difference of the position at the beginning and end of each time step. The displacement, which is the measure of the cells position relative to its starting point over time, was calculated by subtracting the cells origin point from its current position. This was done for each cell at each time point. The mean of the square of the values was calculated to give the mean square displacement (D^2) vs time. D^2 measures the deviation of the position

of a cell with respect to a reference position over time, and is useful in determining if the movement of a cell is solely down to diffusivity or if an external force is directing the motion. Tortuosity, τ , can be defined as the property of a curve being tortuous i.e. having many turns (a twisted path). Tortuosity can be estimated using the arc-chord ratio (Figure 3-1): the ratio of the length of the curve (L) i.e. the actual path travelled by the cell to the straight-line distance between the ends of this path (C), namely:

$$\tau = \frac{L}{C} \quad (3-1)$$

L is the total curved-line distance and is measured by obtaining the total distance travelled by the fibroblast from $t=0$ to $t=160$. C is the straight-line distance travelled by the fibroblast and can be obtained by measuring the distance of the cell's position at $t=160$ from its starting position at $t=0$.

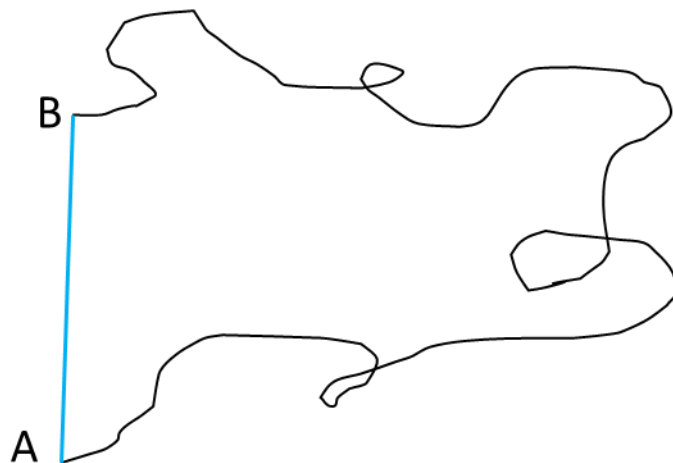


Figure 3-1. Schematic illustration of tortuosity calculation of cell migration path. Black line represents the migratory path taken by fibroblast cell from its origin (A) to its destination point (B). Using this example, L equals the length of the black line and C equals the length of the blue line.

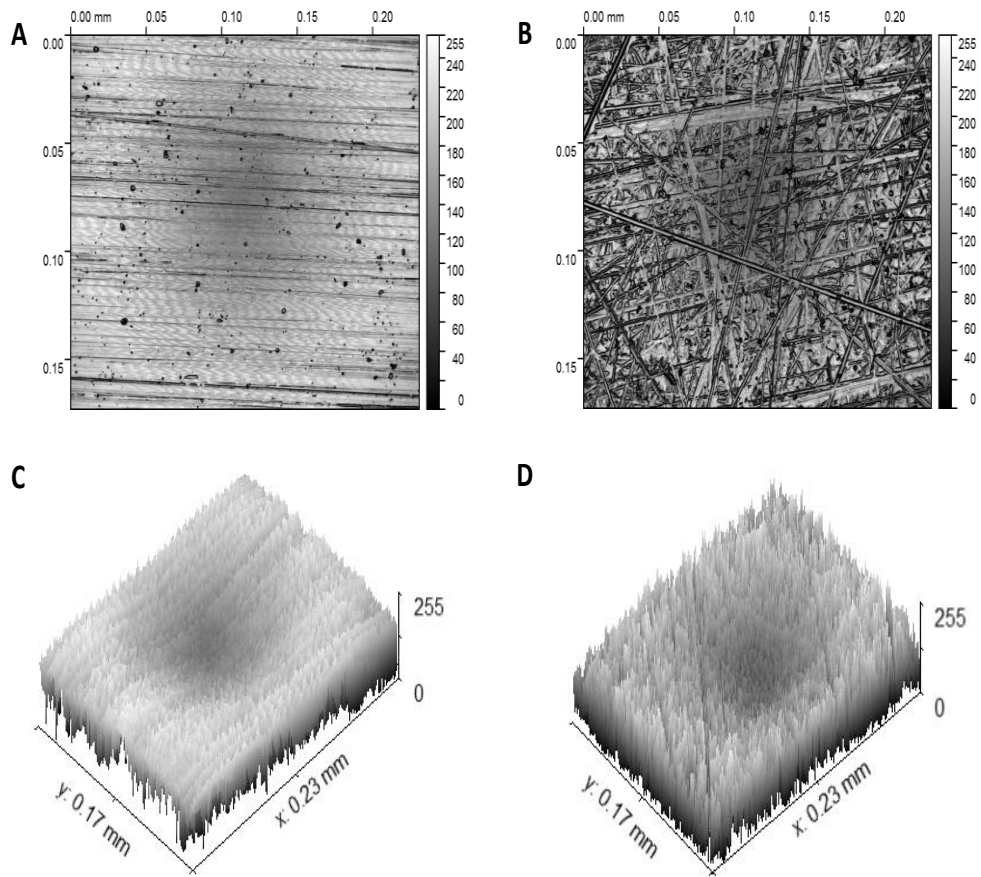


Figure 3-2. Microscope images of the patterned surfaces. (A & B) These images show the linear and random patterned surfaces, respectively. The linear surface exhibits features in a ‘ploughed field’ pattern with straight lines etched from left to right. The random surface exhibits features producing a network of overlapping lines. (C & D) These are 3D schematic images of the linear patterned surface and random patterned surfaces, respectively. The scale in the z-axis represents intensity which is subsequently used to represent feature depth/height in the *in-silico* simulations.

3.2.4 Mathematical model

The cell motility is studied in terms of a stochastic O-U process which is used to describe a random cell motility model, updated via a Markov process. This means that only the current state of the cell is taken into account and the cell's previous positions have no bearing on its future movements; i.e. there is no memory to the motion (white noise) [291]. Although this may seem oversimplified, Dunn and Brown [295] showed that this process is sufficient to describe random motility in fibroblast cells. Initially, this model is used to describe an unbiased random walk process (i.e., cells moving on a smooth surface). Then, through the addition of a haptotactic gradient term, it is extended to a biased random walk model. For this model, it is assumed that the cell responds to a spatial gradient of focal adhesions between the cellular membrane and the surface topography, although there are no assumptions made about the cell's actual underlying mechanism of perception. It is also assumed that the fibroblast cell moves perpendicular to the gradient of the features of the surface i.e. the cell migrates along the surface grooves rather than up/down them.

The details of the mathematical model are as follows: Equation 3-2 describes the velocity of a single cell as it evolves across an $(x, y) \in \mathbb{R}^2$ plane with time; a second equation (Equation 3-3) is then used to determine the cell's (x, y) position from this velocity, producing a calculated trajectory for the cell; from this trajectory, the squared displacement and tortuosity can be calculated. Comparison of these predicted metrics to those obtained experimentally will allow us to: (1) examine the validity of the model and (2) determine values of the model parameters, appropriate for the fibroblast migration.

The rate of change of cell velocity is the sum of three components: the first two components represent the random motility behaviour, and the third represents the haptotactic, or directed, behaviour. For random motility, the first term describes the deterministic resistance to the cell's current velocity, and the second represents the random accelerations (or fluctuations) of this velocity. The third component that describes the haptotactic behaviour provides a directional bias in the presence of a patterned surface gradient. Mathematically, these three components are summed to give the following stochastic differential equation for the rate of change of the cell velocity, \underline{V} :

$$d\underline{V}(t) = -\beta\underline{V}(t)dt + \sqrt{\alpha}d\underline{W}(t) + \underline{\Psi}(t)dt, \quad (3-2)$$

where α ($\mu\text{m}^2/\text{min}^4$) and β ($1/\text{min}$) are the motility parameters, t (min) is time, \underline{W} is the vector Weiner process (white noise), and $\underline{\Psi}$ is the haptotaxis function (see Equation 3-4), which describes the effect of the surface features on the velocity of the cell. The terms \underline{V} , $\underline{\Psi}$ and \underline{W} are vectors in \mathbb{R}^2 , capturing the x and y components of the cell velocity. As the velocity of the cell is a rate of change of the cell's position, the position of the cell, $\underline{x} \in \mathbb{R}^2$ can be obtained from the following:

$$\frac{d\underline{x}}{dt} = \underline{V}(t). \quad (3-3)$$

The parameter β can be viewed as the magnitude of resistance to motion, leading to a decrease in the persistence of velocity as β increases. The haptotactic term provides the directional bias in velocity caused by a cell reacting to the presence of surface topologies. As previously mentioned, it is assumed that the cell responds to a spatial gradient of focal adhesions between the surface of the cell and the surrounding environment. The gradient will be dependent on the steepness of the surrounding

pattern features, denoted by ∇a , where a is the height of the feature (see Figure 3-2(D)) and ∇ is the spatial gradient. Let the haptotactic term be proportional to $\cos \theta$, where θ is the angle between the direction of the cell and the direction of the surface pattern at the cells current position. Thus, introducing κ as the proportionality constant gives:

$$\underline{\Psi} = \kappa \nabla a \cos \theta. \quad (3-4)$$

Equations (3-2) and (3-4) provide a description of the velocity process of a single cell moving with the properties represented by the random motility parameters α and β and the haptotaxis parameter κ ($\mu\text{m}/\text{min}^2$). Each cell described by equations (3-2 – 3-4) with a given set of parameters, α , β and κ , will have a different path or trajectory (owing to different realisations of the random noise process, \underline{W}) but the same 'degree' of randomness (described by α), velocity decay rate constant, and sensitivity to attractant gradients.

For this framework to be meaningful, it must first be demonstrated that it is a valid description of the experimental cell trajectories. Before estimation of the haptotactic responsiveness (κ) can be accomplished, the polyurethane surface patterns and features need to be encoded in the model. A flow diagram depicting this process is available in Figure 3-3. This was achieved by taking the microscope image data, from Figure 3-2, saving it as an ASCII-delimited file and using the MATLAB function 'dlmread' to convert it into a matrix. This matrix now contains numerical values which represent intensity values between 0 and 255 for each point of the image (0 = lowest height feature; 255 = tallest feature). These intensity values represent the depth and height of the surface features and were subsequently normalised to [0,1] and then converted into gradient values, using the Matlab function scatteredInterpolant, for

each x - y coordinate (denoted ∇a). The 'scatteredInterpolant' creates an interpolant that fits a surface of the form $v = F(x, y)$. Vectors x and y specify the (x, y) coordinates of the gradient values and v contains the gradient values associated with the points (x, y) . This allowed the steepness of the topological features of the experimental polymers to be incorporated into the simulations. Firstly, experimental metrics were used to optimise the parameters α and β for the flat model simulation ($\kappa = 0$). These α and β values were then fixed for all subsequent simulations on each of the patterned surfaces. In these subsequent simulations, cell velocity was updated using Equation 3-2 with $\kappa \neq 0$. For Equation 3-4, θ is calculated using the dot product between the vector ∇a (i.e. describing the gradient of the surface topology at the cell position (x, y)) and the cell velocity vector $\underline{V}=(V_x, V_y)$, namely:

$$\theta = \cos^{-1} \left(\frac{\underline{V} \cdot \nabla a}{\|\underline{V}\| \cdot \|\nabla a\|} \right), \quad (3-5)$$

where θ is the angle between \underline{V} and ∇a .

The key aim of all these simulations is to obtain values for the parameters α , β and κ , which then provide a quantitative description of the characteristics of the actual cell's intrinsic motility properties on the different polyurethane surfaces from which predictions can be made about how the different patterned surfaces affect the cell movement.

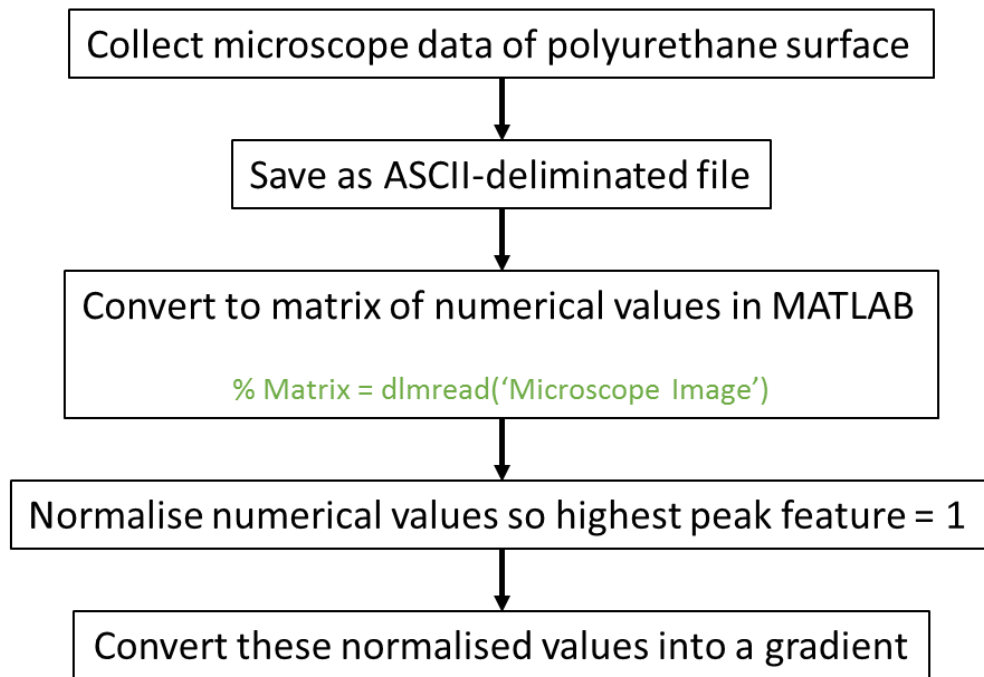


Figure 3-3: Schematic of image conversion to code. Flow diagram shows basic steps involved to convert microscopic data into MATLAB code to have accurate gradient information for simulated cell to migrate upon.

3.3 Results

3.3.1 Cell trajectories

Several typical cell paths for fibroblast cell migration on the experimental polyurethane surfaces are shown in Figure 3-4. The paths reveal that fibroblast cells migrate with a combination of smooth and twisted trajectories. The persistence time in a given direction does not appear to be very long. The duration of all cell paths ranged from 140-160 minutes. The final measurement of the cell path is represented by the round head feature of the trace (—●), whereas the origin of the cell trajectory is represented by the tail like feature (—). The cells that extended beyond the reach of the domain were ignored. The cell paths for fibroblast cell migration on the Linear and Random patterned surfaces are shown in Figure 3-4B and Figure 3-4C, respectively. These paths represent the movement of the centroid of the cell area. Qualitatively, directional changes in the cell paths appear smooth initially, before more frequent turns in trajectory. Certainly, initial inspection suggests that the fibroblast cells on the linear pattern (Figure 3-4B) travel a greater distance from their origin site compared to the cells on the other polyurethane surfaces.

3.3.2 Experimental metrics

Individual fibroblast cells were tracked using ImageJ ($n=13$ for flat and random, $n=41$ for linear), as previously described in section 3.2.3. Firstly, the multiple individual cell trajectories were averaged and the tortuosity was calculated for each of the three surfaces (Flat, Linear and Random). These values are plotted with associated error bars indicating standard deviation in Figure 3-5A. The mean tortuosity measured for each surface was 3.4 ± 2.12 (Flat), 2.95 ± 0.31 (Linear) and 2.96 ± 1.62 (Random). For reference, if a cell were to have a tortuosity ratio equal to 1, that cell path would have a trajectory in a perfect straight line. There is a

large variance in tortuosity on the flat and random surfaces, compared to that of the linear surface. This suggests that there is a greater persistence time in cell direction for fibroblast cells migrating on a surface with linear features. However, note that there is no statistical significance in tortuosity between the three surface types (Figure 3-4). What is apparent from the values outputted from these measurements is that the cells have a slightly more directed migration on the surfaces containing the linear and random nano-scratch features i.e. have a lower tortuosity value indicating greater straight line movement. Recall that the curved line distance is the total distance travelled by the cell and the straight-line distance is the distance the cell has travelled from its point of origin. For illustration, the means of both these metrics for the migration of the fibroblast cells on each surface were plotted in Figure 3-5B. The flat surface had a mean curved line distance of 76 μm and straight-line distance of 25 μm . Similarly, the mean curved line distance travelled by the cell population on the random surface was 62 μm with a straight-line distance of 23 μm . Contrastingly, the distances travelled by the fibroblast cells on the linear surface were much greater. The mean curved line distance and straight-line distance measured for this surface was 134 μm and 53 μm , respectively. Again, as with the tortuosity measurements, there is a smaller variance in individual cell distance travelled along the linear surface compared to the other surfaces, particularly for the curved distance metric.

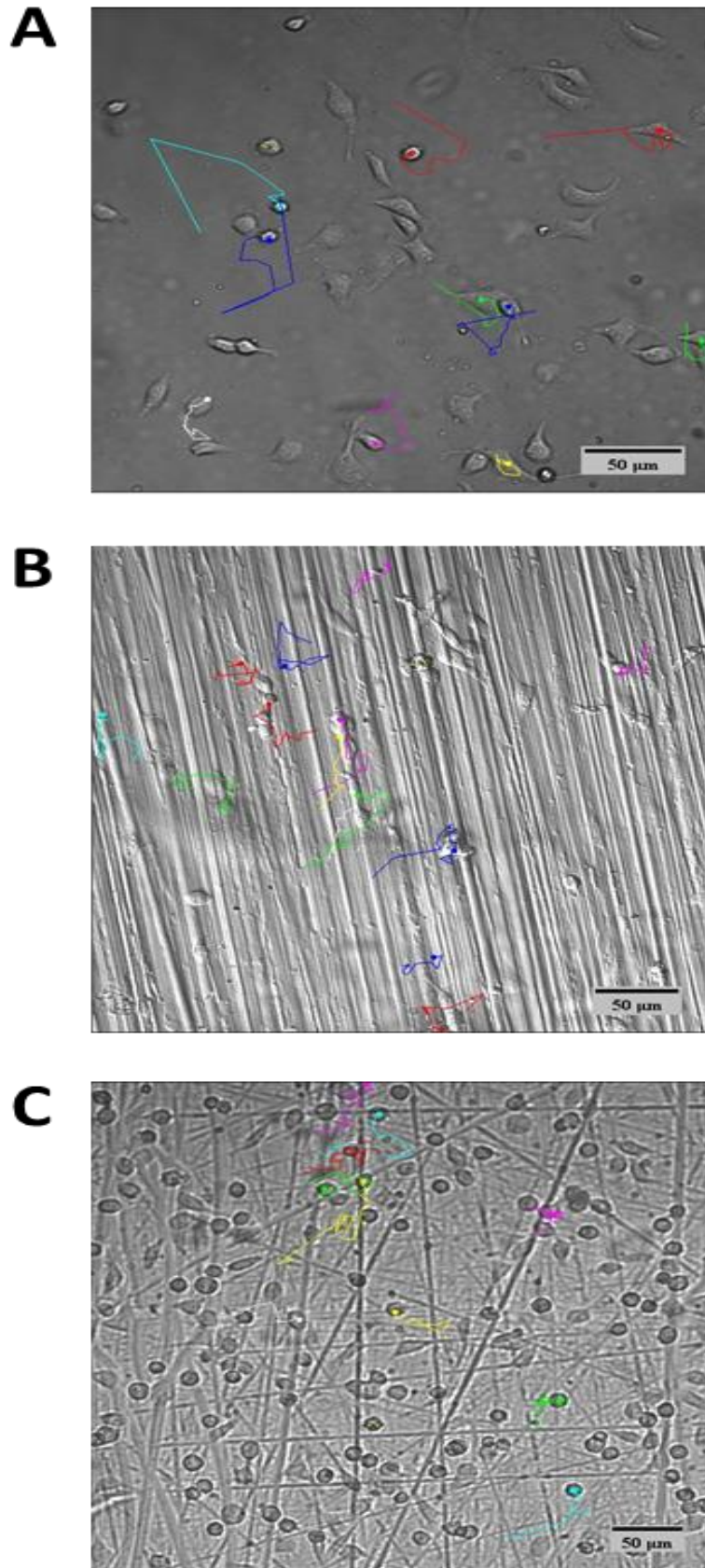


Figure 3-4. Tracking of cell migration on the polyurethane surfaces. Image showing the migratory paths of fibroblast cells on the flat surface (A), Linear surface (B) and Random surface (C). Scale in microns at bottom right corner.

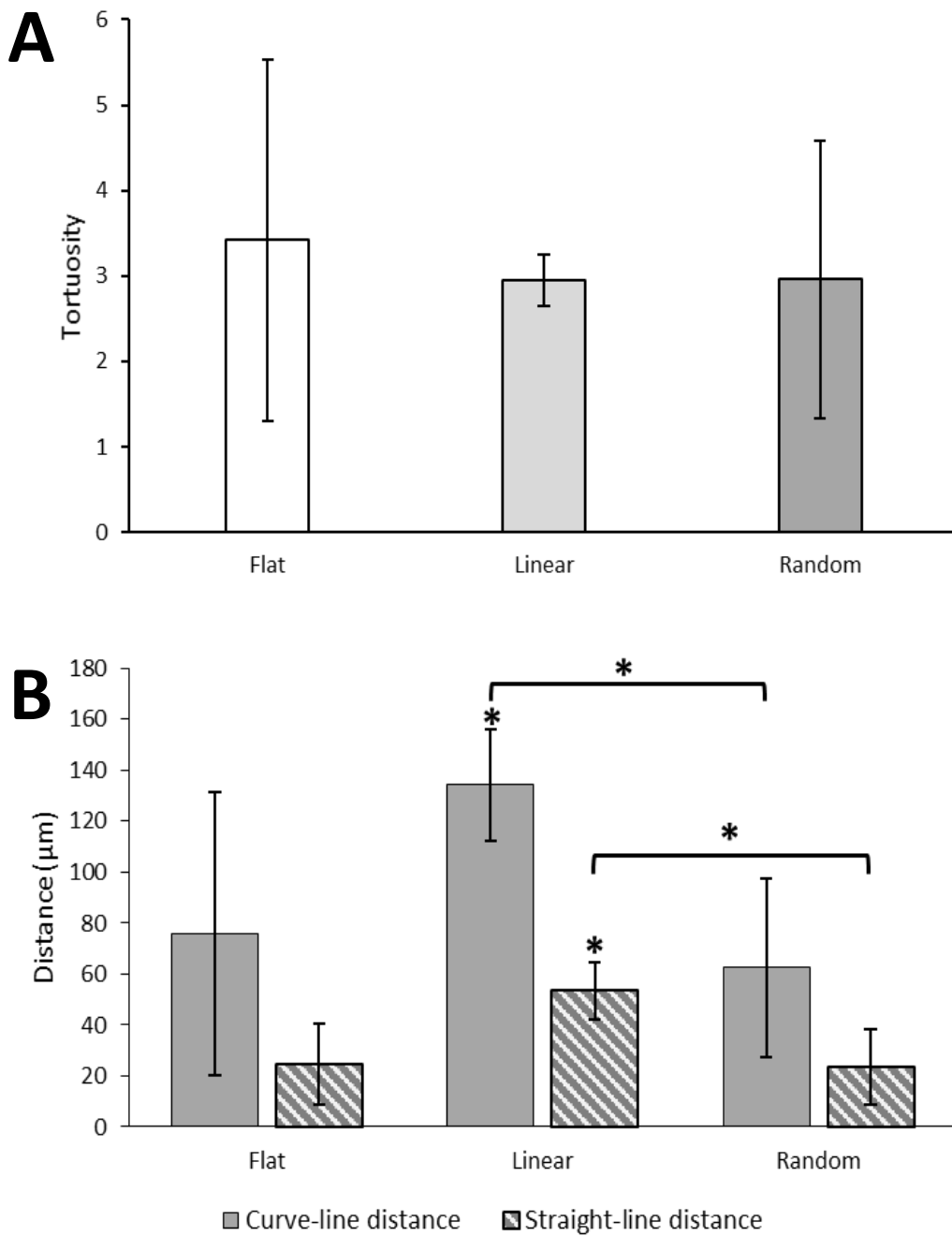


Figure 3-5. Experimental metrics from cell migration experiments. Column chart showing the tortuosity (A) and distances travelled (B) by the fibroblast cells on each polyurethane surface. (*) denotes $P < 0.01$.

A single factor ANOVA was conducted to compare the tortuosity, curved line and straight-line distance between the different surface types. There was no significant effect on tortuosity at the $p < 0.05$ level for the three surfaces ($p = 0.53$). However, there was a significant effect on the curved-line distance ($p = 4.4 \times 10^{-6}$) and the straight-line distance ($p = 5 \times 10^{-6}$) between the three surfaces. A Bonferroni correction test was utilised to counteract the problem of multiple comparisons and to reduce the chance of false positives. In other words, the confidence intervals are adjusted to compensate for the increase in number of hypotheses tested, using the following calculation $\frac{p}{n}$. In this example, $p = 0.05$ and $n = 3$, to represent each surface type. Therefore, the Bonferroni correction now tests each individual hypothesis at $p = 0.0167$. Post hoc comparisons using a Bonferroni corrected t-test indicated that the mean for the curved-line distance for the flat surface was significantly different ($p = 7.5 \times 10^{-4}$) than the linear surface. This was also true for comparison between the linear surface and the random surface ($p = 1.2 \times 10^{-5}$). However, the flat surface mean did not significantly differ from the random surface mean ($p = 0.34$). Similarly, this trend of significance was upheld for the straight-line distance means between the flat and linear ($p = 2.7 \times 10^{-4}$), flat and random ($p = 0.79$) and linear and random ($p = 1.4 \times 10^{-4}$) surfaces. Taken together, these results suggest that the linear surface has a statistically significant effect on the migration of the fibroblast cells, compared to migration on flat and random surfaces.

In Figure 3-6, the mean squared displacement (D^2), is plotted against time. The time course of the experiments varies between 130-160 minutes. This is due to the initial frames of some of the time-lapse videos having fibroblast cells still in the attachment phase of the experiment. For comparison of the D^2 measurements, between the different surfaces, we focus on the D^2 values at the end time of the experiments (i.e. at $t = 160$ min). These D^2 values

were: for the flat surface $1076 \mu\text{m}^2$; the linear surface $2367 \mu\text{m}^2$; and the random surface $1326 \mu\text{m}^2$. There is high variance in all 3 results leading to large error bars in the results, which is to be expected when taking the mean of multiple individual cell migration paths ($n > 10$) from differing starting points on non-uniform surfaces i.e. different feature depths. Once more, it is clear that there is greater directionality of cell migration on the linear surface with approximately twice as much displacement compared with the flat and random surfaces. This is more clearly seen in Figure 3-6D. For the early time frames, the linear and random trajectories are almost identical, suggesting that the movement has a directional bias as the cells they attach to the pattern features. However, as time increases, the random trajectory more resembles the flat trajectory, which is more typical of random motility.

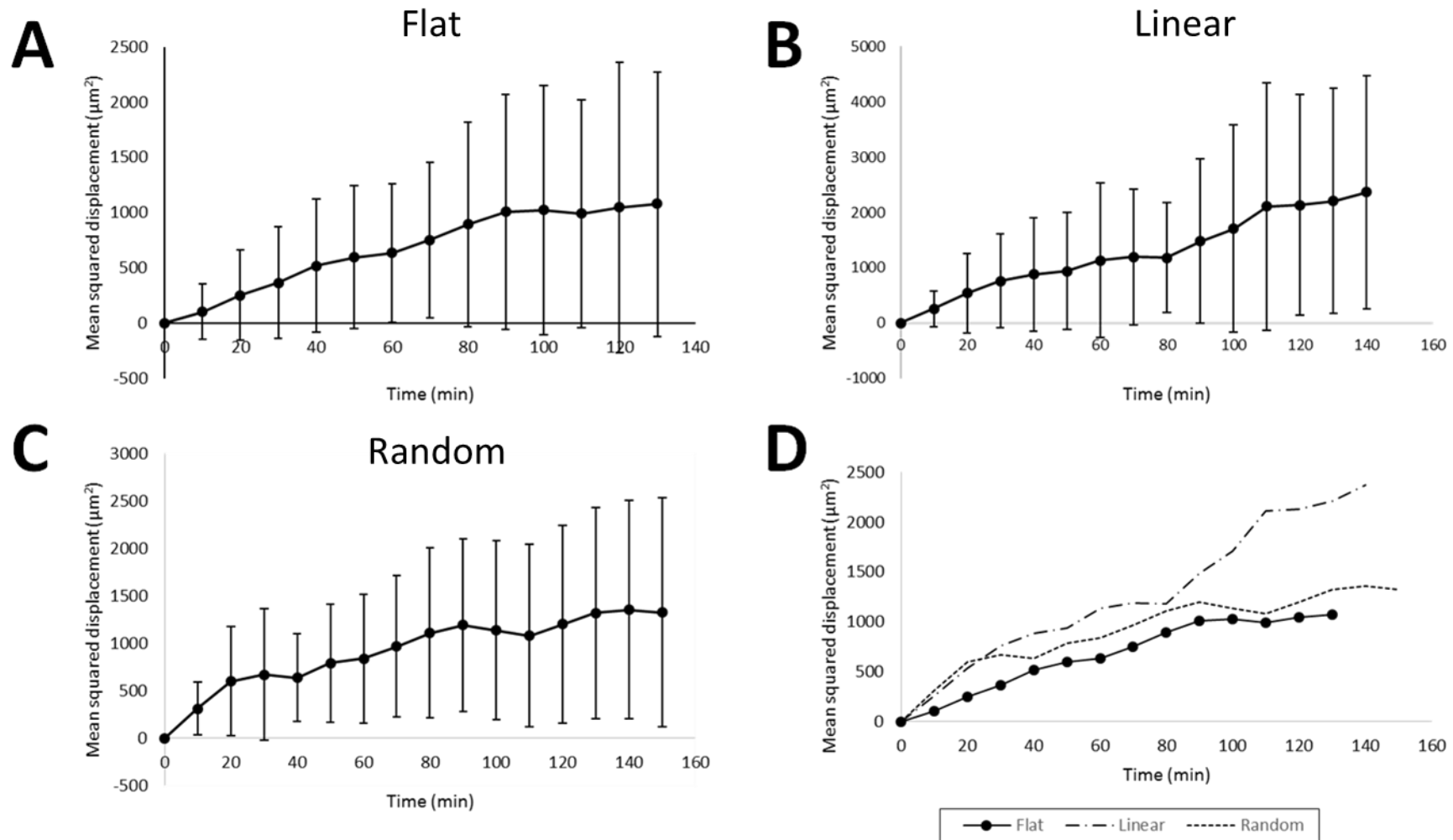


Figure 3-6. Experimental mean squared displacement results. Graphs showing experimental mean squared displacement (D^2) as a function of the time increment for all the migrating cells on the flat (A), linear (B) and random (C) patterned surfaces. (D) All D^2 measurements are plotted on the same graph with legend indicating which trace belongs to which surface.

3.3.3 Applicability of the model for migration on Flat surfaces

The first level of validation of the model is to show that related average metrics produced by the *in-silico* model are the same as those produced by the real cells in the experiments. For the model, the related average metrics are the mean squared displacement of the cells, tortuosity, and curved and straight-line distances. Initially, only the flat surface is modelled using Equation 3-2, without the haptotactic part (Ψ), and Equation 3-3 to yield an actual cell path for the migrating *in-silico* cells.

To initialise the model, the positional coordinates of the cells origin were set to (0, 0) and the initial cell velocity in the x and y directions was randomised to have any value ranging from -10 μ m/min to 10 μ m/min. The time of the *in-silico* experiment, t , was set to match the experimental time ($t = 160$ min) with the time increments, dt , being as small as possible to ensure numerical accuracy ($dt = 0.5$). The two random motility parameters, α and β , were initially set as 73.6 and 0.22, respectively, to mimic the mean values obtained in a comparable O-U model designed by Stokes et al. [291]. Once initialised, the cells velocity and position were updated using Equations 3-2 and 3-3 for the duration of the time course. A flow diagram depicting this process is available in Figure 3-7. These equations were solved using the Euler-Maruyama and Euler method, respectively [296]. The Euler-Maruyama method is used to approximate numerical solutions for stochastic differential equations (SDE), adapted from the use on ODEs for the Euler method. Using the Euler-Maruyama method, the next x-position can be updated if the current x-position is known. This allows for the velocity to be solved and for the positions to be updated with that velocity, using the Euler method. Example velocities and positions of the individual cells are plotted (Figure 3-8) as well as the simulated trajectories of these cells (Figure 3-9). Finally, relevant metrics (tortuosity, curved and straight-line distance) are produced and the mean squared displacement for these *in-silico*

simulations plotted. In Figure 3-8, the velocity changes in both axes are plotted. The influence of the α parameter is evident by the fluctuations observed in the traces. If this parameter were to be set to zero, the deterministic parameter, β , would produce traces showing the velocity reverting to zero over time. The cells were simulated separately in the model. Therefore, cell-cell interactions are not taken into account.

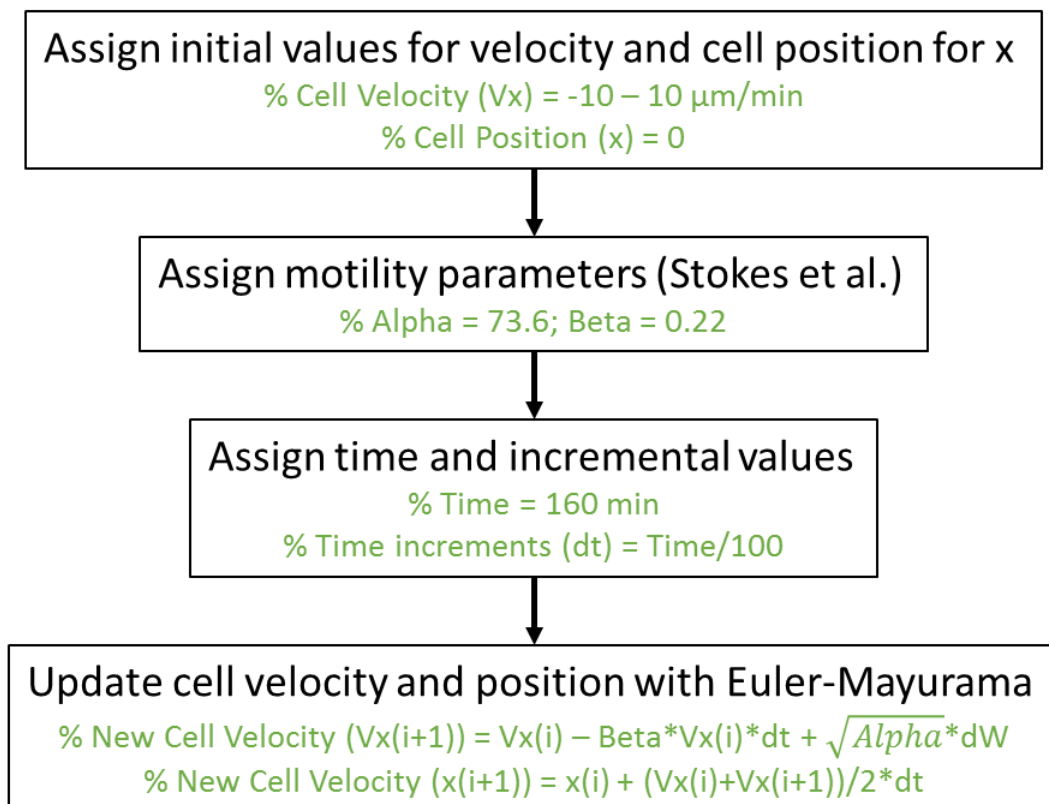


Figure 3-7: Initialisation of Euler-Maruyama equations. Initial parameters were set as stated in the flow diagram (green code). The cell velocity and position is updated every iteration based on the Euler-Maruyama equations and the velocity and position of the previous iteration. The dW parameter represents the Weiner process and is a random number in each iteration.

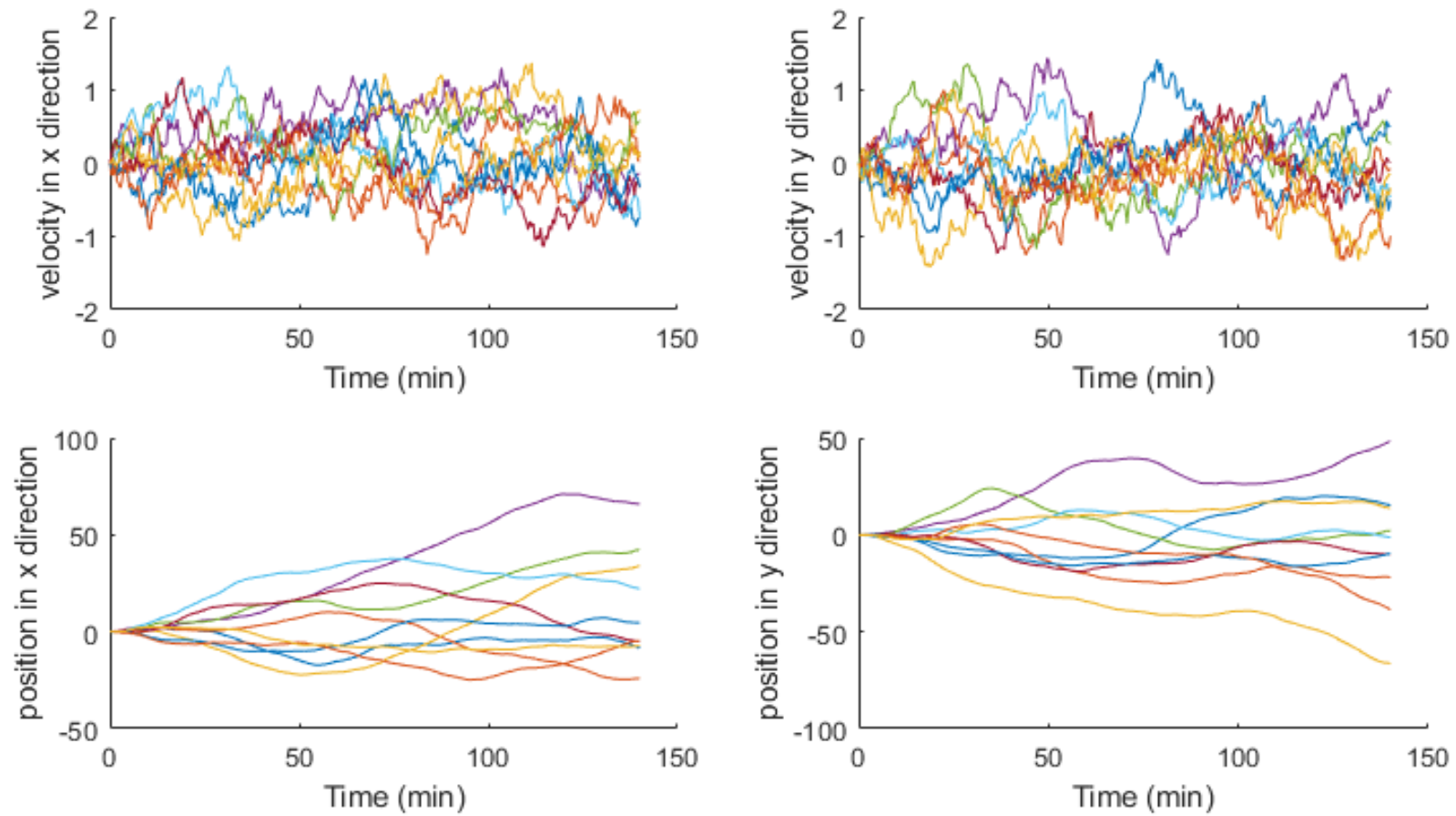


Figure 3-8. Cell velocities ($\mu\text{m}/\text{min}$) and positions (μm) in x and y position over time. Graphs showing the simulated positions and velocities on both axes for 10 migratory model cells for the flat surface simulation. Parameters for this simulation were as follows: $\alpha=73.6$, $\beta=0.22$.

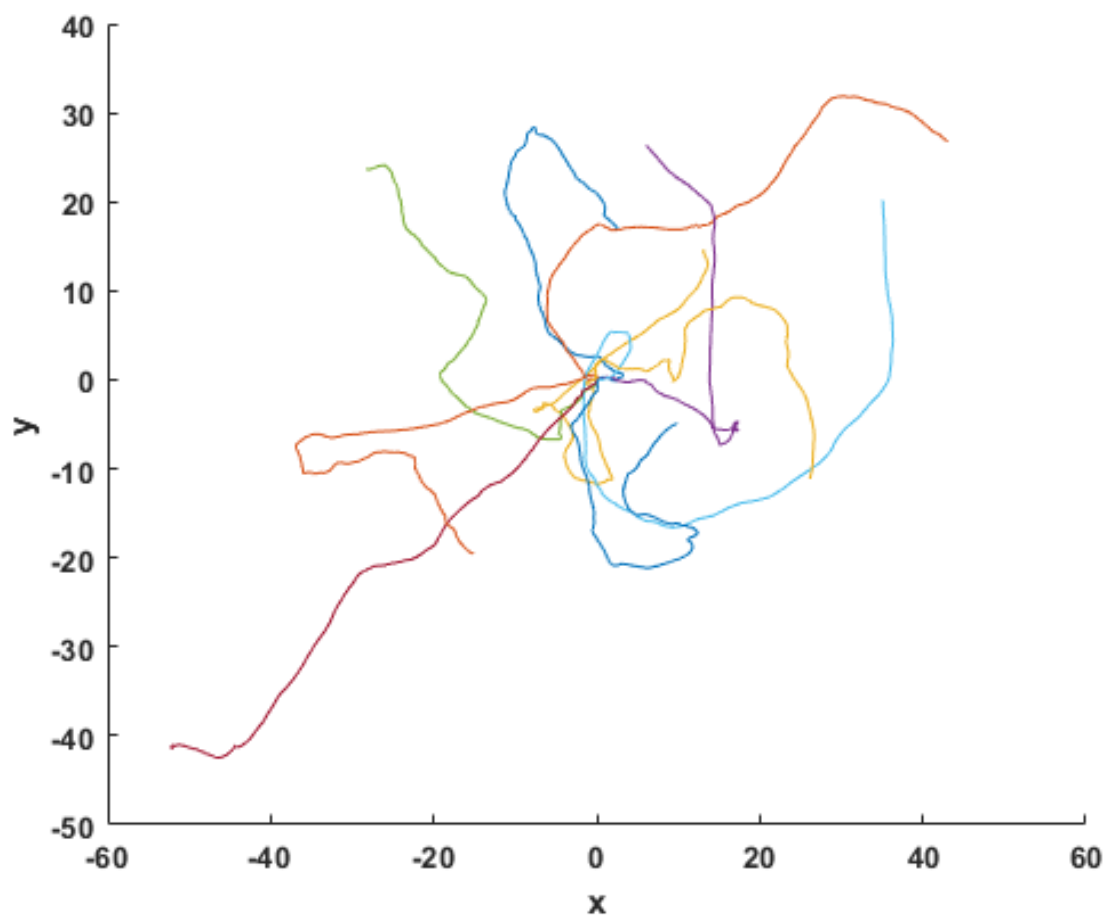


Figure 3-9. Simulation of cell migration paths. This graph shows the 10 simulated cell paths for the flat surface described in Figure 3-8. The initial x and y position (μm) of each cell was (0, 0). The parameters were as those indicated in Figure 3-8.

3.3.4 Determination of random motility parameters

Now that there is a working model of cell migration that visually aligns well with the experimental system, the parameters, α and β , can be optimised to find values that best describe the behaviour of the experimental system. The experimentally derived metrics from this system can be used for parameter (α and β) estimation and production of a value of best fit for the experimental data. To begin, we run the *in-silico* model, varying α and β between the values $\alpha = 0.1-1$ and $\beta = 0-1$. The mean tortuosity, curved line distance, straight-line distance and D^2 (end time) values are then calculated for each individual combination of these α and β values (see Figure 3-10). To aid comparison to the experiments, a contour plot was added to each graph (white curves). These contour plots represent the corresponding experimentally derived metrics from the fibroblast migration experiments on the flat surface. In other words, any α and β combination falling on these contours can be assumed to be an appropriate combination to describe the experiments.

A more quantitative test for goodness of fit between the model and experiments is the sum of squared errors (SSE). The SSE is a measure of the discrepancy between the experimental data and estimation model. In other words, it is used in a test for goodness of fit of an observed set of data to a theoretical one. The SSE calculations for tortuosity, curved line distance, straight-line distance and mean squared displacement were calculated using Equation 3-6, namely;

$$SSE = \sum_{i=1}^n \frac{(S_i - E_i)^2}{E_i}, \quad (3-6)$$

where S_i is the simulated measurement of the metric (e.g. tortuosity, etc.) and E_i is the experimentally derived measurement of the same metric. A small SSE value indicates a tight

fit of the model to the data. Here, it is used as an optimality criterion in parameter selection. In the model, SSE values were calculated for each of the four flat surface metrics (tortuosity, curved line distance, straight line distance and mean squared displacement) and used to generate plots to help determine the optimal value of α and β (Figure 3-11).

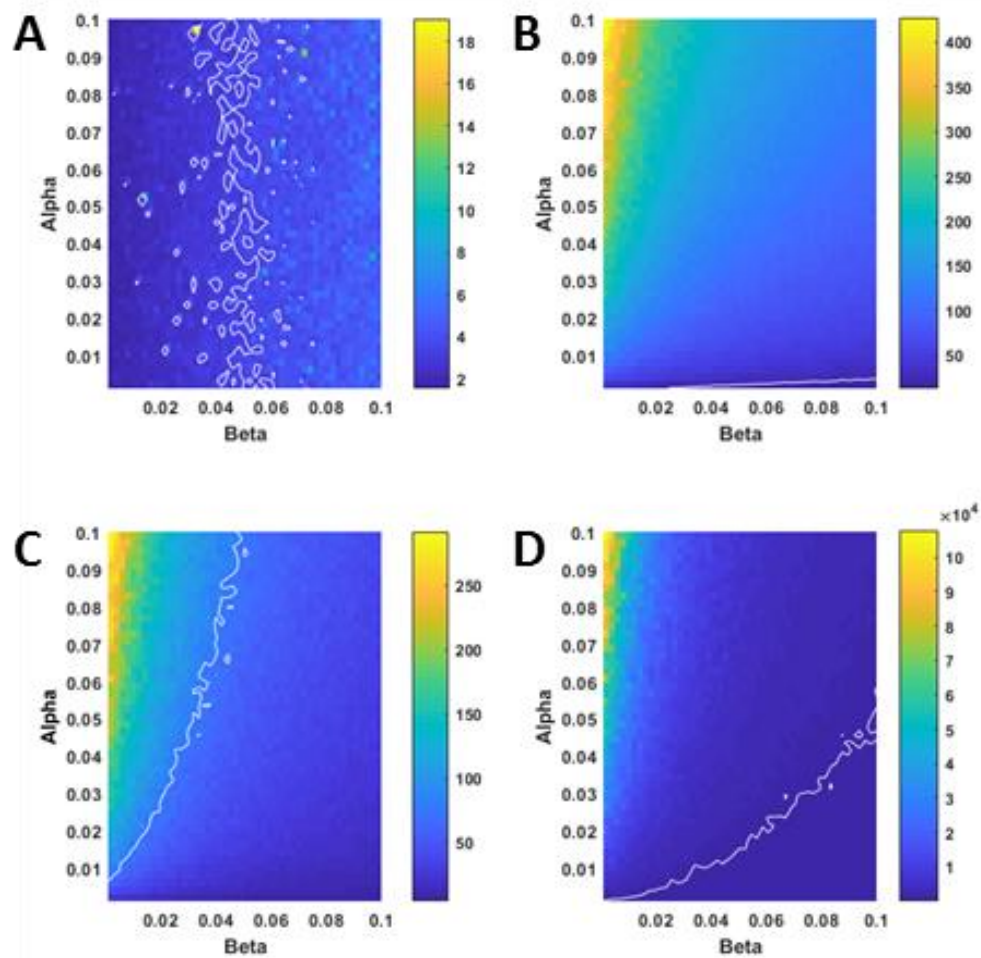


Figure 3-10. *In-silico* generated metrics. Plots show a range of α and β values (0 – 0.1) with tortuosity (A), curved line distance (B), straight line distance (C) and the end time mean squared displacement values (D), plotted on a colour scale with values indicated on the relevant colour bar. The white contours indicate the experimentally derived values for the metrics.

The SSE values for each of the metrics are plotted against the same range of α and β values (Figure 3-11). To find a combination of α and β values that will give a good fit (i.e. the minimum) of all four metrics simultaneously, their respective SSE values were totalled and plotted against α and β (Figure 3-3A). Figure 3-3B show the minimum SSE values from the respective plots in Figure 3-11 for the four metrics, i.e. contour plot of the minimum SSE for the α - β pairs. This plot shows that lower values of α and β appear to give the best fits for the experimental data. Therefore, the total SSE values were alternatively plotted as a colour projection against the range of α and β values (Figure 3-3C). The darker colours indicate a lower SSE value. Subsequently, it was found that a quadratic curve (Equation 3-7) maps well onto the minimum SSE values as indicated in (Figure 3-12C), suggesting (α,β) pairs given by this relationship predicted cell migration paths comparable to the experiments. The best fit polynomial given in Figure 3-11D is as follows:

$$\alpha = 4.975\beta^2 + 0.002781. \quad (3-7)$$

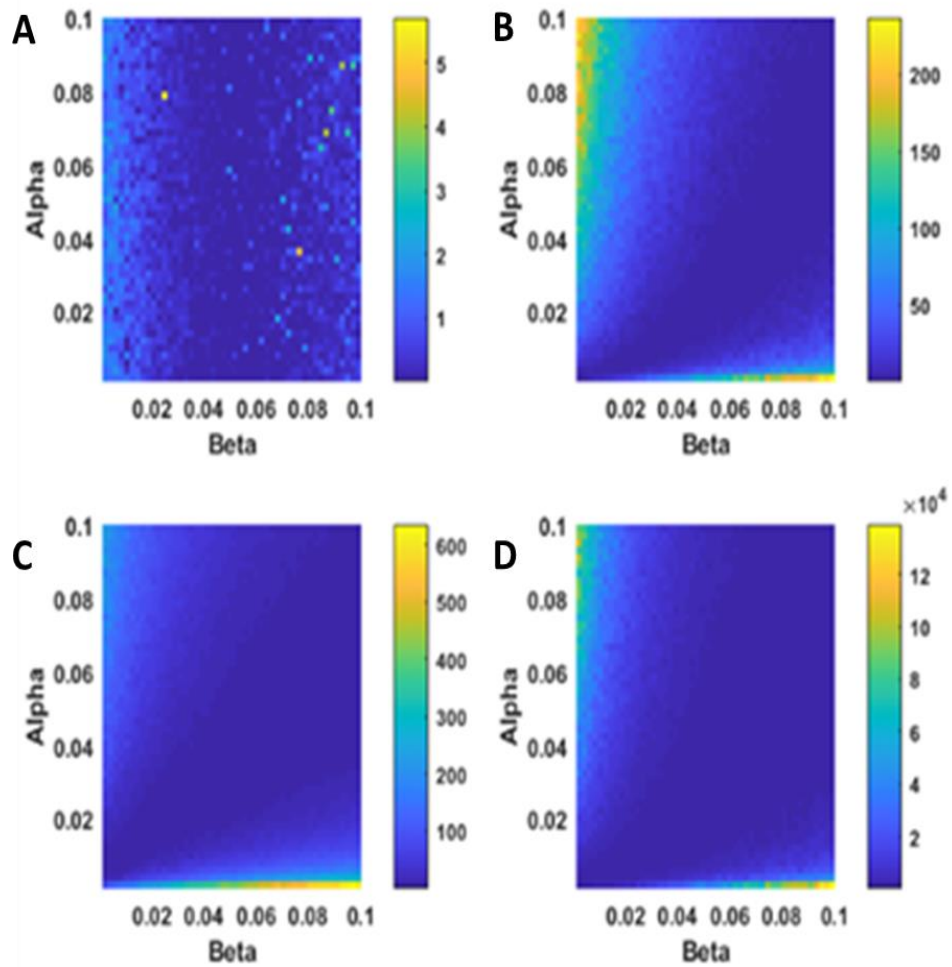


Figure 3-11. Sum of squared Errors (SSE) plots for metrics. Individual SSE- values are given in the colour bar for α versus β plots for the (A) tortuosity, (B) curved line distance, (C) straight line distance and (D) end time mean squared displacement.

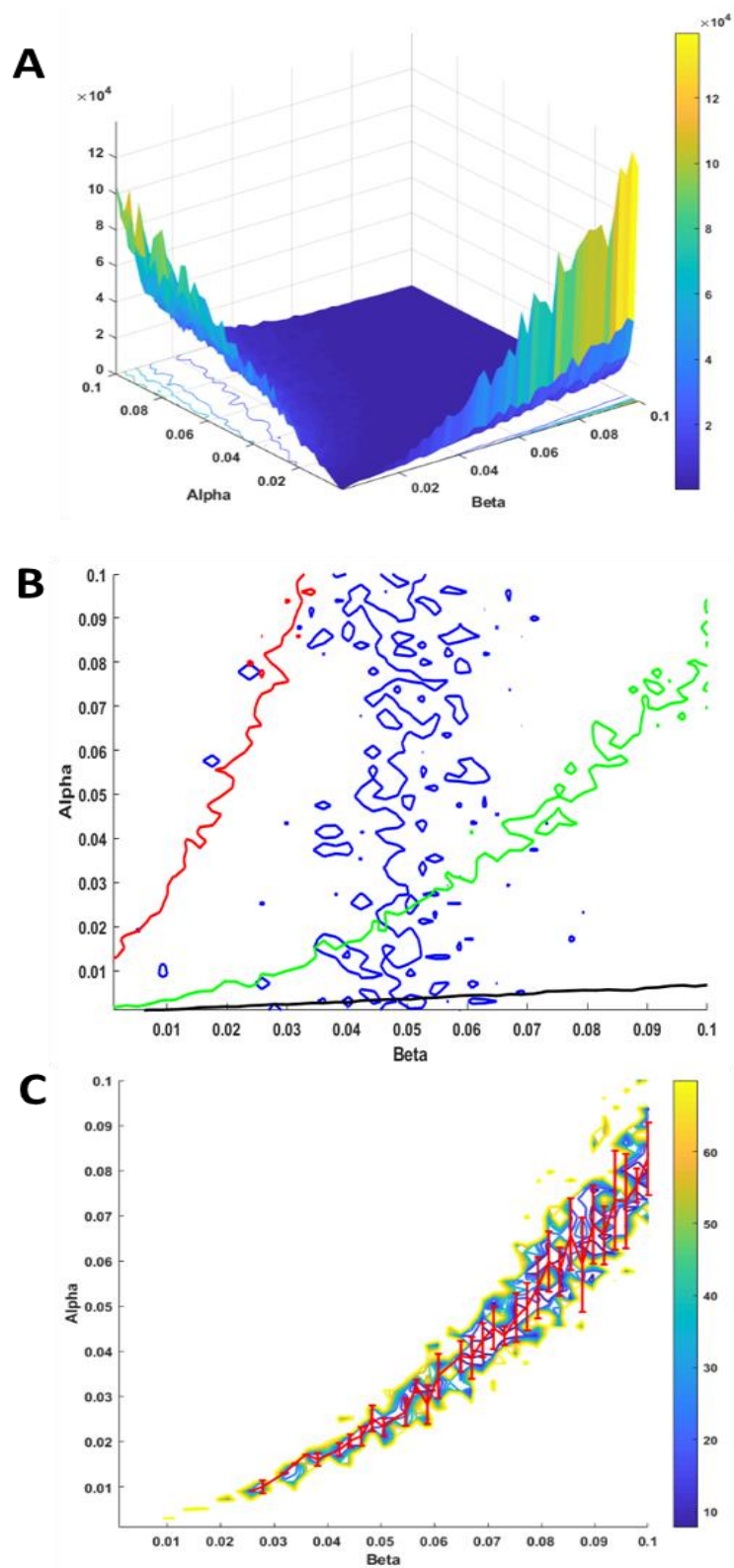


Figure 3-3. Sum of Squared Errors (SSE) plots. (A) Total SSE- values (i.e. $SSE_{total} = SSE_{tortuosity} + SSE_{curved\ line} + SSE_{straight\ line} + SSE_{mean\ squared\ displacement}$) are plotted on z-axis for α versus β plot. (B) Plots showing minimum values of the tortuosity (blue), curve-line (red), straight line (black) and D^2 (green) SSE values on alpha versus beta plot. (C) Polynomial curve fitting plot for the minimum of the total SSE- values.

3.3.5 Determination of haptotactic responsiveness

The experimental metrics for the patterned surfaces can be used along with the full version of Equation 3-2 (i.e., with $\underline{\Psi} = 0$) to optimise and determine the haptotactic responsiveness parameter, κ . The α and β values are fixed at 0.01 and 0.04, according to Equation 3-7. These low values of α and β are chosen to prevent the simulated cells from 'exiting the boundary' of the topographical space i.e., the data uploaded from the microscopic images in Figure 3-2. 100 cells were simulated with a range of 1000 κ -values from 0.1 to 0.8 and the resulting mean values for tortuosity, curved distance, straight-line distance and the mean end-time squared displacement ($D^2_{t=160}$) were plotted against the range of κ -values for the linear (Figure 3-4 – 3-15) and random (Figure 3-7 – 3-18) surfaces. Figure 3-4 and 3-16 show the simulated predicted values with mean (black curves) and standard deviation (grey error bars) indicated. These simulated metric values, for the wide range of κ -values inputted into the model, can be optimised using the experimentally derived metrics. Thus, the most appropriate κ -value that best describes the *in-vitro* experiments can be determined. For the linear surface case, the experimental numbers were superimposed onto the plots (Figure 3-5 – red line) for tortuosity (2.95 μm), curved distance (134.26 μm), straight-line distance (53.60 μm) and the end time mean squared displacement (2367 μm^2). Additionally, the SSE values were also calculated for these metrics, using Equation 3-6 and Figure 3-14, and the total SSE plotted against κ (Figure 3-6). Through comparison of these plots (in particular, see Figure 3-6), it can be observed that a κ -value in the range 0.5-0.6 would be optimal to describe the linear experiments (i.e., minimise $\text{SSE}_{\text{total}}$). Similarly, on Figure 3-8, the experimental values for the random surface were superimposed on the plots for tortuosity (2.94 μm), curved distance (62.62 μm), straight-line distance (23.62 μm) and the end time mean squared displacement (1326 μm^2). Again, the most appropriate κ -value can be derived from comparing the total SSE

values against κ . In this case, it yields a much lower optimal κ -value (i.e., min SSE_{total}) in the range of $\kappa = 0.01 - 0.07$.

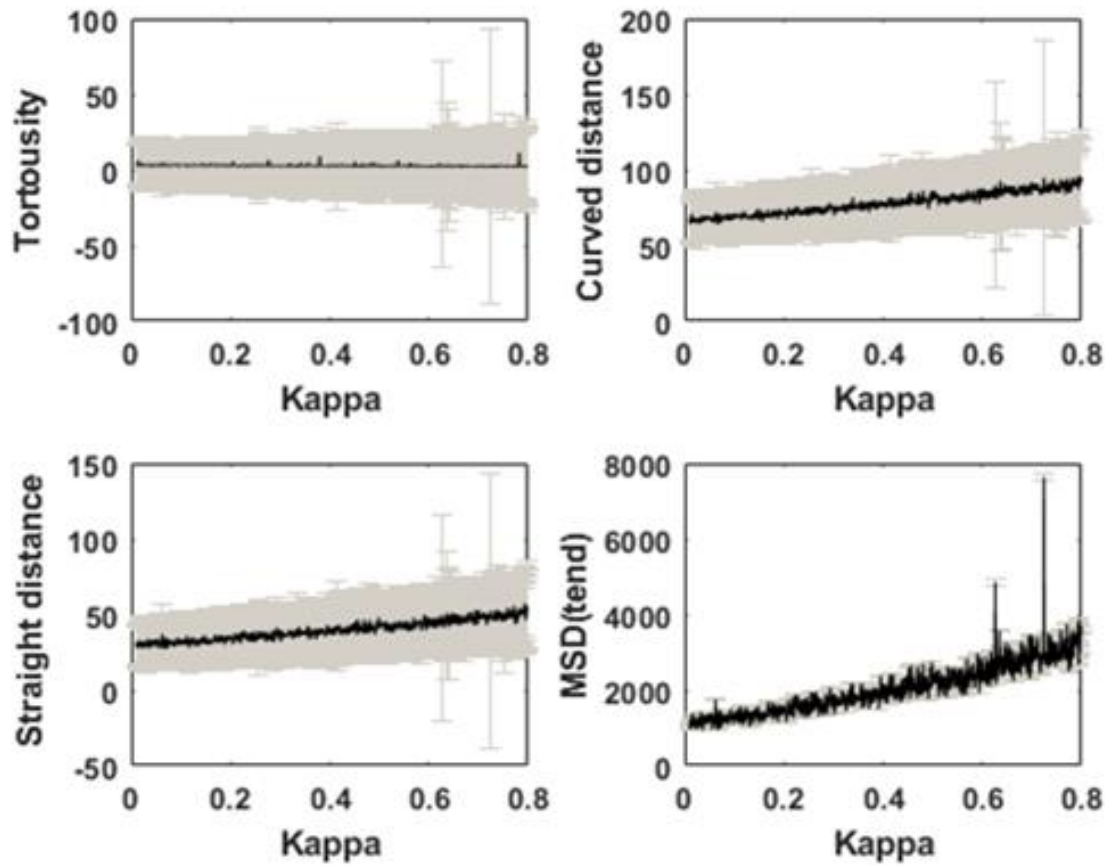


Figure 3-4. Determining the haptotactic gradient for the linear surface. Graphs showing simulated mean metric values (black curves) with standard deviation (grey) for range of κ -values (0 – 0.8).

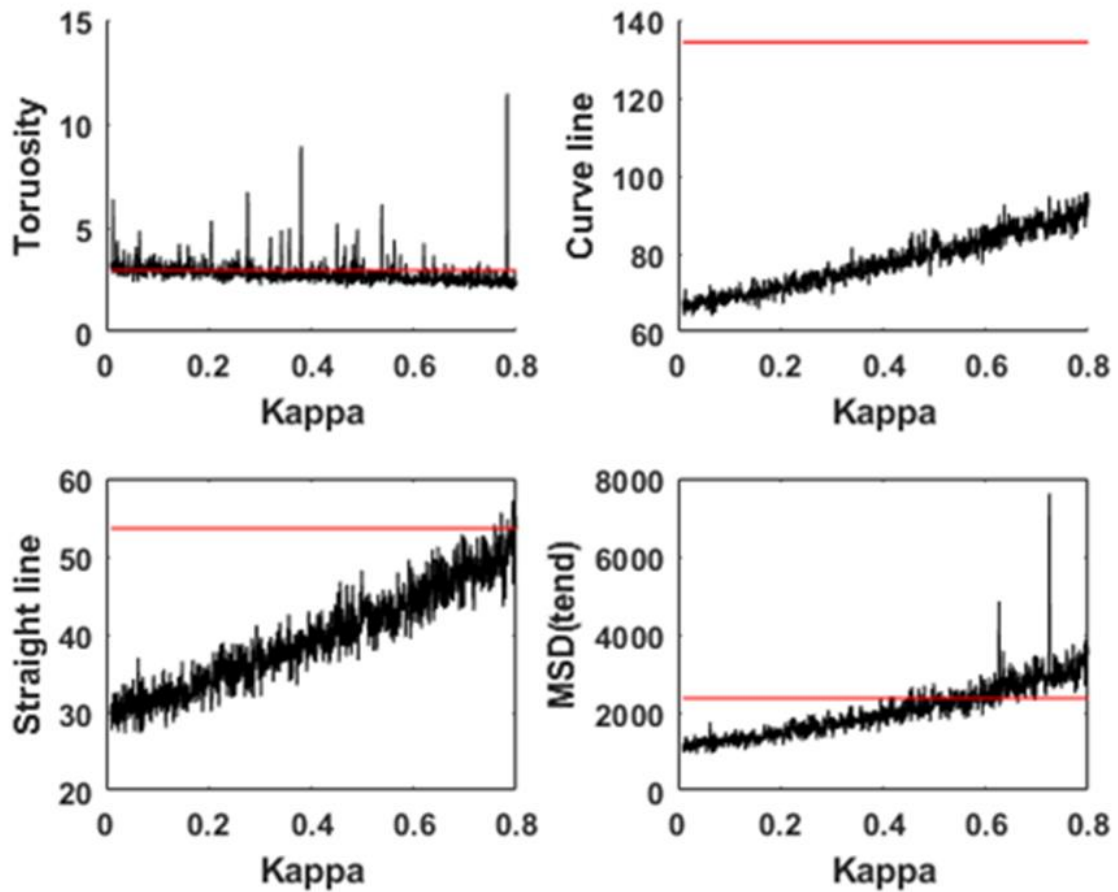


Figure 3-5. Optimisation of κ for the linear surface for individual metrics. Experimentally derived values (red) superimposed over simulated mean values against κ (see Figure 3-13). Optimal values of κ selected from points of crossover for each metric.

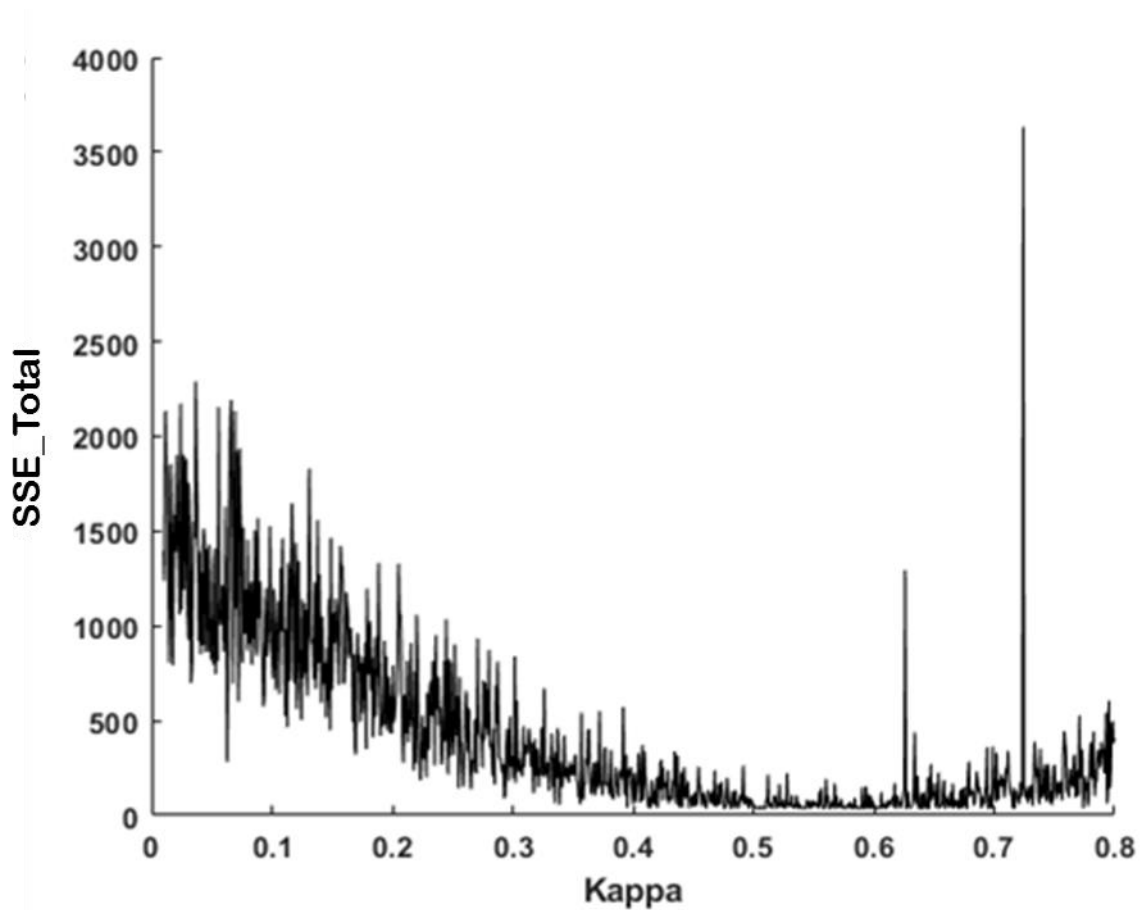


Figure 3-6. Optimisation of the haptotactic term for the linear surface. Total SSE-values (i.e. $SSE_{total} = SSE_{tortuosity} + SSE_{curved\ line} + SSE_{straight\ line} + SSE_{mean\ squared\ displacement}$) of the four metrics plotted against κ . Lower SSE-value indicates a stronger fit between the experimental data and the model.

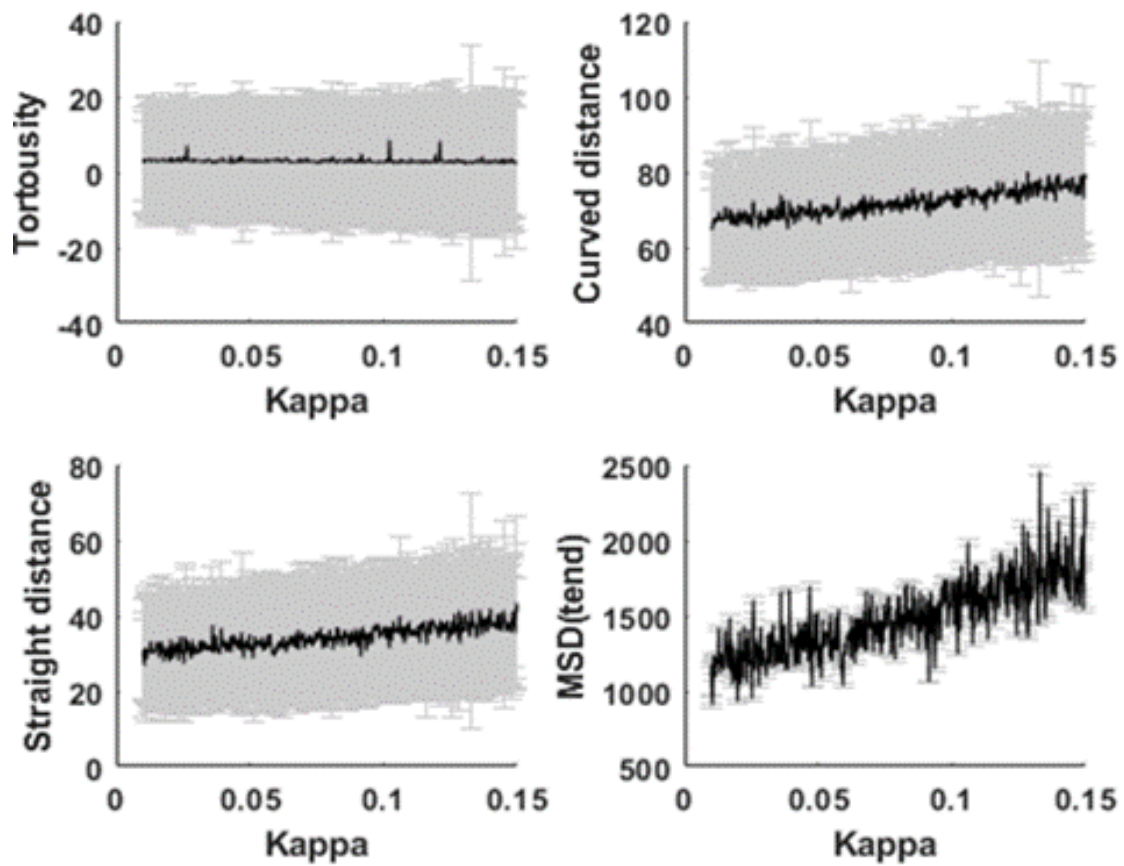


Figure 3-7. Determining the chemotactic gradient for the random surface. Graphs showing simulated mean metric values (black curves) with standard deviation (grey) for range of κ -values (0 – 0.15).

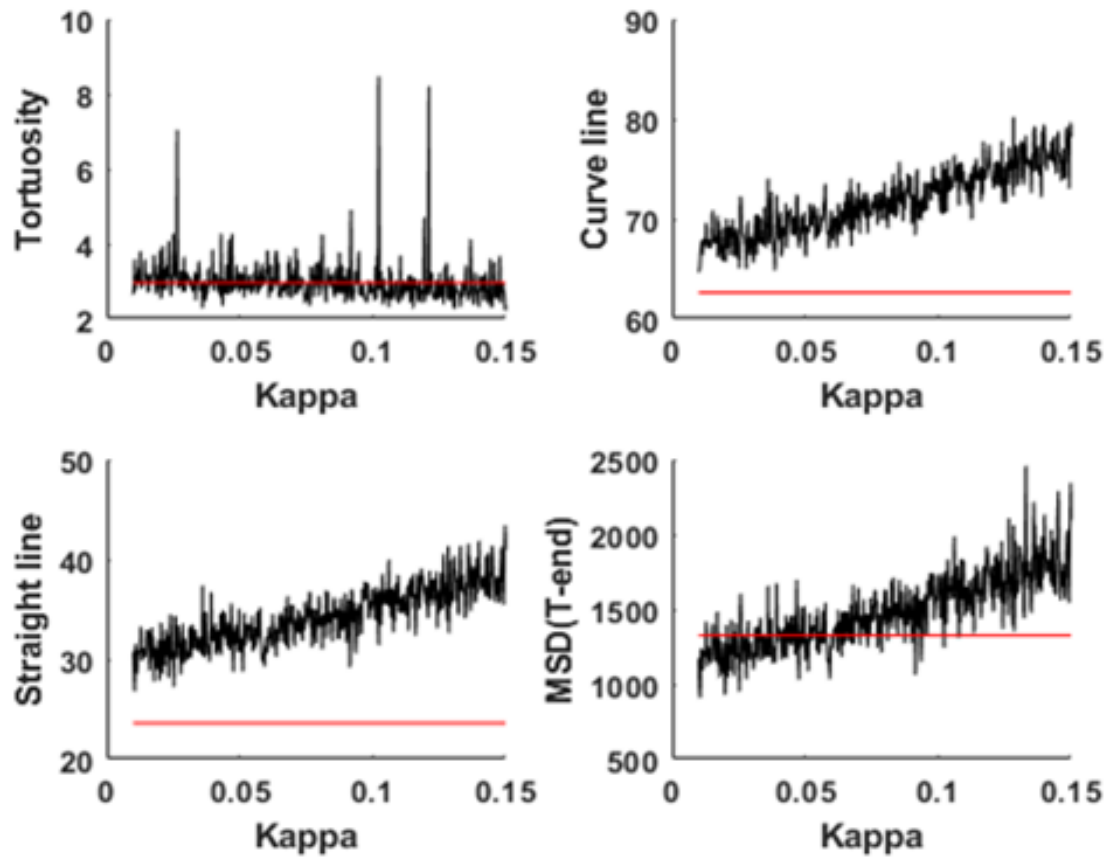


Figure 3-8. Optimisation of κ for the random surface for individual metrics. Experimentally derived values (red) superimposed over simulated mean values against κ (see Figure 3-16). Optimal values of κ selected from points of crossover for each metric.

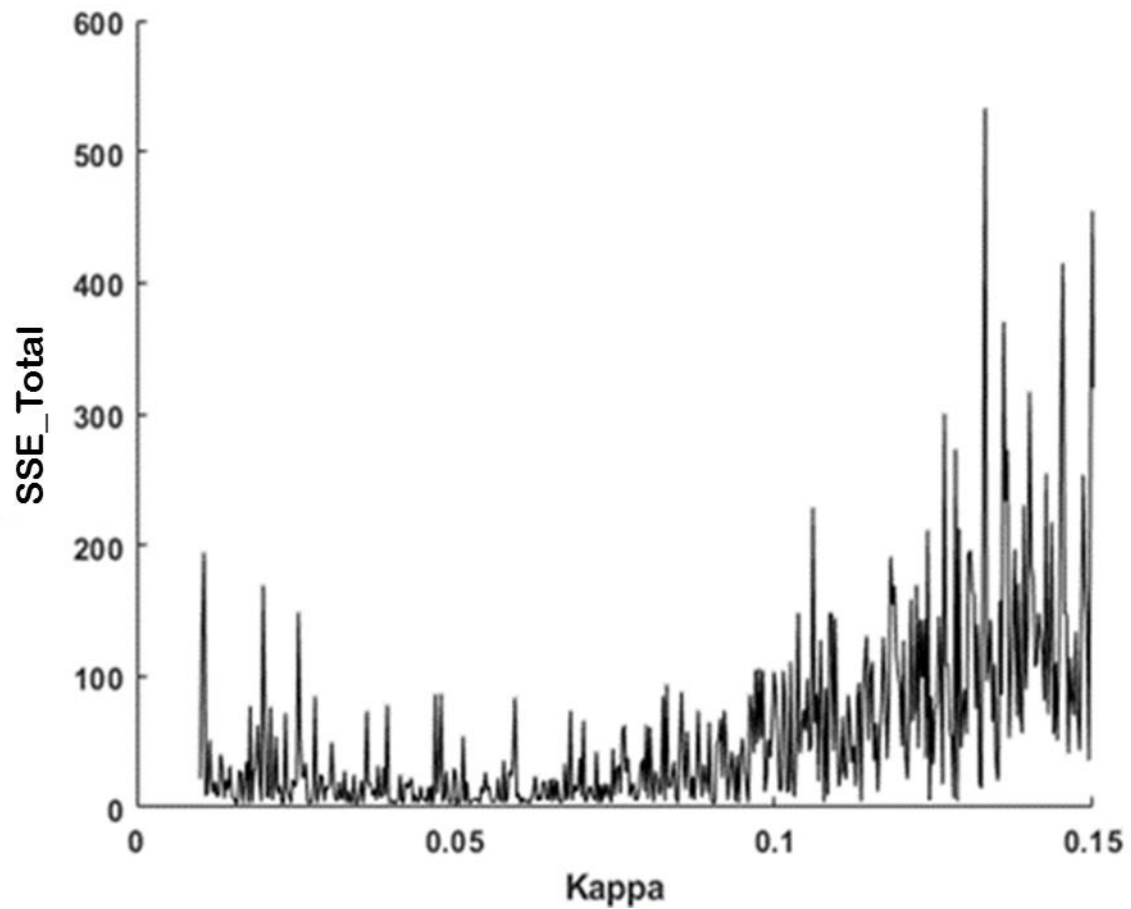


Figure 3-9. Optimisation of the haptotactic term for the random surface. Total SSE-values (i.e. $SSE_{total} = SSE_{tortuosity} + SSE_{curved\ line} + SSE_{straight\ line} + SSE_{mean\ squared\ displacement}$) of the four metrics plotted against κ . Lower SSE-values indicate a stronger fit between the experimental data and the model.

The *in-silico* model is now simulated using the fixed $\alpha = 0.01$ and $\beta = 0.04$ (satisfying Equation 3-7) and κ values representing the linear ($\kappa = 0.5$) and random ($\kappa = 0.02$) patterned surface experiments. The resulting 10 model cell migration paths derived from these simulations are shown in Figure 3-10 and the corresponding mean squared displacement values were also plotted (Figure 3-20). Table 3-1 shows comparisons of the migration metrics (for tortuosity, curved line distance, straight line distance and mean squared displacement) for all three surfaces. The model parameters were those identified as being optimal in the above analysis for these surfaces. Significance levels are derived using a paired Z-test to calculate the difference between the observed means in the experimentally derived and simulated samples. There is an excellent comparison between the data in the flat surface with no significant difference shown for tortuosity ($p=0.79$), curved line distance ($p=0.63$), straight line distance ($p=0.23$) and mean squared displacement ($p=0.58$). Similarly, there is no significant difference between the experimentally derived and simulated means in the random surface for these metrics, respectively ($p = 0.4$, $p=0.59$, $p=0.12$ and $p=0.98$). However, there is an inconsistency in the curved line distance for the linear surface ($p<0.0001$). This outlier can be also be observed in Figure 3-14. This is likely an artefact of lowering the α - β values to prevent simulated cells from migrating off the simulated polyurethane surface. Subsequently, this significance is present between the tortuosity values ($p<0.0001$) for the linear surface. There is no significant difference between the means for the straight-line distance ($p=0.12$) and mean squared displacement ($p=0.77$) for the linear surface. Otherwise, the models show a good recreation of the key migratory features as observed in the experiments.

	Tortuosity		Curved-line distance (μm)		Straight-line distance (μm)		Mean squared end-time displacement (μm^2)	
	Exp	Sim	Exp	Sim	Exp	Sim	Exp	Sim
Flat	3.4 ± 2.12	3.2 ± 1.55 P=0.79	75.89 ± 55.6	84.56 ± 14.2 P=0.63	24.81 ± 15.9	32.22 ± 16.7 P=0.23	1075 ± 1196.4	1291 ± 406.4 P=0.58
Linear	2.95 ± 0.31	2.01 ± 0.8 P<0.0001	134.3 ± 21.8	86.09 ± 19.2 P<0.0001	53.6 ± 11.2	47.87 ± 17.5 P=0.12	2367 ± 2111	2566 ± 801.4 P=0.77
Random	2.96 ± 1.62	2.5 ± 0.73 P=0.4	62.62 ± 35.1	68.9 ± 14.9 P=0.59	23.62 ± 14.9	33.17 ± 17.3 P=0.12	1326 ± 1211.7	1318 ± 414.2 P=0.98

Table 3-1. Experimental and simulated values for the metric values. Table showing the mean and standard deviations for the *in-vitro* (Exp) and *in-silico* (Sim) results for tortuosity, curved-line distance, straight-line distance and the final mean squared end-time displacement on each of the three polyurethane surfaces (Flat, Linear and Random). P-values indicate significance between the *in-vitro* and *in-silico* results for each metric on each surface.

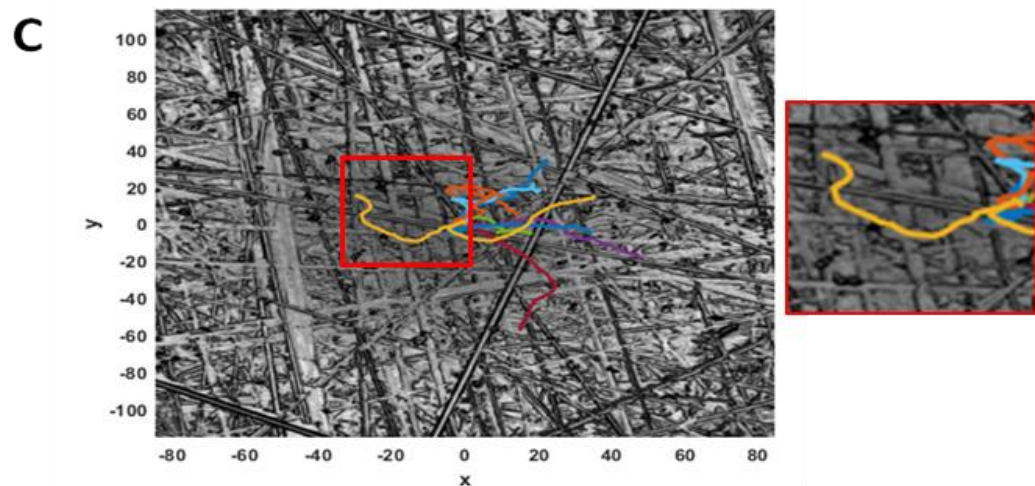
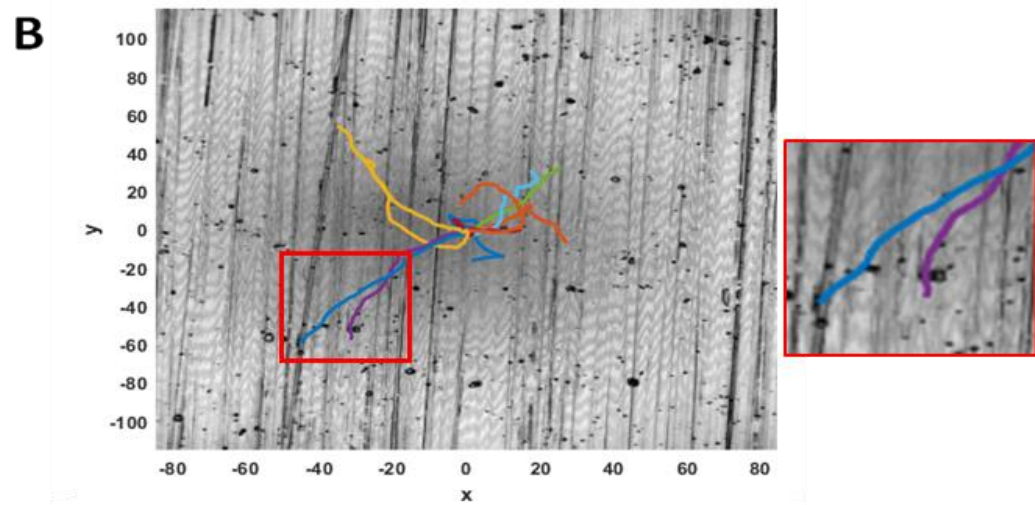
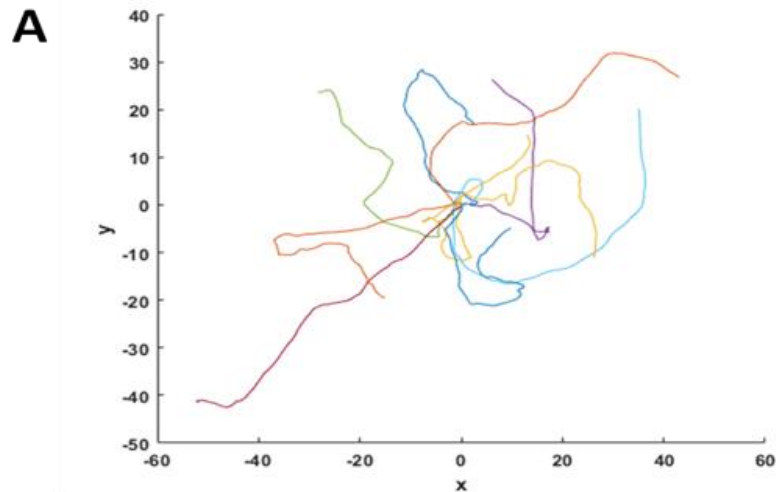


Figure 3-10. Simulation of cell migration paths. Example of 10 simulated cell paths for flat (A), linear (B) and random (C) surfaces. A magnified look at the cell paths across the features is included for the linear and random surfaces. All simulations had a starting point of (0, 0). The α and β values were fixed to 0.01 and 0.04 for all simulations. The κ values were fixed to 0.5 and 0.02 for B and C, respectively.

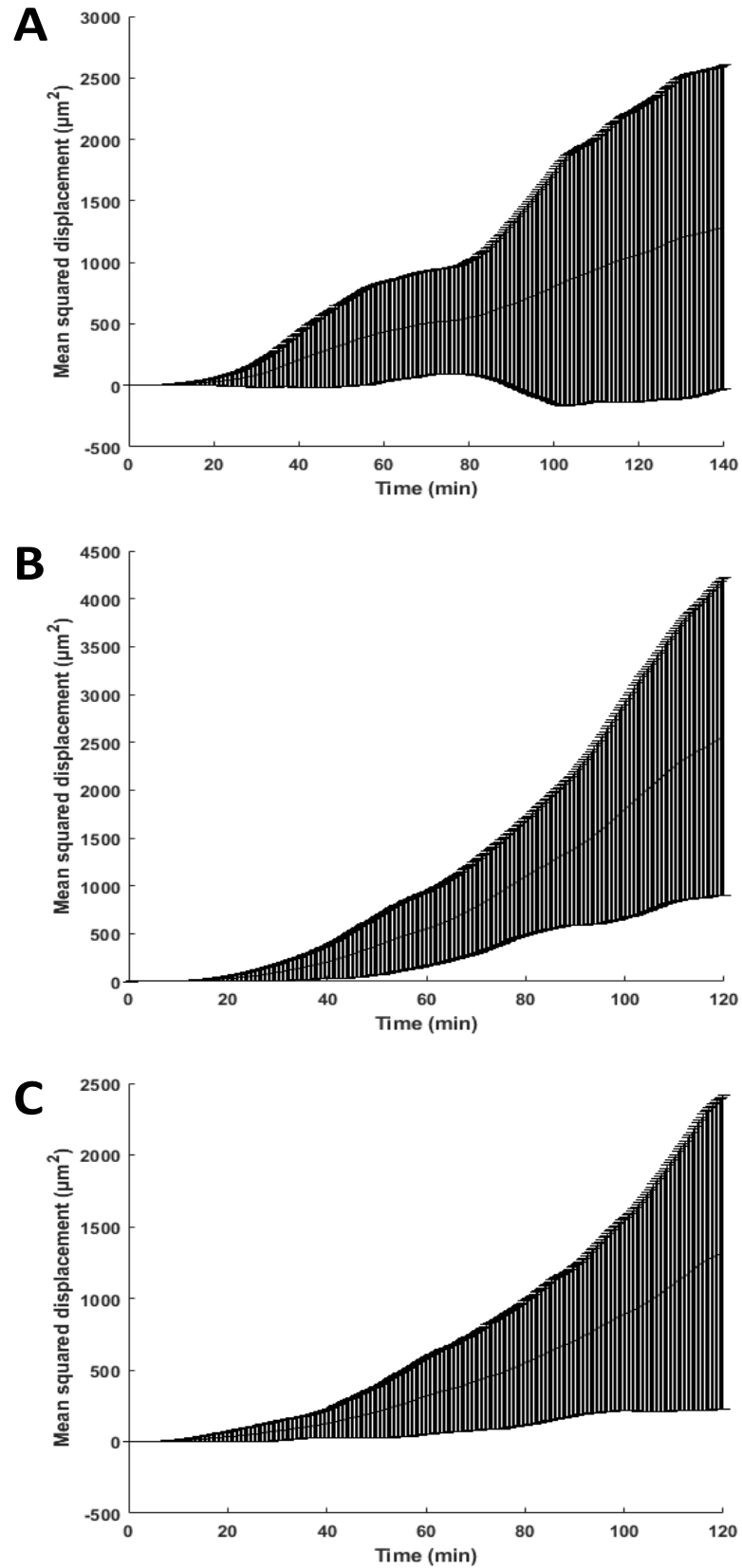


Figure 3-20. Simulated mean squared displacement results. Examples of simulated mean squared displacement (D^2) as a function of time increment for all the migrating cells on the Flat (A), Linear (B) and Random (C) patterned surfaces. Same parameters as Figure 3-19.

3.4 Chapter Discussion

This chapter describes the development of an *in-silico* model for analysing the migration of fibroblast cells on polyurethane surfaces with varying nanotopographical features, based on the stochastic O-U process introduced by Dunn and Brown (1987) [295]. In addition, we have extended this process to include a surface topology bias. In this model, random motility can be described as a mixture of random fluctuations and deterministic decay in cell velocity. These respective unknown quantitative parameters were optimised by comparing experimental results to the *in-silico* output. This permitted comparison of a large range of parameter values to be narrowed down to a specific subset of α - β pairs, which when inputted back into the simulation, results in an *in-silico* model that accurately describes the experimental cell migration patterns. A third term was added to the O-U process to account for the effects of the surface gradient on the cells velocity. This term is proportional to the deviation of the current direction of the cell from the surface gradient. Again, this term was determined through a combination of experimental results and multiple model simulations, producing a range of values for each surface. Further simulations, with the parameters fixed to the predicted optimal values, resulted in *in-silico* models showing a good match to the *in-vitro* experiments. Therefore, the extended quantitative framework appears to be an appropriate description of the motility observed in the cell migration assays.

Comparison of the metrics derived from the experiments (Figure 3-5) reveal that there was a significant difference between the flat and linear surfaces and the linear and random surfaces. There was no observable significant difference between the

flat and random surfaces for the curved-line distance ($p=0.34$) and straight-line distance ($p=0.79$) travelled by the fibroblast cells (Figure 3-5B) or for any of the tortuosity values generated (Figure 3-5A). An explanation for this lack of significance could be due to the orientation of the surface pattern features on the random polymer (Figure 3-2B). It is possible that the cells could be adhering and migrating along the pattern features while simultaneously exhibiting random motility, as observed on the flat surface, thanks in part to the criss-cross (random) nature of the pattern. However, the tortuosity for this experiment is almost identical to the tortuosity of the linear experiment (Figure 3-5A), suggesting that the motility in this experiment is more directed. Furthermore, observation of the mean squared displacement plot (Figure 3-6D) infers that, initially, the displacement of the cells on the random surface closely match that of the linear surface. However, as time increases, this trend changes and migration on the random surface more closely resembles the displacement of the fibroblast cells on the flat surface. Therefore, even though it is likely that the fibroblast cells on the random surface are influenced by the nano-features present on the polymer, it can't be shown to have any significant effect on the cell migration pattern.

As shown by the match of the O-U process to data for mean squared displacement (Table 3-1), the random motility parameters provide appropriate description of the fibroblast migration. This agreement strengthens the verification of the applicability of the model. While the actual mechanical and biochemical processes that α and β should represent are not presently defined, these parameters provide a direct means of relating observable quantities, such as cell speed, to basic motility mechanisms. These parameters are fixed for all subsequent simulations meaning the only

differences between the *in-silico* models for the different surfaces are the value of the haptotactic parameter κ and the surface gradients obtained from the microscopic data. By taking the SSE-values for the motility parameters, α and β , and fitting them to a polynomial curve (Figure 3-11D), a range of α - β pair values can be acquired. This suggests there is a quadratic relationship between the ratio of random fluctuations and velocity decay. Theoretically, any α - β value can be chosen as long as it satisfies this relationship. However, as alluded to in the results, smaller α - β values were chosen to prevent the simulated cells from leaving the simulated polymer surface. Experimentally, this isn't a problem as the fibroblasts that migrated 'out of frame' in the time-lapse microscopy results were discounted. Nonetheless, when this event occurs in the model simulations it results in massive skewing of the data. Lowering the α - β pair values reduced the distance possible for the simulate cells to migrate into which allowed for simulated cells to remain within the boundary of the *in-silico* polymer space. A combination of this solution with each simulated cell having a starting origin in the middle of the polymer space (0,0) contributes towards the poor fit of between the experimentally derived mean curved-line and straight-line distance values and the simulated mean values for the linear (Figure 3-14) and random (Figure 3-17) polyurethane surfaces. However, for the purposes of optimising the haptotactic parameter, the ratio of these distances was more important than the values. Ultimately, the mean squared displacement plots were the biggest indicator of optimal κ values for the linear and random polyurethane surface.

SSE-values for the haptotactic parameter were also utilised in the optimisation of κ . The parameter κ represents the ability of the cells to respond to a perceived surface

gradient in its surrounding environment. A range of 0.5-0.6 for the κ -parameter was predicted as optimal for the linear surface. For the random surface a much lower κ -value range of 0.01-0.07 was predicted. This lower value of κ suggests the random surface features have less effect on the migrating fibroblast cells compared to those features present on the linear surface, as κ represents a bias towards the surface gradient in the model. This result is in line with the statistical analysis as it was stated previously that there was no statistical significance between the flat and random surfaces (Figure 3-5). Ultimately, the lower κ -value is needed on the random surface to generate the best fit to the experimental data. The higher κ -value associated with the linear surface simulations would suggest that these features activate a more prolonged mechanism of sustained migration biologically within the fibroblast cells. Full simulation of the model, incorporating optimised derived values for α , β and κ , result in the production of D^2 plots (Figure 3-20) that accurately mimic what occurred in the *in-vitro* experiments (Figure 3-5).

In summary, I have proposed a mathematical model of fibroblast migration and haptotaxis across varying polyurethane surfaces, containing nano-topographical features through abrasive polishing, which provides a quantitative framework in which to assess cell migration on these surfaces. The model has been shown to accurately replicate key migratory features observed in the *in-vitro* experiments and establishes a precise relationship between α and β values for fitting of the experimental data. The model was also able to provide distinct κ -values for the linear and random surfaces. These values indicated the amount of bias shown by the cells to each particular surface. This information can be utilised in the design of smart materials to influence the adhesion and migration of cells.

Chapter 4: Mathematical modelling of Nrf2 dynamics

4.1 Introduction

In this chapter, an *in-silico* model designed to highlight the subcellular machinations of the Nrf2 protein signalling pathway is introduced. As previously described in section **Error! Reference source not found.**, the Nrf2 protein is a vital transcriptional regulator in response to oxidative stress. However, the key characteristic of this transcription factor is its very low basal activity and stringent regulation [212]. Some of the key questions the model aims to address involve the basic rates of interactions and translocations of Nrf2. These include production and decay rates, as well as the import-export rates across the nuclear membrane. To begin, the Nrf2 pathway is reduced to only include the essential components necessary to capture these rate profiles, based upon a review of the literature (section 1.6.1). For simplicity, within the cytoplasm, it is assumed that the Nrf2 protein undergoes the processes of production, decay, proteasomal degradation and nuclear translocation. Proteasomal degradation involves interactions with Keap1, the best understood negative regulator of Nrf2 [214]. For the model, it is assumed that Keap1 is constantly available to inhibit newly formed Nrf2, as it would under normal *in-vivo* conditions [211]. As such, there is no need to include the production or decay of Keap1 within the model. Instead, its involvement within the model includes binding to the Nrf2 protein and ubiquitously marking it for degradation. Within the nucleus, it is assumed the Nrf2 has two pathways for decay and degradation. The simulated Nrf2 protein either undergoes a basal decay within the nucleus or it is exported back to the cytoplasm, to be degraded by the Keap1 protein. This is explained in more depth in the methods (section 4.2.2 below).

A novel component of this work is the close interplay of the *in-silico* model with experimentally derived data. Note that the work in this chapter involves collaboration with Professor Chris Sanderson's lab in the University of Liverpool. They provided experimental data sets for the validation of the Nrf2 signalling pathway model. These data sets contain experimental results of Nrf2 expression in wildtype cells and cells that have undergone various treatments to perturb the Nrf2 signalling system. A brief overview of the key information obtained from this experimental data is provided in section 4.2. Moreover, a detailed description of the experiments conducted by Dr Jo Wardyn (Sanderson lab) is included in Appendix B (section 7.2).

4.1.1 Chapter aims

1. To design an *in-silico* model to accurately describe the Nrf2 signalling pathway and capture the system dynamics based on a review of the literature.
2. To parameterise the model using initial input values obtained from the Khalil et al. paper
3. To validate the optimised *in-silico* output based upon agreement with the experimental data
4. Use the *in-silico* model outputs to quantify the key mechanisms of Nrf2 regulation in the cytoplasm and nucleus, proposed by Sanderson lab

4.2 Methods

As mentioned above, this chapter was completed in collaboration with the University of Liverpool and all imaging experiments were performed by Dr Jo Wardyn (Sanderson lab). The raw data generated from these experiments were used as the basis for building the mathematical model. However, for completeness, a brief overview of the key information obtained from these experiments is provided below.

4.2.1 Summary of wet lab experiments

Real time imaging experiments were conducted on live cells with the aim of measuring Nrf2 expression via fluorescence. This was achieved by transfecting primary cells with fluorescent protein plasmids. Two cell types were used in these experiments with each cell type expressing a different fluorescent protein. BAC (bacterial artificial chromosome) cells stably expressed the Nrf2-Venus fluorescent protein, which exhibits a very low expression. These cells will be referred to as 'BAC cells' throughout the chapter. The photoswitchable fluorescent protein pDendra2 was transiently expressed in SK-N-AS cells and will be referred to as 'pDendra cells' from this point forward. The pDendra2 emits naturally in a green light spectrum. However UV irradiation results in irreversible transition in emission to the bright and photostable red fluorescent protein (RFP) spectrum. The BAC cells were treated with MG132 (proteasome inhibitor) and CHX (translation inhibitor) to perturb the system and the results were recorded, containing nuclear fluorescence measurements only, which were then normalised to the initial value. These BAC cell data sets only contain nuclear fluorescent measurements, as Nrf2-Venus fluorescence is confirmed to be a nuclear fluorescent signal under lambda scanning [297]. Similarly, wildtype

experiments were conducted in the pDendra cells and measurements of green fluorescence were normalised to the initial fluorescence intensity. Note that the red data is normalised to the value after photoconversion. Experiments in these cells were also repeated with a knockdown of Keap1 (siKeap). Data obtained from the pDendra experiments provide distinct measurements for cytoplasm and nucleus. Therefore, there are four experimental data sets to validate the model, namely two data sets from the pDendra cells (wildtype and siKeap) and two data sets from the BAC cells (MG132 and CHX).

4.2.2 Mathematical Model

The starting point in the creation of the model involved the inclusion of the most important processes involved in the Nrf2-Keap1 interaction. These processes include the production, translocation, degradation and decay of the Nrf2 protein. The model, shown schematically in Figure 4-1, represents the regulation of Nrf2 within two compartments, the cell nucleus and the cytoplasm. Nrf2 is produced (at rate r_4) in the cytoplasm and can translocate into the nucleus (rate r_2). Due to the different transfection methods for pDendra cells and BAC cells, an additional parameter (z) is required to modify the production rate of Nrf2 in the cytoplasm. That is the r_4 parameter is multiplied by the $z < 1$ parameter to give a reduced basal synthesis rate for the BAC cell experiments. In the nucleus, the Nrf2 protein is either exported to the cytoplasm (rate r_1) or decays within the nucleus (rate r_5). Cytoplasmic Nrf2 can also bind with Keap1 whereupon it is targeted for proteasomal degradation (maximal rate r_3). This Keap1-mediated removal of cytoplasmic Nrf2 protein is governed by a threshold (r_6). This simple description of Nrf2 dynamics in the cell is used for modelling the green fluorescent data. The red-Nrf2 system is modelled in the same

way as the green, but lacks the basal synthesis rate ($r_4 = 0$) as there are no newly synthesised Nrf2 proteins emitting red fluorescence by definition.

The mathematical model, comprises two ordinary differential equations (ODEs) for each of the two cellular compartments (subscript c for cytoplasm and n for nucleus):

$$\frac{dG_c}{dt} = r_4 + r_1 G_n \frac{V_n}{V_c} - r_2 G_c - \frac{r_3 G_c}{G_c + r_6}, \quad (4-1)$$

$$\frac{dR_c}{dt} = r_1 R_n \frac{V_n}{V_c} - r_2 R_c - \frac{r_3 R_c}{R_c + r_6}, \quad (4-2)$$

$$\frac{dG_n}{dt} = r_2 G_c \frac{V_c}{V_n} - r_1 G_n - r_5 G_n, \quad (4-3)$$

$$\frac{dR_n}{dt} = r_2 R_c \frac{V_c}{V_n} - r_1 R_n - r_5 R_n, \quad (4-4)$$

where G_c denotes the concentration of green-Nrf2 in the cytoplasm, G_n represents the concentration in the nucleus, V_c denotes the volume of the cytoplasm and V_n denotes the volume of the nucleus. The variables R_n and R_c represent the concentration of red-Nrf2 protein present in the nucleus and cytoplasm, respectively. All these dynamic processes are governed by parameters whose description and respective units are given in Table 4-1.

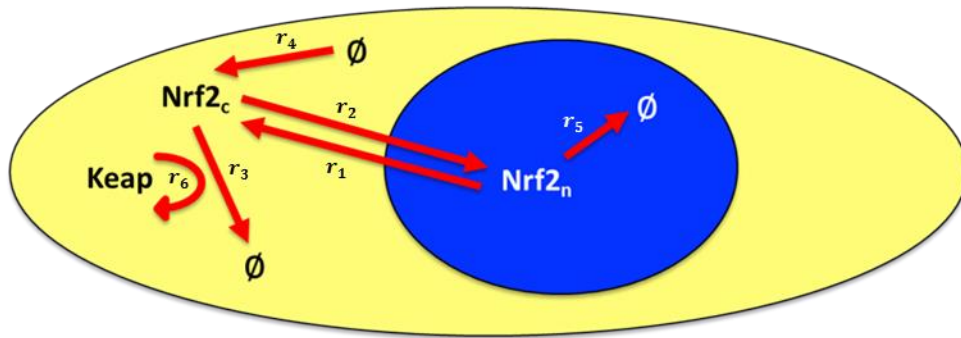


Figure 4-1. Minimal Mathematical Model. Schematic diagram showing the cycle of the Nrf2 protein within the cytoplasm and nucleus. In the cytoplasm, Nrf2 is produced and then sequestered by Keap1 and marked for degradation. The other elements of the minimal-model include nuclear import, nuclear decay and export of the nuclear Nrf2 protein to the cytoplasm. Rate descriptions included in Table 4-1.

Parameter	Description [units]
r_1	Nuclear export rate [1/min]
r_2	Nuclear import rate [1/min]
r_3	Maximal Keap-mediated cytoplasmic removal rate [nM/min]
r_4	Basal synthesis rate of pDendra cells [nM/min]
r_5	Nuclear removal rate [1/min]
r_6	Keap-mediated cytoplasmic removal threshold [nM]
z	Modifier for BAC basal synthesis rate [dimensionless]

Table 4-1. Description and units of the seven parameters. Table showing the seven parameters for the Nrf2 signalling processes included within the *in-silico* model design. A description of what each parameter represents and the respective units is also provided.

4.2.3 Parameterisation and Latin Hypercube sampling

To initialise the model, the preliminary model uses values for the six parameters ($r_1 - r_6$) obtained from a publication by Khalil et al. [269]. A description of each of the parameters used in this study, the values of these parameters and how they correspond to the parameters outlined in the model above are given in Table 4-2. The value for the z parameter (0.01) was obtained experimentally from the Sanderson lab. Parameter optimisation was conducted in order to modify these initial parameter values and give the best possible fit between the model and the data. Latin hypercube sampling (LHS) was used to generate a distributed sample set of initial parameter estimates for this fitting. LHS is a way of generating random samples of parameter values [298]. The reasoning behind the use of LHS in the model is due to the computational power needed to optimise these parameters using general random sampling methods. In random sampling, the model would not take into account previously generated sample points when selecting new sample points, which has the potential to generate a poor spread of the data points. However, with LHS it can be decided how many sample points are needed and the sampling also accounts for which ranges of values have already been selected. Therefore, LHS sampling provides initial parameter estimates that incorporate the entire spread while remaining computationally efficient and preventing the model becoming trapped in local minima. A paper by Pan et al. [299] shows how LHS sampling can be used to improve the efficiency in terms of computational time and space-filling properties. LHS has also shown to optimally represent the multivariate distribution of input datasets better than other sampling methods [300].

Parameter	Initial value [269]	Description and source [269]
r_1	0.1 min ⁻¹	Rate of cytoplasmic/nucleus exchange of Nrf2 [269]
r_2	0.1 min ⁻¹	Rate of cytoplasmic/nucleus exchange of Nrf2 [269]
r_3	0.1 μM ⁻¹ min ⁻¹	Reaction rate of the binding of Nrf2 with Keap1 [269]
r_4	2x10 ⁻² μM/min	Synthesis rate of Nrf2 [269]
r_5	5x10 ⁻² min ⁻¹	Degradation rate of Nrf2 [269]
r_6	5 nM	Dissociation constant of Nrf2 with Keap1 [269]
z	0.01	Modifier for BAC basal synthesis rate (Sanderson)
V_c	2.2x10 ⁻¹² L	Cytoplasmic volume [301]
V_n	5x10 ⁻¹³ L	Nuclear volume [301]

Table 4-2. Parameter values derived from literature. Table showing the initial values derived from Khalil et al. for the parameters $r_1 - r_6$. These values are used for the initial parameterisation of the mathematical model. A description of what each parameter represents in the Khalil et al paper is also provided for clarity. Also included in this table are the other parameters used within the model. The z parameter was derived from the Sanderson lab (as described in the main text). The volume parameters were adapted from red blood cell volumes from the literature [301].

4.2.4 Fitting algorithm

Optimised model parameter values were obtained by fitting the model to the experimental data, using the non-linear optimisation function (“fminsearch”) in Matlab. The fminsearch function finds the minimum of a scalar function of several variables, starting with the initial estimates. This is an unconstrained multivariable function using a derivative-free method based on the Nelder-Mead simplex method [302]. Simply, this function identifies parameter values that correspond to the minimum distance between the model output and the data. A limitation of this function is its tendency to only give local solutions if the initial parameter estimates do not fall near the global optimal solution. This is another benefit to using initial guesses from a spread of LHS generated samples as it provides a wide range of initial parameter estimates, diminishing the chances of the fminsearch algorithm becoming trapped within local minima. A range was taken for each parameter e.g. for parameter r_1 , the range generated was $[r_1/10, 10r_1]$. This range was then subdivided into 200 intervals, using a logarithmic scale, and then numbers were drawn from each of these 200 intervals using LHS. This gave a set of 200 randomly perturbed numbers from $r_1/10$ to $10r_1$. This was repeated for each parameter and each time the fitting was conducted, a random value was selected from these numbers for each parameter. Therefore, through the combination of LHS and fitting to the experimental data, 200 samples were optimised. This was further reduced to 98 samples through further optimisation, described in the results section (4.3). From here further parameterisation was conducted, utilising experimental estimates, until the most appropriate parameter values for fitting the experimental data were identified. A flow diagram depicting this process is available in Figure 4-2.

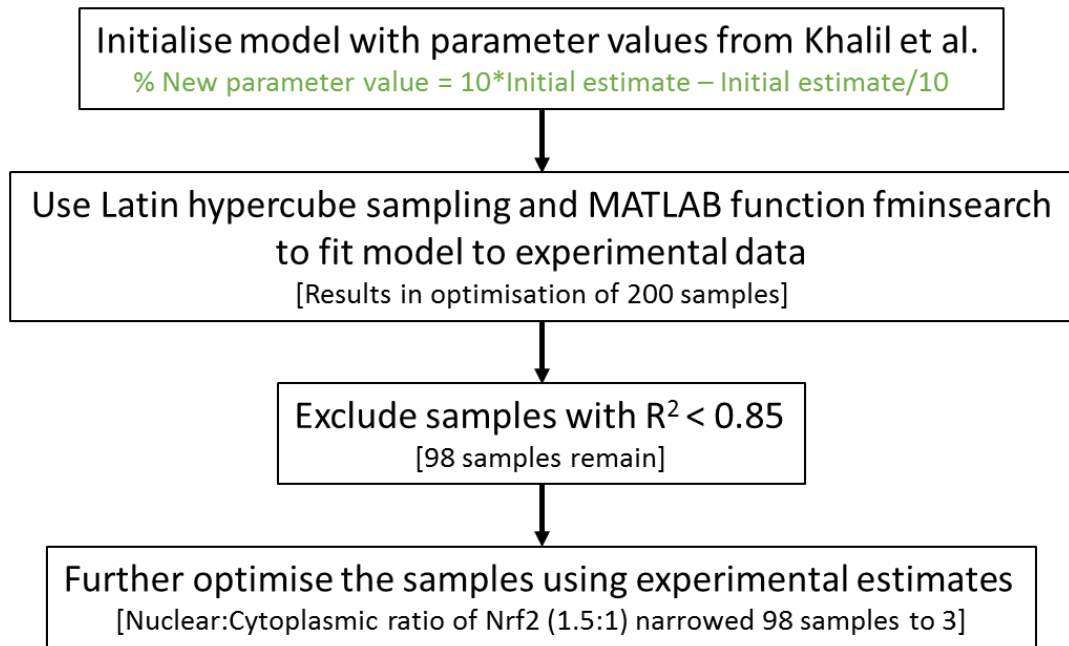


Figure 4-2 Schematic of modelling strategy. This general schematic specifically highlights the simplified process implemented to optimise the model from 200 potential samples to 3.

4.3 Results

4.3.1 Nrf2 expression in cells using pDendra2

pDendra2 is a green-to-red photoswitchable fluorescent protein. This fluorescent protein is fused with Nrf2 and irreversibly changes to emit red fluorescence when UV light is applied [303]. At the beginning of the experiment, all Nrf2 cells emit green fluorescence. When the pDendra2 is irradiated at time 4 minutes by UV light, approximately 50% of the Nrf2 cells switch to red fluorescence (Figure 4-3). This half maximal fluorescence change was deliberate by Sanderson's lab to measure the equivalent import and export rates between nuclear and cytoplasmic compartments in their experiments. The fluorescence of the cells is measured in the cytoplasm and the nucleus to give two distinct measurements. The fluorescence scale is normalised, such that a value of 1 arbitrary unit (AU) corresponds to maximum fluorescence.

There should be zero cells emitting red fluorescence before UV application. However, in Figure 4-3B, it can be seen that the initial red fluorescence measurement is approximately 0.2 AU. This is most likely due to background fluorescence in the experiment possibly due to e.g. autofluorescence, spectral overlap or undesirable antibody binding [304]. To allow comparison with the mathematical model, it is important to rescale this data (Figure 4-4) to remove any background signal that was measured in the experiment. This rescaling of the data was achieved by using equation 4-5 combined with the raw data values, namely:

$$x_{NEW}(t) = \frac{x_{RAW}(t) - x_{BACKGROUND}}{1 - x_{BACKGROUND}}, \quad (4-5)$$

where x_{NEW} represents the rescaled pDendra2 fluorescence, x_{RAW} represents the pDendra2 fluorescence from the raw data at time point t and $x_{BACKGROUND}$ represents the observed background pDendra fluorescence at $t=0$ (approx. 0.2 AU).

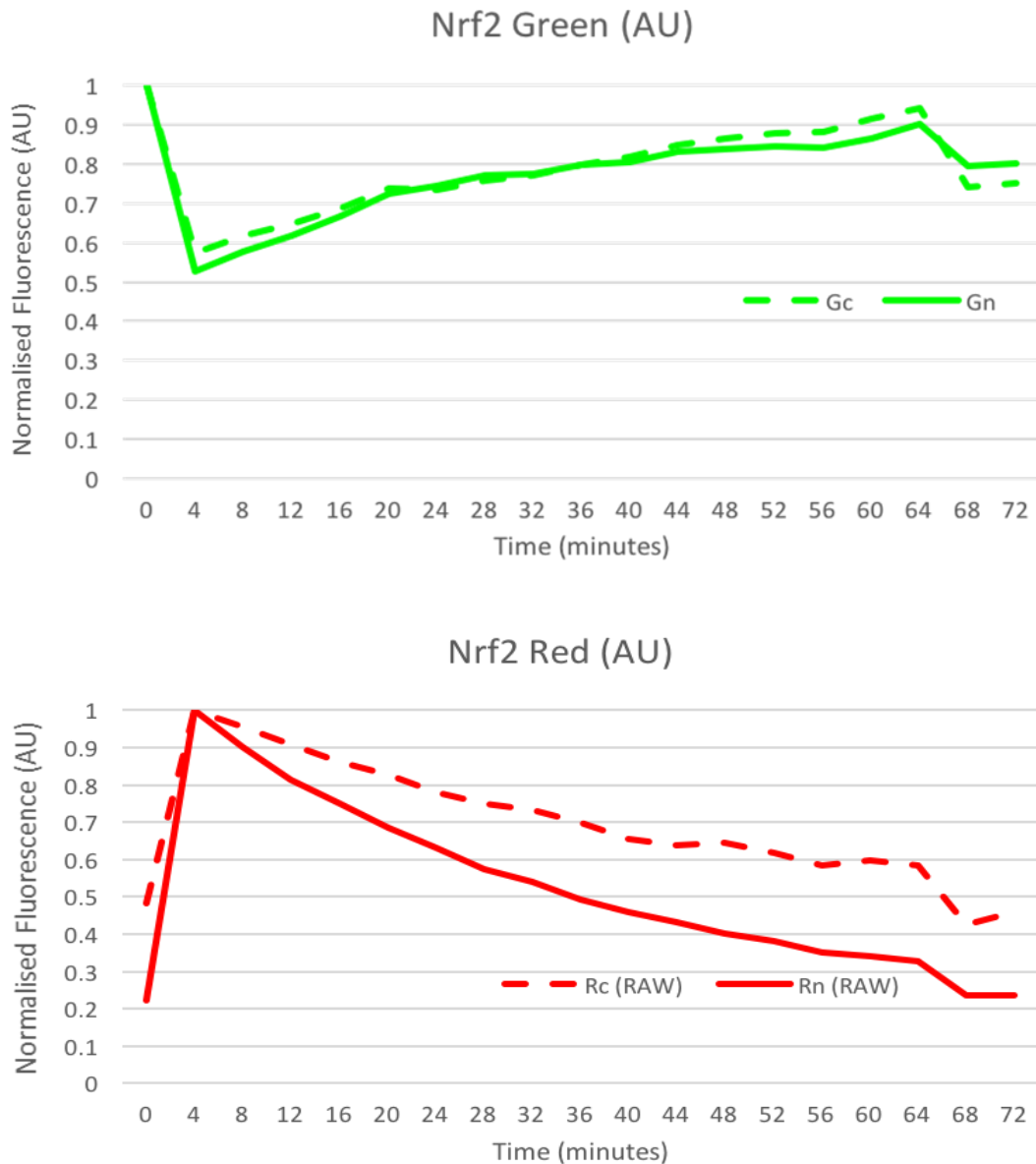


Figure 4-3. Green-Red pDendra-Nrf2 data. UV treatment is applied at $t=4$ min and irreversibly switches pDendra-Nrf2 from green to red fluorescence. (A) Graph showing Green pDendra-Nrf2 fluorescence levels in the cytoplasm (dotted line) and in the nucleus (solid line). (B) Graph showing Red pDendra-Nrf2 fluorescence levels in the cytoplasm (dotted line) and in the nucleus (solid line). Green data normalised to initial fluorescence intensity and red data normalised to the value after photoconversion.

The photoconversion experiment was repeated with Nrf2 cells treated with siKeap1 (Figure 4-5), which is a short interfering RNA (siRNA) that targets human Keap1 and silences the expression of this protein, which would be expected to lead to an increase in Nrf2 abundance. To achieve this in the model the parameter r_3 was set to zero. One effect of silencing this protein appears to be a faster recovery of newly synthesised green pDendra-Nrf2 protein. At time point 40 minutes in Figure 4-3, the green pDendra-Nrf2 measurement is approximately 0.8 AU compared with a measurement of 0.9 AU at the same time point in Figure 4-5. This would suggest that overall production of Nrf2 is higher when Keap1 is silenced, which is what would be expected. Contrastingly, there is no comparative difference between the red pDendra-Nrf2 measurements at the same time point in Figure 4-4 and 4-5, which result in a measurement of approximately 0.3 AU. This would suggest that the rate of Nrf2 removal is unchanged.

To measure the relative effect of proteasome-mediated degradation, an experiment was performed in stably expressed Nrf2-Venus cells imaged after treatment with 10 μ M of MG132. MG132 is a proteasome inhibitor that blocks degradation. As a result, nuclear Nrf2 fluorescence increases twelve-fold over the duration of the experiment (Figure 4-6). The measurements in this experiment represent nuclear values only and are normalised based upon the initial fluorescence intensity in the nucleus. To mimic the inhibition of proteasomal degradation in the model, basal decay rates r_3 and r_5 are set to zero. Also, as these experiments were performed in BAC cells, parameter r_4 is multiplied by parameter z to represent the reduced Nrf2 production in this cell type

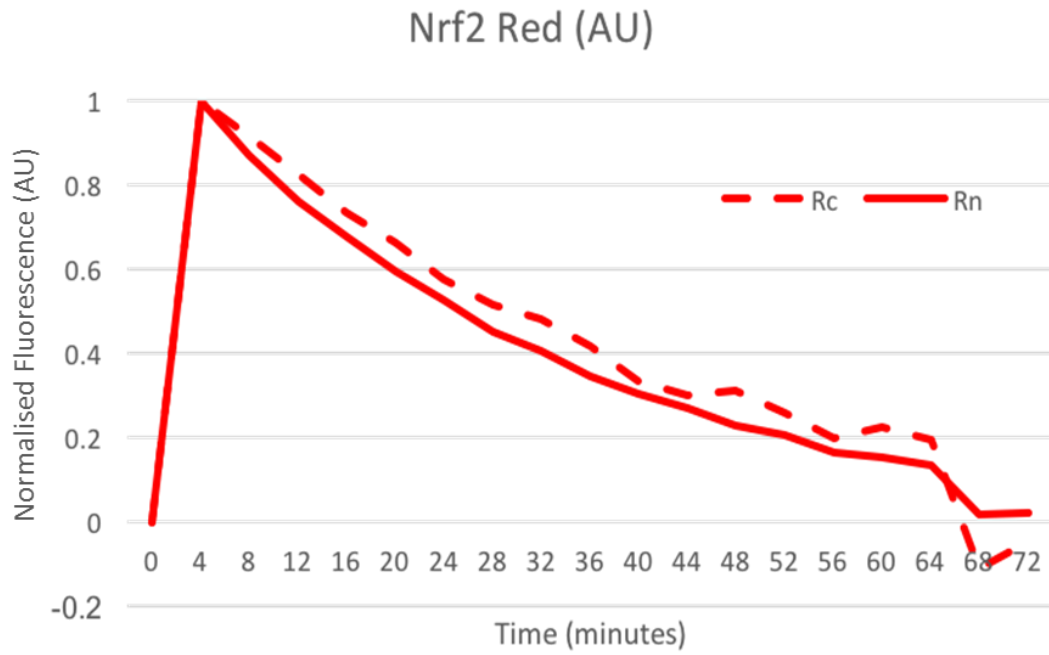


Figure 4-4. Re-scaling of red data. The data is re-scaled to zero at $t = 0$ minutes to remove any background fluorescence and allow for model comparison.

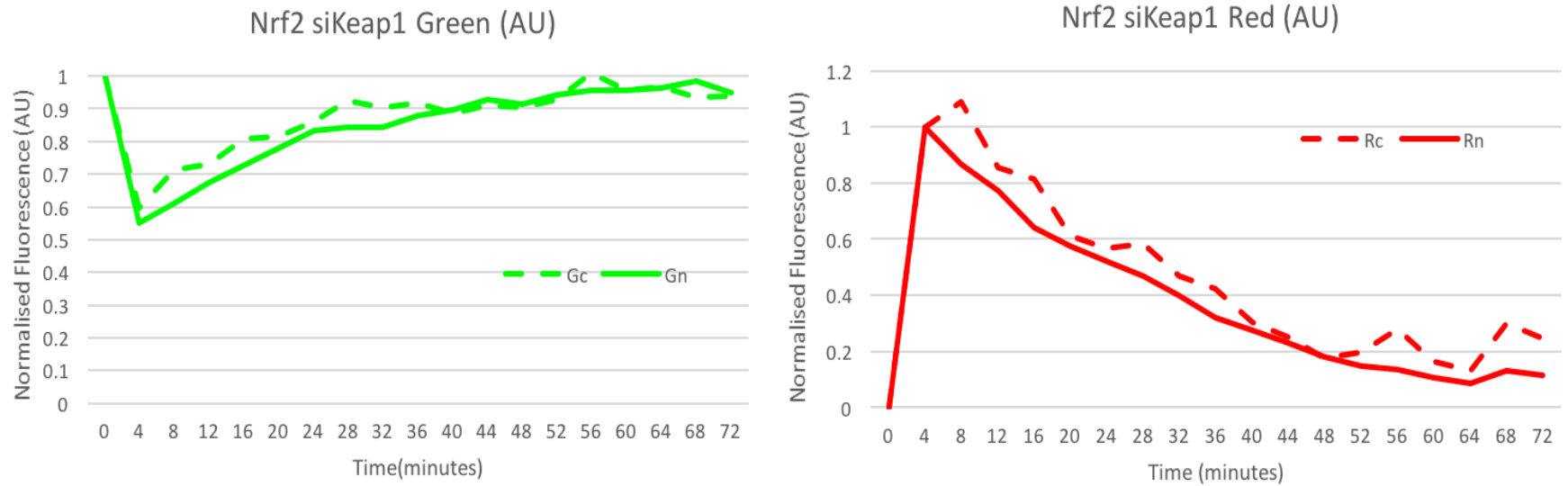


Figure 4-5. Green-Red pDendra-Nrf2 experiment using siKeap-1. Green-Red experiments repeated with knockdown of Keap-1. UV treatment applied at t = 4 minutes. (A) Graph showing Green pDendra-Nrf2 fluorescence levels in the cytoplasm (dotted line) and in the nucleus (solid line). (B) Graph showing Red pDendra-Nrf2 fluorescence levels in the cytoplasm (dotted line) and in the nucleus (solid line).

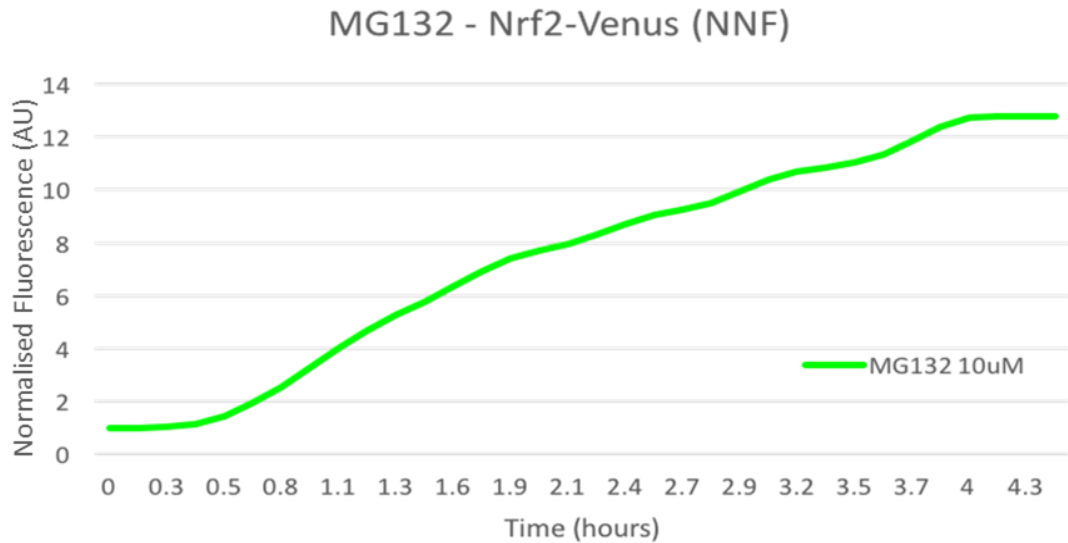


Figure 4-6. Nrf2-Venus experiment using MG132. MG132 treatment was applied at $t=0.4$ hours. The experiment measures the Nrf2-Venus fluorescence levels in BAC cells. The data includes nuclear fluorescence measurements only and was normalised to the initial value. MG132 is a proteasome inhibitor.

The relative nuclear fluorescence of green Nrf2-Venus is measured after treatment with 5 μg/ml of CHX (Figure 4-7). CHX is an inhibitor of translation and effectively prevents the synthesis of Nrf2 proteins. This is clearly evident from the results in Figure 4-7. Previously, Nrf2 exhibited a distinct recovery pattern (Figure 4-3 & 4-5) which is absent in Figure 4-7. Instead, Nrf2 levels in Figure 4-7 decrease gradually until it reaches a steady state of approximately 0.2 AU (due to background fluorescence). As above, this data is rescaled to omit background fluorescence (compare Figure 4-7 and Figure 4-8).

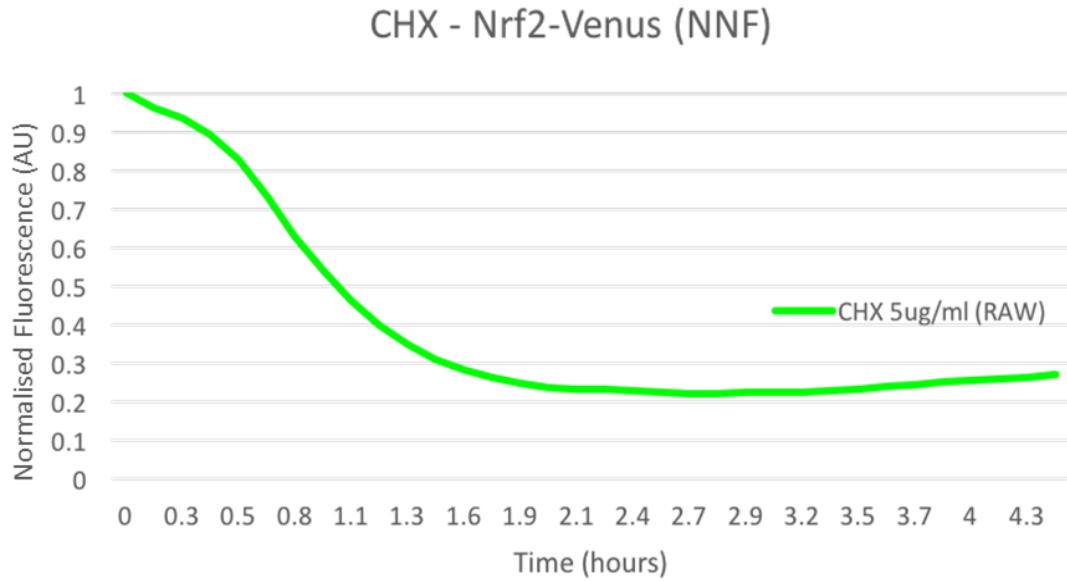


Figure 4-7. Nrf2-Venus experiment using CHX. CHX treatment was applied at $t = 0.4$ hours. The experiment measures the Nrf2-Venus fluorescence levels in BAC cells. The data includes nuclear fluorescence measurements only and was normalised to the initial value. CHX inhibits the synthesis of Nrf2.

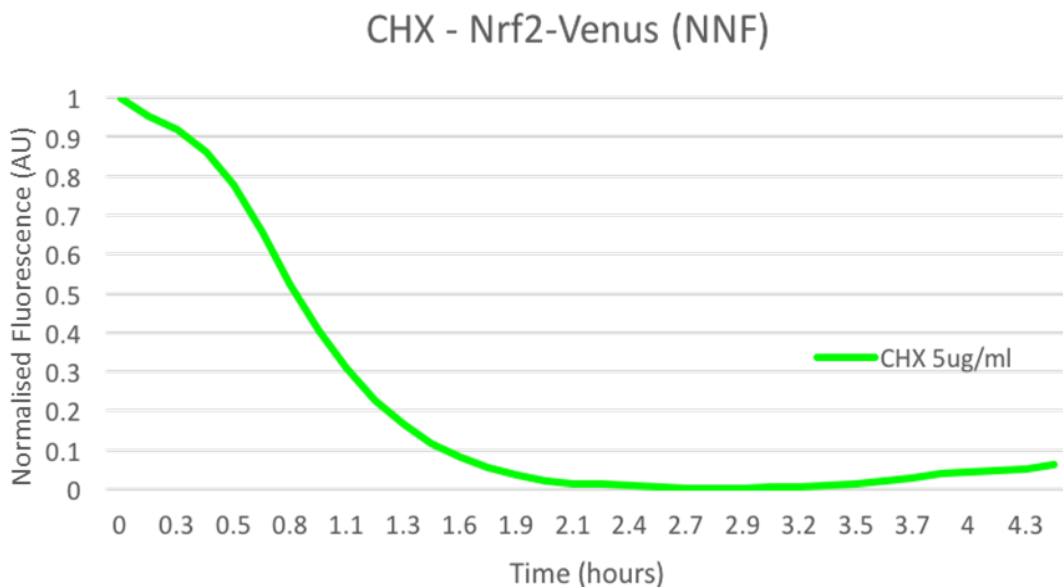


Figure 4-8. Re-scaling of CHX data. Data re-scaled to remove background signal. According to the structure of the model, Nrf2 should decay to zero with the addition of CHX.

4.3.2 Model optimisation through data fitting

The model was run as described above (in section 4.2.3) using a range of initial parameter estimates centred on the values given in Khalil et al. [269]. The fitting routine was sensitive to the initial parameter estimates which motivates the use of Latin hypercube sampling (LHS) to supply a range of initial parameter estimates. Of the 200 initial parameter estimates, 98 samples produced a fit between the model and the data that gave R-squared (R^2) values of 0.85 or higher. The model was fit to the different data sets simultaneously, with the appropriate scenario-dependant model terms omitted to represent the silencing of Keap1 (siKeap), inhibition of proteasomal degradation (MG132) and inhibition of translation (CHX). These 98 optimised values were plotted against the corresponding initial parameters for each of the initial parameter sets, to identify trends in parameter sensitivity (Figure 4-9). Parameters are optimised using MATLAB function `fminsearch` to minimise the relative error, χ , for the 10 time-series (4 WT, 4 siKeap, 1 MG132 and 1 CHX):

$$\chi = \sum_{i=1}^{10} \sum_t \left(\frac{Model_i(t) - Data_i(t)}{Data_i(t)} \right)^2. \quad (4-6)$$

The main result to be seen from this graph is the relatively small variability in optimised parameter values for the parameter sets r_3 (Figure 4-9C), r_4 (Figure 4-9D), r_6 (Figure 4-9F) and z (Figure 4-9G). For these parameters, there are a wide range of initial parameter estimates imported into the model which produce a reasonably tight range of optimised parameter values. Compare that to the r_1 (Figure 4-9A), r_2 (Figure 4-9B) and r_5 (Figure 4-9E) parameter sets, where the range of optimised parameter values are much wider. Some clustering of optimised values can be

observed and becomes more apparent when the initial parameters are plotted against the optimised parameters (Figure 4-10). Red circles indicate possible clustering of the optimised parameter values for each of the seven sets. For example, for the r_1 parameter, the initial estimate range of 0 to 10 results in an optimised range of 0 to 2 (Figure 4-10A). The initial estimate range for parameter r_2 (Figure 4-10B) is the same as parameter r_1 but results in a much tighter optimised parameter range of 0.055 to 0.065. The optimal ranges for the other 5 parameter sets are produced at the low end of the initial ranges for r_3 (Figure 4-10C), r_4 (Figure 4-10D), r_5 (Figure 4-10E), r_6 (Figure 4-10F) and z (Figure 4-10G).

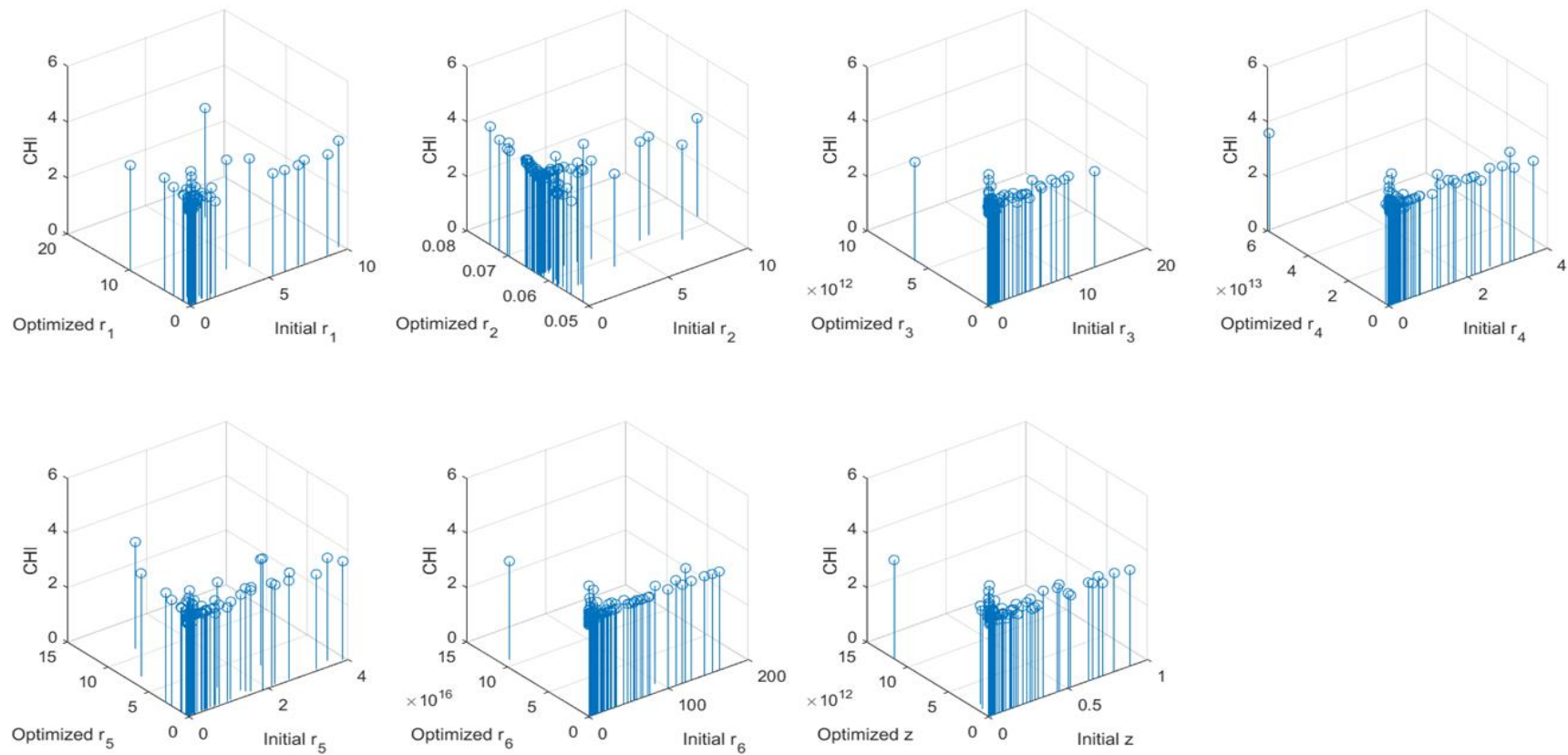


Figure 4-9. Goodness of fit estimates between initial and optimised parameters. Graphs showing initial parameter estimates against the optimised parameter values with $R^2 \geq 0.85$. CHI represents the relative error calculated using Equation 4-6.

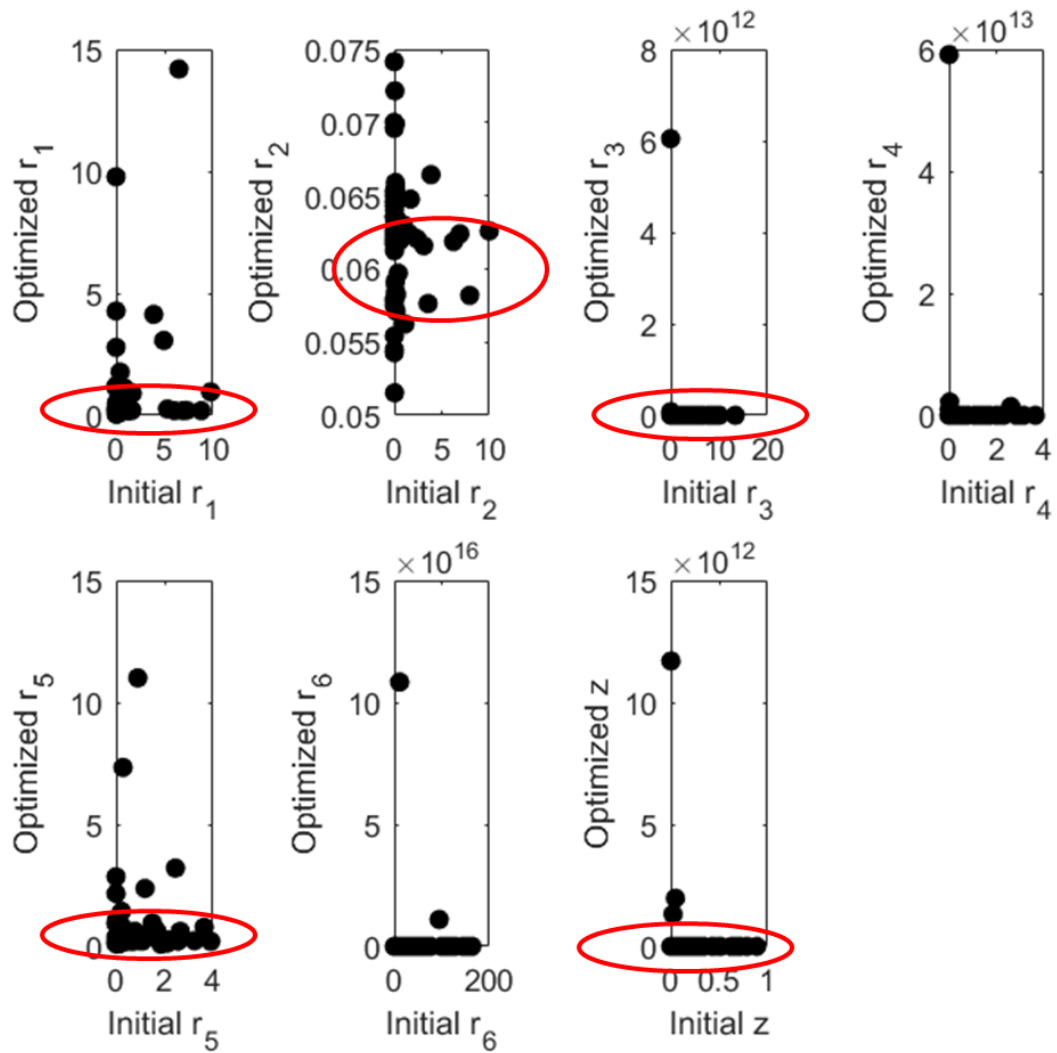
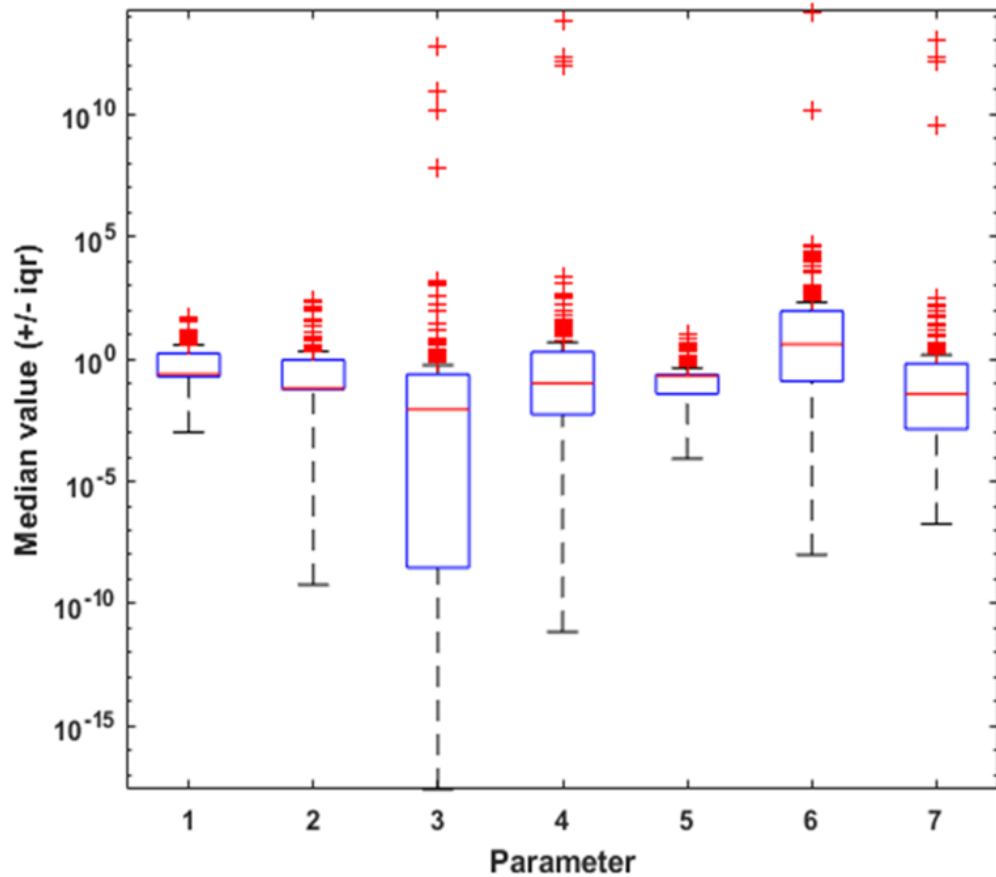


Figure 4-10. Observed clustering of parameters. Graphs showing the initial parameter estimates against the optimised parameter values for $r_1, r_2, r_3, r_4, r_5, r_6$ and z . Red circles show clustering of optimised parameter values.

Another way to display the distribution of data obtained from the parameter optimisation is to look at the median optimised values and the corresponding interquartile ranges (Figure 4-3). From this, the full range of variation and the average value (median) for each parameter set can be displayed. In Figure 4-3, parameters 1, 2 and 5 have comparatively shorter ranges than the other 4 parameters. This trend suggests that these parameter sets are potentially sensitive to perturbations from the median value.



Median: 0.245 0.063 0.009 0.101 0.203 4.073 0.037

IQR: 1.475 0.856 0.240 1.952 0.197 90.38 0.642

Figure 4-3. Box plots for each of the seven parameters. Box plots showing a range of parameter values with a $R^2 > 0.85$. Parameters 1-7 correspond $r_1, r_2, r_3, r_4, r_5, r_6$ and z values respectively. The median and IQR values for each parameter set are given below the box plot. Outliers are denoted by crosses (+).

4.3.3 Further parameterisation of the model

The next step is to narrow down the 98 ($R^2 > 0.85$) samples and identify the most appropriate parameterisations for the model. One way of doing this is to exclude the samples that do not actually replicate features of the *in-vivo* system that the model is supposed to be simulating, e.g. the steady state concentration of nuclear Nrf2 (estimated to be 2.8nM) and the cytoplasmic estimate (1.88nM) result in a $G_n:G_c$ ratio of 1.5:1 (personalised communication, Sanderson). Figure 4-4 shows a plot of the $G_n:G_c$ steady state ratio for each of the 98 samples. The $G_n:G_c$ experimental steady state is represented by the horizontal blue line. Of the 98 optimised samples, 3 were selected based upon the similarity of their $G_n:G_c$ ratios to the 1.5:1 experimental estimate. The seven parameter values (r_1 to r_6 and z) were then extracted from these three samples (#14, #27 and #53 out of the 98 parameter sets) and compared in Table 4-3 along with a value for $1/z$ and the $G_n:G_c$ ratios. Note that $1/z$ is equivalent to the ratio between pDendra2 and BAC Nrf2 expression. Parameters r_1, r_2 and r_5 show the least percentage difference, which were calculated using Equation 4-7 and 4-8, across the three sample sets. Note that the parameter values in set #27 were used as reference values to calculate percentage differences:

$$\% \text{ diff } 1 = \left| 2 \times \frac{\#14 - \#27}{\#14 + \#27} \times 100 \right| \quad (4-7)$$

$$\% \text{ diff } 2 = \left| 2 \times \frac{\#53 - \#27}{\#53 + \#27} \times 100 \right|. \quad (4-8)$$

These parameter sets are almost identical between samples #27 and #53. However, the other 4 parameter values show approximately 200% difference between the sample sets. In contrast, there is an approximately 90% difference between samples

#14 and #27 for parameters r_4 and z . Sample #53 has a very large $1/z$ value compared to the other two samples and is too large to be considered to be biologically viable, which would suggest that samples #14 and #27 are more appropriate and representative. Parameter sensitivity analysis was then performed on the three samples and displayed in Figure 4-5. The seven parameters were plotted with their corresponding χ values (Figure 4-5, left hand panel) and R^2 values (Figure 4-5, right hand panel) over a two-fold change (-2 to 2) in optimised values for each of the optimised sets #14, #27 and #53. Again, parameters r_1 , r_2 and r_5 exhibit the most sensitivity to variation as the change in χ was comparatively greater than for the others. Sample #14 show the least sensitivity for the other four parameter values, whereas samples #27 and #53 show increased χ values for r_3 , r_4 , r_6 and z as the fold change reached its upper and lower limit. Similarly, the behaviour was observed for the three parameter sets when also looking at the respective R^2 values. For sample #14, parameters r_1 , r_2 and r_5 drop below an R^2 value of 0.85 with only small changes in their respective parameter values. The R^2 value for the other parameters remains relatively constant for parameter changes. This sensitivity analysis shows that r_1 , r_2 and r_5 are the most sensitive, i.e. the model output varies significantly with only small variations in the parameters. These parameters are the most consistent across all three parameter sets. This indicates the values predicted for these parameters are most likely to be optimal. Subsequently, the sensitivity analysis also indicates less confidence in the other parameters. Now that optimised parameter sets have been identified, the *in-silico* results can be compared to the experimental results. For the point of illustration, the optimised parameter set #14 is used for the input values for the model.

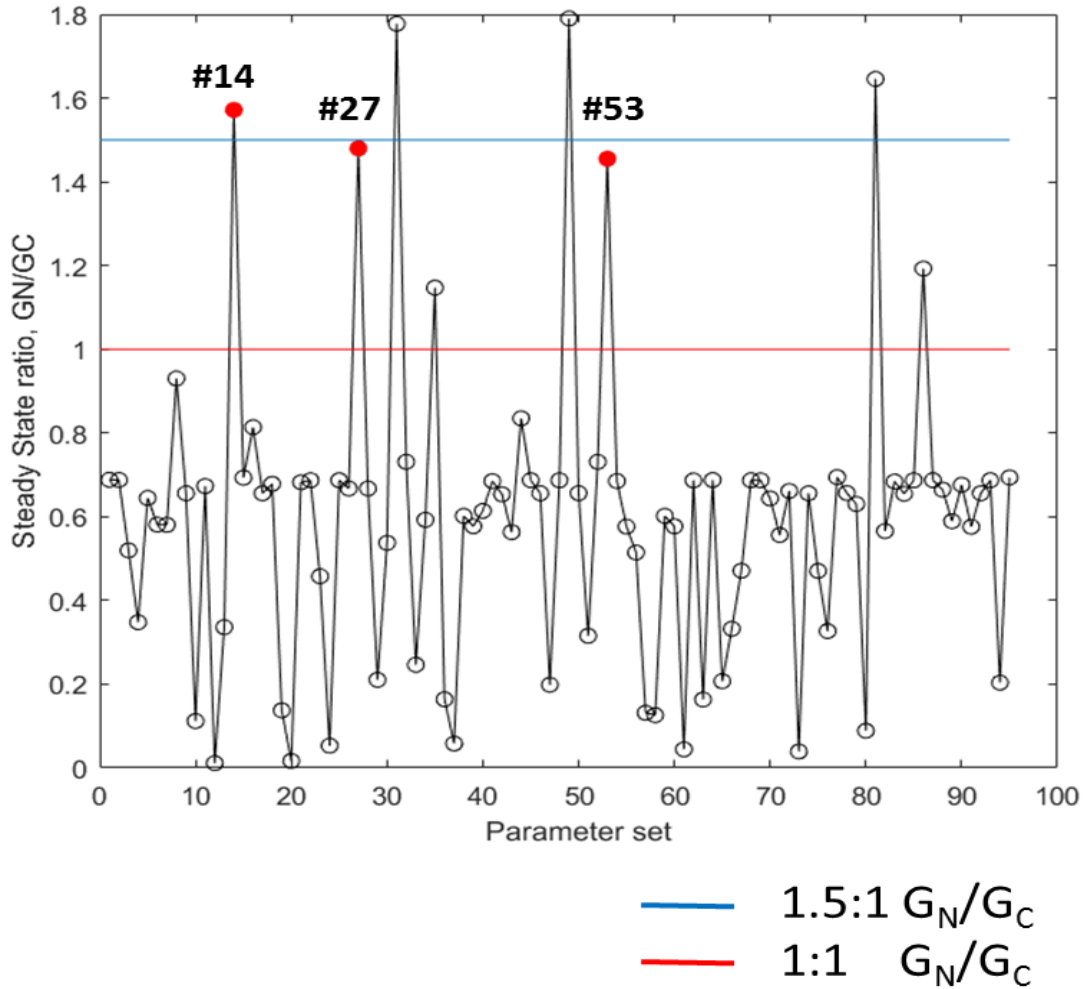


Figure 4-4. Nuclear vs cytoplasm steady state ratios. Graph showing the nuclear/cytoplasm steady state ratios for each of the 98 parameter sets. Red line shows level of 1:1 ratio and blue line shows the level for 1.5:1 ratio. The parameter sets closest to the blue line are highlighted with red circles (#14, #27 and #53).

Parameter	Units	#14	% diff 1	#27	% diff 2	#53
r_1	[1/min]	0.086	38.1	0.0585	2.8145	0.0601
r_2	[1/min]	0.696	21.2	0.0562	0.0248	0.0563
r_3	[nM/min]	0.0059	199.8	15.382	199.99	1.38×10^{-5}
r_4	[nM/min]	5.1345	89.4	1.9599	195.51	172.93
r_5	[1/min]	0.1089	0.1438	0.1087	1.1002	0.1099
r_6	[nM]	322.93	195.99	3.2×10^4	175.21	4.85×10^5
z	n.d	0.0135	90.4	0.0358	195.52	4.05×10^{-4}
$1/z$	n.d	74.07		27.96		2.47×10^3
$G_n: G_c$	ratio	1.57:1		1.48:1		1.46:1

Table 4-3. Optimised parameter sets. The optimised values for the three samples #14, #27 and #53 are given in column 3, 5 and 7. % diff 1 and %diff2 refer to the percentage difference between parameter estimates for sets #14 and #27 and #27 and #53, respectively (calculated by equations 4-7 and 4-8).

Parameter set:

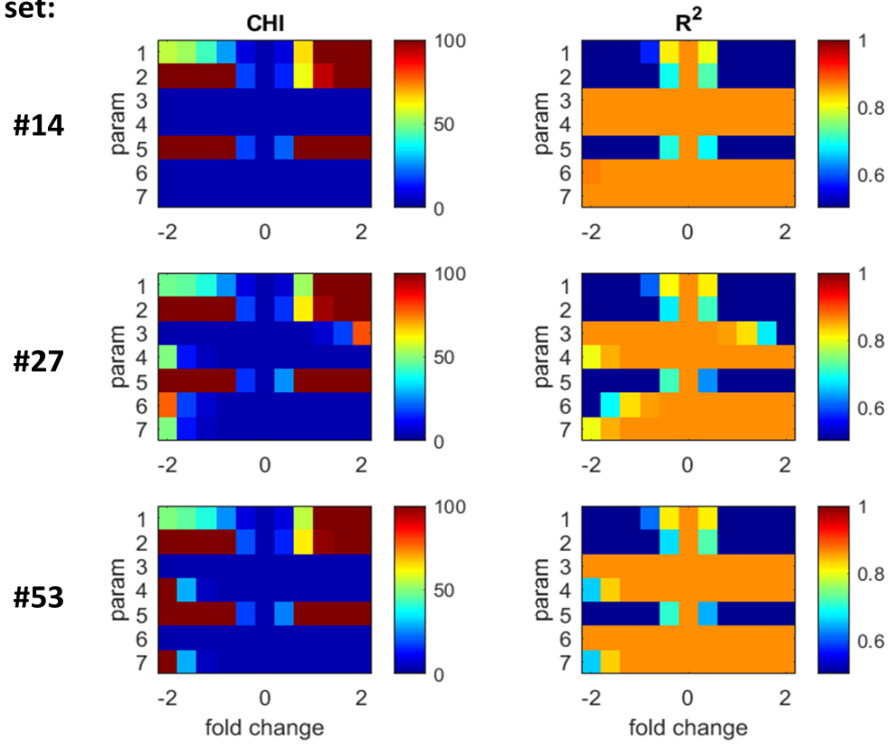


Figure 4-5. Sensitivity analysis for each of the seven parameter (#14, #27 and #53). Box plots showing a range of parameter values with a $R^2 \geq 0.85$. Parameters 1-7 correspond to $r_1, r_2, r_3, r_4, r_5, r_6$ and z values respectively. Left hand panel shows the effect on the relative error χ as each parameter is varied from a -2 to 2 fold change. Right hand panel shows corresponding effect on R^2 .

4.3.4 Fitting of the experimental data

Figure 4-6 shows the green and red-Nrf2 results in the wild type pDendra-Nrf2 experiments and simulations. The solid and dashed lines with circular markers represent the results from the wet lab experiments and the solid and dashed lines without markers represent the results from the *in-silico* simulation. The simulated results fit to the experimental results for both the green and red components giving confidence in the design of the model structure. Figure 4-7 shows the pDendra-Nrf2 results that were treated with siKeap1. To achieve this knockdown effect in the model, the r_3 parameter, representing the proteasomal degradation of cytoplasmic Nrf2 by Keap1, is set to zero. Again, the impact of these results adds weight to the reliability of the model. Figure 4-8 displays the Nrf2 dynamics after treatment with MG132. Comparison of the traces show another strong correlation of results. The final experiment involved the nuclear Nrf2 measurements in BAC cells in the presence of CHX. As CHX interferes with the synthesis of newly formed Nrf2 proteins, the basal synthesis parameter, r_4 , is set to zero for this simulation. The results are plotted in Figure 4-9. The fit between the experimental and simulated results is again encouraging. The overall outcome from these simulations shows that the optimised parameter set accurately depicts the dynamics of the Nrf2 system. The overall rate ratios for these three parameter sets are given in Table 4-4. These relative rates (nucleus influx/efflux and cytoplasmic vs nuclear decay) are of interest to biologists, and currently unknown from the experiments. Estimates of these rates can be calculated using the optimised parameters and taking steady state levels for G_C and G_N . From these calculations, the rate of influx is more than twice (2.26, 2.86) that of the rate of efflux across the nuclear membrane and that there is much less decay

(4.7×10^{-4} , 0.0132) in the cytoplasm compared with the nucleus. Note that set #53 is discounted because of the unrealistic $1/z$ value produced in Table 4-3.

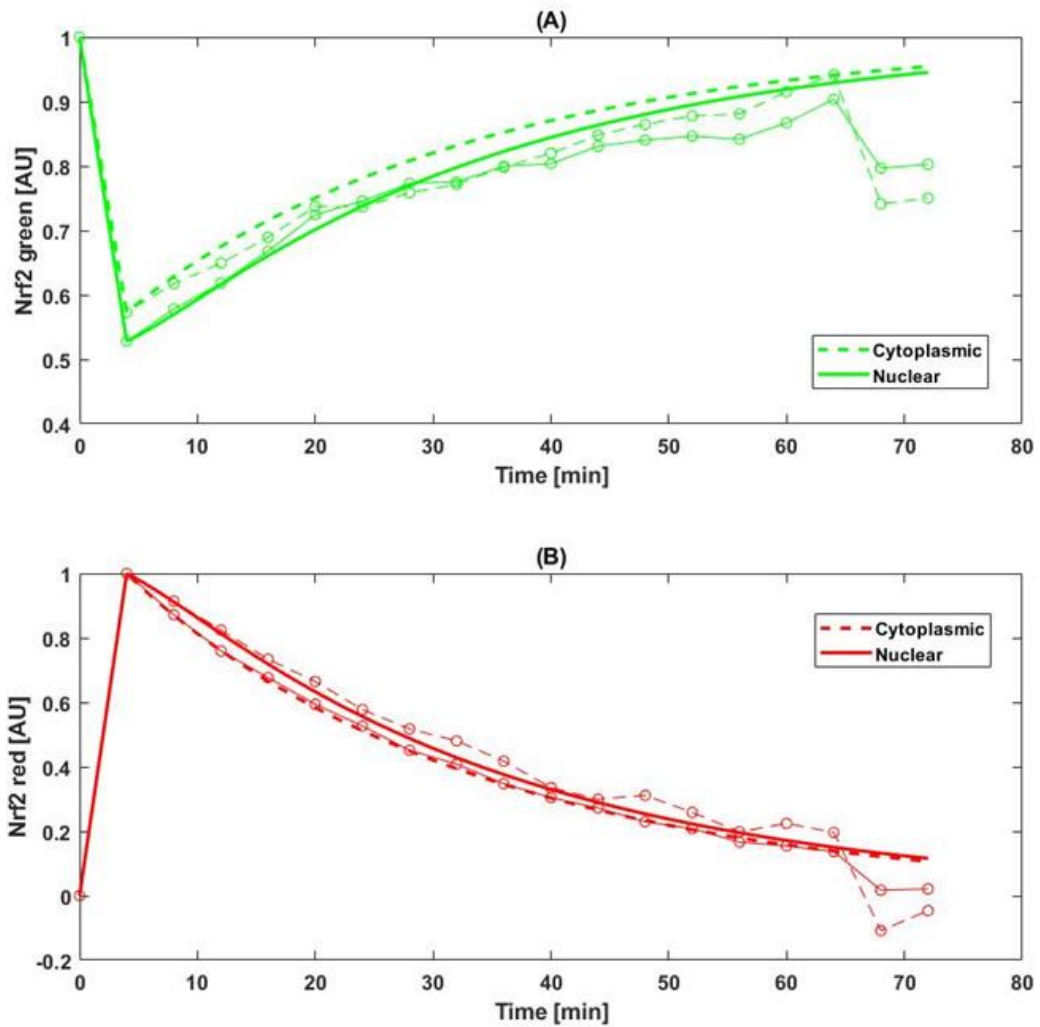


Figure 4-6. Wildtype experiment fitting. Nrf2 values are plotted in the graph for the cytoplasm (dashed line) and the nucleus (solid line). The experimental results are depicted by the traces with circular markers and the simulated results lack any markers.

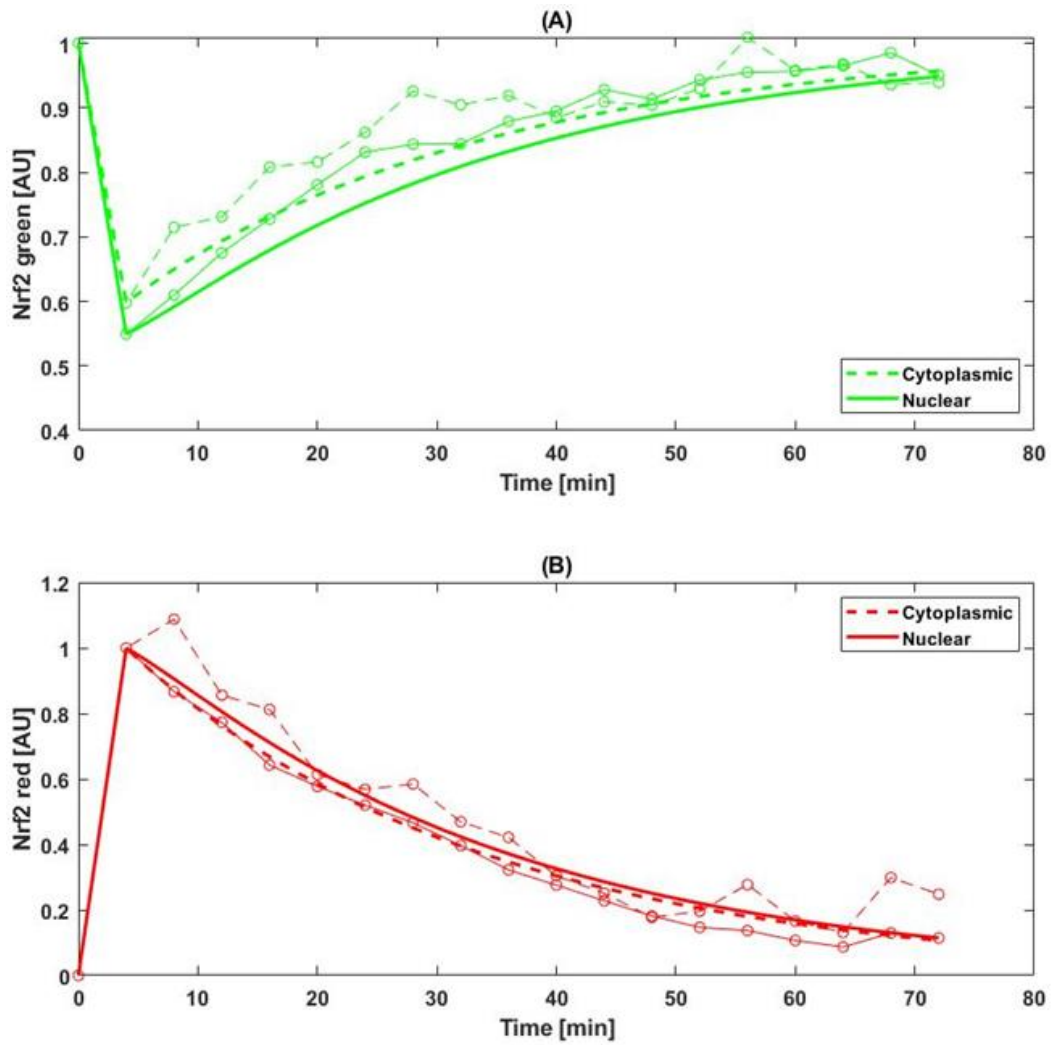


Figure 4-7. siKeap experiment fitting. Nrf2 values are plotted in the graph for the cytoplasm (dashed line) and the nucleus (solid line). The experimental results are depicted by the traces with circular markers and the simulated results lack any markers. The r_3 parameter value is set to zero for the simulated result to mimic the siKeap in the experiment.

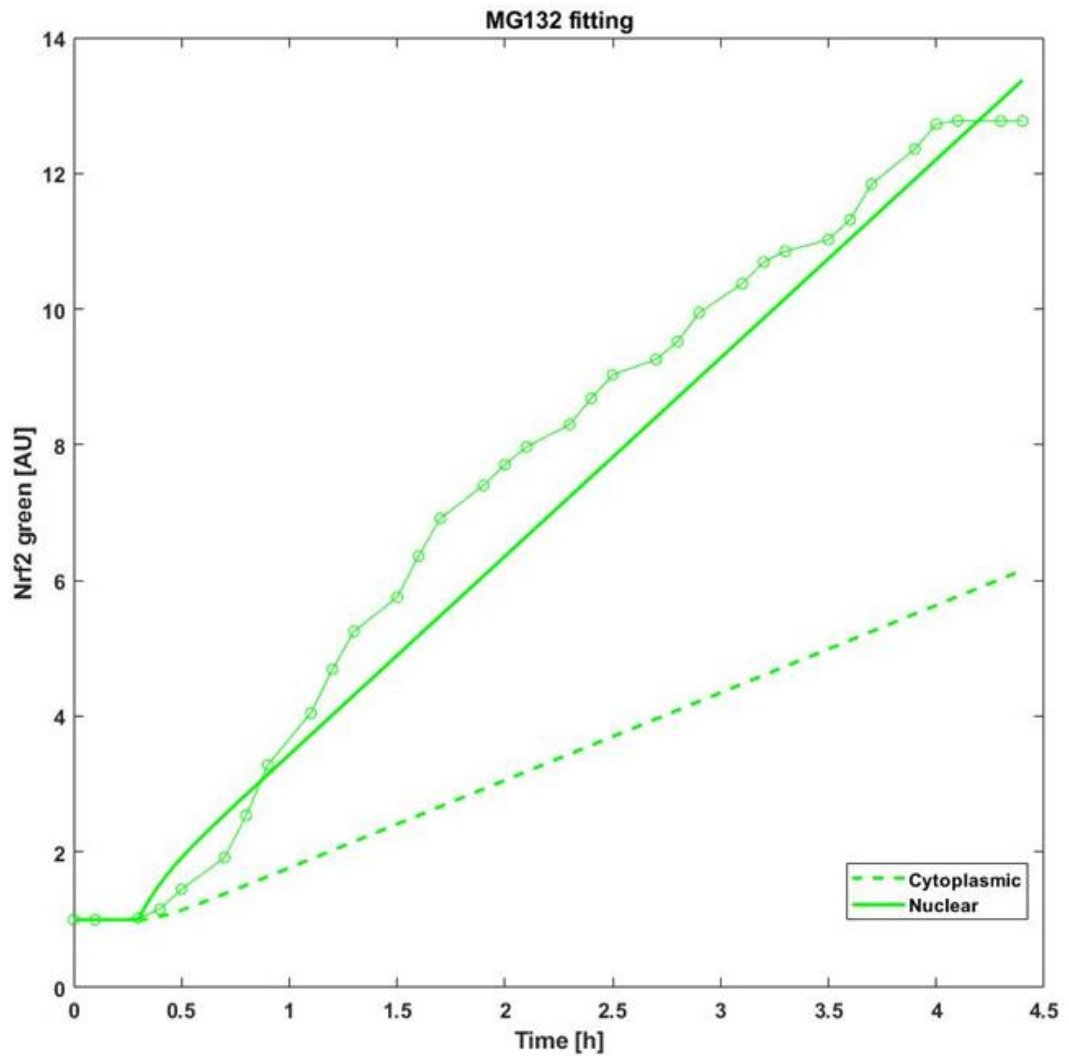


Figure 4-8. MG132 experiment fitting. Nrf2 values are plotted in the graph for the cytoplasm (dashed line) and the nucleus (solid line). The experimental results are depicted by the traces with circular markers and the simulated results lack any markers. The r_3 and r_5 parameter values are set to zero for the simulated result to mimic the effect of MG132 in the experiment.

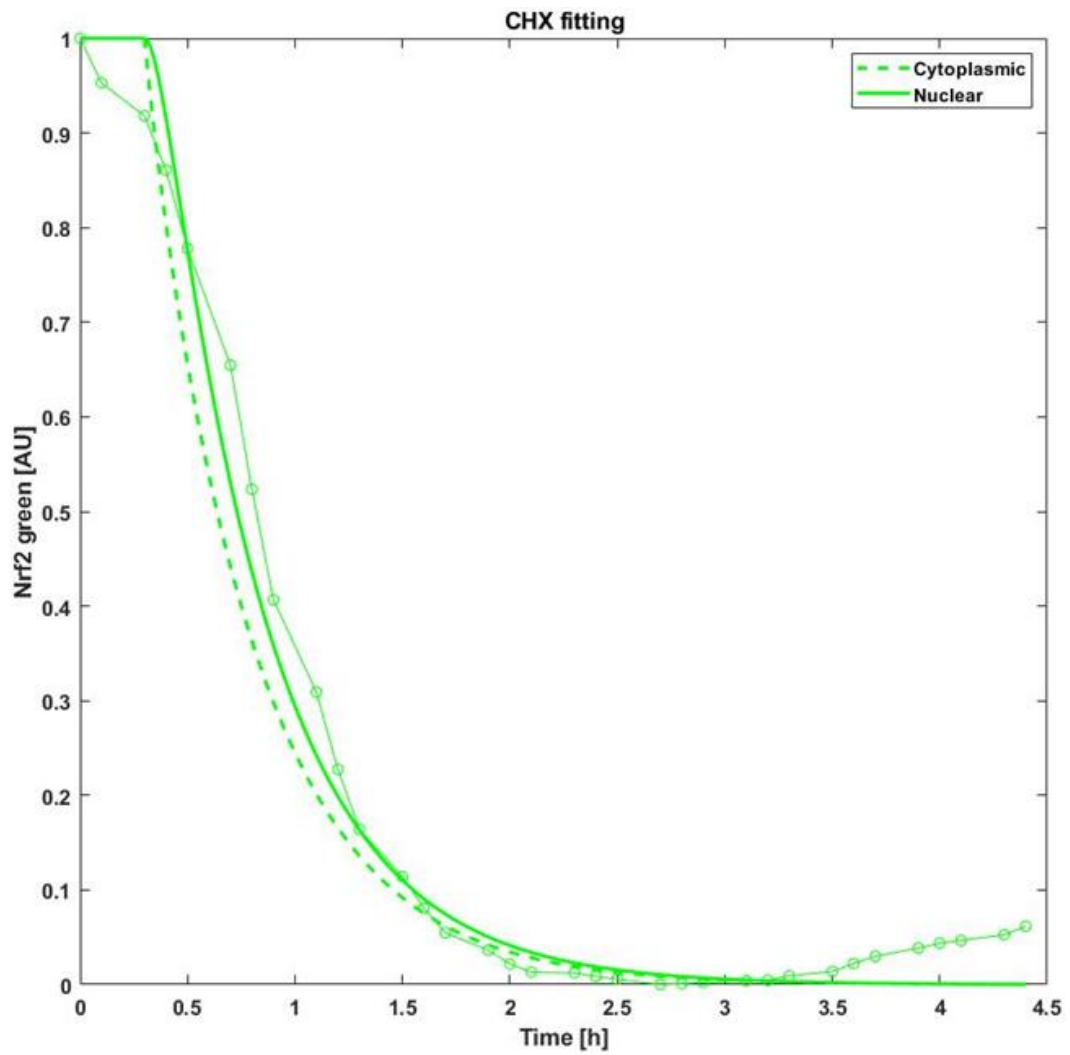


Figure 4-9. CHX experiment fitting. Nrf2 values are plotted in the graph for the cytoplasm (dashed line) and the nucleus (solid line). The experimental results are depicted by the traces with circular markers and the simulated results lack any markers. The r_4 parameter value is set to zero for the simulated result to mimic the effect of CHX in the experiment.

Rate ratios	Calculation	#14	#27	#53	
Nucleus influx/efflux	$\frac{r_2 G_c V_c}{r_1 G_n V_n}$	2.2664	2.8597	2.8281	
Relative cytoplasm/ nuclear decay	$\frac{V_c r_3 G_c}{(G_c + r_6)(V_n r_5 G_n)}$	BAC (stable)	4.7×10^{-4}	0.0132	7.83×10^{-10}
		pDendra (transient)	3.36×10^{-4}	0.0131	7.75×10^{-10}

Table 4-4. Characterisation of the key mechanisms of Nrf2 regulation in the cytoplasm and nucleus. Table showing the relative rate ratios for the nuclear influx/efflux and cytoplasm/nuclear decay for the three optimal parameter sets #14, #27 and #53. The rates produced for each of the cell types (BAC and pDendra) are also given.

4.4 Discussion

This chapter describes the development of an *in-silico* model of Nrf2-Keap1 interaction in the subcellular cytoplasmic and nuclear compartments. This model is validated through parameterisation and fitting of experimentally-derived data sets to provide key insights on associated mechanistic rate profiles of the proteins. Normalised data sets of Nrf2 expression in untreated cells and cells treated with siKeap, the proteasome inhibitor MG132 and the translational inhibitor CHX were used to inform the model. In order to establish the model, initial parameter values were obtained from the literature [269]. By taking appropriate ranges of values around these initial estimates and fitting against the data, optimised values were obtained for the seven model parameters. A sub group of our initial parameter sets were determined to be a good fit through comparison of goodness of fit R^2 values ($R^2 > 0.85$). These sub samples (Figures 4-9 – 4-11) were further analysed by plotting the initial parameter estimates against the optimised values. A trend from these plots appeared to suggest that some parameters are more sensitive to variation. Outliers from these sub samples increased the range for parameters r_3 , r_4 , r_6 and z leading to the conclusion that these parameters are less sensitive to initial input values. This trend continued in subsequent analysis wherein the parameter sets were compared against data for steady-state cytoplasmic-nuclear concentration derived from experimental analysis (personal communication). The parameter values from these three sets were compared in Table 4-3. Interestingly, the percentage difference between parameters for r_1 (nuclear export rate), r_2 (nuclear import rate) and r_5 (nuclear removal rate) are much smaller than the percentage difference for the other

parameter values across the three sets. These sensitive parameters have the same unit of 1/min (Table 4-2) and do not rely on concentrations as the other parameters do. This may indicate one of the reasons why they are more sensitive to perturbations within the model, as the experimental data provided was measured in arbitrary units instead of concentration i.e., normalised data sets were provided. Therefore, to resolve this problem and increase reliability in the model, the experimental data for these concentration dependent parameters needs to be measured in non-normalised units. However, the datasets provided were sufficient to answer the key rate questions (Table 4-4) proposed by the collaborators (Sanderson lab). Further comparison of Table 4-3 shows that one of the optimised parameter sets predicts a very large ratio of Nrf2 expression between the pDendra and BAC cells. It is unlikely that the Nrf2 expression would be 3 orders of magnitude greater from one cell type to the other. Therefore, the remaining two parameter sets were identified to be more appropriate. Simulation of the model results in a good fit to the data (Figure 4-6, 4-15, 4-16 & 4-17). However, Figure 4-14 and 4-15 exhibit a 'blip' in the experimental measurements at t=68h. This artefact is also present at the same time point in Figure 4-3 and 4-5. The reason for the presence of this 'blip' remains unclear and is most likely a result of a technical malfunction in the fluorescence equipment towards the end of the experiment. In addition, the optimisation and identification of these three parameter sets allowed us to evaluate the key rate profiles addressed in the conception of the model (Table 4-4). That is, the motivation for creating an *in-silico* model of the Nrf2 signalling pathway was to establish and quantify the translocation and removal rates of the Nrf2 protein, as this is difficult to determine experimentally due to the rapid half-life of Nrf2. The rates

produced by the model for the influx/efflux are tightly regulated across the three parameter sets. This could again be attributed to the calculation requiring those rates (r_1 and r_2) which were shown to be most sensitive to perturbations in the previous simulations and therefore have little variation across the three optimal parameter sets (Table 4-3). The relative rate ratio for the nuclear influx/efflux produced by the model shows that the rate of influx is over twice that of the efflux rate. A greater amount of Nrf2 is being imported into the nucleus than out meaning that Nrf2 accumulates in the nucleus. The other key ratio established by the model is the relative cytoplasmic/nuclear decay rate. There are two results provided for each parameter set as a result of the differing transfection methods for the pDendra and BAC cells, meaning different background Nrf2 production rates in the simulation. Both cell types produce rates showing a higher decay in the nucleus, which is appropriate given the previous result regarding the influx of Nrf2.

In summary, I have developed a novel *in-silico* model capable of simulating the Nrf2 signalling pathway and producing results that provide key insights into the relative transport rates into and out of the nucleus, based upon the experimental data sets provided. Reliability of the accuracy of the model can be improved through validation of the simulation output with the raw experimentally-derived data sets highlighting Nrf2 expression in differing cell types undergoing various treatments designed to perturb the system.

Chapter 5: Understanding Nrf2 and NF- κ B cross-talk using *in-silico* modelling

5.1 Introduction

5.1.1 Overview

In this chapter, a stochastic Petri net (PN) model is developed to describe the dynamical cross-talk behaviour of the Nrf2 – NF- κ B signalling pathways. In the previous chapter, an *in-silico* ODE model of the Nrf2 signalling pathway parameterised with experimentally-derived Nrf2 expression data was designed. Ideally, the same approach would be adopted for the creation of an extended Nrf2 model and encompass the NF- κ B pathway. However, there is a lack of experimental data available to parameterise this scale of ODE model for Nrf2 and NF- κ B. Therefore, the framework of this model design is to be reduced to be less dependent on parameters and more reliant on the overall topology of the signalling pathways and their interactions. Following this approach, the key components of the pathways, as well as their points of interaction, can be compiled into a Petri net model. PNs have been extensively used for simulating the dynamics of signalling networks (such as MAPK and EGFR) [277-279].

Both Nrf2 and NF- κ B pathways have been previously described in depth in section **Error! Reference source not found.** To recap, a brief description of the proteins and processes selected to represent the structure of this PN model from these pathways will be provided. For the Nrf2 pathway, the Keap1, cullin-3 and GSK-3 β proteins are included. During steady state conditions, the Nrf2 protein is initially bound to Keap1 in the cytoplasm before being marked for proteasomal degradation in combination with cullin-3 [215]. GSK-3 β performs a similar process of proteasomal degradation of Nrf2 within the nucleus [220]. However, when the system is perturbed in the model,

phosphorylation events inhibit both the Keap1 and GSK-3 β proteins allowing newly formed Nrf2 to translocate to the nucleus and transcribe cytoprotective genes (HO-1). For the NF- κ B pathway section of the PN model, the IKK and I κ B α proteins are included. During steady state conditions, the NF- κ B heterodimer is sequestered in the cytoplasm by association with I κ B α [232,235,236]. Perturbation of the system results in phosphorylation of the IKK α catalytic subunit which results in further downstream phosphorylation of the I κ B α protein, driving ubiquitination and proteasomal degradation, ultimately releasing NF- κ B into the cytoplasm [244]. Subsequently, NF- κ B translocates to the nucleus activating transcription of the pro-inflammatory and anti-inflammatory genes. Within the PN model, it is assumed that NF- κ B transcribes A20, I κ B α and Nrf2. Therefore, this transcription provides several negative feedback loops in the NF- κ B pathway branch of the PN model. It is also assumed that there are three points of interactions between the Nrf2 and NF- κ B pathways within the PN. The first assumption is that the product of Nrf2 transcription (HO-1) modifies NF- κ B, preventing it from translocating to the nucleus [224,251]. Secondly, it is assumed that NF- κ B transcription results in increased Nrf2 production [224,305]. Finally, it is assumed that the IKK protein is inhibited by Keap1 [224,252].

In the following section, simulations of the PN model are calibrated against experimentally-derived data of Nrf2 and NF- κ B expression, again provided by the Sanderson lab. In these experiments, Nrf2-Venus and p65-dsRED fluorescence were measured in BAC cells for Nrf2 and NF- κ B, respectively. Co-administration of CDDO and TNF α in these experiments initiate perturbations in the Nrf2 and NF- κ B pathways, respectively. Note that CDDO is an activator of the Nrf2 pathway [224] whereas TNF α is a potent activator of NF- κ B -mediated gene expression [240,241].

Once calibrated, the model is used to determine key characteristics about the dynamics of the signalling pathway and their cross-talk interactions. Understanding of these mechanisms is important as Nrf2 and NF- κ B have been shown to, for example, play a role in neurodegenerative disease. Nrf2 has been identified as a promising target in treating several neurodegenerative diseases, such as multiple sclerosis and Parkinson's disease [253]. Also, a review has indicated that NF- κ B plays a role in amyloid plaque accumulation in Alzheimer's disease [306]. This highlights the importance in understanding the interaction between these pathways and utilising this information to develop potential therapeutic targets.

5.1.2 Chapter aims

1. To create a Petri net model that accurately replicates observed NF- κ B dynamics and also includes the major Nrf2 pathway components with critical cross-over links.
2. To calibrate the initial PN simulations with the experimental data.
3. Use the PN model outputs to characterise the key mechanisms and dynamics of both signalling pathways and their cross-talk interactions.

5.2 Material & Methods

This chapter was completed in collaboration with the University of Liverpool and all experiments were again performed by Dr Jo Wardyn (Sanderson lab). The raw data generated from these experiments were used as the basis for calibrating the PN model. The imaging experiments conducted in this chapter are the same as those conducted for the data used in the previous chapter (Appendix B).

The Nrf2 and NF- κ B pathways and their interactions are modelled using a stochastic PN model. PNs model signal flow as the pattern of token accumulation and dissipation within places (proteins) over time. Transitions in the network represent directed protein interactions; each transition models the effect of a source protein on a target protein, transfection, production and decay. Through transition firings, the source can influence the number of tokens assigned to the target, called the token-count, thereby modelling the way that signals propagate through protein interactions in cellular signalling networks. In order to overcome the issue of modelling reaction rates in the network, signalling dynamics are simulated by executing the signalling Petri net (SPN) for a set number of steps (called runs), each time beginning from some initial marking. For each step, the individual signalling rates are simulated via generation of random orders of transition firings (interaction occurrences). The results of multiple runs are then averaged together. Note that the tokenized activity-levels computed by the PN method should be taken as abstract quantities whose changes over time correlate to changes that occur in the amounts of active proteins present in the cell. It is worth noting that some of the most widely used experimental techniques for protein quantification—western blots and

microarrays—also yield results that are treated as indications, but not exact measurements, of protein activity-levels within the cell. Similarly, the PN method is designed to operate on tokenized models of signalling networks with the ultimate intent of predicting the activity-level changes of proteins in the underlying signalling network over time. In the next sections, the core design decisions underlying the PN method are discussed, such as the signalling PN, transition firing, constructing the initial marking for the model, and sampling signalling rates, followed by a discussion on how the PN approach can be used to predict the outcome of perturbation experiments.

5.2.1 Stochastic Petri Net model

In Figure 5-1, the PN for the Nrf2-NF- κ B model (described in overview above) is depicted. The PN model was built using a unifying PN tool called Snoopy [307]. The classical PN is a directed bipartite graph [274]. The two types of nodes are called *places* and *transitions*. In a PN, places and transitions are connected via *arcs*. Places are graphically represented by circles, transitions by boxes or bars. Places can store *tokens*, represented by black dots or numbers. A distribution of tokens on the places of a net is called a *marking*, and corresponds to the “state” of the PN (m_t is used to denote the marking of a PN at time t). A transition of a net is *enabled* at a marking if all its input places (the places from which some arc leads to it) contain at least one token. An enabled transition can fire: it then removes one token from each of the input places, and then adds one token to each of its output places. This is called the *firing rule*. For example, when a signalling interaction $A \rightarrow B$ (A activates B) occurs, it has the effect of changing the activity level of A and/or B. Thus the associated

transition will fire at time, t , and produce a marking m_{t+1} from m . When this transition fires, some number of tokens are moved from place A to place B via an arc. In a single time block every enabled transition fires once exactly. The order of the firing sequence is chosen randomly and changes for each time block. Therefore, within each time block all transitions are evaluated once, though not necessarily in the same order [308]. Since the rate parameters are not known, many simulation runs are executed to sample the space of possible outcomes and markings returned by these runs are averaged. The initial marking for the system is constructed on the assumption that the system is in an initial basal state until acted upon by an external stimulus. The basal initial state is a distribution of activation levels when the cell has no impulses propagating through it. For this reason, the model is run to a steady state before perturbations are executed. Assigning the correct number of tokens to each place as an initial condition to get to this basal state was the main challenge of constructing the model. Tests were performed to assess the effect of differing token values for each place (protein), ranging from 1-100 tokens. It was found that 10-20 tokens, for Nrf2, Keap1, Cullin-3, GSK-3 β , pFyn, IKK and I κ B, were sufficient to replicate the results observed *in-vitro*. The accuracy and performance of the method was tested by simulating the activation of NF- κ B and Nrf2 simultaneously, and compared the outputs to the experimentally derived data provided by the Sanderson lab.

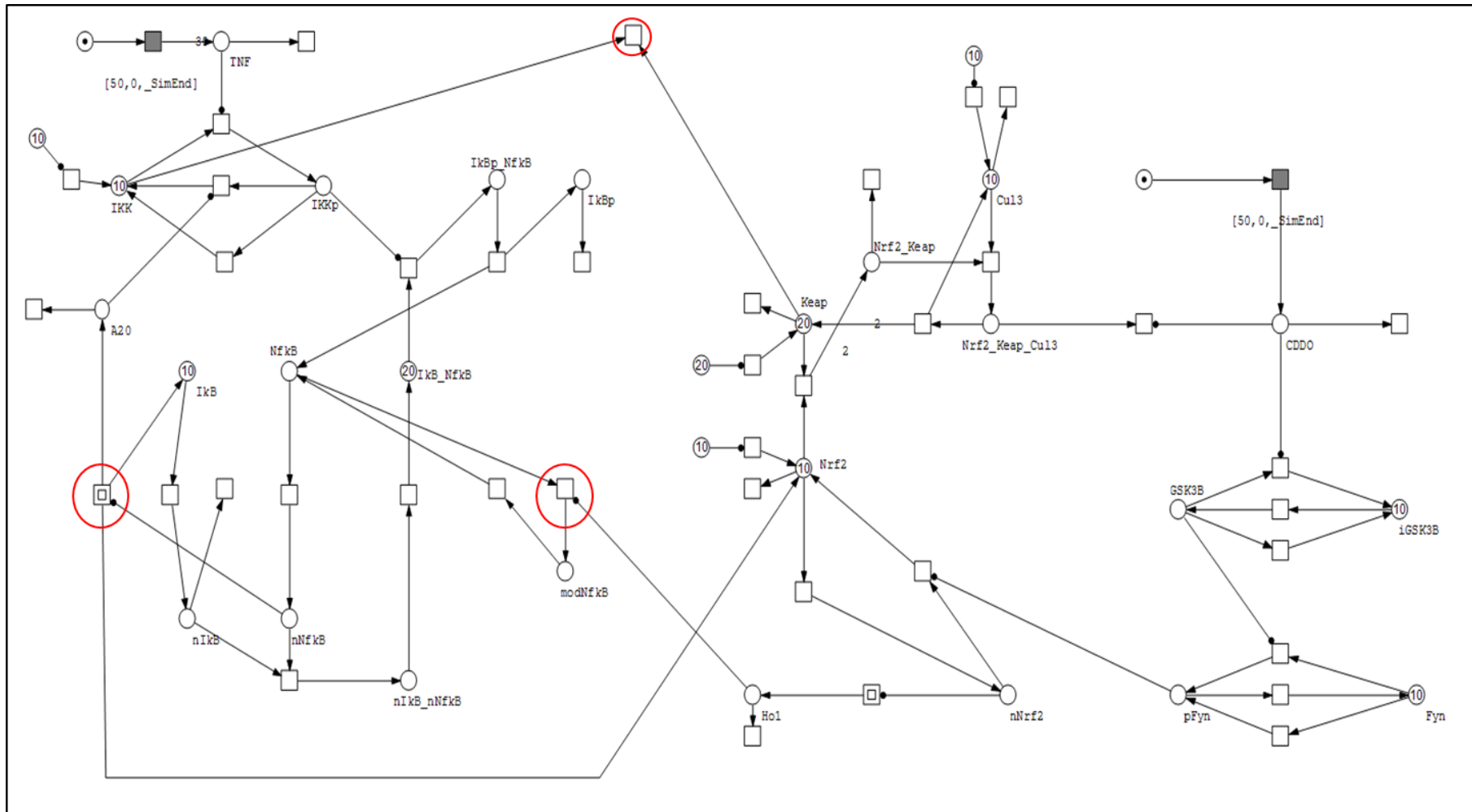


Figure 5-1. The Petri Net model. Schematic outlay of the PN model. The model contains the Nrf2 and NF-κB pathways and the interactions between both indicated by red circles (nNF-κB/Nrf2, Keap1/IKK, HO-1/NF-κB).

5.3 Results

To simulate the effects of TNF α and CDDO in the PN model, the firing of two time delayed places (both shown on the signalling network in Figure 5-1 in shaded squares) were used. These perturbations are set to occur 50 time units (AU) in order to allow the simulated system to reach a steady state before the perturbation takes place. The PN model has been minimised to only include functional parts, i.e. downstream proteins that do not provide feedback or alter the overall outcome of the pathway activation are omitted for clarity. The inclusion and omission of pathway components was decided through reading literature detailing the workings of both pathways. For further readability, Figure 5-2 shows the PN model as a simplified schematic diagram of both the Nrf2 (green) and NF- κ B (red) pathways with some minor components removed, such as pFyn and intermediary states of activated/inactivated proteins. Three points were chosen to demonstrate the cross-talk between both pathways. These three components are: 1) Nrf2 gene transcription modifies NF- κ B preventing it from translocating into the nucleus [224,251], 2) NF- κ B gene transcription of Nrf2 [224,305] and 3) Keap1 mediated inhibition of IKK [224,252]. In order to evaluate the accuracy of the stochastic model and these three cross points, the model simulation output was tested against the experimental data results (Figure 5-3).

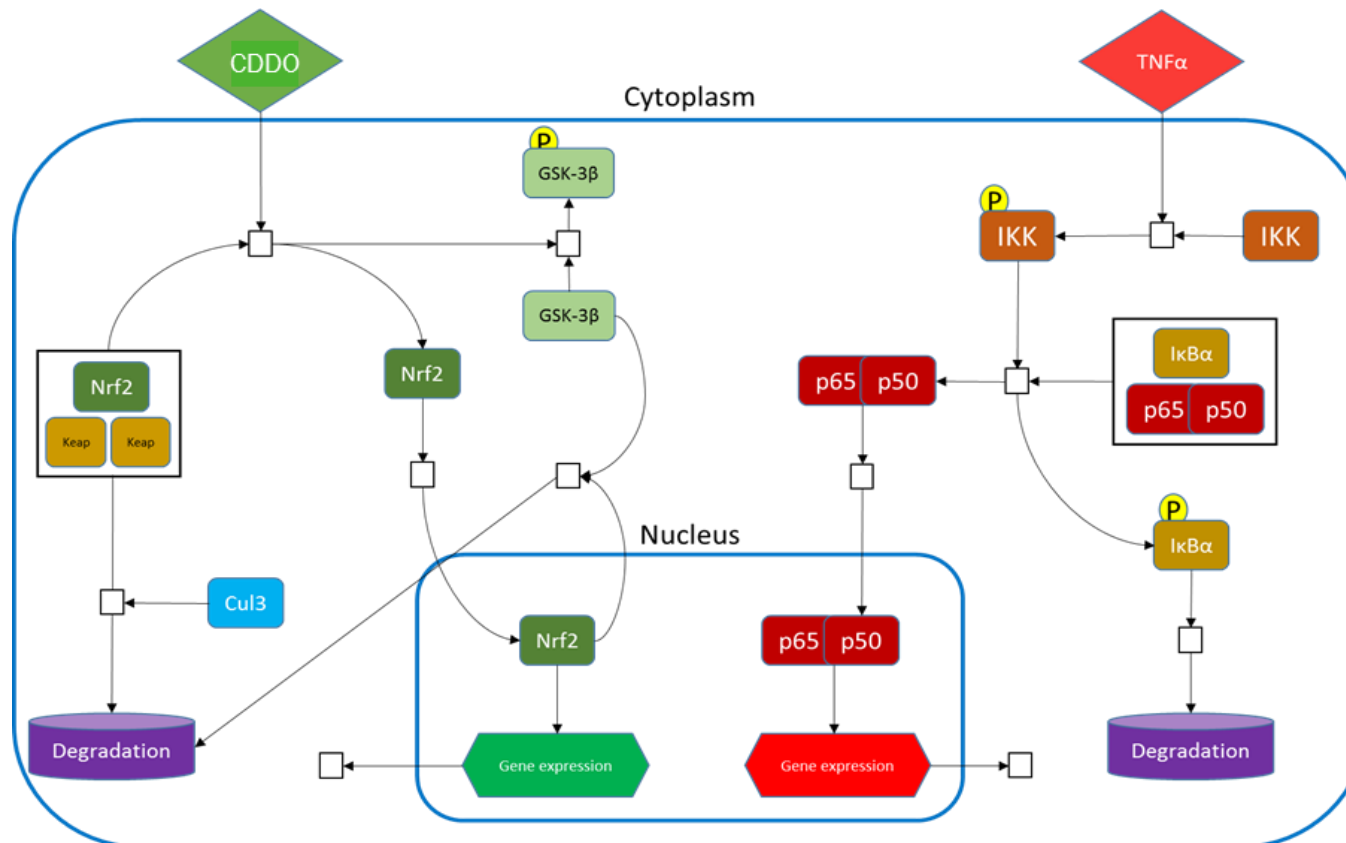


Figure 5-2. Diagram showing key elements of the Petri Net model. Schematic outlay of the PN model. The minimal Nrf2 pathway is shown in green. Nrf2 is initially bound to Keap1 (Keap) and marked and degraded in combination with Cullin-3 (Cul 3). CDDO perturbs the system releasing Nrf2, where it translocates to the nucleus activating transcription. GSK-3 β removes Nrf2 from the nucleus as the effects of CDDO decay. The NF- κ B (p65/50) pathway is shown in red. NF- κ B is initially inhibited by I κ B α . Similarly, perturbation by TNF α releases NF- κ B into the cytoplasm, where it translocates to the nucleus activating transcription. Phosphorylation events are indicated by P.

5.3.1 Validation of PN model against experimental results

CDDO activates the Nrf2 pathway and mimics the effect of the cells response to oxidative stress. The introduction of CDDO *in-vitro* results in an increased peak of Nrf2 activity followed by smaller damped oscillations before returning to a steady state level (Figure 5-3A). Mimicking this perturbation in the PN model, NF- κ B activity increases, in response to the administration of TNF α , giving off a singular large peak followed by several smaller damped oscillations before returning to its original steady state level (Figure 5-3B). When a transition is fired in the model there is an increase in the activity of both NF- κ B and Nrf2 levels followed by smaller peaks and a return to a base line level. It is known from the literature that these oscillations are present in the pathways, ultimately being used to control expression of the target genes [309]. This validation gives us confidence that the regulatory mechanisms encoded in the structure of the PN, informed by pathway information in the literature, are well suited to simulate the dynamics observed experimentally, consistent with expected oscillatory response of these signalling pathways. To add a quantitative element to the results, the time units were converted from arbitrary units to hours. This was achieved by matching the first peak of the NF- κ B trace in Figure 5-3A with the subsequent peak in the simulated result (Figure 5-3B). The same conversion of time units in the PN is used in all subsequent simulations. The levels of NF- κ B were altered in the PN model by changing the multiplicity on the relevant arcs (NF- κ B \rightarrow nNF- κ B) to 2- and 4-fold the amount of tokens transferred. These changes were made to assess if the oscillatory behaviour shown by Nrf2 was driven by NF- κ B.

All 3 Nrf2 runs were plotted on the same graph for comparison (Figure 5-4). The original values were plotted in blue, the 2-fold NF- κ B increase was plotted in red and the 4-fold increase was plotted in yellow. The corresponding NF- κ B traces are also shown in Figure 5-4B. In the original Nrf2 trace, the initial peak is approximately 9 arbitrary units high. This initial peak then increases to approximately 16 and 25 arbitrary units respectively when NF- κ B is doubled and quadrupled, respectively. Increasing NF- κ B results in larger and smoother oscillations in the Nrf2 trace, suggesting it could play a part in the overall oscillatory behaviour of the Nrf2 protein. It is expected that Nrf2 would increase as NF- κ B increases, as NF- κ B transcribes the Nrf2 protein.

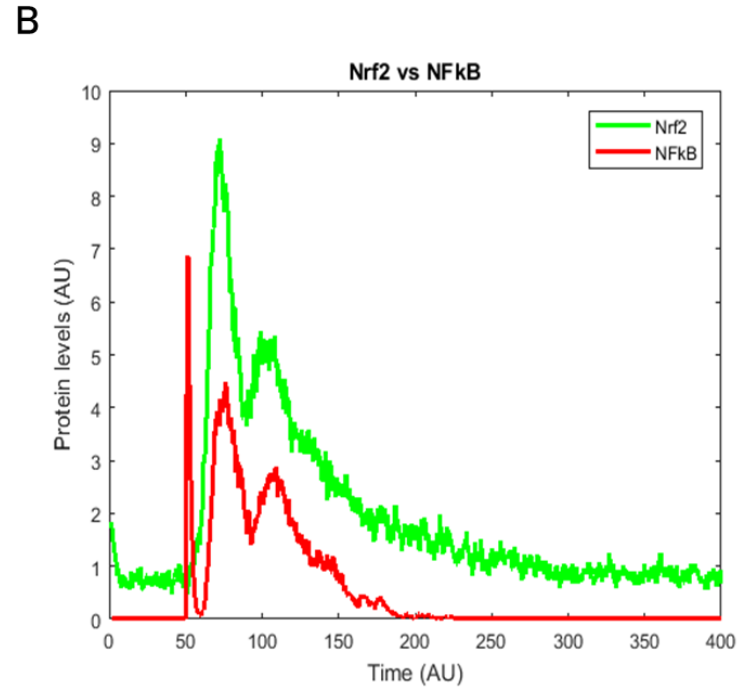
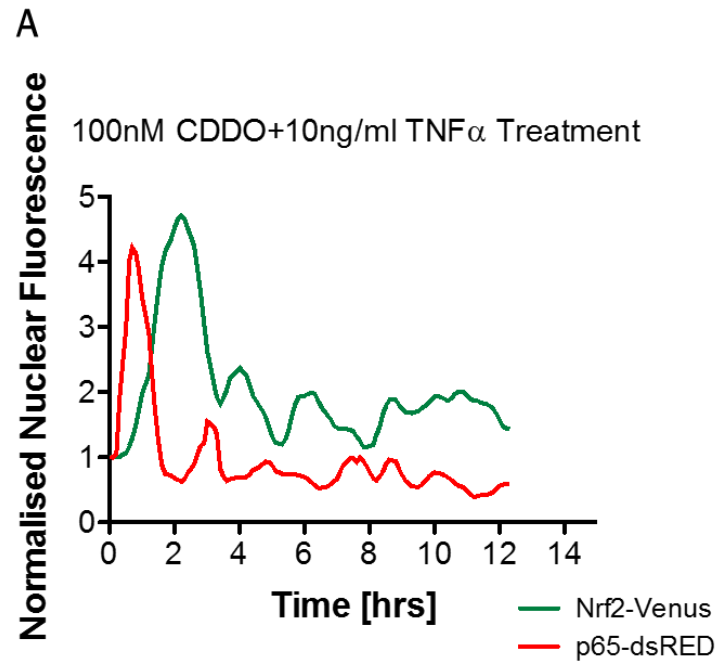


Figure 5-3. Qualitative validation of the Petri net model through comparison of experimental vs simulated data. (A) Co-administration of CDDO and TNF α in BAC cells expressing p65-dsRED. Peaks in p65 (NF- κ B) nuclear levels (red) induce subsequent Nrf2 (green) accumulation. (B) Co-stimulation of CDDO-Me and TNF α by the model produce peaks in NF- κ B levels that also lead to Nrf2 accumulation. The PN qualitatively represents Nrf2/NF- κ B dynamics.

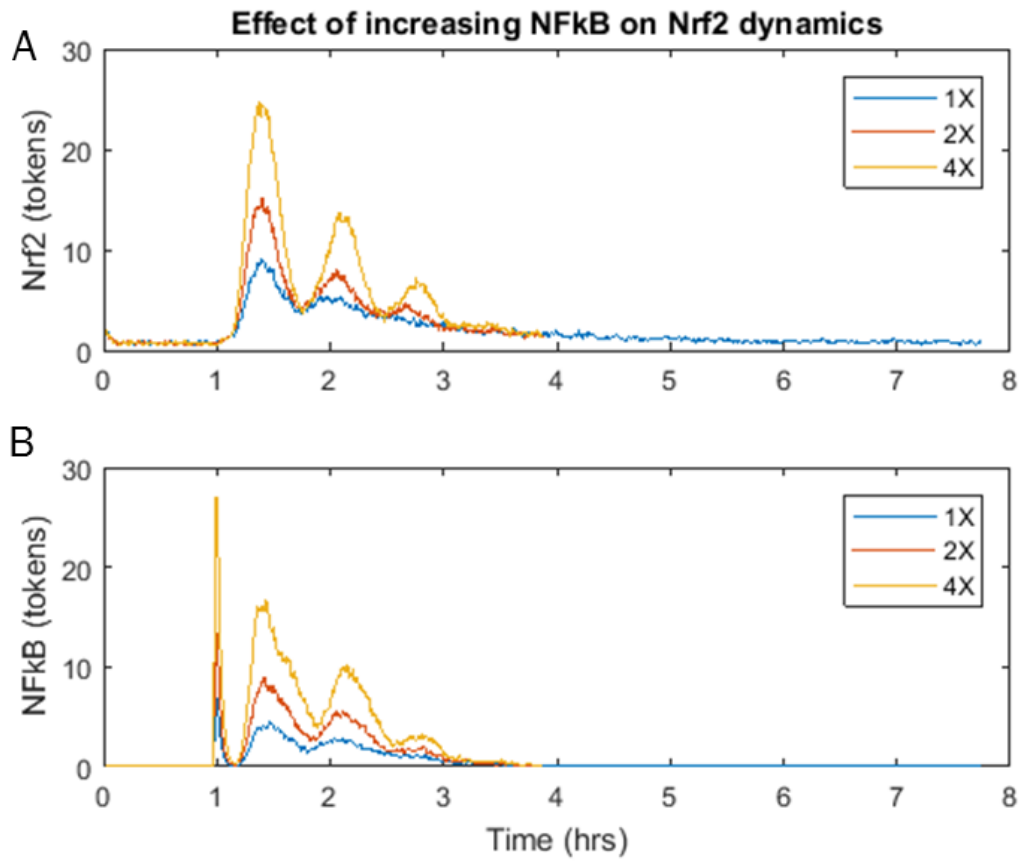


Figure 5-4. High levels of NF-κB expression promote oscillatory behaviour in Nrf2. (A) Plot showing Nrf2 levels when NF-κB is background (blue), increased 2-fold (red) and increased 4-fold (yellow). (B) Plot showing NF-κB levels when NF-κB is background (blue), increased 2-fold (red) and increased 4-fold (yellow).

5.3.2 Characterisation of the dynamics of the pathways

One of the biggest limiting factors in the Nrf2 pathway is Keap1 [211]. Therefore, it is important to show the effect of Keap1 on the dynamics of the model. The initial level of Keap1 in the original simulation (Figure 5-3B) was 20 tokens. To showcase the effect of Keap1 on Nrf2 activity, the initial amount of Keap1 was altered across a 3-fold range (0-3) and plotted against the resulting maximal peak of Nrf2 (Figure 5-5). The obvious trend shown from the results is that a decrease in Keap1 leads to an increase in Nrf2 and vice-versa. More specifically, a 2-fold increase in Keap1 causes an approximately 90% reduction in Nrf2 whereas half the initial amount of Keap1 results in approximately 1.5 times more Nrf2 protein.

Next, the model is modified to answer key questions about the mechanisms of the coupled signalling pathways. The key questions to be addressed are as follows: (1) what effect does an increase in Keap1 due to the CDDO have on Nrf2 and NF- κ B? (2) What effect does an increase of Keap1 due to transcriptional activity have on Nrf2 and NF- κ B? (3) What effect does an increase in cullin-3 due to transcriptional activity have on Nrf2 and NF- κ B? (4) What effect does decreasing A20 have on Nrf2 and NF- κ B? (5) Is there an upper threshold limit of Nrf2 concentration in the model? (6) What is the effect on Nrf2 if GSK-3 β plays a role in nuclear decay or acts as a nuclear exporter?

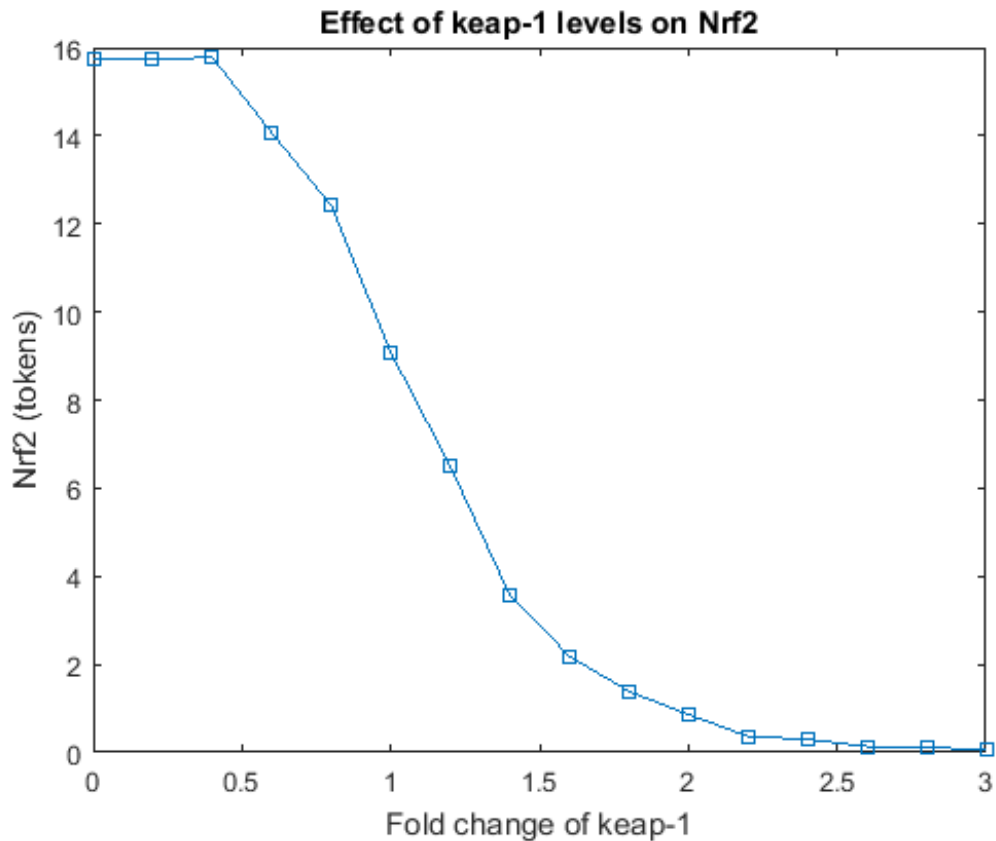


Figure 5-5. Changing Keap1 levels alter network dynamics. Decrease in the representative peak number of Nrf2 tokens when initial Keap1 token levels are increased.

Figure 5-6 shows the results of increasing Keap1 through varying CDDO activity. The goal in this simulation is to show how any dynamical changes in the system are affected by an external increase in Keap1. This result was achieved by adding an edge between Keap1 and CDDO, within the model, and increasing the multiplicity of tokens from one- to eight-fold. Biologically, this would represent increased transcription of Keap1. Figure 5-6A shows the Nrf2 trace as Keap1 is increased. As the amount of Keap1 increases, the overall level of Nrf2 activity decreases. At normal background Keap1 levels, the number of Nrf2 tokens at the maximal peak is

approximately 9 tokens compared with 5 tokens when Keap1 is at an eight-fold increase. Figure 5-6B displays the NF- κ B trace for each fold increase of Keap1. There is very little difference in NF- κ B activity as the Keap1 is increased, as expected.

In contrast, when Keap1 is increased via transcription, rather than via CDDO, there is very little difference between the Nrf2 activity (Figure 5-7A) and NF- κ B activity (Figure 5-7B) for any of the Keap1 fold increases. This result was achieved in a similar way to Figure 5-6, i.e. an extra arc was added from nuclear Nrf2 to Keap1 and the multiplicity changed from one-fold to eight-fold. Again, biologically this would represent increased transcription of the Keap1 protein. This corresponding Keap1 trace is shown in Figure 5-7C. This result is again reiterated in Figure 5-8. When cullin-3 levels are increased through the addition of an arc between nuclear Nrf2 and the cullin-3 place, there is very little change in the activity levels for Nrf2 (Figure 5-8A) and NF- κ B (Figure 5-8B).

A20 was decreased to observe the effect it has on the Nrf2 and NF- κ B traces (Figure 5-9). Again, this was achieved by altering the multiplicity on the arc (A20 \rightarrow IKK) to 50% and 25% of its initial value (Figure 5-9C). This decrease had relatively more effect on the Nrf2 trace (Figure 5-9A) than the NF- κ B trace (Figure 5-9B). For example, when the amount of A20 was reduced to a quarter there was a subsequent decrease of ~25% in the Nrf2 trace (Figure 5-9 – yellow).

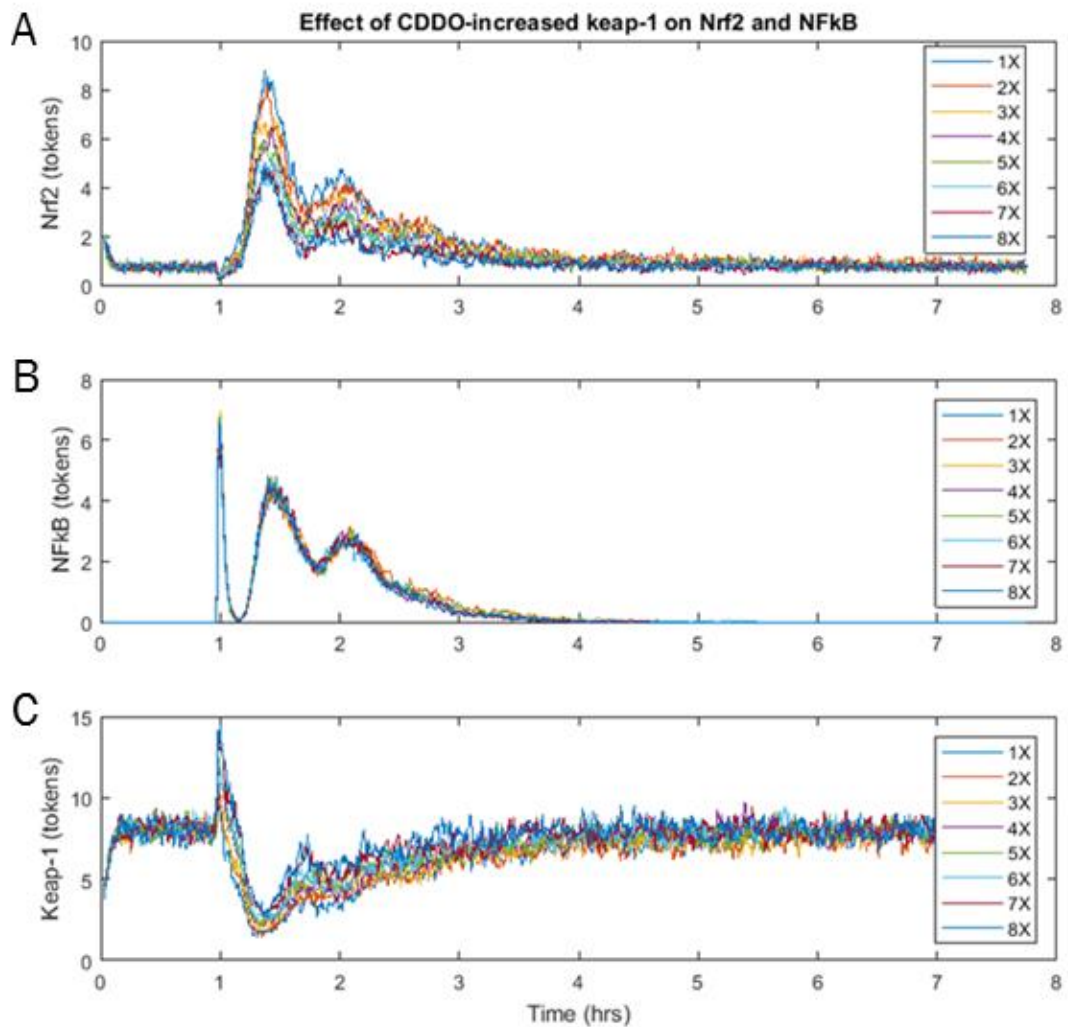


Figure 5-6. Effect of CDDO-increased Keap1 on Nrf2 and NF- κ B. (A) Simulated plot showing Nrf2 levels in response to the increasing fold change of CDDO on Keap1. (B) Simulated plot showing NF- κ B levels in response to this change. (C) Plot showing Keap1 traces for each fold change.

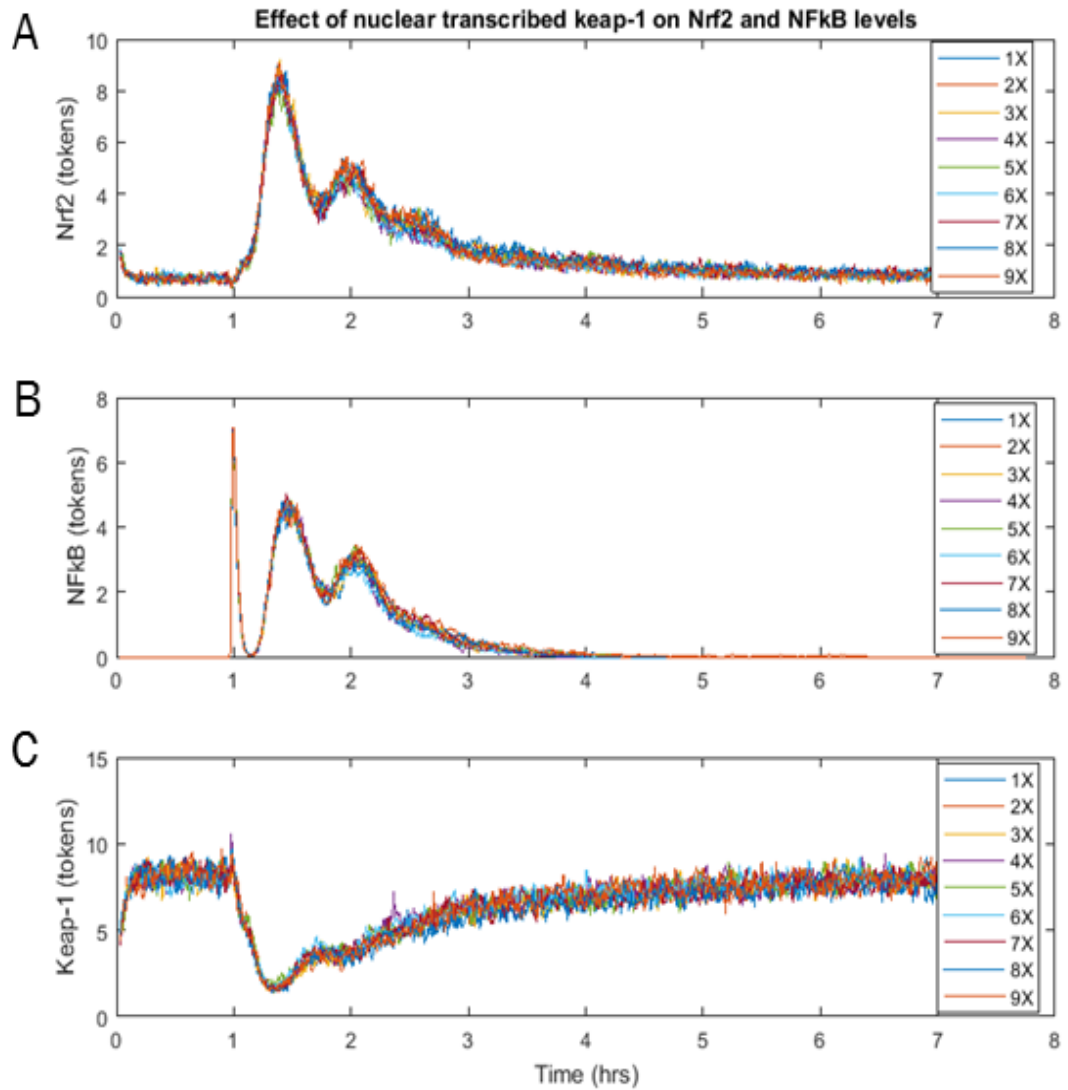


Figure 5-7. Effect of transcribed Keap1 on Nrf2 and NF-κB. (A) Simulated plot showing Nrf2 levels in response to the increased fold change of transcriptionally produced Keap1. (B) Simulated plot showing NF-κB levels in response to this increase. (C) Plot showing Keap1 traces for each fold change.

Another key question that was proposed involves whether or not an upper limit exists for Nrf2 activity. As CDDO is used as an Nrf2 activator, the initial number of tokens in this place were increased up to 200-fold, representing an increase in the transcription of Nrf2 protein (Figure 5-10). The Nrf2 trace remains relatively unchanged when CDDO is increased up to ten-fold (Figure 5-10 – light blue, Figure 5-10 – orange). However, for the twenty-fold trace (Figure 5-10 – yellow) the Nrf2 token count for the maximal peak increases to 13 tokens from 9 tokens. This threshold is maintained for all the following fold changes in CDDO with only the time taken for each trace to return to steady state increasing.

Another feature of the model is the delayed response of GSK-3 β in the removal of Nrf2 from the nucleus. The model was designed to include the GSK-3 β -mediated response as a nuclear exporter of Nrf2 (Figure 5-11 - blue) or as a decaying factor of Nrf2 (Figure 5-11 - red). The decay rate of both was plotted against the peak level of cytoplasmic Nrf2 (Figure 5-11). As an exporter, GSK-3 β maintains an Nrf2 peak between 8 and 10 arbitrary units across a range of decay rates. In contrast, as an agent of decay, the GSK-3 β maintains a lower threshold of Nrf2 activity (4 -6 AU). In Figure 5-11B, the corresponding nuclear Nrf2 levels were plotted. This plot shows that GSK-3 β has a much greater effect on the nuclear Nrf2 levels than on cytoplasmic Nrf2. The level of Nrf2 increases in both circumstances, as the rate at which GSK-3 β exports (Figure 5-11B –red) and decays (Figure 5-11B – blue) nuclear Nrf2 decreases.

At the lowest rate, the number of tokens has increased 5-fold for the export trace and 7-fold for the decay trace.

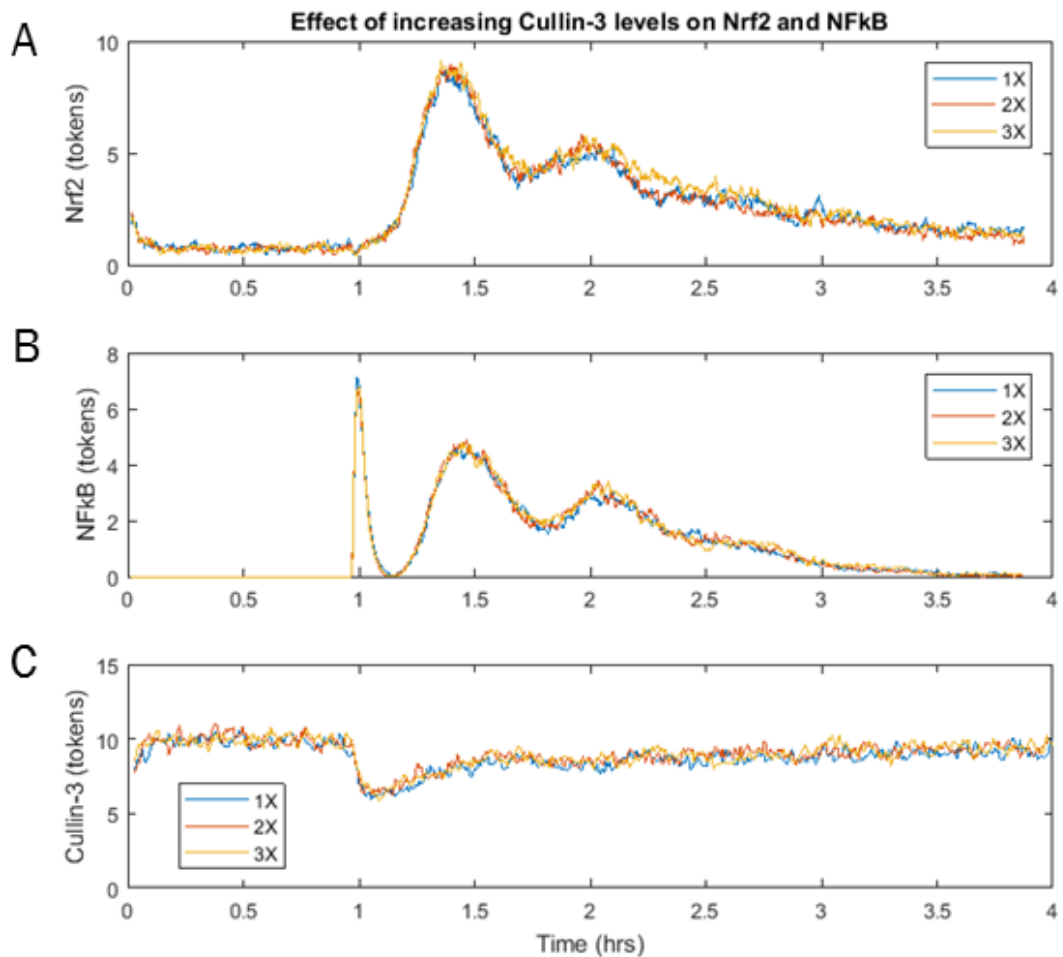


Figure 5-8. Effect of transcribed cullin-3 on Nrf2 and NF- κ B. (A) Simulated plot showing Nrf2 levels in response to the increase of the Nrf2-dependent transcription rate of cullin-3. (B) Simulated plot showing NF- κ B levels in response to this increase. (C) Plot showing cullin-3 traces for each fold change.

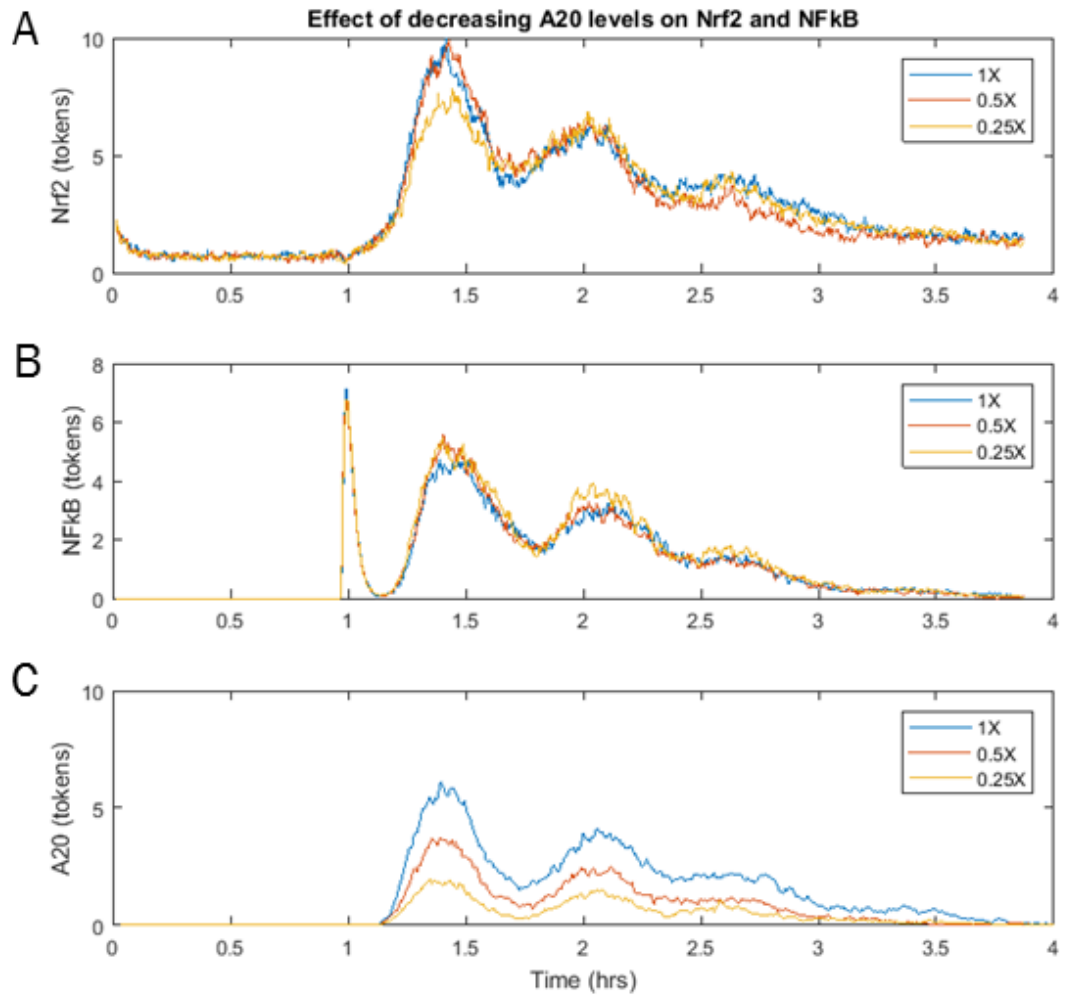


Figure 5-9. Effect of decreased A20 on Nrf2 and NF-κB. (A) Simulated plot showing Nrf2 levels in response to a decrease in A20. (B) Simulated plot showing NF-κB levels in response to a decrease in A20. (C) Plot showing corresponding A20 traces.

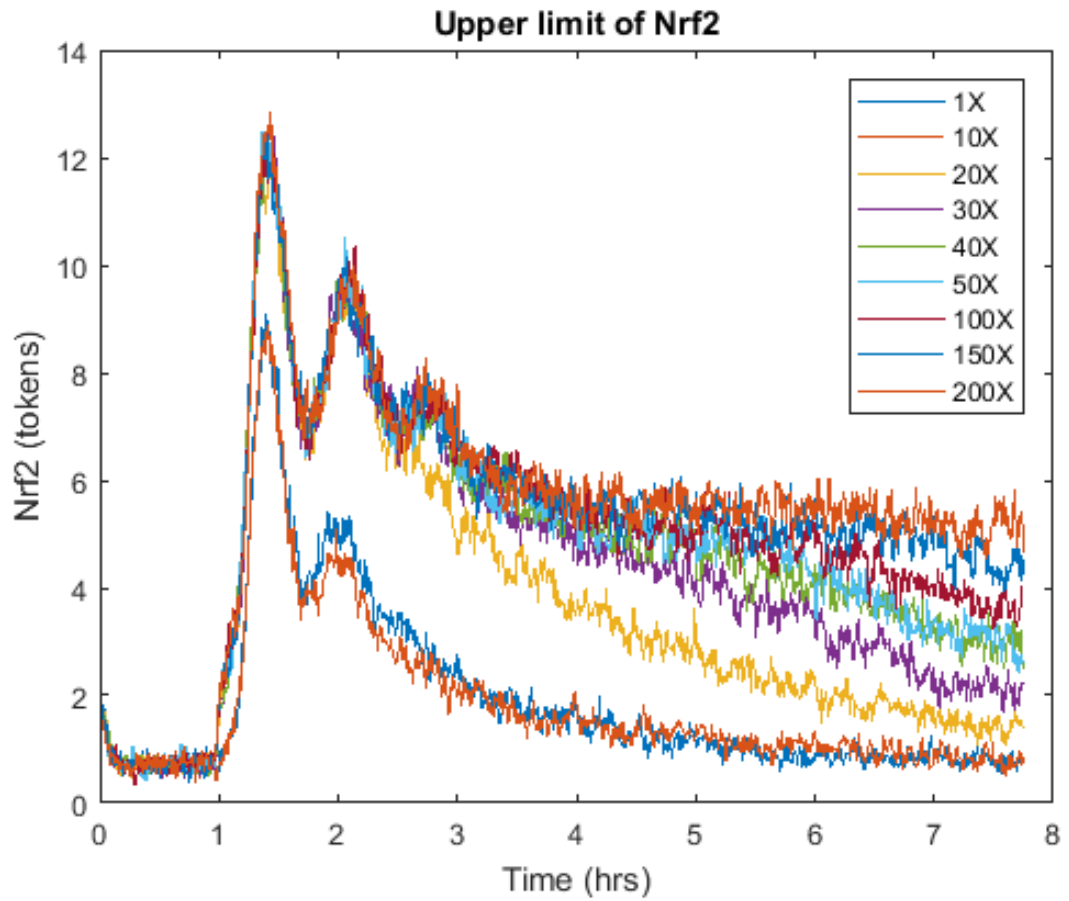


Figure 5-10. Upper limit of Nrf2. Plot showing Nrf2 activity against time for CDDO fold changes in the range x1 – x200.

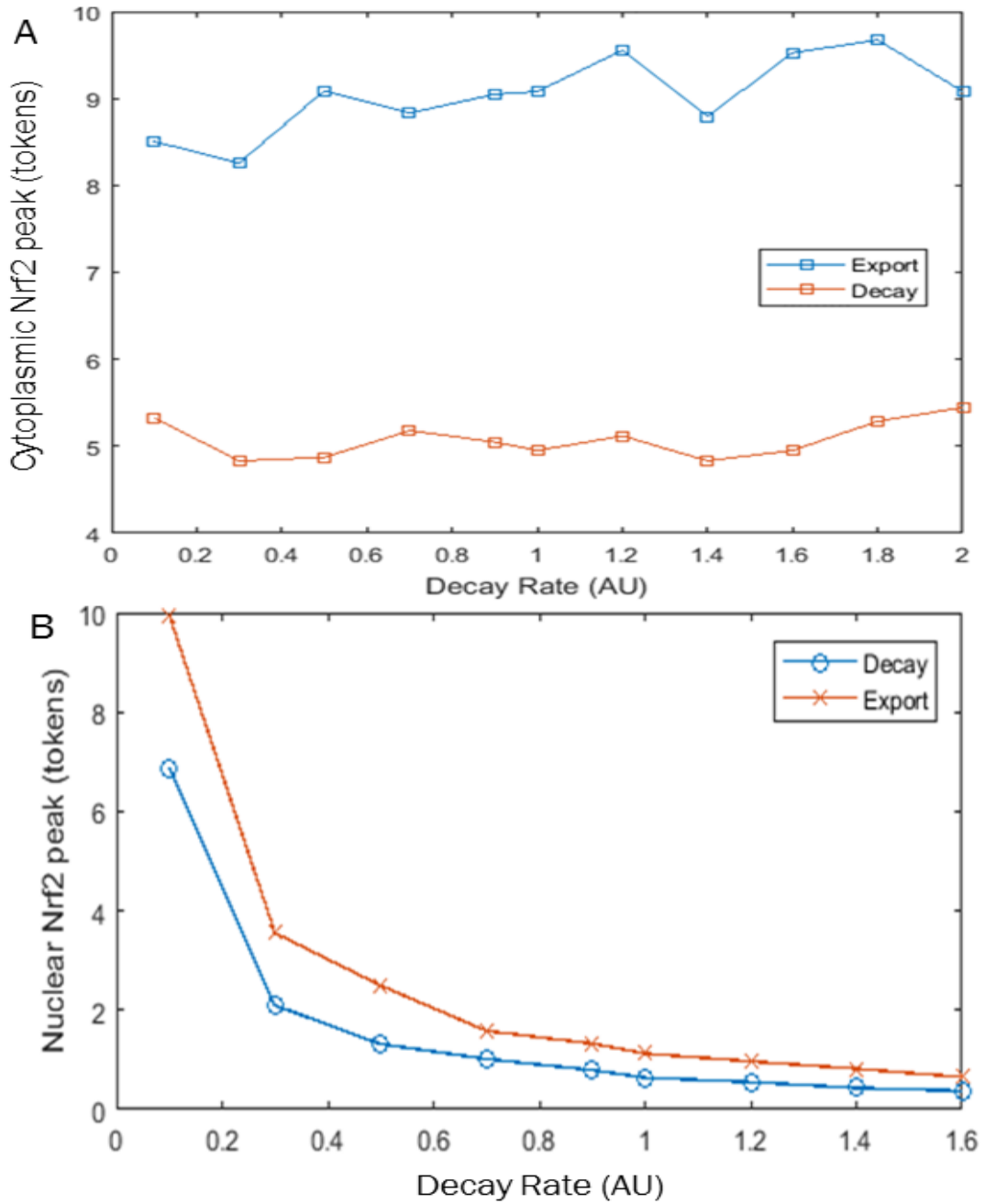


Figure 5-11. Effect of GSK-3 β -mediated nuclear export and nuclear decay. (A) Simulated plot showing cytoplasmic Nrf2 levels after the addition of nuclear export (blue) and decay (red). (B) Simulated plot showing nuclear Nrf2 levels after the addition of nuclear export (red) and decay (blue).

5.4 Discussion

In this chapter, a Petri net-based method that qualitatively predicts the dynamics between the Nrf2 and NF- κ B pathways is described. Once the scheduled transition fires in the model, representing the activation of the signalling pathway (Nrf2 and NF- κ B), there is a rapid increase in Nrf2 before both Nrf2 and NF- κ B display damped oscillations that tend towards a steady state. This result mimics the outcome of the observed experimental behaviour (Figure 5-3). It has been noted that this oscillatory behaviour is a hallmark of the interaction of these pathways and it is suggested that this is driven by NF- κ B [309]. Capturing this key known feature present in these pathways is important for showing the reliability of the model. However, the lack of replicates in the datasets provided introduces uncertainty in the results. Therefore, integration of the PN model with more datasets would be the next logical step in the progression of this work. Despite this, the PN model captures the dynamics we would expect to see in these pathways. Figure 5-4 shows the effect of increasing NF- κ B levels on the system. It is clear to see that larger, smoother oscillations of Nrf2 are produced when NF- κ B is elevated. For lower values of NF- κ B, a singular peak is observed in the Nrf2 trace (Figure 5-4, blue). There are two and three peaks observed respectively when NF- κ B is doubled (Figure 5-4, red) and quadrupled (Figure 5-4, yellow), respectively. Also, the ratio between both proteins (Nrf2: NF- κ B) during these NF- κ B changes is maintained. Therefore, the PN model adds weight to the hypothesis that NF- κ B drives Nrf2 dynamics. The biggest limiting factor in the Nrf2

pathway is the presence of Keap1 [211]. Therefore, Keap1 levels were varied in the *in-silico* model to observe the effect on the Nrf2 levels (Figure 5-5). The simulations conclude that increasing Keap1 levels leads to a decrease in Nrf2 activity and, conversely, a decrease in Keap1 levels give rise to higher amounts of Nrf2. Thus, Keap1 is indeed crucial in the maintenance of Nrf2 levels and acts as the dominant mechanism of decay in this model. Additionally, Keap1 has a basal production and decay rate which maintains it at a constant level. It quickly reaches a steady state and only subsequently changes when CDDO perturbs the system and it becomes sequestered in an Nrf2 complex. In Figure 5-6 and 5-7, the model explores what would happen when there is an addition of an extra source of Keap1. In Figure 5-6, Keap1 levels are altered by varying the amount of CDDO added. This leads to modest decreases in cytoplasmic Nrf2 levels as Keap1 is more readily available, as shown in Figure 5-6C. However, in Figure 5-7, when instead Keap1 has an additional source via transcription, the overall levels of Nrf2 and Keap1 remain relatively unchanged. A possible explanation for this difference may be that, once CDDO perturbs the system, it becomes the dominant mechanism and overpowers any response from the transcription of Keap1, which is a much slower process. Similar conclusions can be drawn from the cullin-3 results (Figure 5-8), and again, a comparable trend can be observed in the traces of Nrf2 and NF- κ B when changing A20 levels (Figure 5-9). This can be partially explained by the time delay of sending tokens through the transcription pathways. This time delay represents the period between gene activation and protein formation within the cell. As the rate of A20 is decreased, in

the PN model, the level of Nrf2 also slightly decreases. This change is not large enough to draw any conclusions from and is most likely due to noise of the system. The next question proposed to the model was whether or not it can replicate an upper limit of Nrf2. In Figure 5-10, it can be clearly seen that from a 20-fold to 200-fold increase of CDDO activity the level of Nrf2 reaches an upper limit. It would therefore seem that the dynamical behaviour of the model does not allow for an unchecked increase of Nrf2 and that Nrf2 does indeed have an upper limit. Another consideration in the design of the PN model was whether to include a nuclear exporter or nuclear decay via the GSK-3 β pathway. It has been shown in the literature that GSK-3 β degrades the Nrf2 protein in the nucleus [310]. Therefore, this GSK-3 β mediated decay (Figure 5-11A) results in the decrease of cytoplasmic Nrf2 levels. However, the level of Nrf2 remains constant as the amount of decay changes. This suggests that there is an upper limit on the amount of cytoplasmic Nrf2 that is susceptible to a decay pathway in the nucleus. The decay transition was then removed and GSK-3 β -mediated nuclear export was introduced to the model. In Figure 5-11B, the same conditions were applied and the nuclear Nrf2 traces were plotted. These results showed that there is an increase in Nrf2 levels within the nucleus when the rate of GSK-3 β activity is decreased. As with the cytoplasmic values, the export trace has a higher value than the decay trace. We observe that there is very little variability in Nrf2 activity upon the addition of an export transition. This suggests that the inclusion of the nuclear export is more appropriate as it upholds the network dynamics as observed experimentally (Figure 5-3).

Despite the complexity of the network dynamics, it was straightforward to find and integrate the connectivity information to build the model. However, although the information sources [210,224,232,236] provided information on existing pathways, little was offered in the way of biochemical or kinetic detail. Thus, it is difficult to use the evidence in the literature to assemble a parameterised ODE model. This further underlies the advantage of using the PN model as a way of quickly characterising the network dynamics of the pathways without the need for extensive model parameterisation.

Although the predictions derived from the PN model may not be as quantitative as results returned from a parameterized ODE system, biologists using the PN method can derive information about a network's qualitative dynamical behaviour without having to conduct extensive experimentation and computationally expensive parameter estimation. This novel capability offers scientists the exciting prospect of being able to test hypotheses regarding signal propagation *in-silico*. Furthermore, by using the PN method, researchers can evaluate a wide array of network responses in order to determine the most promising experiments before even entering the laboratory.

Chapter 6: Discussion

Systems Biology aims to provide a simpler and more tractable framework to explain complex biological phenomena. Most research labs focus on specific proteins and genes of interest or particular sections of a cell signalling pathway, with the goal of deriving as much information as possible about the structure, function, etc. of that particular protein. This has led to the availability of a wealth of experimentally derived data sets that can be integrated into *in-silico* models to generate testable hypotheses or allow the dynamical properties of the system to be deduced providing potential novel insights into the role and function of the system components [5]. Other potential benefits from designing robust predictive models include the identification of new biomarkers of disease, stratification of medicine, based on unique genetic patient profiles, and the targeting of drugs and other treatments, etc. Within this thesis, several models are presented across three individual biological scales (macroscopic, mesoscopic and microscopic). These include the description of cancer and immune cells interactions (multicellular), the movement of fibroblast cells on varying surface structures (cellular) and cell signalling models within the cytoplasm and nucleus (subcellular). One of the key strengths of these models is the integration with experimentally derived results. This corroboration is important as it provides confidence in the results produced, such as dynamical properties and parameter estimates. Further benefits of such systems biology approaches include the reusability of the algorithms and their versatility in terms of being adapted and extended to fit similar biological systems and cell signalling pathways.

Chapter 2 describes a continuous macroscopic *in-silico* model of a highly simplified version of the tumour microenvironment of the gut. Specifically, this model was developed to characterise the underlying mechanism of reaction between epithelial cancer cells and cancer associated stromal immune cells, namely myofibroblasts. Due to problems with technical equipment and relocation to a new university, the data collection was insufficient for a more complex model of the tumour microenvironment. Therefore, this model was purely explorative and was tasked with qualitatively identifying the mechanism of interaction. Migration assays between these cell types produced data on the diffusion rates of the cells when co-cultured. Initially, the observed interaction was described through the design of a simple diffusion model. This description was found to be inadequate for defining the mechanism of interaction observed in the migration experiments. Therefore, the model was adapted to simulate density-dependent diffusion. This method produced a much more appropriate portrayal of the qualitative dynamics observed on the distal side of the epithelial cancer cells. However, this model only provided an adequate description of one side of the experiment. This promoted the incorporation of a chemotaxis type term into the model, as it has been well documented that myofibroblasts release a plethora of chemicals [37,73,311]. Thus, an inhibitory chemical was incorporated into the model framework. One such extended model depicted the inhibitory profile of the chemotaxis on the proximal side of the epithelial cells whereas a second model portrayed the distal side. Each side of the AGS cell monolayer (proximal and distal) needed an individual inhibitory profile term due to

differences in the distance from the source and direction of migration. This additional refinement of the model provided a better comparison of the experimental data than the previous model iterations, suggesting a possible chemical/signalling interaction between the two cell types. However, this comparison remained insufficient in characterising the exact mechanism of interaction present between the cell types. Further experimentation and incorporation of controls into this study is clearly needed in order to select appropriate model design progression and theories of interaction. Therefore, this simplified model of interaction highlights which mechanisms do not describe the underlying mechanism which is novel as it rejects previous theories and can inform new hypotheses.

This was the first model investigating the mechanisms of interaction between these two cell types in the GI tract. Although the model wasn't able to provide any definitive/quantitative answers on the underlying mechanism driving the interplay between the cells, it was clearly able to show which mechanisms were insufficient in describing the cellular phenomenon observed in the time-lapse experiments. The data derived from these experiments was instrumental in terms of motivating the evolution and subsequent iterations of the model. Cumulatively, these iterations produced a model capable of replicating several features of the underlying cell movements. This is encouraging as there is now potential for further modification that can potentially highlight the missing component that would allow for accurate

representation of this multicellular interaction. As mentioned above, with more substantial data to work with, a more detailed and complex model of these cellular interactions can be developed. This more complex model can feature elements present in current wound healing models, as the experiment design is similar to a scratch wound assay. For example, Dallon et al. [312,313] use force balance equations in mechanical models to define the interaction between fibroblast cells and newly reforming ECM. This specific feature would be of interest as a possible theory in describing the AGS cell migration was whether or not it remodelled ECM formed by the 308/1 cells [80]. It would provide insight into the role tissue tension plays in the cells migratory behaviour. Another potential theory to investigate was the effect of contact inhibition on these cells [314]. This would require switching the continuous model to an agent-based model, in which the biological cells are represented as individual entities governed by a set of rules. Walker et al. [315] were able to successfully show how this method can accurately model wound healing in epithelial scratch wound assays.

Chapter 3 described a discrete cell based *in-silico* model of fibroblast migration, in the mesoscopic scale, utilising cell movement data derived from cell migration assays. A novel component of these cell migration assays was the use of engineered polyurethane surfaces containing different surface topologies, which have been 'nano-scratched' through abrasive polishing [180]. Initially, the cell motility was modelled in terms of a stochastic Ornstein-Uhlenbeck process [291]. Cell velocity,

position and random fluctuations were all incorporated into the stochastic model through a series of differential equations, resulting in a model producing random cell walk migratory paths. Parameterisation of the model with the experimental data resulted in the optimisation of the model parameters, yielding an *in-silico* model depicting the cell's intrinsic motility properties on 'flat' surfaces. This approach was extended to the 'linear' and 'random' surfaces, where optimisation of the parameters with the experimental metrics resulted in the production of values for the haptotactic parameter for each surface. The model was able to replicate the *in-vitro* experiments accurately, while also providing values for the parameters of random motility and haptotaxis.

To the best of my knowledge, there are no other mathematical models of fibroblast migration on polyurethane surfaces. However, the model depicts the evolution of random walk models that are present in the literature [199]. To begin, the model is simply a basic random walk model with no topographical features present to affect the migratory behaviour of the cells. By defining mechanical cues in the design of the topographical features of the polyurethane surfaces, it allowed *in-vitro* quantification and real time visualisation of the cell migration paths and upgraded the model to a biased random walk. This model confirms the findings by Irving et al. [180] that these machine ground polyurethane surfaces enhance cell migration. It also reaffirms that grinding technology can be used as an alternative, cost effective method to generate functional surfaces that can be used to control fibroblast

behaviour. One improvement that could be made to this model is the inclusion of a barrier to confine cell movement to the polyurethane domain i.e., migrating fibroblast cells will automatically turn and move away in the opposite direction upon reaching the barrier. Although, this isn't necessary as the model produced satisfactory results without this feature. However, it would be beneficial in future iterations if longer migration times are needed, particularly on the linear surface as cell migration is less tortuous and therefore spreads into space quickly. Mechanistic insights derived from this model could now be applied to investigate the possibility of controlling cell behaviour on other surfaces i.e., implants, thereby improving clinical outcomes [178,290].

Chapter 4 describes the development of an *in-silico* model of Nrf2-Keap1 interaction in the subcellular cytoplasmic and nuclear compartments. Key components of the pathway incorporating this protein interaction were consolidated into a mathematical framework to create an ODE minimal model. This ODE model was validated against several experimental data sets. Seven parameters were identified to describe all the interactions within the ODE model. Parameter estimates were optimised through parameterisation with experimental data. Simulation of the model resulted in three optimal parameter sets to describe the Nrf2-Keap1 network. This was further reduced to two parameter sets using experimental data to compare Nrf2 production rates. Sensitivity analysis revealed that the parameters for nuclear influx, efflux and decay were the most sensitive to the model output. The model was

able to estimate the relative nuclear influx/efflux rate of Nrf2 and the relative cytoplasmic vs nuclear decay of Nrf2 (Table 4-4). Nuclear influx was shown to be more than two times greater than nuclear efflux and decay of the Nrf2 protein was also greater in the nucleus.

Although the Nrf2 pathway is widely recognised as an important stress pathway, few dynamical models have been developed for it [268,269]. This outcome is a consequence of the lack of quantitative data available. Using the Khalil et al. [269] model as a starting point for parameterising the minimalist model developed in Chapter 4, the model was able to answer key questions proposed by the collaborators of this project i.e. relative nuclear influx/efflux rate of Nrf2 and the relative cytoplasmic vs nuclear decay of Nrf2. This model was essential to obtaining these results, as these rates are experimentally challenging to quantitate due, in part, to the short half-life of the Nrf2 protein. The reliability of the model is justified through its ability to fit multiple experimental data sets of differing drug incubations. However, only normalised datasets were provided for the integration with this model. Therefore, the integration with raw datasets would further increase the reliability of the model. This integrated *in-vitro* – *in-silico* framework offers a novel approach for the investigation of the Nrf2 pathway.

Chapter 5 describes a stochastic Petri net model describing dynamical cross-talk between the Nrf2 and NF- κ B pathways. A reductionist approach was considered to remove dependence on parameterisation as sufficient data was unavailable to

parameterise a model of this scale. Nrf2 and NF- κ B expression data combined with initial *in-silico* results allowed confirmation that the underlying dynamics in the model reflected those *in-vitro*. This step provided assurance that the model was capable of replicating typical dynamical behaviour associated with both pathways, namely the oscillations of the Nrf2 and NF- κ B proteins [270,309]. Subsequently, the model was utilised in a predictive capacity to answer questions about the Nrf2-NF- κ B network. Firstly, the model was tasked with determining the effect of increasing Keap1 levels on the network. As expected, the results concluded that there would be a marked decrease in Nrf2 protein, as the Nrf2 protein decreased approximately 90% for a 2-fold increase in Keap1. Further model predictions were used to explore other scenarios, such as increased production of interacting proteins, removal of key components and how particular proteins behave when assigned specific roles (i.e. as a transporter of decay or exportation). The advantages of the stochastic PN model are underlined by its ability to quickly characterise the network dynamics of these pathways, without parameterisation, and provide a means for testing hypotheses regarding the propagation of signals throughout the network.

Nrf2 and NF- κ B pathways are key for regulating the fine balance of cellular redox status in response to stress and inflammation, respectively [217]. Extensive research has provided convincing evidence that functional cross-talk exists between these two networks [224,227,249,316-318]. However, many aspects of the conditional and dynamic nature of this interplay remain unknown. Although, there are many models

dedicated to investigating the NF- κ B pathway, the limited amount of computational Nrf2 models means there are very few models depicting functional cross-talk between the two. In particular, there are no PN models describing these pathways. This stochastic PN model highlights several points of interaction, providing insight into many undefined features of co-regulation, negative feedback loops and post transcriptional mechanisms through validation with experimental data. Therefore, this novel systematic model provides the capacity to define many important aspects of these regulatory pathways as well as driving the development of improved strategies to manipulate the balance between the pathway responses, under both physiological and disease conditions.

The results presented in this thesis provide motivation for utilising experimental data in the development and validation of mathematical models. In order to obtain complex robust models, researchers should seek to obtain high quality quantitative data of the system of interest. However, the results of this thesis also demonstrate how dynamic qualitative behaviour can be obtained from *in-silico* models using simplistic inputs such as pathway design. There are numerous and variable approaches to addressing researchers questions, via *in-silico* modelling, dependent upon on the level of information known about the system of interest and quality of data available. Overall, combination of the experimental and modelling worlds allows for key biological questions to be addressed and new hypotheses to be theorised. Ideally, a model built with experimental input would yield results that

would promote the development of new hypotheses and experimentation which would then, in turn, feed back into the model building up multiple iterations and increasing the robustness and reliability of its output. A future challenge in the field of systems biology is the generation of such large-scale robust models, containing the data of multiple signalling networks and protein pathways. The availability of data on particular systems can present its own challenge, resulting in models that are built upon assumptions. These challenges can be addressed through continued collaboration of biologists and mathematicians, as well as improvements in model design and computational power.

Chapter 7: Appendix

7.1 Appendix A – Mark Murphy lab methods

7.1.1 Preparation of stainless steel moulds

All patterned surfaces were generated upon a biocompatible polyurethane polymer. Patterns were developed on the polymer indirectly, by casting the flat end surface of a cylindrical stainless steel mould that had been cut from stainless steel rods (grade 316, cylinder height 13 mm, diameter 18 mm). To prepare the stainless steel moulds for patterning, their flat surfaces were first polished to remove all marks caused by the cutting process. This was achieved using a METASERV universal polisher and silicon carbide sheets of decreasing grit size (60 to 1200 B) followed by a polishing cloth. This resulted in the stainless steel cylinder having a mirrored surface finish (mean Ra value of approximately 0.02 μm) which could then be used for processing.

7.1.2 Abrasive patterned surface development

Machine grinding was used for this purpose to generate the topographical patterns on the polyurethane surfaces. This method involves the micro-patterning of stainless steel, which can then be used to cast polymer substrates for observing the migration of fibroblasts [180]. An unprocessed plain polymer surface was used as a control and was labelled as 'Flat'. Next, a pattern of parallel lines was cast on the polymer surface and was labelled as 'Linear'. Finally, a pattern of random lines varying in direction was etched into the polymer surface and labelled appropriately as 'Random'. Subsequently, a previous study has shown that these machine ground surfaces

promote adhesion and migration in fibroblast cells compared to unprocessed, flat surfaces [180].

Once polished to achieve an initial mirrored finish (as described above in Section 1.2.1) the stainless steel cylinder was then polished to achieve a topographical surface patterning through the use of abrasive paper (1200 B). By controlling the motion of the stainless steel cylinders relative to the silicon carbide abrasive paper, surfaces having either directional, or random, sub-micron abrasive marks could be produced, termed here as 'nano-scratches'. The directional (linear) features are a result of the METASEV universal polisher's spinning motion, while the more random features are the result of manually rubbing the steel mould across the surface in different directions. The surface topography was subsequently characterised by white light interferometry and scanning electron microscopy. These stainless steel cylinders could then be used as master moulds to cast polymer substrates. In total two different patterns were produced; having linear and randomly organised features.

7.1.3 Casting polymer substrates

Casting the polymer over the stainless steel moulds produces an inverted pattern on the polymer surface. Employing this indirect processing method ensures that only the surface topography/roughness of the material is altered and not the material chemistry. The polymer used here was polyurethane and was provided by Biomer Technology Ltd. The polymer substrates were produced using 8% polyurethane in 2:1

Dimethylformamide (DMF) and Tetrahydrofuran (THF). This was poured onto the stainless steel moulds and cured at 60°C for 2 h. Following this the mould/cast was allowed to cool before peeling off the polymer from the mould following the grain of the pattern. Prior to cell culture all polymer surfaces were sterilised by washing with 70% ethanol then exposed to UV light for 30 min. Finally, the polymers were washed with sterilised distilled H₂O.

7.1.4 White light interferometry for surface characterisation

A Bruker Contour GT-K 3D optical microscope equipped with Vision 64 software was used to image the surfaces of the patterned polymers. This enabled feature heights/widths and roughness to be determined.

7.2 Appendix B – Chris Sanderson lab methods

7.2.1 Live Cell Imaging

BAC^{Nrf2-Venus} were generated by stable integration of bacterial artificial chromosome (BAC) encoding Nrf2-Venus fluorescent protein fusion into neuroblastoma SK-N-AS cells. The pDendra2-Nrf2 fusion was transiently expressed in SK-N-AS cells. BAC^{Nrf2-Venus} were treated with 10 μ M MG132 and 10 μ g/ml in separate experiments. To silence the expression of the Keap1 protein in the pDendra2-Nrf2 experiments, short interfering RNA (siRNA) duplexes targeting human Keap1 (siKeap) (SMART pool ON-TARGET plus Keap2 siRNA, Dharmacon, L-012453-00-000) were transfected at 10nM final concentration alongside a scrambled control (siCTR) siGENOME Non-Targeting siRNA Pool no 1 (Dharmacon, D-001206-13-05). For real-time imaging of live cells, cells were seeded onto the 1 or 4 compartment 35mm glass bottom dishes (Greiner Bio-One). The 4 compartments allowed imaging of 4 different experimental conditions in parallel. The imaging experiments were performed under humidified atmosphere, at 5% CO₂ and 37°C on two imaging systems. The primary cells expressing plasmid encoded fluorescent protein fusions were imaged on the Zeiss Axiovert 5.10 (Zeiss Germany) confocal microscope using 40x oil immersion objective with numerical aperture (NA) of 1.4. The image acquisition on this system was coupled with autofocus Marco (Ellenberg lab, EMBL), which enabled maintenance of stable Z-plane position of the imaged cells, avoiding the problems of focal drifts that can occur during the long acquisition times. The LSM 7.80 (Zeiss, Germany) system

was used for monitoring low expression of fluorescent proteins, as it has superior resolution and sensitivity of detection, using 40x oil immersion objective (1.4 NA) and LSM ZEN 2010 image acquisition software (Zeiss). In both systems the image acquisition was performed, using 512x512 pixel resolution, 7 scanning speed with the pinhole diameter adjusted to the fluorescence intensity of imaged samples. The image acquisition of single fluorophore was performed by taking one acquisition frame at 8min interval in 1-20 imaging locations, and the time taken to acquire image at all selected positions did not exceed the 8min interval. When imaging two separate channels (or fluorescent probes) the image acquisition was performed every 7min at up to 16 locations. The drug treatment was usually performed following initial three frames were acquired, which served as a baseline fluorescence measurement. Both imaging protocols were carried out at various lengths of time between 2-14h, and the drug of interest was added following 3 initial frames, which were taken to establish a signal baseline.

7.2.2 Lambda Scan

Lambda Scan imaging mode was used for spectral unmixing of fluorophores with overlapping fluorescence emission peaks. This mode was predominantly used to image cells exhibiting very low expression of fluorescent protein fusions such as BAC^{Nrf2-Venus} or primary astrocytes transduced with *2kb-Venus-msNrf2*. The levels of Venus fluorescence in those models was close to autofluorescent signal and therefore there was a considerable autofluorescent noise being detected. The spectral images were then combined using LSM ZEN 2010 software (Zeiss).

7.2.3 pDendra2 Imaging

The photoswitchable fluorescent protein pDendra2 was isolated from *Octocoral Dendronephthya*. It matures completely at 37°C, its pH stable and monomeric. The pDendra2 emits naturally in a green light spectrum, however UV irradiation results in irreversible transition in emission to bright and photostable red fluorescent protein (RFP) spectrum. The pDendra2-Nrf2 fusion was transiently expressed in SK-N-AS cells (3µg of plasmid p/35mm dish) 24h before the experiment. To image the turnover of Nrf2, four locations were selected with each localization treated with a different compound (4 compartment dishes) and the 2 regions of interest (ROIs) were selected, each of 13x13 pixel size. The fluorescent signal was collected for the Green and the Red channels and following acquisition of three imaging frames, the drug was added and one more frame was collected (3min interval between acquisitions). Then the photoconversion of pDendra2 was performed by a UV lamp at 75% power for 45s. Local pDendra photoconversion was used to monitor nuclear import and export rates of pDendra2-Nrf2. The data measurements were performed using ZEN 2010 and exported and averaged using Microsoft Excel, the averaged data was exported to GraphPad Prism 5.

7.2.4 Image Analysis

Image analysis post-acquisition was performed using Cell Tracker software Version 6.0 (www.dbbkgroup.org/celltracker/). The nucleus was drawn manually and adjusted on every acquisition image, either manually or automatically by cell tracker software. The data was averaged and exported to Excel file format. It was normalized

to the initial fluorescence levels and the noise was reduced by averaging the values using third order moving average (three frame smoothing).

7.2.5 Fluorescence Cross Correlation Spectroscopy (FCCS)

The data collection was performed using LSM 780 with confocor 3 mounted on Axio observer Z1 microscope using oil immersion 100x lens (N.A. 1.46) and using ZEN2010 software (Zeiss). The pinhole was set to 1 airy unit and the laser power was typically set to 1% laser power, adjusted to avoid photobleaching and to maximize the count per minute (cpm) fluorescent signal to minimum 0.5 kHz value. The data collection protocols were carried out 10x for 10s each and the fluorescence signal of channels was then compared using first correlation and then cross-correlation logarithms using LSM ZEN 2010B FCS function.

Chapter 8: Bibliography

- [1] VA Likic, MJ McConville, T Lithgow, A Bacic. Systems biology: the next frontier for bioinformatics, *Adv.Bioinformatics*. (2010) 268925.
- [2] Z Xie, X Duan, Z Ouyang, P Zhang. Quantitative Analysis of the Interdisciplinarity of Applied Mathematics, *PLoS One*. 10 (2015) e0137424.
- [3] L Liljeroos, E Malito, I Ferlenghi, MJ Bottomley. Structural and Computational Biology in the Design of Immunogenic Vaccine Antigens, *J.Immunol.Res.* 2015 (2015) 156241.
- [4] M Craig. Towards Quantitative Systems Pharmacology Models of Chemotherapy-Induced Neutropenia, *CPT Pharmacometrics Syst.Pharmacol.* 6 (2017) 293-304.
- [5] SW Robinson, M Fernandes, H Husi. Current advances in systems and integrative biology, *Comput.Struct.Biotechnol.J.* 11 (2014) 35-46.
- [6] T Sevimoglu, KY Arga. The role of protein interaction networks in systems biomedicine, *Comput.Struct.Biotechnol.J.* 11 (2014) 22-27.
- [7] MT Smith, KM Wilding, JM Hunt, AM Bennett, BC Bundy. The emerging age of cell-free synthetic biology, *FEBS Lett.* 588 (2014) 2755-2761.
- [8] ES Lander, LM Linton, B Birren, C Nusbaum, MC Zody, J Baldwin, et al. Initial sequencing and analysis of the human genome, *Nature*. 409 (2001) 860-921.
- [9] H Kacser, JA Burns. The control of flux, *Symp.Soc.Exp.Biol.* 27 (1973) 65-104.
- [10] DR Cumming, SB Furber, DJ Paul. Beyond Moore's law, *Philos.Trans.A.Math.Phys.Eng.Sci.* 372 (2014) 20130376.
- [11] S Middha, S Baheti, SN Hart, JP Kocher. From days to hours: reporting clinically actionable variants from whole genome sequencing, *PLoS One*. 9 (2014) e86803.
- [12] National Center for Biotechnology Information (NCBI)[Internet]. Bethesda (MD): National Library of Medicine (US), National Center for Biotechnology Information; [1988] – [cited 2018 Mar 26]. Available from: <https://www.ncbi.nlm.nih.gov/>, 2018.
- [13] P Flecknell. Replacement, reduction and refinement, *ALTEX*. 19 (2002) 73-78.

- [14] PK Kreeger, DA Lauffenburger. Cancer systems biology: a network modeling perspective, *Carcinogenesis*. 31 (2010) 2-8.
- [15] B Zhang, C Gaiteri, LG Bodea, Z Wang, J McElwee, AA Podtelezhnikov, et al. Integrated systems approach identifies genetic nodes and networks in late-onset Alzheimer's disease, *Cell*. 153 (2013) 707-720.
- [16] EL Berg. Systems biology in drug discovery and development, *Drug Discov.Today*. 19 (2014) 113-125.
- [17] BM Bakker, PA Michels, FR Opperdoes, HV Westerhoff. What controls glycolysis in bloodstream form *Trypanosoma brucei*? *J.Biol.Chem*. 274 (1999) 14551-14559.
- [18] JJ Tyson, K Chen, B Novak. Network dynamics and cell physiology, *Nat.Rev.Mol.Cell Biol*. 2 (2001) 908-916.
- [19] M Kastantin, BB Langdon, DK Schwartz. A bottom-up approach to understanding protein layer formation at solid-liquid interfaces, *Adv.Colloid Interface Sci*. 207 (2014) 240-252.
- [20] M Scianna, *Cellular Potts models : multiscale extensions and biological applications*, CRC Press, Boca Raton, 2013.
- [21] M Scianna, L Preziosi. A node-based version of the cellular Potts model, *Comput.Biol.Med*. 76 (2016) 94-112.
- [22] J Walpole, JA Papin, SM Peirce. Multiscale computational models of complex biological systems, *Annu.Rev.Biomed.Eng*. 15 (2013) 137-154.
- [23] M Fallahi-Sichani, DE Kirschner, JJ Linderman. NF-kappaB Signaling Dynamics Play a Key Role in Infection Control in Tuberculosis, *Front.Physiol*. 3 (2012) 170.
- [24] JD Scheff, PD Mavroudis, SE Calvano, SF Lowry, IP Androulakis. Modeling autonomic regulation of cardiac function and heart rate variability in human endotoxemia, *Physiol.Genomics*. 43 (2011) 951-964.
- [25] EO Voit, HA Martens, SW Omholt. 150 Years of the Mass Action Law, *PLoS Comput.Biol*. 11 (2015) e1004012.
- [26] AA Patel, ET Gawlinski, SK Lemieux, RA Gatenby. A cellular automaton model of early tumor growth and invasion, *J.Theor.Biol*. 213 (2001) 315-331.

- [27] DG Mallet, LG De Pillis. A cellular automata model of tumor-immune system interactions, *J.Theor.Biol.* 239 (2006) 334-350.
- [28] J Galle, D Sittig, I Hanisch, M Wobus, E Wandel, M Loeffler, et al. Individual cell-based models of tumor-environment interactions: Multiple effects of CD97 on tumor invasion, *Am.J.Pathol.* 169 (2006) 1802-1811.
- [29] P Li, JO Dada, D Jameson, I Spasic, N Swainston, K Carroll, et al. Systematic integration of experimental data and models in systems biology, *BMC Bioinformatics.* 11 (2010) 582-2105-11-582.
- [30] P Kirk, T Thorne, MP Stumpf. Model selection in systems and synthetic biology, *Curr.Opin.Biotechnol.* 24 (2013) 767-774.
- [31] TR Xu, V Vyshemirsky, A Gormand, A von Kriegsheim, M Girolami, GS Baillie, et al. Inferring signaling pathway topologies from multiple perturbation measurements of specific biochemical species, *Sci.Signal.* 3 (2010) ra20.
- [32] E Balsa-Canto, M Peifer, JR Banga, J Timmer, C Fleck. Hybrid optimization method with general switching strategy for parameter estimation, *BMC Syst.Biol.* 2 (2008) 26-0509-2-26.
- [33] J Liepe, P Kirk, S Filippi, T Toni, CP Barnes, MP Stumpf. A framework for parameter estimation and model selection from experimental data in systems biology using approximate Bayesian computation, *Nat.Protoc.* 9 (2014) 439-456.
- [34] Trisilowati, DG Mallet. In silico experimental modeling of cancer treatment, *ISRN Oncol.* 2012 (2012) 828701.
- [35] F Balkwill, A Mantovani. Inflammation and cancer: back to Virchow? *Lancet.* 357 (2001) 539-545.
- [36] TM Yeung, C Buskens, LM Wang, NJ Mortensen, WF Bodmer. Myofibroblast activation in colorectal cancer lymph node metastases, *Br.J.Cancer.* 108 (2013) 2106-2115.
- [37] M Quante, SP Tu, H Tomita, T Gonda, SS Wang, S Takashi, et al. Bone marrow-derived myofibroblasts contribute to the mesenchymal stem cell niche and promote tumor growth, *Cancer.Cell.* 19 (2011) 257-272.
- [38] S Sekiya, S Miura, K Matsuda-Ito, A Suzuki. Myofibroblasts Derived from Hepatic Progenitor Cells Create the Tumor Microenvironment, *Stem Cell.Reports.* 7 (2016) 1130-1139.

- [39] J Roland. Fibroblast and myofibroblast in the granulation tissue, *Ann.Anat.Pathol.(Paris)*. 21 (1976) 37-44.
- [40] JJ Tomasek, G Gabbiani, B Hinz, C Chaponnier, RA Brown. Myofibroblasts and mechano-regulation of connective tissue remodelling, *Nat.Rev.Mol.Cell Biol.* 3 (2002) 349-363.
- [41] DC Radisky, PA Kenny, MJ Bissell. Fibrosis and cancer: do myofibroblasts come also from epithelial cells via EMT? *J.Cell.Biochem.* 101 (2007) 830-839.
- [42] F Klingberg, B Hinz, ES White. The myofibroblast matrix: implications for tissue repair and fibrosis, *J.Pathol.* 229 (2013) 298-309.
- [43] DW Powell, RC Mifflin, JD Valentich, SE Crowe, JI Saada, AB West. Myofibroblasts. I. Paracrine cells important in health and disease, *Am.J.Physiol.* 277 (1999) C1-9.
- [44] KC Wu, LM Jackson, AM Galvin, T Gray, CJ Hawkey, YR Mahida. Phenotypic and functional characterisation of myofibroblasts, macrophages, and lymphocytes migrating out of the human gastric lamina propria following the loss of epithelial cells, *Gut.* 44 (1999) 323-330.
- [45] E Choi, JT Roland, BJ Barlow, R O'Neal, AE Rich, KT Nam, et al. Cell lineage distribution atlas of the human stomach reveals heterogeneous gland populations in the gastric antrum, *Gut.* 63 (2014) 1711-1720.
- [46] GJ Dockray, A Moore, A Varro, DM Pritchard. Gastrin receptor pharmacology, *Curr.Gastroenterol.Rep.* 14 (2012) 453-459.
- [47] R Hakanson, XQ Ding, P Norlen, E Lindstrom. CCK2 receptor antagonists: pharmacological tools to study the gastrin-ECL cell-parietal cell axis, *Regul.Pept.* 80 (1999) 1-12.
- [48] N Barker, M Huch, P Kujala, M van de Wetering, HJ Snippert, JH van Es, et al. Lgr5(+ve) stem cells drive self-renewal in the stomach and build long-lived gastric units in vitro, *Cell.Stem Cell.* 6 (2010) 25-36.
- [49] DH Yang, S Tsuyama, YB Ge, D Wakamatsu, J Ohmori, F Murata. Proliferation and migration kinetics of stem cells in the rat fundic gland, *Histol.Histopathol.* 12 (1997) 719-727.
- [50] SM Karam. Lineage commitment and maturation of epithelial cells in the gut, *Front.Biosci.* 4 (1999) D286-98.

- [51] B Hinz, SH Phan, VJ Thannickal, A Galli, ML Bochaton-Piallat, G Gabbiani. The myofibroblast: one function, multiple origins, *Am.J.Pathol.* 170 (2007) 1807-1816.
- [52] G Serini, ML Bochaton-Piallat, P Ropraz, A Geinoz, L Borsi, L Zardi, et al. The fibronectin domain ED-A is crucial for myofibroblastic phenotype induction by transforming growth factor-beta1, *J.Cell Biol.* 142 (1998) 873-881.
- [53] EL Spaeth, JL Dembinski, AK Sasser, K Watson, A Klopp, B Hall, et al. Mesenchymal stem cell transition to tumor-associated fibroblasts contributes to fibrovascular network expansion and tumor progression, *PLoS One.* 4 (2009) e4992.
- [54] M Quante, SP Tu, H Tomita, T Gonda, SS Wang, S Takashi, et al. Bone marrow-derived myofibroblasts contribute to the mesenchymal stem cell niche and promote tumor growth, *Cancer.Cell.* 19 (2011) 257-272.
- [55] TJ Shaw, P Martin. Wound repair at a glance, *J.Cell.Sci.* 122 (2009) 3209-3213.
- [56] ER Lacy, S Ito. Rapid epithelial restitution of the rat gastric mucosa after ethanol injury, *Lab.Invest.* 51 (1984) 573-583.
- [57] RA Clark, JM Lanigan, P DellaPelle, E Manseau, HF Dvorak, RB Colvin. Fibronectin and fibrin provide a provisional matrix for epidermal cell migration during wound reepithelialization, *J.Invest.Dermatol.* 79 (1982) 264-269.
- [58] RA Clark. Fibrin and wound healing, *Ann.N.Y.Acad.Sci.* 936 (2001) 355-367.
- [59] M Gawaz, FJ Neumann, T Dickfeld, W Koch, KL Laugwitz, H Adelsberger, et al. Activated platelets induce monocyte chemotactic protein-1 secretion and surface expression of intercellular adhesion molecule-1 on endothelial cells, *Circulation.* 98 (1998) 1164-1171.
- [60] WJ Kim, GK Gittes, MT Longaker. Signal transduction in wound pharmacology, *Arch.Pharm.Res.* 21 (1998) 487-495.
- [61] BC McKaig, SS Makh, CJ Hawkey, DK Podolsky, YR Mahida. Normal human colonic subepithelial myofibroblasts enhance epithelial migration (restitution) via TGF-beta3, *Am.J.Physiol.* 276 (1999) G1087-93.
- [62] O De Wever, M Mareel. Role of tissue stroma in cancer cell invasion, *J.Pathol.* 200 (2003) 429-447.
- [63] JM Otte, IM Rosenberg, DK Podolsky. Intestinal myofibroblasts in innate immune responses of the intestine, *Gastroenterology.* 124 (2003) 1866-1878.

- [64] JI Saada, IV Pinchuk, CA Barrera, PA Adegboyega, G Suarez, RC Mifflin, et al. Subepithelial myofibroblasts are novel nonprofessional APCs in the human colonic mucosa, *J.Immunol.* 177 (2006) 5968-5979.
- [65] D Fan, A Takawale, J Lee, Z Kassiri. Cardiac fibroblasts, fibrosis and extracellular matrix remodeling in heart disease, *Fibrogenesis Tissue Repair.* 5 (2012) 15-1536-5-15.
- [66] VW van Hinsbergh, MA Engelse, PH Quax. Pericellular proteases in angiogenesis and vasculogenesis, *Arterioscler.Thromb.Vasc.Biol.* 26 (2006) 716-728.
- [67] MA Olman, N Mackman, CL Gladson, KM Moser, DJ Loskutoff. Changes in procoagulant and fibrinolytic gene expression during bleomycin-induced lung injury in the mouse, *J.Clin.Invest.* 96 (1995) 1621-1630.
- [68] M Madlener, WC Parks, S Werner. Matrix metalloproteinases (MMPs) and their physiological inhibitors (TIMPs) are differentially expressed during excisional skin wound repair, *Exp.Cell Res.* 242 (1998) 201-210.
- [69] M Lukaszewicz-Zajac, B Mroczko, M Szmitkowski. Gastric cancer - The role of matrix metalloproteinases in tumor progression, *Clin.Chim.Acta.* 412 (2011) 1725-1730.
- [70] M Groblewska, M Siewko, B Mroczko, M Szmitkowski. The role of matrix metalloproteinases (MMPs) and their inhibitors (TIMPs) in the development of esophageal cancer, *Folia Histochem.Cytobiol.* 50 (2012) 12-19.
- [71] MD Sternlicht, Z Werb. How matrix metalloproteinases regulate cell behavior, *Annu.Rev.Cell Dev.Biol.* 17 (2001) 463-516.
- [72] S Bamba, A Andoh, H Yasui, Y Araki, T Bamba, Y Fujiyama. Matrix metalloproteinase-3 secretion from human colonic subepithelial myofibroblasts: role of interleukin-17, *J.Gastroenterol.* 38 (2003) 548-554.
- [73] T Okuno, A Andoh, S Bamba, Y Araki, Y Fujiyama, M Fujiyama, et al. Interleukin-1beta and tumor necrosis factor-alpha induce chemokine and matrix metalloproteinase gene expression in human colonic subepithelial myofibroblasts, *Scand.J.Gastroenterol.* 37 (2002) 317-324.
- [74] C McCaig, C Duval, E Hemers, I Steele, DM Pritchard, S Przemack, et al. The role of matrix metalloproteinase-7 in redefining the gastric microenvironment in response to *Helicobacter pylori*, *Gastroenterology.* 130 (2006) 1754-1763.

- [75] LJ McCawley, LM Matrisian. Matrix metalloproteinases: they're not just for matrix anymore! *Curr.Opin.Cell Biol.* 13 (2001) 534-540.
- [76] D Ribatti. The contribution of Harold F. Dvorak to the study of tumor angiogenesis and stroma generation mechanisms, *Endothelium.* 14 (2007) 131-135.
- [77] D Hanahan, RA Weinberg. The hallmarks of cancer, *Cell.* 100 (2000) 57-70.
- [78] JC Tse, R Kalluri. Mechanisms of metastasis: epithelial-to-mesenchymal transition and contribution of tumor microenvironment, *J.Cell.Biochem.* 101 (2007) 816-829.
- [79] NA Bhowmick, EG Neilson, HL Moses. Stromal fibroblasts in cancer initiation and progression, *Nature.* 432 (2004) 332-337.
- [80] M Otranto, V Sarrazy, F Bonte, B Hinz, G Gabbiani, A Desmouliere. The role of the myofibroblast in tumor stroma remodeling, *Cell.Adh Migr.* 6 (2012) 203-219.
- [81] A Orimo, RA Weinberg. Stromal fibroblasts in cancer: a novel tumor-promoting cell type, *Cell.Cycle.* 5 (2006) 1597-1601.
- [82] A Raza, MJ Franklin, AZ Dudek. Pericytes and vessel maturation during tumor angiogenesis and metastasis, *Am.J.Hematol.* 85 (2010) 593-598.
- [83] M Quante, TC Wang. Inflammation and stem cells in gastrointestinal carcinogenesis, *Physiology (Bethesda).* 23 (2008) 350-359.
- [84] A Boussioutas, H Li, J Liu, P Waring, S Lade, AJ Holloway, et al. Distinctive patterns of gene expression in premalignant gastric mucosa and gastric cancer, *Cancer Res.* 63 (2003) 2569-2577.
- [85] L Jiang, TA Gonda, MV Gamble, M Salas, V Seshan, S Tu, et al. Global hypomethylation of genomic DNA in cancer-associated myofibroblasts, *Cancer Res.* 68 (2008) 9900-9908.
- [86] CF Singer, D Gschwantler-Kaulich, A Fink-Retter, C Haas, G Hudelist, K Czerwenka, et al. Differential gene expression profile in breast cancer-derived stromal fibroblasts, *Breast Cancer Res.Treat.* 110 (2008) 273-281.
- [87] KD Grugan, CG Miller, Y Yao, CZ Michaylira, S Ohashi, AJ Klein-Szanto, et al. Fibroblast-secreted hepatocyte growth factor plays a functional role in esophageal squamous cell carcinoma invasion, *Proc.Natl.Acad.Sci.U.S.A.* 107 (2010) 11026-11031.

- [88] SL Schor, AM Schor, G Rushton. Fibroblasts from cancer patients display a mixture of both foetal and adult-like phenotypic characteristics, *J.Cell.Sci.* 90 (Pt 3) (1988) 401-407.
- [89] C Holmberg, M Quante, I Steele, JD Kumar, S Balabanova, C Duval, et al. Release of TGFbetaig-h3 by gastric myofibroblasts slows tumor growth and is decreased with cancer progression, *Carcinogenesis.* 33 (2012) 1553-1562.
- [90] NC Direkze, K Hoidalva-Dilke, R Jeffery, T Hunt, R Poulson, D Oukrif, et al. Bone marrow contribution to tumor-associated myofibroblasts and fibroblasts, *Cancer Res.* 64 (2004) 8492-8495.
- [91] SS Muerkoster, V Werbing, D Koch, B Sipos, O Ammerpohl, H Kalthoff, et al. Role of myofibroblasts in innate chemoresistance of pancreatic carcinoma--epigenetic downregulation of caspases, *Int.J.Cancer.* 123 (2008) 1751-1760.
- [92] JN Ihle. Cytokine receptor signalling, *Nature.* 377 (1995) 591-594.
- [93] CH Heldin. Dimerization of cell surface receptors in signal transduction, *Cell.* 80 (1995) 213-223.
- [94] G Buchanan, RA Irvine, GA Coetzee, WD Tilley. Contribution of the androgen receptor to prostate cancer predisposition and progression, *Cancer Metastasis Rev.* 20 (2001) 207-223.
- [95] S Harvey, CG Martinez-Moreno, M Luna, C Aramburo. Autocrine/paracrine roles of extrapituitary growth hormone and prolactin in health and disease: An overview, *Gen.Comp.Endocrinol.* 220 (2015) 103-111.
- [96] R Kalluri, M Zeisberg. Fibroblasts in cancer, *Nat.Rev.Cancer.* 6 (2006) 392-401.
- [97] KG Murphy, SR Bloom. Gut hormones and the regulation of energy homeostasis, *Nature.* 444 (2006) 854-859.
- [98] S Barrientos, O Stojadinovic, MS Golinko, H Brem, M Tomic-Canic. Growth factors and cytokines in wound healing, *Wound Repair Regen.* 16 (2008) 585-601.
- [99] LA Poniatowski, P Wojdasiewicz, R Gasik, D Szukiewicz. Transforming growth factor Beta family: insight into the role of growth factors in regulation of fracture healing biology and potential clinical applications, *Mediators Inflamm.* 2015 (2015) 137823.

- [100] UH Lerner, C Ohlsson. The WNT system: background and its role in bone, *J.Intern.Med.* 277 (2015) 630-649.
- [101] S Yamamoto, KL Schulze, HJ Bellen. Introduction to Notch signaling, *Methods Mol.Biol.* 1187 (2014) 1-14.
- [102] SW Choy, SH Cheng. Hedgehog signaling, *Vitam.Horm.* 88 (2012) 1-23.
- [103] MK Jones, M Tomikawa, B Mohajer, AS Tarnawski. Gastrointestinal mucosal regeneration: role of growth factors, *Front.Biosci.* 4 (1999) D303-9.
- [104] Y Rochman, R Spolski, WJ Leonard. New insights into the regulation of T cells by gamma(c) family cytokines, *Nat.Rev.Immunol.* 9 (2009) 480-490.
- [105] DC Palomino, LC Marti. Chemokines and immunity, *Einstein (Sao.Paulo).* 13 (2015) 469-473.
- [106] C Angelucci, G Maulucci, G Lama, G Proietti, A Colabianchi, M Papi, et al. Epithelial-stromal interactions in human breast cancer: effects on adhesion, plasma membrane fluidity and migration speed and directness, *PLoS One.* 7 (2012) e50804.
- [107] A Moustakas, CH Heldin. Signaling networks guiding epithelial-mesenchymal transitions during embryogenesis and cancer progression, *Cancer.Sci.* 98 (2007) 1512-1520.
- [108] K Shiga, M Hara, T Nagasaki, T Sato, H Takahashi, H Takeyama. Cancer-Associated Fibroblasts: Their Characteristics and Their Roles in Tumor Growth, *Cancers (Basel).* 7 (2015) 2443-2458.
- [109] M Lin, HZ Lin, SP Ma, P Ji, D Xie, JX Yu. Vascular endothelial growth factor-A and -C: expression and correlations with lymphatic metastasis and prognosis in colorectal cancer, *Med.Oncol.* 28 (2011) 151-158.
- [110] T Nagasaki, M Hara, H Nakanishi, H Takahashi, M Sato, H Takeyama. Interleukin-6 released by colon cancer-associated fibroblasts is critical for tumour angiogenesis: anti-interleukin-6 receptor antibody suppressed angiogenesis and inhibited tumour-stroma interaction, *Br.J.Cancer.* 110 (2014) 469-478.
- [111] LK Cheng, R Komuro, TM Austin, ML Buist, AJ Pullan. Anatomically realistic multiscale models of normal and abnormal gastrointestinal electrical activity, *World J.Gastroenterol.* 13 (2007) 1378-1383.

- [112] LK Cheng, G O'Grady, P Du, JU Egbuji, JA Windsor, AJ Pullan. Gastrointestinal system, Wiley Interdiscip.Rev.Syst.Biol.Med. 2 (2010) 65-79.
- [113] LK Cheng, P Du, G O'Grady. Mapping and modeling gastrointestinal bioelectricity: from engineering bench to bedside, Physiology (Bethesda). 28 (2013) 310-317.
- [114] P Du, G O'Grady, J Gao, S Sathar, LK Cheng. Toward the virtual stomach: progress in multiscale modeling of gastric electrophysiology and motility, Wiley Interdiscip.Rev.Syst.Biol.Med. 5 (2013) 481-493.
- [115] A Corrias, ML Buist. Quantitative cellular description of gastric slow wave activity, Am.J.Physiol.Gastrointest.Liver Physiol. 294 (2008) G989-95.
- [116] A Beyder, JL Rae, C Bernard, PR Strege, F Sachs, G Farrugia. Mechanosensitivity of Nav1.5, a voltage-sensitive sodium channel, J.Physiol. 588 (2010) 4969-4985.
- [117] YC Poh, A Beyder, PR Strege, G Farrugia, ML Buist. Quantification of gastrointestinal sodium channelopathy, J.Theor.Biol. 293 (2012) 41-48.
- [118] A Corrias, ML Buist. A quantitative model of gastric smooth muscle cellular activation, Ann.Biomed.Eng. 35 (2007) 1595-1607.
- [119] JD Huizinga, WJ Lammers. Gut peristalsis is governed by a multitude of cooperating mechanisms, Am.J.Physiol.Gastrointest.Liver Physiol. 296 (2009) G1-8.
- [120] M Buist, G Sands, P Hunter, A Pullan. A deformable finite element derived finite difference method for cardiac activation problems, Ann.Biomed.Eng. 31 (2003) 577-588.
- [121] P Kohl, D Noble. Systems biology and the virtual physiological human, Mol.Syst.Biol. 5 (2009) 292.
- [122] FA Meineke, CS Potten, M Loeffler. Cell migration and organization in the intestinal crypt using a lattice-free model, Cell Prolif. 34 (2001) 253-266.
- [123] IM van Leeuwen, GR Mirams, A Walter, A Fletcher, P Murray, J Osborne, et al. An integrative computational model for intestinal tissue renewal, Cell Prolif. 42 (2009) 617-636.
- [124] N Beerenwinkel, RF Schwarz, M Gerstung, F Markowetz. Cancer evolution: mathematical models and computational inference, Syst.Biol. 64 (2015) e1-25.

- [125] JD Murray, *Mathematical biology*, 3rd ed., Springer, New York ; London, 2002.
- [126] Roose T., Chapman S., Maini P. Mathematical models of avascular tumor growth. *SIAM Review*. 49 (2007) 179.
- [127] MJ Deutsch A. Cellular automaton models of tumor development: A critical review, *Ad. Complex Syst*. 05 (2002) 247.
- [128] R Panigrahi, S Kubiszewski-Jakubiak, J Whelan, A Vrieling. The Design and Structure of Outer Membrane Receptors from Peroxisomes, Mitochondria, and Chloroplasts, *Structure*. 23 (2015) 1783-1800.
- [129] JB Moseley. An expanded view of the eukaryotic cytoskeleton, *Mol.Biol.Cell*. 24 (2013) 1615-1618.
- [130] DN Wilson, JH Doudna Cate. The structure and function of the eukaryotic ribosome, *Cold Spring Harb Perspect.Biol*. 4 (2012) 10.1101/cshperspect.a011536.
- [131] S Zhou, Y Sun, X Kuang, S Hou, Y Yang, Z Wang, et al. Mitochondria-targeting nanomedicine: An effective and potent strategy against aminoglycosides-induced ototoxicity, *Eur.J.Pharm.Sci*. (2018).
- [132] WG Nelson, MC Haffner, S Yegnasubramanian. The structure of the nucleus in normal and neoplastic prostate cells: untangling the role of type 2 DNA topoisomerases, *Am.J.Clin.Exp.Urol*. 6 (2018) 107-113.
- [133] GL Nicolson. Cell membrane fluid-mosaic structure and cancer metastasis, *Cancer Res*. 75 (2015) 1169-1176.
- [134] S Li, NF Huang, S Hsu. Mechanotransduction in endothelial cell migration, *J.Cell.Biochem*. 96 (2005) 1110-1126.
- [135] FC Ramaekers, FT Bosman. The cytoskeleton and disease, *J.Pathol*. 204 (2004) 351-354.
- [136] A Wegner, J Engel. Kinetics of the cooperative association of actin to actin filaments, *Biophys.Chem*. 3 (1975) 215-225.
- [137] L Blanchoin, R Boujemaa-Paterski, C Sykes, J Plastino. Actin dynamics, architecture, and mechanics in cell motility, *Physiol.Rev*. 94 (2014) 235-263.
- [138] TD Pollard, JA Cooper. Actin, a central player in cell shape and movement, *Science*. 326 (2009) 1208-1212.

- [139] M Almonacid, ME Terret, MH Verlhac. Actin-based spindle positioning: new insights from female gametes, *J.Cell.Sci.* 127 (2014) 477-483.
- [140] J Lowery, ER Kuczmariski, H Herrmann, RD Goldman. Intermediate Filaments Play a Pivotal Role in Regulating Cell Architecture and Function, *J.Biol.Chem.* 290 (2015) 17145-17153.
- [141] DL Gard, E Lazarides. The synthesis and distribution of desmin and vimentin during myogenesis in vitro, *Cell.* 19 (1980) 263-275.
- [142] MG Mendez, D Restle, PA Janmey. Vimentin enhances cell elastic behavior and protects against compressive stress, *Biophys.J.* 107 (2014) 314-323.
- [143] A Akhmanova, MO Steinmetz. Control of microtubule organization and dynamics: two ends in the limelight, *Nat.Rev.Mol.Cell Biol.* 16 (2015) 711-726.
- [144] GJ Brouhard, LM Rice. The contribution of alphabeta-tubulin curvature to microtubule dynamics, *J.Cell Biol.* 207 (2014) 323-334.
- [145] A Akhmanova, CC Hoogenraad. Microtubule minus-end-targeting proteins, *Curr.Biol.* 25 (2015) R162-71.
- [146] T Horio, T Murata. The role of dynamic instability in microtubule organization, *Front.Plant.Sci.* 5 (2014) 511.
- [147] DD Tang, BD Gerlach. The roles and regulation of the actin cytoskeleton, intermediate filaments and microtubules in smooth muscle cell migration, *Respir.Res.* 18 (2017) 54-017-0544-7.
- [148] M Ghibaud, L Trichet, J Le Digabel, A Richert, P Hersen, B Ladoux. Substrate topography induces a crossover from 2D to 3D behavior in fibroblast migration, *Biophys.J.* 97 (2009) 357-368.
- [149] P Friedl, D Gilmour. Collective cell migration in morphogenesis, regeneration and cancer, *Nat.Rev.Mol.Cell Biol.* 10 (2009) 445-457.
- [150] P Martin. Wound healing--aiming for perfect skin regeneration, *Science.* 276 (1997) 75-81.
- [151] WT Gerthoffer. Migration of airway smooth muscle cells, *Proc.Am.Thorac.Soc.* 5 (2008) 97-105.

- [152] RA Cleary, R Wang, O Waqar, HA Singer, DD Tang. Role of c-Abl tyrosine kinase in smooth muscle cell migration, *Am.J.Physiol.Cell.Physiol.* 306 (2014) C753-61.
- [153] MF Carlier, J Pernier, P Montaville, S Shekhar, S Kuhn, Cytoskeleton Dynamics and Motility group. Control of polarized assembly of actin filaments in cell motility, *Cell Mol.Life Sci.* 72 (2015) 3051-3067.
- [154] AM Samarel. Costameres, focal adhesions, and cardiomyocyte mechanotransduction, *Am.J.Physiol.Heart Circ.Physiol.* 289 (2005) H2291-301.
- [155] DD Tang. Critical role of actin-associated proteins in smooth muscle contraction, cell proliferation, airway hyperresponsiveness and airway remodeling, *Respir.Res.* 16 (2015) 134-015-0296-1.
- [156] A Murali, K Rajalingam. Small Rho GTPases in the control of cell shape and mobility, *Cell Mol.Life Sci.* 71 (2014) 1703-1721.
- [157] C Leduc, S Etienne-Manneville. Intermediate filaments in cell migration and invasion: the unusual suspects, *Curr.Opin.Cell Biol.* 32 (2015) 102-112.
- [158] MG Mendez, S Kojima, RD Goldman. Vimentin induces changes in cell shape, motility, and adhesion during the epithelial to mesenchymal transition, *FASEB J.* 24 (2010) 1838-1851.
- [159] S Etienne-Manneville. Microtubules in cell migration, *Annu.Rev.Cell Dev.Biol.* 29 (2013) 471-499.
- [160] DJ Tschumperlin. Fibroblasts and the ground they walk on, *Physiology (Bethesda).* 28 (2013) 380-390.
- [161] DE Ingber. Cellular mechanotransduction: putting all the pieces together again, *FASEB J.* 20 (2006) 811-827.
- [162] B Martinac. Mechanosensitive ion channels: molecules of mechanotransduction, *J.Cell.Sci.* 117 (2004) 2449-2460.
- [163] F Guilak, LG Alexopoulos, ML Upton, I Youn, JB Choi, L Cao, et al. The pericellular matrix as a transducer of biomechanical and biochemical signals in articular cartilage, *Ann.N.Y.Acad.Sci.* 1068 (2006) 498-512.

- [164] M Chiquet, L Gelman, R Lutz, S Maier. From mechanotransduction to extracellular matrix gene expression in fibroblasts, *Biochim.Biophys.Acta.* 1793 (2009) 911-920.
- [165] NQ Balaban, US Schwarz, D Riveline, P Goichberg, G Tzur, I Sabanay, et al. Force and focal adhesion assembly: a close relationship studied using elastic micropatterned substrates, *Nat.Cell Biol.* 3 (2001) 466-472.
- [166] A Bershadsky, M Kozlov, B Geiger. Adhesion-mediated mechanosensitivity: a time to experiment, and a time to theorize, *Curr.Opin.Cell Biol.* 18 (2006) 472-481.
- [167] H Wang, TA Brennan, E Russell, JH Kim, KP Egan, Q Chen, et al. R-Spondin 1 promotes vibration-induced bone formation in mouse models of osteoporosis, *J.Mol.Med.(Berl).* 91 (2013) 1421-1429.
- [168] A Huttenlocher, AR Horwitz. Integrins in cell migration, *Cold Spring Harb Perspect.Biol.* 3 (2011) a005074.
- [169] CA Aguilar, Y Lu, S Mao, S Chen. Direct micro-patterning of biodegradable polymers using ultraviolet and femtosecond lasers, *Biomaterials.* 26 (2005) 7642-7649.
- [170] SJ Liliensiek, S Campbell, PF Nealey, CJ Murphy. The scale of substratum topographic features modulates proliferation of corneal epithelial cells and corneal fibroblasts, *J.Biomed.Mater.Res.A.* 79 (2006) 185-192.
- [171] PM Reynolds, RH Pedersen, MO Riehle, N Gadegaard. A dual gradient assay for the parametric analysis of cell-surface interactions, *Small.* 8 (2012) 2541-2547.
- [172] AS Curtis, B Casey, JO Gallagher, D Pasqui, MA Wood, CD Wilkinson. Substratum nanotopography and the adhesion of biological cells. Are symmetry or regularity of nanotopography important? *Biophys.Chem.* 94 (2001) 275-283.
- [173] B Wojciak-Stothard, A Curtis, W Monaghan, K MacDonald, C Wilkinson. Guidance and activation of murine macrophages by nanometric scale topography, *Exp.Cell Res.* 223 (1996) 426-435.
- [174] YG Ko, CC Co, CC Ho. Directing cell migration in continuous microchannels by topographical amplification of natural directional persistence, *Biomaterials.* 34 (2013) 353-360.

- [175] JA Alaerts, VM De Cupere, S Moser, Van den Bosh de Aguilar,P., PG Rouxhet. Surface characterization of poly(methyl methacrylate) microgrooved for contact guidance of mammalian cells, *Biomaterials*. 22 (2001) 1635-1642.
- [176] NW Karuri, TJ Porri, RM Albrecht, CJ Murphy, PF Nealey. Nano- and microscale holes modulate cell-substrate adhesion, cytoskeletal organization, and -beta1 integrin localization in SV40 human corneal epithelial cells, *IEEE Trans.Nanobioscience*. 5 (2006) 273-280.
- [177] P Clark, P Connolly, AS Curtis, JA Dow, CD Wilkinson. Topographical control of cell behaviour: II. Multiple grooved substrata, *Development*. 108 (1990) 635-644.
- [178] SW Lee, SY Kim, MH Lee, KW Lee, R Leesungbok, N Oh. Influence of etched microgrooves of uniform dimension on in vitro responses of human gingival fibroblasts, *Clin.Oral Implants Res*. 20 (2009) 458-466.
- [179] NW Karuri, S Liliensiek, AI Teixeira, G Abrams, S Campbell, PF Nealey, et al. Biological length scale topography enhances cell-substratum adhesion of human corneal epithelial cells, *J.Cell.Sci*. 117 (2004) 3153-3164.
- [180] M Irving, MF Murphy, F Lilley, PW French, DR Burton, S Dixon, et al. The use of abrasive polishing and laser processing for developing polyurethane surfaces for controlling fibroblast cell behaviour, *Mater.Sci.Eng.C.Mater.Biol.Appl*. 71 (2017) 690-697.
- [181] R Rey, JM Garcia-Aznar. A phenomenological approach to modelling collective cell movement in 2D, *Biomech.Model.Mechanobiol*. 12 (2013) 1089-1100.
- [182] Y Jamali, M Azimi, MR Mofrad. A sub-cellular viscoelastic model for cell population mechanics, *PLoS One*. 5 (2010) 10.1371/journal.pone.0012097.
- [183] ME Gracheva, HG Othmer. A continuum model of motility in ameboid cells, *Bull.Math.Biol*. 66 (2004) 167-193.
- [184] B Flaherty, JP McGarry, PE McHugh. Mathematical models of cell motility, *Cell Biochem.Biophys*. 49 (2007) 14-28.
- [185] FJ Vermolen, A Gefen. A semi-stochastic cell-based formalism to model the dynamics of migration of cells in colonies, *Biomech.Model.Mechanobiol*. 11 (2012) 183-195.

- [186] C Borau, RD Kamm, JM Garcia-Aznar. Mechano-sensing and cell migration: a 3D model approach, *Phys.Biol.* 8 (2011) 066008-3975/8/6/066008. Epub 2011 Nov 25.
- [187] NJ Armstrong, KJ Painter, JA Sherratt. A continuum approach to modelling cell-cell adhesion, *J.Theor.Biol.* 243 (2006) 98-113.
- [188] JC Arciero, Q Mi, MF Branca, DJ Hackam, D Swigon. Continuum model of collective cell migration in wound healing and colony expansion, *Biophys.J.* 100 (2011) 535-543.
- [189] MJ Simpson, RE Baker, SW McCue. Models of collective cell spreading with variable cell aspect ratio: a motivation for degenerate diffusion models, *Phys.Rev.E.Stat.Nonlin Soft Matter Phys.* 83 (2011) 021901.
- [190] RT Tranquillo, JD Murray. Continuum model of fibroblast-driven wound contraction: inflammation-mediation, *J.Theor.Biol.* 158 (1992) 135-172.
- [191] JA Sherratt, JC Dallon. Theoretical models of wound healing: past successes and future challenges, *C.R.Biol.* 325 (2002) 557-564.
- [192] D Ambrosi, A Gamba, G Serini. Cell directional persistence and chemotaxis in vascular morphogenesis. *Bull Math Biol.* 66 (2005) 1851.
- [193] G Fenteany, PA Janmey, TP Stossel. Signaling pathways and cell mechanics involved in wound closure by epithelial cell sheets, *Curr.Biol.* 10 (2000) 831-838.
- [194] T Omelchenko, JM Vasiliev, IM Gelfand, HH Feder, EM Bonder. Rho-dependent formation of epithelial "leader" cells during wound healing, *Proc.Natl.Acad.Sci.U.S.A.* 100 (2003) 10788-10793.
- [195] JH Kim, LJ Dooling, AR Asthagiri. Intercellular mechanotransduction during multicellular morphodynamics, *J.R.Soc.Interface.* 7 Suppl 3 (2010) S341-50.
- [196] RJ Pelham Jr, Y Wang. Cell locomotion and focal adhesions are regulated by substrate flexibility, *Proc.Natl.Acad.Sci.U.S.A.* 94 (1997) 13661-13665.
- [197] T Takebayashi, M Iwamoto, A Jikko, T Matsumura, M Enomoto-Iwamoto, F Myoukai, et al. Hepatocyte growth factor/scatter factor modulates cell motility, proliferation, and proteoglycan synthesis of chondrocytes, *J.Cell Biol.* 129 (1995) 1411-1419.

- [198] MH Zaman, RD Kamm, P Matsudaira, DA Lauffenburger. Computational model for cell migration in three-dimensional matrices, *Biophys.J.* 89 (2005) 1389-1397.
- [199] EA Codling, MJ Plank, S Benhamou. Random walk models in biology, *J.R.Soc.Interface.* 5 (2008) 813-834.
- [200] R Brown. A brief account of microscopical observations made in the months of June, July and August, 1827, on the particles contained in the pollen of plants; and the general existence of active molecules in organic and inorganic bodies. *Philos. Mag.* 4 (1928) 161.
- [201] A1[a Einstein, Über die von der molekularkinetischen Theorie der Wärme geforderte Bewegung von in ruhenden Flüssigkeiten suspendierten Teilchen, Johann Ambrosius Barth, Leipzig, 1905.
- [202] S Benhamou. Detecting an orientation component in animal paths when the preferred direction is individual-dependent, *Ecology.* 87 (2006) 518-528.
- [203] W Alt. Biased random walk models for chemotaxis and related diffusion approximations, *J.Math.Biol.* 9 (1980) 147-177.
- [204] HG Othmer, SR Dunbar, W Alt. Models of dispersal in biological systems, *J.Math.Biol.* 26 (1988) 263-298.
- [205] TM Embley, W Martin. Eukaryotic evolution, changes and challenges, *Nature.* 440 (2006) 623-630.
- [206] A Cuadrado, P Moreno-Murciano, J Pedraza-Chaverri. The transcription factor Nrf2 as a new therapeutic target in Parkinson's disease, *Expert Opin.Ther.Targets.* 13 (2009) 319-329.
- [207] JM Lee, MJ Calkins, K Chan, YW Kan, JA Johnson. Identification of the NF-E2-related factor-2-dependent genes conferring protection against oxidative stress in primary cortical astrocytes using oligonucleotide microarray analysis, *J.Biol.Chem.* 278 (2003) 12029-12038.
- [208] HK Jyrkkanen, S Kuosmanen, M Heinaniemi, H Laitinen, E Kansanen, E Mella-Aho, et al. Novel insights into the regulation of antioxidant-response-element-mediated gene expression by electrophiles: induction of the transcriptional repressor BACH1 by Nrf2, *Biochem.J.* 440 (2011) 167-174.

- [209] Y Hirotsu, F Katsuoka, R Funayama, T Nagashima, Y Nishida, K Nakayama, et al. Nrf2-MafG heterodimers contribute globally to antioxidant and metabolic networks, *Nucleic Acids Res.* 40 (2012) 10228-10239.
- [210] T Suzuki, M Yamamoto. Molecular basis of the Keap1-Nrf2 system, *Free Radic.Biol.Med.* 88 (2015) 93-100.
- [211] HK Bryan, A Olayanju, CE Goldring, BK Park. The Nrf2 cell defence pathway: Keap1-dependent and -independent mechanisms of regulation, *Biochem.Pharmacol.* 85 (2013) 705-717.
- [212] I Bellezza, AL Mierla, A Minelli. Nrf2 and NF-kappaB and Their Concerted Modulation in Cancer Pathogenesis and Progression, *Cancers (Basel)*. 2 (2010) 483-497.
- [213] JM Lee, J Li, DA Johnson, TD Stein, AD Kraft, MJ Calkins, et al. Nrf2, a multi-organ protector? *FASEB J.* 19 (2005) 1061-1066.
- [214] M Ghosh, Y Yang, JD Rothstein, MB Robinson. Nuclear factor-kappaB contributes to neuron-dependent induction of glutamate transporter-1 expression in astrocytes, *J.Neurosci.* 31 (2011) 9159-9169.
- [215] L Baird, D Lleres, S Swift, AT Dinkova-Kostova. Regulatory flexibility in the Nrf2-mediated stress response is conferred by conformational cycling of the Keap1-Nrf2 protein complex, *Proc.Natl.Acad.Sci.U.S.A.* 110 (2013) 15259-15264.
- [216] I Figiel. Pro-inflammatory cytokine TNF-alpha as a neuroprotective agent in the brain, *Acta Neurobiol.Exp.(Wars)*. 68 (2008) 526-534.
- [217] J Chiu, IW Dawes. Redox control of cell proliferation, *Trends Cell Biol.* 22 (2012) 592-601.
- [218] T Suzuki, T Shibata, K Takaya, K Shiraishi, T Kohno, H Kunitoh, et al. Regulatory nexus of synthesis and degradation deciphers cellular Nrf2 expression levels, *Mol.Cell.Biol.* 33 (2013) 2402-2412.
- [219] J Lee, MS Kim. The role of GSK3 in glucose homeostasis and the development of insulin resistance, *Diabetes Res.Clin.Pract.* 77 Suppl 1 (2007) S49-57.
- [220] S Chowdhry, Y Zhang, M McMahon, C Sutherland, A Cuadrado, JD Hayes. Nrf2 is controlled by two distinct beta-TrCP recognition motifs in its Neh6 domain, one of which can be modulated by GSK-3 activity, *Oncogene.* 32 (2013) 3765-3781.

- [221] Al Rojo, ON Medina-Campos, P Rada, A Zuniga-Toala, A Lopez-Gazcon, S Espada, et al. Signaling pathways activated by the phytochemical nordihydroguaiaretic acid contribute to a Keap1-independent regulation of Nrf2 stability: Role of glycogen synthase kinase-3, *Free Radic.Biol.Med.* 52 (2012) 473-487.
- [222] RK Thimmulappa, KH Mai, S Srisuma, TW Kensler, M Yamamoto, S Biswal. Identification of Nrf2-regulated genes induced by the chemopreventive agent sulforaphane by oligonucleotide microarray, *Cancer Res.* 62 (2002) 5196-5203.
- [223] JD Hayes, AT Dinkova-Kostova. The Nrf2 regulatory network provides an interface between redox and intermediary metabolism, *Trends Biochem.Sci.* 39 (2014) 199-218.
- [224] JD Wardyn, AH Ponsford, CM Sanderson. Dissecting molecular cross-talk between Nrf2 and NF-kappaB response pathways, *Biochem.Soc.Trans.* 43 (2015) 621-626.
- [225] W Lin, RT Wu, T Wu, TO Khor, H Wang, AN Kong. Sulforaphane suppressed LPS-induced inflammation in mouse peritoneal macrophages through Nrf2 dependent pathway, *Biochem.Pharmacol.* 76 (2008) 967-973.
- [226] JH Suh, SV Shenvi, BM Dixon, H Liu, AK Jaiswal, RM Liu, et al. Decline in transcriptional activity of Nrf2 causes age-related loss of glutathione synthesis, which is reversible with lipoic acid, *Proc.Natl.Acad.Sci.U.S.A.* 101 (2004) 3381-3386.
- [227] H Pan, H Wang, X Wang, L Zhu, L Mao. The absence of Nrf2 enhances NF-kappaB-dependent inflammation following scratch injury in mouse primary cultured astrocytes, *Mediators Inflamm.* 2012 (2012) 217580.
- [228] AE Frakes, L Ferraiuolo, AM Haidet-Phillips, L Schmelzer, L Braun, CJ Miranda, et al. Microglia induce motor neuron death via the classical NF-kappaB pathway in amyotrophic lateral sclerosis, *Neuron.* 81 (2014) 1009-1023.
- [229] B Kaltschmidt, D Widera, C Kaltschmidt. Signaling via NF-kappaB in the nervous system, *Biochim.Biophys.Acta.* 1745 (2005) 287-299.
- [230] C Mauro, SC Leow, E Anso, S Rocha, AK Thotakura, L Tornatore, et al. NF-kappaB controls energy homeostasis and metabolic adaptation by upregulating mitochondrial respiration, *Nat.Cell Biol.* 13 (2011) 1272-1279.
- [231] ST Smale. Hierarchies of NF-kappaB target-gene regulation, *Nat.Immunol.* 12 (2011) 689-694.

- [232] MS Hayden, S Ghosh. Shared principles in NF-kappaB signaling, *Cell*. 132 (2008) 344-362.
- [233] H Zhong, MJ May, E Jimi, S Ghosh. The phosphorylation status of nuclear NF-kappa B determines its association with CBP/p300 or HDAC-1, *Mol.Cell*. 9 (2002) 625-636.
- [234] ND Perkins, TD Gilmore. Good cop, bad cop: the different faces of NF-kappaB, *Cell Death Differ*. 13 (2006) 759-772.
- [235] S Mincheva-Tasheva, RM Soler. NF-kappaB signaling pathways: role in nervous system physiology and pathology, *Neuroscientist*. 19 (2013) 175-194.
- [236] Q Li, IM Verma. NF-kappaB regulation in the immune system, *Nat.Rev.Immunol*. 2 (2002) 725-734.
- [237] CK Glass, K Saijo, B Winner, MC Marchetto, FH Gage. Mechanisms underlying inflammation in neurodegeneration, *Cell*. 140 (2010) 918-934.
- [238] HL Pahl. Activators and target genes of Rel/NF-kappaB transcription factors, *Oncogene*. 18 (1999) 6853-6866.
- [239] DA Turner, P Paszek, DJ Woodcock, DE Nelson, CA Horton, Y Wang, et al. Physiological levels of TNFalpha stimulation induce stochastic dynamics of NF-kappaB responses in single living cells, *J.Cell.Sci*. 123 (2010) 2834-2843.
- [240] L Liu, C Chan. The role of inflammasome in Alzheimer's disease, *Ageing Res.Rev*. 15 (2014) 6-15.
- [241] RE Lee, SR Walker, K Savery, DA Frank, S Gaudet. Fold change of nuclear NF-kappaB determines TNF-induced transcription in single cells, *Mol.Cell*. 53 (2014) 867-879.
- [242] C Liu, G Cui, M Zhu, X Kang, H Guo. Neuroinflammation in Alzheimer's disease: chemokines produced by astrocytes and chemokine receptors, *Int.J.Clin.Exp.Pathol*. 7 (2014) 8342-8355.
- [243] H Sakurai, S Suzuki, N Kawasaki, H Nakano, T Okazaki, A Chino, et al. Tumor necrosis factor-alpha-induced IKK phosphorylation of NF-kappaB p65 on serine 536 is mediated through the TRAF2, TRAF5, and TAK1 signaling pathway, *J.Biol.Chem*. 278 (2003) 36916-36923.

- [244] JT Winston, P Strack, P Beer-Romero, CY Chu, SJ Elledge, JW Harper. The SCFbeta-TRCP-ubiquitin ligase complex associates specifically with phosphorylated destruction motifs in I κ B α and beta-catenin and stimulates I κ B α ubiquitination in vitro, *Genes Dev.* 13 (1999) 270-283.
- [245] S Bergqvist, V Alverdi, B Mengel, A Hoffmann, G Ghosh, EA Komives. Kinetic enhancement of NF- κ B-DNA dissociation by I κ B α , *Proc.Natl.Acad.Sci.U.S.A.* 106 (2009) 19328-19333.
- [246] J Chen, ZJ Chen. Regulation of NF- κ B by ubiquitination, *Curr.Opin.Immunol.* 25 (2013) 4-12.
- [247] IE Wertz, KM O'Rourke, H Zhou, M Eby, L Aravind, S Seshagiri, et al. De-ubiquitination and ubiquitin ligase domains of A20 downregulate NF- κ B signalling, *Nature.* 430 (2004) 694-699.
- [248] RK Thimmulappa, H Lee, T Rangasamy, SP Reddy, M Yamamoto, TW Kensler, et al. Nrf2 is a critical regulator of the innate immune response and survival during experimental sepsis, *J.Clin.Invest.* 116 (2006) 984-995.
- [249] V Ganesh Yerra, G Negi, SS Sharma, A Kumar. Potential therapeutic effects of the simultaneous targeting of the Nrf2 and NF- κ B pathways in diabetic neuropathy, *Redox Biol.* 1 (2013) 394-397.
- [250] T Jiang, F Tian, H Zheng, SA Whitman, Y Lin, Z Zhang, et al. Nrf2 suppresses lupus nephritis through inhibition of oxidative injury and the NF- κ B-mediated inflammatory response, *Kidney Int.* 85 (2014) 333-343.
- [251] MP Soares, MP Seldon, IP Gregoire, T Vassilevskaia, PO Berberat, J Yu, et al. Heme oxygenase-1 modulates the expression of adhesion molecules associated with endothelial cell activation, *J.Immunol.* 172 (2004) 3553-3563.
- [252] JE Kim, DJ You, C Lee, C Ahn, JY Seong, JI Hwang. Suppression of NF- κ B signaling by KEAP1 regulation of IKK β activity through autophagic degradation and inhibition of phosphorylation, *Cell.Signal.* 22 (2010) 1645-1654.
- [253] A Neymotin, NY Calingasan, E Wille, N Naseri, S Petri, M Damiano, et al. Neuroprotective effect of Nrf2/ARE activators, CDDO ethylamide and CDDO trifluoroethylamide, in a mouse model of amyotrophic lateral sclerosis, *Free Radic.Biol.Med.* 51 (2011) 88-96.
- [254] LO Brandenburg, M Kipp, R Lucius, T Pufe, CJ Wruck. Sulforaphane suppresses LPS-induced inflammation in primary rat microglia, *Inflamm.Res.* 59 (2010) 443-450.

- [255] CA Danilov, K Chandrasekaran, J Racz, L Soane, C Zielke, G Fiskum. Sulforaphane protects astrocytes against oxidative stress and delayed death caused by oxygen and glucose deprivation, *Glia*. 57 (2009) 645-656.
- [256] RA Williams, J Timmis, EE Qwarnstrom. Computational Models of the NF-kappaB Signalling Pathway, (2014) 131.
- [257] S Choudhary, M Kalita, L Fang, KV Patel, B Tian, Y Zhao, et al. Inducible tumor necrosis factor (TNF) receptor-associated factor-1 expression couples the canonical to the non-canonical NF-kappaB pathway in TNF stimulation, *J.Biol.Chem.* 288 (2013) 14612-14623.
- [258] M Pogson, M Holcombe, R Smallwood, E Qwarnstrom. Introducing spatial information into predictive NF-kappaB modelling--an agent-based approach, *PLoS One*. 3 (2008) e2367.
- [259] P Paszek, S Ryan, L Ashall, K Sillitoe, CV Harper, DG Spiller, et al. Population robustness arising from cellular heterogeneity, *Proc.Natl.Acad.Sci.U.S.A.* 107 (2010) 11644-11649.
- [260] F Carlotti, SK Dower, EE Qwarnstrom. Dynamic shuttling of nuclear factor kappa B between the nucleus and cytoplasm as a consequence of inhibitor dissociation, *J.Biol.Chem.* 275 (2000) 41028-41034.
- [261] A Hoffmann, A Levchenko, ML Scott, D Baltimore. The IkappaB-NF-kappaB signaling module: temporal control and selective gene activation, *Science*. 298 (2002) 1241-1245.
- [262] EL O'Dea, D Barken, RQ Peralta, KT Tran, SL Werner, JD Kearns, et al. A homeostatic model of IkappaB metabolism to control constitutive NF-kappaB activity, *Mol.Syst.Biol.* 3 (2007) 111.
- [263] DE Nelson, V See, G Nelson, MR White. Oscillations in transcription factor dynamics: a new way to control gene expression, *Biochem.Soc.Trans.* 32 (2004) 1090-1092.
- [264] T Lipniacki, P Paszek, AR Brasier, B Luxon, M Kimmel. Mathematical model of NF-kappaB regulatory module, *J.Theor.Biol.* 228 (2004) 195-215.
- [265] J Stark, C Chan, AJ George. Oscillations in the immune system, *Immunol.Rev.* 216 (2007) 213-231.

- [266] M Cohn, J Mata. Quantitative modeling of immune responses, *Immunol.Rev.* 216 (2007) 5-8.
- [267] M Pogson, R Smallwood, E Qvarnstrom, M Holcombe. Formal agent-based modelling of intracellular chemical interactions, *BioSystems.* 85 (2006) 37-45.
- [268] N Ambrozova, J Ulrichova, A Galandakova. Models for the study of skin wound healing. The role of Nrf2 and NF-kappaB, *Biomed.Pap.Med.Fac.Univ.Palacky Olomouc Czech.Repub.* 161 (2017) 1-13.
- [269] HS Khalil, A Goltsov, SP Langdon, DJ Harrison, J Bown, Y Deeni. Quantitative analysis of NRF2 pathway reveals key elements of the regulatory circuits underlying antioxidant response and proliferation of ovarian cancer cells, *J.Biotechnol.* 202 (2015) 12-30.
- [270] S Krishna, MH Jensen, K Sneppen. Minimal model of spiky oscillations in NF-kappaB signaling, *Proc.Natl.Acad.Sci.U.S.A.* 103 (2006) 10840-10845.
- [271] P Yde, B Mengel, MH Jensen, S Krishna, A Trusina. Modeling the NF-kappaB mediated inflammatory response predicts cytokine waves in tissue, *BMC Syst.Biol.* 5 (2011) 115-0509-5-115.
- [272] SL Werner, D Barken, A Hoffmann. Stimulus specificity of gene expression programs determined by temporal control of IKK activity, *Science.* 309 (2005) 1857-1861.
- [273] DM Longo, J Selimkhanov, JD Kearns, J Hasty, A Hoffmann, LS Tsimring. Dual delayed feedback provides sensitivity and robustness to the NF-kappaB signaling module, *PLoS Comput.Biol.* 9 (2013) e1003112.
- [274] S Hardy, PN Robillard. Modeling and simulation of molecular biology systems using petri nets: modeling goals of various approaches, *J.Bioinform Comput.Biol.* 2 (2004) 595-613.
- [275] Z Heidary, J Ghaisari, S Moein, M Naderi, Y Gheisari. Stochastic Petri Net Modeling of Hypoxia Pathway Predicts a Novel Incoherent Feed-Forward Loop Controlling SDF-1 Expression in Acute Kidney Injury, *IEEE Trans.Nanobioscience.* 15 (2016) 19-26.
- [276] C Chaouiya. Petri net modelling of biological networks, *Brief Bioinform.* 8 (2007) 210-219.

- [277] A Doi, S Fujita, H Matsuno, M Nagasaki, S Miyano. Constructing biological pathway models with hybrid functional Petri nets, *In.Silico Biol.* 4 (2004) 271-291.
- [278] S Hardy, PN Robillard. Modeling and simulation of molecular biology systems using petri nets: modeling goals of various approaches, *J.Bioinform Comput.Biol.* 2 (2004) 595-613.
- [279] H Matsuno, Y Tanaka, H Aoshima, A Doi, M Matsui, S Miyano. Biopathways representation and simulation on hybrid functional Petri net, *In.Silico Biol.* 3 (2003) 389-404.
- [280] A Sackmann, M Heiner, I Koch. Application of Petri net based analysis techniques to signal transduction pathways, *BMC Bioinformatics.* 7 (2006) 482.
- [281] Z Drebert, M MacAskill, D Doughty-Shenton, K De Bosscher, M Bracke, PWF Hadoke, et al. Colon cancer-derived myofibroblasts increase endothelial cell migration by glucocorticoid-sensitive secretion of a pro-migratory factor, *Vascul Pharmacol.* 89 (2017) 19-30.
- [282] F Graner, JA Glazier. Simulation of biological cell sorting using a two-dimensional extended Potts model, *Phys.Rev.Lett.* 69 (1992) 2013-2016.
- [283] P Lecca, D Morpurgo. Modelling non-homogeneous stochastic reaction-diffusion systems: the case study of gemcitabine-treated non-small cell lung cancer growth, *BMC Bioinformatics.* 13 Suppl 14 (2012) S14-2105-13-S14-S14. Epub 2012 Sep 7.
- [284] O De Wever, P Demetter, M Mareel, M Bracke. Stromal myofibroblasts are drivers of invasive cancer growth, *Int.J.Cancer.* 123 (2008) 2229-2238.
- [285] A Seluanov, C Hine, J Azpurua, M Feigenson, M Bozzella, Z Mao, et al. Hypersensitivity to contact inhibition provides a clue to cancer resistance of naked mole-rat, *Proc.Natl.Acad.Sci.U.S.A.* 106 (2009) 19352-19357.
- [286] H Najgebauer, T Liloglou, PV Jithesh, OT Giger, A Varro, CM Sanderson. Integrated Omics Profiling Reveals Novel Patterns of Epigenetic Programming in Cancer-Associated Myofibroblasts, *Carcinogenesis.* (2019).
- [287] N Hoiby, O Ciofu, HK Johansen, ZJ Song, C Moser, PO Jensen, et al. The clinical impact of bacterial biofilms, *Int.J.Oral Sci.* 3 (2011) 55-65.
- [288] E Drenkard. Antimicrobial resistance of *Pseudomonas aeruginosa* biofilms, *Microbes Infect.* 5 (2003) 1213-1219.

- [289] VJ Savage, I Chopra, AJ O'Neill. Staphylococcus aureus biofilms promote horizontal transfer of antibiotic resistance, *Antimicrob.Agents Chemother.* 57 (2013) 1968-1970.
- [290] R Xing, SP Lyngstadaas, JE Ellingsen, S Taxt-Lamolle, HJ Haugen. The influence of surface nanoroughness, texture and chemistry of TiZr implant abutment on oral biofilm accumulation, *Clin.Oral Implants Res.* 26 (2015) 649-656.
- [291] CL Stokes, DA Lauffenburger, SK Williams. Migration of individual microvessel endothelial cells: stochastic model and parameter measurement, *J.Cell.Sci.* 99 (Pt 2) (1991) 419-430.
- [292] MH Gail, CW Boone. The locomotion of mouse fibroblasts in tissue culture, *Biophys.J.* 10 (1970) 980-993.
- [293] A Wright, YH Li, C Zhu. The differential effect of endothelial cell factors on in vitro motility of malignant and non-malignant cells, *Ann.Biomed.Eng.* 36 (2008) 958-969.
- [294] JR Howse, RA Jones, AJ Ryan, T Gough, R Vafabakhsh, R Golestanian. Self-motile colloidal particles: from directed propulsion to random walk, *Phys.Rev.Lett.* 99 (2007) 048102.
- [295] GA Dunn, AF Brown. A unified approach to analysing cell motility, *J.Cell Sci.Suppl.* 8 (1987) 81-102.
- [296] PE Kloeden, Numerical solution of stochastic differential equations, Springer-Verlag, Berlin ; London, 1992.
- [297] A Olayanju, IM Copple, HK Bryan, GT Edge, RL Sison, MW Wong, et al. Brusatol provokes a rapid and transient inhibition of Nrf2 signaling and sensitizes mammalian cells to chemical toxicity-implications for therapeutic targeting of Nrf2, *Free Radic.Biol.Med.* 78 (2015) 202-212.
- [298] MD Shields, J Zhang, The generalization of Latin hypercube sampling, (2016) 1 online resource.
- [299] G Pan, P Ye, P Wang. A Novel Latin hypercube algorithm via translational propagation, *ScientificWorldJournal.* 2014 (2014) 163949.
- [300] W Ng, B Minasny, B Malone, P Filippi. In search of an optimum sampling algorithm for prediction of soil properties from infrared spectra, *PeerJ.* 6 (2018) e5722.

- [301] SC Gifford, MG Frank, J Derganc, C Gabel, RH Austin, T Yoshida, et al. Parallel microchannel-based measurements of individual erythrocyte areas and volumes, *Biophys.J.* 84 (2003) 623-633.
- [302] AF Ali, MA Tawhid. A hybrid cuckoo search algorithm with Nelder Mead method for solving global optimization problems, *Springerplus.* 5 (2016) 473-016-2064-1. eCollection 2016.
- [303] SM Baker, RW Buckheit 3rd, MM Falk. Green-to-red photoconvertible fluorescent proteins: tracking cell and protein dynamics on standard wide-field mercury arc-based microscopes, *BMC Cell Biol.* 11 (2010) 15-2121-11-15.
- [304] R Hulspas, MR O'Gorman, BL Wood, JW Gratama, DR Sutherland. Considerations for the control of background fluorescence in clinical flow cytometry, *Cytometry B.Clin.Cytom.* 76 (2009) 355-364.
- [305] M Yu, H Li, Q Liu, F Liu, L Tang, C Li, et al. Nuclear factor p65 interacts with Keap1 to repress the Nrf2-ARE pathway, *Cell.Signal.* 23 (2011) 883-892.
- [306] L Zuo, BT Hemmelgarn, CC Chuang, TM Best. The Role of Oxidative Stress-Induced Epigenetic Alterations in Amyloid-beta Production in Alzheimer's Disease, *Oxid Med.Cell.Longev.* 2015 (2015) 604658.
- [307] C Rohr, W Marwan, M Heiner. Snoopy--a unifying Petri net framework to investigate biomolecular networks, *Bioinformatics.* 26 (2010) 974-975.
- [308] M Chaves, R Albert, ED Sontag. Robustness and fragility of Boolean models for genetic regulatory networks, *J.Theor.Biol.* 235 (2005) 431-449.
- [309] M Xue, H Momiji, N Rabbani, G Barker, T Bretschneider, A Shmygol, et al. Frequency Modulated Translocational Oscillations of Nrf2 Mediate the Antioxidant Response Element Cytoprotective Transcriptional Response, *Antioxid.Redox Signal.* 23 (2015) 613-629.
- [310] P Rada, AI Rojo, S Chowdhry, M McMahon, JD Hayes, A Cuadrado. SCF/ β -TrCP promotes glycogen synthase kinase 3-dependent degradation of the Nrf2 transcription factor in a Keap1-independent manner, *Mol.Cell.Biol.* 31 (2011) 1121-1133.
- [311] DW Powell, RC Mifflin, JD Valentich, SE Crowe, JI Saada, AB West. Myofibroblasts. I. Paracrine cells important in health and disease, *Am.J.Physiol.* 277 (1999) C1-9.

- [312] JC Dallon, M Scott, WV Smith. A force based model of individual cell migration with discrete attachment sites and random switching terms, *J.Biomech.Eng.* 135 (2013) 71008.
- [313] JC Dallon, JA Sherratt, PK Maini. Mathematical modelling of extracellular matrix dynamics using discrete cells: fiber orientation and tissue regeneration, *J.Theor.Biol.* 199 (1999) 449-471.
- [314] A Seluanov, C Hine, J Azpurua, M Feigenson, M Bozzella, Z Mao, et al. Hypersensitivity to contact inhibition provides a clue to cancer resistance of naked mole-rat, *Proc.Natl.Acad.Sci.U.S.A.* 106 (2009) 19352-19357.
- [315] DC Walker, G Hill, SM Wood, RH Smallwood, J Southgate. Agent-based computational modeling of wounded epithelial cell monolayers, *IEEE Trans.Nanobioscience.* 3 (2004) 153-163.
- [316] W Lin, RT Wu, T Wu, TO Khor, H Wang, AN Kong. Sulforaphane suppressed LPS-induced inflammation in mouse peritoneal macrophages through Nrf2 dependent pathway, *Biochem.Pharmacol.* 76 (2008) 967-973.
- [317] MP Soares, MP Seldon, IP Gregoire, T Vassilevskaia, PO Berberat, J Yu, et al. Heme oxygenase-1 modulates the expression of adhesion molecules associated with endothelial cell activation, *J.Immunol.* 172 (2004) 3553-3563.
- [318] JE Kim, DJ You, C Lee, C Ahn, JY Seong, JI Hwang. Suppression of NF-kappaB signaling by KEAP1 regulation of IKKbeta activity through autophagic degradation and inhibition of phosphorylation, *Cell.Signal.* 22 (2010) 1645-1654.